

Transport properties of 2D semi-Dirac systems: Effects of spin-orbit coupling and magnetic field

PRIYANKA SINHA
Roll No. 166121018

Supervisor: Prof. Saurabh Basu



DEPARTMENT OF PHYSICS
INDIAN INSTITUTE OF TECHNOLOGY GUWAHATI
AMINGAON, GUWAHATI, ASSAM-781039, INDIA

*A dissertation submitted to IIT Guwahati
for the partial fulfilment of the requirements for the Degree of
Doctor of Philosophy*

Dec 2021



DISCLAIMER

The bibliography included in this thesis is by no means complete but contains the ones which are consulted thoroughly by me. I apologize for inadvertently missing out some of the research papers, review articles and other scientific documents pertaining to the focus of this thesis, which should also have been cited. For illustration purposes, some of the figures in this thesis are taken from other sources and properly cited.







I dedicate this thesis to

My parents



DECLARATION OF AUTHORSHIP

Date: 27/12/2021

I, Priyanka Sinha with Registration No. 166121018, hereby declare that the work contained in this thesis entitled “**Transport properties of 2D semi-Dirac systems: Effects of spin-orbit coupling and magnetic field**”, submitted by me to the Indian Institute of Technology Guwahati, for the award of the degree of PhD, are the results of my own work under the supervision of Prof. Saurabh Basu. To the best of my knowledge, it neither contains materials previously published or written by any other person, nor it has been submitted for any degree/diploma or any other academic award anywhere before.

Priyanka Sinha

Priyanka Sinha

Department of Physics

Indian Institute of Technology Guwahati

Amingaon 781039, Assam, North Guwahati, India



CERTIFICATE FROM SUPERVISOR

Date: 27/12/2021

This is to certify that the thesis entitled “**Transport properties of 2D semi-Dirac systems: Effects of spin-orbit coupling and magnetic field**”, submitted by Ms. Priyanka Sinha with Registration No. 166121018, a student of Department of physics of the PhD Program of IIT Guwahati, is based upon her own research work under my supervision. This is also to certify that neither the thesis nor any part of it has been submitted for any degree/diploma or any other academic award anywhere before. In my opinion, the thesis fulfils the requirement for the award of the degree of Doctor of Philosophy.



Prof. Saurabh Basu

Professor

Department of Physics

Indian Institute of Technology Guwahati

Amingaon 781039, Assam, North Guwahati, India



ACKNOWLEDGMENTS

I would like to acknowledge each and everyone who showed me the right path in “Ph.D., The Journey to My Dreams” and contributed directly or indirectly with their support and love.

First and foremost, my deep gratitude goes to my supervisor Prof. Saurabh Basu for his direct support, tremendous patience, and complete dedication to my research career. His guidance helped me in all the time of research and writing of this thesis. The development of many of the ideas in this thesis would not have been possible without him. I have learned many things from our discussions and his insightful comments towards my research. I would often come to him with my doubts, and he provided me with brilliant ideas at his best every time. The best quality that I am particularly grateful to him for giving me the full freedom to pursue my research. I am privileged to be a member of his research group.

I am forever indebted to my father, who has been a great support for me throughout my career as it is quoted, “Behind every great daughter is a truly amazing dad”. Even though he did not find leisure time for himself, he still managed to travel everywhere with me and encouraged me to pursue my career goals. The lady who has always been there for me with sleepless night, is my mother. My parents had been like a pillar of strength in the most challenging phases of my career. My one and only little sister Sriyanka added a bunch of happiness along with them. Without their kindness and unconditional love, I couldn't live my dreams.

I would also convey special thanks to my mentor Prof. Shuichi Murakami with whom I have completed my last two projects. It has been a great pleasure to work under his guidance. I have learned a lot from him. His tremendous input in my research has sharpened and polished my scientific skills. I want to thank Dr. Sudin Ganguly for being my collaborator and mentor in my initial phases.

I am grateful to the chairman of my doctoral committee, Prof. Subhradip Ghosh, doctoral committee members Prof. Dilip pal and Prof. Muhammad Qureshi for their comments and valuable suggestions.

I would like to thank my seniors Dr. SK Noor Nabi, Dr. Priyadarshini Kapri, Dr. Sunayana Dutta, and my juniors Shilpi, Sayan, Mijanur, Dipendu, Srijata, Koustav for many

useful discussions and constant support throughout my journey. I am thankful to Dr. Sk Firoz Islam, with whom I have interacted during my Ph.D. and had numerous fruitful discussions. I must thank Dr. Krishnanjan pramanik, Dr. Rashidul Islam, Dr. Sourav Chattopadhyay, who helped me whenever I had short technical queries. I am grateful to Dr. Debasis Das, who helped me in learning DFT at my earlier phase after joining. I am thankful to all my friends, seniors, and juniors for making my stay at IITG a memorable one.

I am thankful to the Indian Institute of Technology Guwahati, and the Government of India, Ministry of Human Resource Development for the financial support. I must thank all the technical staff of the department of physics, especially Mr. Basab Bijoy Purkayastha and Mr. Hemanta Medhi for their cooperation during my Ph.D. journey. I am also thankful to other staff members Mr. Lokesh Chakravorty, Himanku da and Ambarish da for their kindness and helping nature.

I would like to thank all my teachers for their support and encouragement to pursue my dreams over the years. Especially, I am thankful to two of my home tutors Mr. Kishore Bhakat and the late Prasanta Singh, who influenced me greatly when I was in school.

I wish to thank all my family members and friends for supporting me throughout my life. I must appreciate the IIT Guwahati campus for its mesmerizing beauty. And finally, I am thankful to Dr. Rafiqul Rahaman, without whom it would not have been possible. His extreme support, both scientific and emotional, made my Ph.D. journey beautiful.

Priyanka Sinha

ABSTRACT

In this thesis, our work addresses the outcomes of the transport measurements in the presence of spin-orbit couplings and an external magnetic field in a two-dimensional (2D) semi-Dirac system. Semi-Dirac systems are characterized by a parabolic band dispersion along one direction in the Brillouin zone, and linear along the other direction. All the while, we have compared our results with those for the Dirac materials, a well-known example being graphene. Our results have exciting prospects for engineering tunable transport properties for 2D materials in the presence of spin-orbit couplings and magnetic field. Thus, our work mainly focuses on two novel phenomena, that is, the quantum spin Hall effect and the quantum Hall effect in a semi-Dirac system. To begin with, in the presence of spin-orbit coupling, we essentially study the quantum transport properties of a 2D semi-Dirac system modeled by a Kane-Mele Hamiltonian. We have systematically explored the relative strengths of the intrinsic (Haldane type, but with different fluxes for different spin degrees of freedom) and Rashba spin-orbit couplings on the edge states of a nanoribbon both analytically and numerically, and its band structures. Further, we have numerically studied the transport properties, such as the charge conductance, local density of states, etc via Landauer-Büttiker approach. We have observed significant deviations in the transport properties owing to the anisotropic band dispersion of the semi-Dirac system as compared to the results known for Dirac materials. In the next part, we have introduced a uniform magnetic field perpendicular to the plane of the system and hence explored its effects on the transport characteristics using Kubo formula. We looked into the features of the density of states, properties of the Landau levels, Hofstadter butterfly spectrum, and as well as the magneto-transport properties, such as the longitudinal and the transverse (Hall) conductivities. In addition, we have also explored the magneto-optical properties as a function of the incident photon energies in the near ultraviolet-visible regime and studied the effects of electron filling, circular polarization, Faraday rotation, etc.



List of Publications (included in this thesis)

Publications in journals:

1. **P. Sinha**, S. Ganguly, and S. Basu, “Analytic and numeric computation of edge states and conductivity of a Kane-Mele nanoribbon”, [Physica E : Low dimensional systems and nanostructures](#) 103, 314 (2018).
2. **P. Sinha** and S. Basu, “Study of edge states and conductivity in spin-orbit coupled bilayer graphene”, [Eur. Phys. J. B](#) 92, 207 (2019).
3. **P. Sinha**, S. Murakami and S. Basu, “Quantum Hall studies of a semi-Dirac nanoribbon”, [Phys. Rev. B](#) 102, 085416 (2020).

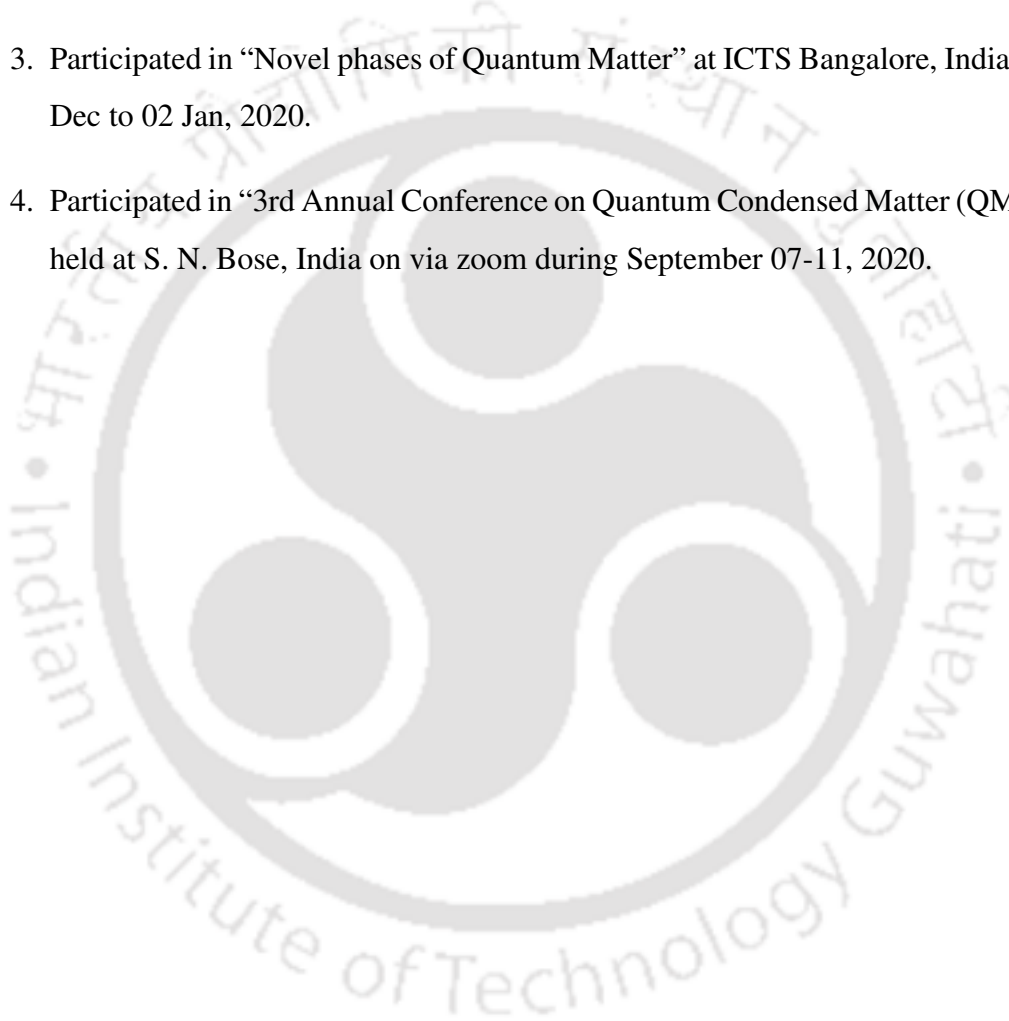
Paper submitted to journals:

4. **P. Sinha**, S. Murakami and S. Basu, “Magneto-optical properties of a semi-Dirac system in the near ultraviolet-visible frequency regime”, accepted in [Phys. Rev. B](#), earlier version is also available at [arXiv:2110.12670](#).



School and Conference attended

1. Participated in the mini-school on “Topology and Interactions in Quantum Matter” held at the Department of Physical Sciences (DPS), Indian Institute of Science Education and Research (IISER) Kolkata from 08-10 January, 2018.
2. Poster presented on “ Conductivity and edge states in zigzag graphene ribbon” in the International Conference on “Topological Aspects of quantum matter” held at TIFR, Mumbai, India, December 17-20, 2018.
3. Participated in “Novel phases of Quantum Matter” at ICTS Bangalore, India from 23rd Dec to 02 Jan, 2020.
4. Participated in “3rd Annual Conference on Quantum Condensed Matter (QMAT 2020)” held at S. N. Bose, India on via zoom during September 07-11, 2020.





Contents

List of Figures	xxiii
1 Introduction	1
1.1 General perspectives	1
1.2 Topological phases of matter: quantum Hall and quantum spin Hall phases	6
1.3 Two-dimensional (2D) systems	10
1.3.1 Dirac system (graphene)	10
1.3.2 Semi-Dirac system	13
1.4 Conductivity of 2D systems: formalism	13
1.4.1 Landauer-Büttiker formalism	14
1.4.2 The recursive Green's function	17
1.4.3 The kernel polynomial method	19
1.4.4 The Chebyshev polynomials	20
1.4.5 Chebyshev expansion in terms of Green's function	21
1.4.6 The Kubo-Bastin formula	24
1.5 Outline of the thesis	26
2 Transport properties of 2D Dirac and semi-Dirac nanoribbons: Role of edge states	29
2.1 Landauer formula used for computing transport	32
2.2 Dirac and semi-Dirac systems	32
2.3 Tight-binding model of Dirac nanoribbon.	35
2.3.1 Edge states and band structure	35
2.3.2 LDOS and conductivity	39
2.3.3 Bilayer graphene	40
2.4 Tight-binding model of semi-Dirac nanoribbon	47
2.4.1 Edge states and band structure	49

2.4.2	LDOS and conductivity	50
2.5	Summary	51
3	Transport properties of a Kane-Mele Dirac and semi-Dirac nanoribbon . .	53
3.1	Kane-Mele model in a Dirac system	55
3.1.1	Edge states: Analytical expressions	56
3.1.2	Results and discussion	59
3.1.3	Intrinsic SOC	60
3.1.4	Rashba SOC	62
3.1.5	Intrinsic and Rashba SOC	63
3.1.6	Bilayer system	66
3.2	Kane-Mele model in semi-Dirac system	79
3.2.1	Edge states: Analytical expressions	80
3.2.2	Results and discussion	82
3.2.3	Intrinsic SOC	82
3.2.4	Intrinsic and Rashba SOC	83
3.3	Summary	86
4	Hofstadter butterfly spectra and Landau levels for a semi-Dirac nanoribbon	89
4.1	Magnetic field: Peierls coupling	92
4.2	Hofstadter butterfly spectra in semi-Dirac and Dirac system	93
4.3	Landau levels.	96
4.4	Summary	97
5	Quantum Hall studies of a semi-Dirac nanoribbon	99
5.1	Transport properties	100
5.1.1	Methodology	101
5.1.2	Numerical details	102
5.1.3	Density of states	102
5.1.4	Hall conductivity	104
5.1.5	Longitudinal conductivity	107
5.2	Summary	108

6 Magneto-optical properties of a semi-Dirac system in the near ultraviolet-visible frequency regime	109
6.1 Keldysh formalism.	112
6.2 Results	115
6.2.1 Zero magnetic field	115
6.2.2 Magneto-transport	117
6.2.3 Electron filling	124
6.2.4 Circular polarization	125
6.2.5 Faraday rotation	127
6.3 Summary	128
7 Conclusions and outlooks	131
7.1 Summary of the work done	131
7.2 Future prospects	134
Appendices	135
A Chebyshev expansion	137
Bibliography	139



List of Figures

- 1.1 (Color online) The longitudinal and the Hall resistivities (ρ_{xx} and ρ_{xy}) are shown as a function of the magnetic field. The green line shows the longitudinal resistivity, ρ_{xx} and the red line denotes the Hall resistivity, ρ_{xy} . The Hall resistivity shows quantized plateaus in multiples of h/e^2 . This image is reproduced from Ref. [24]. 7
- 1.2 (Color online) In the upper left panel, for a thin quantum well (that is, when $d < d_c$, d being the width of HgTe layer), the energy of the lowest-energy conduction subband, denoted by E1, is higher than that of the highest-energy valence band, denoted by H1. In the upper right panel, for a thick quantum well (that is when $d > d_c$), the band inversion occurs. In the lower two panels, the energy spectra are shown for a HgTe quantum well for both cases, respectively. The thin quantum well has an insulating energy gap (lower left panel), whereas the edge states are shown by the red and the blue line for the thick quantum well (lower right panel). This image is taken from Ref. [28]. 8
- 1.3 (Color online) A schematic diagram of honeycomb lattice structure (left panel) and its Brillouin zone (right panel) of graphene is shown. \mathbf{a}_1 and \mathbf{a}_2 are the lattice unit vectors, and $\delta_i, (i = 1, 2, 3)$ are the three nearest neighbor vectors. \mathbf{k}_1 and \mathbf{k}_2 are the two non-equivalent Dirac points. This image is reproduced from Ref. [33]. 11
- 1.4 (Color online) A schematic sketch of (a) zigzag graphene nanoribbon and (b) armchair graphene nanoribbon is shown respectively. The direction of arrows denotes the zigzag and armchair edges as mentioned. This image is reproduced from Ref. [35]. 12

- 1.5 (Color online) A coherent conductor is connected to two contacts on both sides of the sample and can be characterized by a scattering matrix at each value of the propagating energy mode. The scattering matrix relates the outgoing mode amplitudes b to the incoming mode amplitudes a . This image is taken for illustration from Ref. [57]. 16
- 1.6 (Color online) A schematic diagram of a two-terminal system discretized on a grid. The size of the mesh is denoted by a . The system has a central region denoted by the matrix \mathbf{A}_S and two semi-infinite leads on both sides of the central region denoted by the matrices \mathbf{A}_L and \mathbf{A}_R . A block tridiagonal matrix is formed by \mathbf{A}_S by grouping the discretized points into vertical slices. Slice ' i ' is represented by the block $\mathbf{A}_{i,i}$. Σ_L and Σ_R (denoted by red color) are the self-energies of the semi-infinite leads. This image is taken from Ref. [61]. 18
- 2.1 (color online) A schematic sketch of lattice geometry of a semi-Dirac system with different hopping parameters, t (denoted by blue) and t_2 (denoted by pink) is shown. Two sublattices are denoted by two different colors, that is, red and green. $\vec{\delta}_1, \vec{\delta}_2, \vec{\delta}_3$ are the real space nearest neighbor vectors mentioned in the text. 33
- 2.2 (Color online) Energy band dispersion of a (a) Dirac system and (b) semi-Dirac system is shown. The anisotropic band dispersion is observed for the semi-Dirac case. In the side panel of (b), we zoom the region near the M point along the k_y and the k_x directions. The dispersion is linear along the y -direction and quadratic along the x -direction. Here a is set to be unity. The dispersion along the high symmetry points $\Gamma \rightarrow K_1 \rightarrow M \rightarrow K_2 \rightarrow \Gamma$ for different strength of hopping parameters (c) $t_2 = t$ (Dirac) and (d) $t_2 = 2t$ (semi-Dirac) respectively. Here we taken $t = 2.8\text{eV}$ 34
- 2.3 (Color online) Graphene nanoribbon geometry with zigzag edges. The blue and the red circles represent A and B sublattices of the ribbon. \vec{a}_1 and \vec{a}_2 are the primitive vectors. (m, n) labels the unit cell. m increases along the positive x -direction, whereas n increases along the negative y -direction. 36
- 2.4 (color online) (a) Probability density of the wavefunction, $|\psi|^2$ as a function of site index, n at $k_x = \frac{2.15\pi}{3\sqrt{3}}$ and (b) the Band structure is shown for $N = 100$ for a Dirac system (zigzag graphene ribbon). 38

- 2.5 (color online) (a) The LDOS is plotted near Fermi energy and (b) the charge conductance, G (in units of e^2/h) is plotted as a function of Fermi energy, E (in units of t) of zigzag nanoribbon for a Dirac system. The value of the quantized conductance is shown by the pink dashed line. 39
- 2.6 (Color online) Bilayer graphene nanoribbon geometry with zigzag edges. The white and the blue circles represent A and B sublattices of the ribbon respectively. \mathbf{a}_1 and \mathbf{a}_2 are the primitive vectors. (m, n) labels the unit cell along the x and the y direction. 41
- 2.7 (color online) (a) Charge density is plotted as a function of site index, n at $k_x = \frac{2.15\pi}{3\sqrt{3}}$ and (b) the band dispersion is shown for $N = 3$ for a zigzag bilayer graphene nanoribbon. Here, we set $t_{\perp} = 0.2$ 45
- 2.8 (color online) The LDOS for a bilayer graphene nanoribbon is plotted for (a) bottom layer and (b) top layer respectively. Here, we set $t_{\perp} = 0.2$ 46
- 2.9 (color online) The charge conductance, G (in units of e^2/h) is plotted as a function of Fermi energy E (in units of t) for a bilayer graphene nanoribbon. The value of the quantized conductance is shown by the pink dashed line. Here, we set $t_{\perp} = 0.2$ 46
- 2.10 (color online) Zigzag nanoribbon of a honeycomb lattice for a semi-Dirac system is shown. The magenta and blue circles represent the A and B sublattices respectively. \mathbf{a}_1 and \mathbf{a}_2 are the primitive vectors. (m, n) labels the positions of the unit cells along x and y directions. The ribbon is infinite along the x -direction shown by the arrow on both side. 47
- 2.11 (color online) Charge density as a function of site index, n at $k_x = \frac{2.15\pi}{3\sqrt{3}}$ and (b) the band structure for $N = 100$ for a semi-Dirac nanoribbon with zigzag edges. Here, we set $t_2 = 2t$. The vertical line (grey dashed) indicates that the flat band gets enhanced in case of semi-Dirac nanoribbon. 50
- 2.12 (color online) (a) The local density of states (LDOS) is plotted near Fermi energy and (b) the charge conductance, G (in units of e^2/h) is plotted as a function of Fermi energy, E (in units of t) of zigzag nanoribbon for a semi-Dirac system. The value of the quantized conductance is shown by the pink dashed line. 51

- 3.1 (color online) Band structure of a zigzag graphene nanoribbon is shown for different values of intrinsic spin-orbit coupling parameter (a) $\lambda_{SO} = 0.1$ and (b) $\lambda_{SO} = 0.5$. Here we put $\lambda_R = 0$ 60
- 3.2 (Color online) Probability density of the wave-function, $|\psi|^2$ is plotted as a function of site index, n for (a) $\lambda_{SO} = 0.1$ and (c) $\lambda_{SO} = 0.5$. The LDOS is plotted for (b) $\lambda_{SO} = 0.1$ and (d) $\lambda_{SO} = 0.5$. Here we put $\lambda_R = 0$ 61
- 3.3 (color online) The charge conductance, G (in units of e^2/h) is plotted as a function of energy, E (in units of t) for (a) $\lambda_{SO} = 0.1$ and (b) $\lambda_{SO} = 0.5$. Here we have considered $\lambda_R = 0$ 62
- 3.4 (color online) Band structure of a zigzag graphene nanoribbon for different values of Rashba spin-orbit coupling strength (a) $\lambda_R = 0.1$ and (b) $\lambda_R = 0.5$. Here we put $\lambda_{SO} = 0$ 62
- 3.5 (Color online) Probability density of the wave-function, $|\psi|^2$ is plotted as a function of site index, n for (a) $\lambda_R = 0.1$ and (c) $\lambda_R = 0.5$. The LDOS is shown for (b) $\lambda_R = 0.1$ and (d) $\lambda_R = 0.5$. The oscillatory pattern is seen in Fig. (c) and (d). Here we put $\lambda_{SO} = 0$ 63
- 3.6 (color online) The charge conductance, G (in units of e^2/h) is plotted as a function of energy, E (in units of t) for (a) $\lambda_R = 0.1$ and (b) $\lambda_R = 0.5$. Here we put $\lambda_{SO} = 0$ 64
- 3.7 (color online) The band structure of zigzag Kane-Mele nanoribbon with (a) $\lambda_{SO} = 0.1$, $\lambda_R = 0.01$ and (b) $\lambda_{SO} = 0.1$, $\lambda_R = 0.2$ 64
- 3.8 (color online) Probability density of the wave-function, $|\psi|^2$ as a function of site index, n for (a) $\lambda_{SO} = 0.1$, $\lambda_R = 0.01$ and (c) $\lambda_{SO} = 0.1$ and $\lambda_R = 0.2$. The corresponding LDOS is plotted for (b) $\lambda_{SO} = 0.1$, $\lambda_R = 0.01$ and (d) $\lambda_{SO} = 0.1$, $\lambda_R = 0.2$ 65
- 3.9 (color online) The charge conductance, G (in units of e^2/h) is plotted as a function of energy E (in units of t) for different values of λ_R (a) $\lambda_R = 0.01$ and (b) $\lambda_R = 0.2$. Here, we have fixed $\lambda_{SO} = 0.1$ 65
- 3.10 (color online) Charge density as a function of site index, n at $k_x = \frac{\pi}{\sqrt{3}}$. Here, we set $t_{\perp} = 0.2$ and $\lambda_{SO} = 0.2$ 69
- 3.11 (color online) The band structure for different values of N (a) $N = 4$, (b) zoomed view of the region encircled by blue as shown in (a) and (c) $N = 5$. Here, we set $t_{\perp} = 0.2$ and $\lambda_{SO} = 0.2$ 70

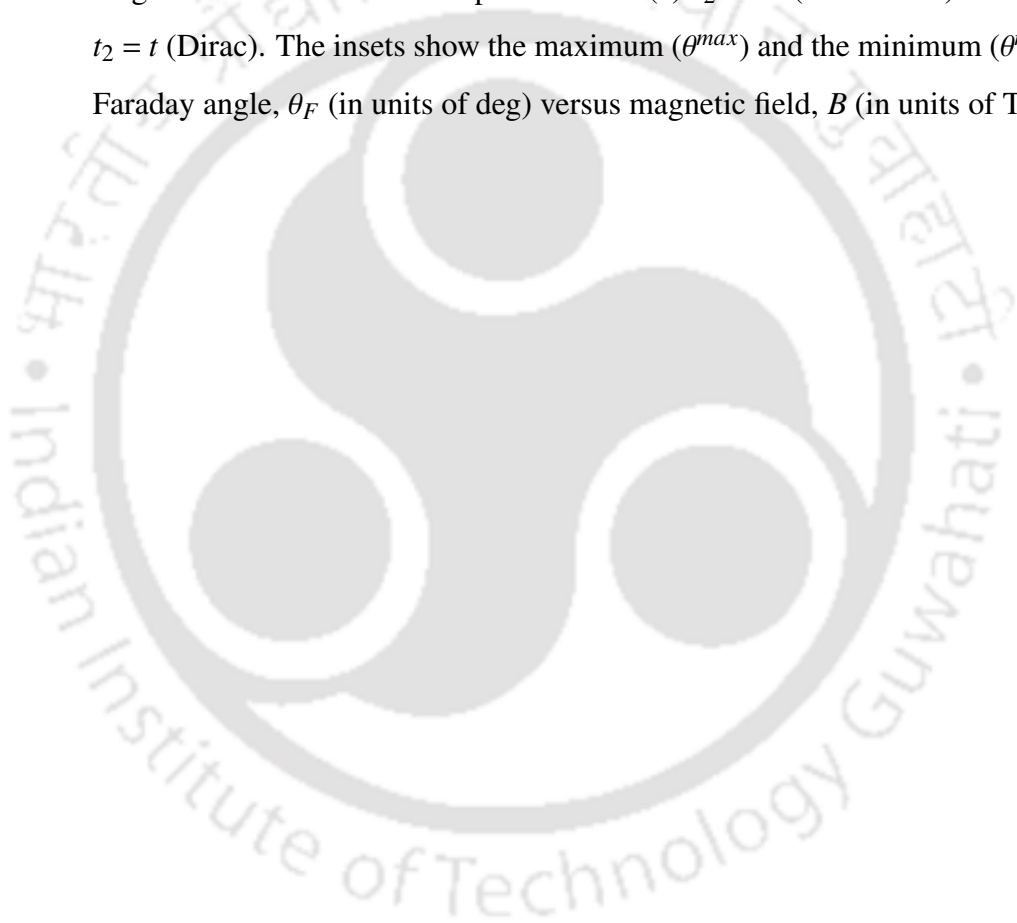
- 3.12 (color online) Charge density as a function of site index, n at $k_x = \frac{\pi}{\sqrt{3}}$ for different values of λ_R^\perp (a) $\lambda_R^\perp = 0.05$ (b) $\lambda_R^\perp = 0.3$. Here, we set $t_\perp = 0.2$, $\lambda_{SO} = 0.2$ and $\lambda_R = 0.1$ 71
- 3.13 (color online) The band structure for (a) $\lambda_R = 0.1$ and $\lambda_R^\perp = 0.05$ (b) $\lambda_R = 0.1$ and $\lambda_R^\perp = 0.3$ (c) $\lambda_R = 0.1$ and $\lambda_R^\perp = 0$ (d) $\lambda_R = 0$ and $\lambda_R^\perp = 0.3$. Here, we set $t_\perp = 0.2$, $\lambda_{SO} = 0.2$ and $N = 5$ 72
- 3.14 (color online) Energy gap, E_g as a function of interlayer Rashba SOC parameter, λ_R^\perp for (a) two different values of λ_R , namely $\lambda_R = 0$ and 0.1 with fixed λ_{SO} (namely $\lambda_{SO} = 0.2$) (b) different values of λ_{SO} with fixed λ_R (namely $\lambda_R = 0.1$). Here, we set $t_\perp = 0.2$ 72
- 3.15 (color online) The band structure for different values of bias voltage $V = 0.03, 0.1, 0.3$ for $N = \text{odd}$ (a-c) and $N = \text{even}$ (d-f) respectively. Here, we set $t_\perp = 0.2$ and $\lambda_{SO} = 0.1$. We also put $\lambda_R = \lambda_R^\perp = 0$ 73
- 3.16 (color online) The band structure for two different values of bias voltage, V (a) $V = 0.1$ and (b) $V = 0.3$. Here, we set $t_\perp = 0.2$, $\lambda_{SO} = 0.1$ and $\lambda_R = 0.1$. We put $\lambda_R^\perp = 0$ 74
- 3.17 (color online) A schematic view of zigzag bilayer graphene sheet which consists of a central region, left and right semi-infinite leads (denoted by the red at the both end of the sample). In the central region, blue and yellow circles denote the A_2 and B_2 sublattices in the top layer, whereas red and green denotes A_1 and B_1 sublattices in the bottom layer. 75
- 3.18 (color online) The charge conductance, G (in units of e^2/h) as a function of Fermi energy, E (in units of t) without intralayer intrinsic SOC (denoted the blue curve) and with intralayer intrinsic SOC for $\lambda_{SO} = 0.1$ (denoted the red curve). Here, we set $t_\perp = 0.2$ 75
- 3.19 (color online) The charge conductance, G (in units of e^2/h) as a function of Fermi energy E (in units of t) for (a) $\lambda_R^\perp = 0$ (b) $\lambda_R^\perp = 0.3$. Here, we set $t_\perp = 0.2$, $\lambda_{SO} = 0.1$ and $\lambda_R = 0.05$ 76
- 3.20 (color online) The charge conductance, G (in units of e^2/h) as a function of Fermi energy E (in units of t) for $\lambda_{SO} = 0$ (blue curve) and $\lambda_{SO} = 0.1$ (red curve). Here we set $t_\perp = 0.2$, $V = 0.1$ 76

- 3.21 (color online) The spin polarized conductance, G_γ^s ($\gamma = x, y, z$) (in units of e^2/h) as a function of Fermi energy E (in units of t) for (a-c) $\lambda_R = 0.05, 0.08$ and 0.1 (Other parameters $t_\perp = 0.2, \lambda_{SO} = 0$ and $\lambda_R^\perp = 0$) and (d-f) $\lambda_R = 0.05, 0.08$ and 0.1 (Other parameters $t_\perp = 0.2, \lambda_{SO} = 0.1$ and $\lambda_R^\perp = 0.3$). 78
- 3.22 (color online) Effective mass, m^* as a function of intralayer Rashba SOC parameter, λ_R for zigzag bilayer graphene. Here, we set $t_\perp = 0.2, \lambda_{SO}$ and λ_R^\perp both are zero. 79
- 3.23 (color online) (a) Probability density, $|\psi|^2$ is plotted as a function of site index, n at $k_x = \frac{\pi}{\sqrt{3}}$ (b) the LDOS is plotted for a semi-Dirac nanoribbon. Here we put $\lambda_{SO} = 0.1$ and $\lambda_R = 0$ 82
- 3.24 (color online) The band structure for a semi-Dirac nanoribbon in presence of intrinsic SOC with coupling strength, λ_{SO} (a) $\lambda_{SO} = 0.01$ and (b) $\lambda_{SO} = 0.1$. Here we put $\lambda_R = 0$ 82
- 3.25 (color online) The charge conductance, G (in units of e^2/h) as a function of Fermi energy, E (in units of t) for (a) $\lambda_{SO} = 0.01$ and $\lambda_{SO} = 0.1$. Here we put $\lambda_R = 0$ 83
- 3.26 (color online) Probability density, $|\psi|^2$ is plotted as a function of site index, n at $k_x = \frac{\pi}{\sqrt{3}}$ for (a) $\lambda_R = 0.01$ and (c) $\lambda_R = 0.2$. The LDOS is plotted for (b) $\lambda_R = 0.01$ and (d) $\lambda_R = 0.2$ for a semi-Dirac nanoribbon. Here we fixed $\lambda_{SO} = 0.1$ 84
- 3.27 (color online) The band structure for a semi-Dirac nanoribbon in the presence of intrinsic and Rashba SOC with coupling strength (a) $\lambda_{SO} = 0.1, \lambda_R = 0.01$ and (b) $\lambda_{SO} = 0.1, \lambda_R = 0.2$ 85
- 3.28 (color online) The charge conductance, G (in units of e^2/h) as a function of Fermi energy, E (in units of t) for (a) $\lambda_R = 0.01$, (b) $\lambda_R = 0.1$ and (c) $\lambda_R = 0.2$. Here we have fixed $\lambda_{SO} = 0.1$ 85
- 4.1 (Color online) Evolution of the Hofstadter butterfly spectrum is shown as a function of ϕ/ϕ_0 for (a) $t_2 = 2t$ (semi-Dirac), (b) $t_2 = 1.8t$, (c) $t_2 = 1.5t$ and (d) $t_2 = t$ (Dirac). 94
- 4.2 (Color online) Evolution of Landau levels for a finite strip with $N = 100$ unit cells in the presence of a magnetic flux (a and b) $\phi = \frac{\phi_0}{100}$, (c and d) $\frac{\phi_0}{200}$, (e and f) $\frac{\phi_0}{500}$ and (g and h) $\frac{\phi_0}{1600}$ is shown for $t_2 = 2t$ (semi-Dirac) in left panel and $t_2 = t$ (Dirac) in right panel. 95

- 5.1 (Color online) Density of states (in units of $1/\text{eV}$) is plotted as a function of energy, E (in units of eV) for (a) $t_2 = 2t$ (semi-Dirac), (b) $t_2 = 1.8t$, (c) $t_2 = 1.3t$ and (d) $t_2 = t$ (Dirac). We put $t = 2.8\text{eV}$ in the calculation. 103
- 5.2 (Color online) Hall conductivity, σ_{xy} (in units of $2e^2/h$) is plotted as a function of Fermi energy, E (in units of eV) for (a) $t_2 = 2t$ (semi-Dirac) and (b) $t_2 = t$ (Dirac) for a very high field (400T) and two moderate fields namely, 30T and 50T. Here t is taken as 2.8eV 104
- 5.3 (Color online) Hall conductivity, σ_{xy} (in units of $2e^2/h$) and the DOS (in units of $1/\text{eV}$) is plotted as a function of Fermi energy, E (in units of eV) for different cases (a) $t_2 = 2t, B = 50\text{T}$ (b) $t_2 = t, B = 50\text{T}$ (c) $t_2 = 2t, B = 400\text{T}$ and (d) $t_2 = t, B = 400\text{T}$ 105
- 5.4 (Color online) Longitudinal conductivities, σ_{xx} and σ_{yy} (in units of $2e^2/h$) are plotted as a function of Fermi energy, E (in units of eV) for different cases (a) $t_2 = 2t, B = 50\text{T}$ (b) $t_2 = t, B = 50\text{T}$ (c) $t_2 = 2t, B = 400\text{T}$ (d) $t_2 = t, B = 400\text{T}$ (e) $t_2 = 2t, B = 0\text{T}$ and (f) $t_2 = t, B = 0\text{T}$ 106
- 6.1 (Color online) A schematic diagram of hexagonal ribbon geometry of a semi-Dirac system irradiated by light is shown. The incident photon energies are of the order of a few eV 112
- 6.2 (Color online) The real and imaginary part of the optical conductivity (in units of e^2/h) as a function of photon energy $\hbar\omega$ (in units of eV) is shown for Dirac ($t_2 = t$) and semi-Dirac ($t_2 = 2t$) systems. The dark-pink (solid curve) corresponds to Dirac system whereas green one (dotted curve) corresponds to semi-Dirac. μ is set to be 0.4eV 116
- 6.3 (Color online) The real part of the optical conductivity, σ_{xx} (in units of e^2/h) as a function of photon energy, $\hbar\omega$ (in units of eV) is shown with the variation of the chemical potential μ namely, $\mu = 0.4, 0.6, 0.8\text{eV}$ for (a) Dirac ($t_2 = t$) and (b) semi-Dirac ($t_2 = 2t$) systems. (b) The inset in the right frame is zoomed in, close to zero frequency. 117

- 6.4 (Color online) The two upper panels give the Landau level energies, E (in units of eV) as a function of the magnetic field, B (in units of Tesla) for various values of Landau level indices n (labelled as 0, 1, 2, 3, 4, ...) for (a) $t_2 = 2t$ (semi-Dirac) and (b) $t_2 = t$ (Dirac). The solid and the dotted lines are obtained from theoretical scaling (E goes as $B^{2/3}$ for semi-Dirac case and \sqrt{B} for Dirac case) and simulation respectively. In the two middle panels ((c) and (d)), a few allowed optical transitions are indicated by the vertical (dark-green) arrows and the chemical potential ($\mu = 0.4$ eV) is shown by the horizontal black dashed line. The left and right panels correspond to $t_2 = 2t$ and $t_2 = t$ at $B = 400$ T respectively. In the two lower panels energy levels, E (in units of eV) versus density of states (DOS) (in units of $1/\text{eV}$) are shown for (e) $t_2 = 2t$ (semi-Dirac) and (f) $t_2 = t$ (Dirac) at $B = 400$ T. 118
- 6.5 (Color online) The real parts of the longitudinal MO conductivities, σ_{xx} and σ_{yy} and the MO Hall conductivity, σ_{xy} (in units of e^2/h) are shown as a function of photon energy, $\hbar\omega$ (in units of eV) for (a) $t_2 = 2t$ (semi-Dirac) and (b) $t_2 = t$ (Dirac) at $B = 400$ T in the main frame (denoted by red curve). The inset plots show the same for more moderate values of magnetic field, say 100T (denoted by blue curve) for $t_2 = 2t$ and $t_2 = t$. μ is set to be 0.4 eV. 120
- 6.6 (Color online) The imaginary parts of the MO Hall conductivity, σ_{xy} (in units of e^2/h) are shown as a function of photon energy, $\hbar\omega$ (in units of eV) for (a) $t_2 = 2t$ (semi-Dirac) and (b) $t_2 = t$ (Dirac) at $B = 400$ T in the main frame (shown by the red curve). The inset plots show the same for moderate values of magnetic field, (for example, $B = 100$ T) for $t_2 = 2t$ and $t_2 = t$. μ is set to be 0.4 eV. 122
- 6.7 (Color online) In the upper two panels, a few allowed optical transitions are shown indicated by arrows for various values of the chemical potential for (a) $t_2 = 2t$ (semi-Dirac) and (b) $t_2 = t$ (Dirac) at $B = 400$ T. Those μ values are marked with the horizontal black dashed lines. In the lower two panels, the real parts of the longitudinal MO conductivity, σ_{xx} in units of e^2/h are shown as a function of photon energy, $\hbar\omega$ in units of eV for various values of chemical potential μ for (c) $t_2 = 2t$ (semi-Dirac) and (d) $t_2 = t$ (Dirac) at $B = 400$ T. 123

- 6.8 (Color online) In the upper two panels, the real parts of the right-handed polarized MO conductivity σ_+ and that of the left-handed polarized one σ_- (in units of e^2/h) are shown as a function of photon energy, $\hbar\omega$ (in units of eV) for a fixed value of chemical potential $\mu = 0.4\text{eV}$ for (a) $t_2 = 2t$ (semi-Dirac) and (b) $t_2 = t$ (Dirac) at $B = 400\text{T}$. The lower two panels ((c) and (d)) depict the same scenario by varying the chemical potential which falls between the $n = 1$ and $n = 2$ Landau levels. 126
- 6.9 (Color online) The Faraday rotation angle, θ_F (in units of deg) is plotted as a function of photon energy, $\hbar\omega$ (in units of eV) for different values of magnetic field and chemical potential for (a) $t_2 = 2t$ (semi-Dirac) and (b) $t_2 = t$ (Dirac). The insets show the maximum (θ^{max}) and the minimum (θ^{min}) Faraday angle, θ_F (in units of deg) versus magnetic field, B (in units of Tesla). 128





1 Introduction

Contents

1.1 General perspectives	1
1.2 Topological phases of matter: quantum Hall and quantum spin Hall phases.	6
1.3 Two-dimensional (2D) systems	10
1.3.1 Dirac system (graphene)	10
1.3.2 Semi-Dirac system	13
1.4 Conductivity of 2D systems: formalism.	13
1.4.1 Landauer-Büttiker formalism	14
1.4.2 The recursive Green's function	17
1.4.3 The kernel polynomial method	19
1.4.4 The Chebyshev polynomials	20
1.4.5 Chebyshev expansion in terms of Green's function	21
1.4.6 The Kubo-Bastin formula	24
1.5 Outline of the thesis	26

1.1 General perspectives

Since the discovery of the wave nature of electrons, the study of the transport phenomena in mesoscopic systems has evolved as the heart of condensed matter physics. By mesoscopic systems (also known as phase-coherent systems [1]), we usually mean the system dimension is somewhere between the microscopic scale and the macroscopic scale [2]. More prominently, they are characterized by the system dimension within the range of nanometer (nm) and micrometer (μm). The wave nature of the electrons in the mesoscopic regime shows

several important quantum effects (for example, quantized conductance) that are absent in macroscopic devices. In a mesoscopic system, a few relevant length scales that characterize the different regimes of transport are the de Broglie wavelength ' λ ' (ranges from a few Angstrom in metals to the order of 50 nm in semiconductors), the mean free path ' l_e ' (the distance that electrons travel before its initial momentum is completely replaced by a scattering event) and the phase relaxation length ' l_ϕ ' (the distance over which the electrons lose their initial phase). These length scales vary from one material to another and may be affected by external agencies, such as temperature, magnetic field, etc. To understand the length scale for the mesoscopic system, let us look at an example of a conductor of size L . It is ohmic (classical) when its dimensions are much larger than the λ , l_e and l_ϕ , and considered as mesoscopic when $L \leq l_\phi$. To make the discussion concrete, we take a planar sheet of the material and connect leads, which could be at two ends of the material or on all four sides, depending on the objective of the measurement. The leads are of the same material as our system, which are connected to the bias voltage. In terms of the above length scales, two distinct regimes can be categorized in an intuitive way for mesoscopic transport. They are,

(a) Ballistic regime: this regime is defined by, $\lambda < L \ll l_\phi, l_e$. There is no phase-breaking or elastic scattering in the bulk when the electrons pass through the material that is, scattering occurs only at the boundary between the leads and the conductor. Hence, no impurity scattering is considered, and the transport properties are determined by the quantum interference effects.

(b) Diffusive regime: In contrast to the ballistic one, this regime is defined by, $\lambda \ll l_e \ll L$. The electrons are scattered by disorders or impurities, and the motion is diffusive in nature.

Over the last two decades, several modern material fabrication techniques have been developed, such as molecular beam epitaxy (MBE), lithography technique, scanning tunneling microscope (STM), etc., to realize dimensions such that, $L < l_\phi$ experimentally. GaAs/AlGaAs is considered one such ideal semiconductor heterostructure that has characteristic dimensions smaller than the mean free path (l_e). At the interface, a thin layer of charges called a two-dimensional electron gas (2DEG) is formed. In this regime, the transport is governed by the Landauer formula as, $G = (e^2/h)T$ [3] (where e denotes the charge of an electron, h is Planck's constant and T is the transmission coefficient). However, the conductance is independent of the length of the object. It is worthy to mention that the transport of electrons in nanoelectronic devices is investigated in the quantum regime based on the above classification.

The above perspectives change dramatically in the presence of a magnetic field. In 1879,

the first experiment to prove the existence of moving charges in metal was done by Edwin Hall [4]. A century later, in 1980s, the discovery of integer quantum Hall effect by von Klitzing [5] as well as fractional quantum Hall effect by Tsui, Störmer, and Gossard [6] gives a boost in the field of transport study in the presence of a strong external magnetic field, of the order of several teslas (T). The former can be understood without taking into account the interactions between electrons, whereas for the latter, the interactions between the electrons play a crucial role. Instead of linear dependence on the magnetic field, as is well-known for the classical Hall effect, Klitzing [5] found that the Hall resistivity exhibits quantized plateaus over a wide range of magnetic fields. This quantized Hall resistivity originates from the discretization of the energies of the cyclotron orbits into macroscopically degenerate flat bands known as the Landau levels (LLs).

Immediately afterward, researchers have found that the Hall quantization has topological implications. For instance, the conductance is facilitated by the modes that reside at the edges of the sample, while the bulk remains perfectly insulating. Such distinct behavior of the ‘bulk’ and ‘edge’ modes has not been realized earlier and hence corresponds to the first-ever ‘topological insulators’ (TIs). In 1982, the connection between the quantized Hall conductance and the topology was explained by Thouless, Kohmoto, Nightingale, and den Nijs, which can be characterized by a topological invariant, known as the Chern number (also known as TKNN invariant [7]). The Chern number is equal to the quantized value of Hall conductivity, σ_{xy} in units of e^2/h . Moreover, these topological states can be understood by the bulk-boundary correspondence, which means that the properties of the boundary modes can be obtained from the behavior of the bulk states. It has important implications on the transport features. According to the classical picture with cyclotron orbits, these orbits collide with the boundary at the edges of the sample, which results in ‘skipping orbits’. This propagates only in a single direction at the one-dimensional edge. In a quantum mechanical situation, the potential due to the presence of edges of the sample and the vacuum is sharp and leads to chiral edge modes that travel in opposite directions at opposite edges. The existence of the chiral modes comes from the topological nature of the two-dimensional (2D) quantum Hall states, and the number of chiral edge modes corresponds necessarily to an integer number, ν which also denotes the quantization Hall conductance.

Let us now talk about a second topological phase of matter which is distinct from the one described above. A little more elaboration is needed here. Similar to the electron charge, the spin of the electron plays a role in the field of spintronics, which has made a vast impact on metal-based information storage devices. In 1971, Dyakonov and Perel [8] predicted

the spin Hall effect theoretically, where they observed the accumulation of spins on the lateral surfaces of a current-carrying sample with the opposite spins at opposite boundaries. Unlike the classical case, the spin Hall effect is driven by spin-orbit coupling (SOC) which occurs in the absence of a magnetic field. In 1988, the most successful discovery of the giant magnetoresistive effect (GMR) [9] is considered as the starting point of this new spin-based electronics. A. Fert and P. Grünberg [10] have been awarded the Physics Nobel Prize for the discovery of the GMR effect in 2007. A large increase in resistance has been observed for a ferromagnet/non-ferromagnetic/ferromagnet multilayer structure in GMR when the magnetization goes from being parallel to antiparallel. The spin-field effect transistor (spin-FET) was first proposed by Datta and Das [11] in 1990 as a development to the GMR set-up. Semiconductor-based spintronics has proven more challenging since it requires a magnetic field by which the electron spin needs to be controlled. To overcome this obstacle, electric fields can be used to manipulate electron spin via a spin-orbit interaction [12]. One can relate such that, as the magnetic field creates a charge separation, thereby producing a Hall voltage in a 2DEG, analogously, in the case of spins, the SOC can do the same job. It segregates opposite spins to move across the opposite edges of the sample, thereby producing a spin current referred to as the spin Hall effect [8]. The GMR effect can be understood by assuming that any spin current is carried by two kinds of carriers, spin-up and spin-down.

The spin-orbit interaction originates from the broken inversion symmetry along the growth direction of the semiconductor heterostructure that hosts a 2DEG. This is called Rashba spin-orbit coupling (RSOC). The Rashba SOC was first predicted in bulk semiconductors by Rashba [13]. The Rashba SOC can be tuned externally by changing the shape of the confining potential [14]. At the interface between the two semiconductors (differently doped), a potential gradient $\mathbf{E} = \nabla V$ may arise, which couples with the motion of the electrons via,

$$H_{\text{Rashba}} \propto (\mathbf{E} \times \mathbf{p}) \cdot \mathbf{s}. \quad (1.1.1)$$

The Rashba Hamiltonian can be written, considering a quantum well along the z direction $\mathbf{E} = E_z \mathbf{z}$ as,

$$H_{\text{Rashba}} = \frac{\alpha}{\hbar} (\mathbf{s} \times \mathbf{p}) \cdot \mathbf{z} = \frac{\alpha}{\hbar} (p_y s_x - p_x s_y), \quad (1.1.2)$$

where $\mathbf{s} = (s_x, s_y, s_z)$ is a vector of three component Pauli matrices and α depends on the material. For a single layer graphene, Rashba SOC may have been interesting consequences, has been predicted by Kane and Mele [15]. However, the coupling strength is very small

in graphene due to the small atomic number of the carbon atoms. Several proposals have been made for enhancing the strength of the interaction by coating the sample surface with adatoms. Rotating magnetic fields can also produced large Rashba SOC [16]. In contrast to the Eq. (1.1.2), the Hamiltonian for a single layer graphene, which depends only on the pseudospin, can be described by approximating it to the lowest order as,

$$H = \frac{\lambda}{2}(s \times \sigma)_z, \quad (1.1.3)$$

where s are the Pauli matrices describing the electron spin and σ denotes the pseudospin.

After the discovery of the quantum Hall (QH) effect, Haldane showed that the necessary condition to observe the QH effect is not the presence of a magnetic field but the breaking of a time-reversal symmetry (TRS) which leads to quantum anomalous Hall (QAH) effect. He proposed that a QAH insulator has chiral edge states in a zero magnetic field which lacks the TRS. The Haldane model describes the spinless electrons, where the TRS is broken through dissipationless currents induced by adding fluxes, which cancel overall. Also, it acquires a quantized Hall conductivity proportional to the Chern index, C as $\sigma_H = Ce^2/h$. Later, a combination of a QAH insulator with its time-reversed copy produces a time-reversal invariant \mathbb{Z}_2 insulator that has spin-polarized chiral edge states, leads to the new topological phases of matter known as quantum spin Hall (QSH) phase .

In the last few decades, TIs have been one of the most promising materials which can lead to high-performance applications ranging from quantum computing [17] to spintronics applications. Graphene and its derivatives are the first proposed TI candidate in history. With the intrinsic SOC on graphene, one can open a topologically nontrivial band gap at the Dirac cones, although the SOC of the carbon atoms is extremely small for topological insulation to be observed experimentally. Furthermore, measuring these intrinsic SOC's through magnetoconductance is challenging due to their relatively weak signatures in transport. This work addresses the challenges in transport measurements from both analytical and numerical approaches on various graphene-based materials. After Kane and Mele, Bernevig *et al.* [18,19] proposed the existence of QSH effect involving HgTe sandwiched between CdTe layers via band inversion for a critical width of the intermediate layer, and their prediction was confirmed by König *et al.* [20] in an experiment. This leads to the discovery of new 2D TIs as well as three-dimensional (3D) TIs. Later, Fu and Kane [21] carried out the new search for 3D TIs in their work which also opened a race for discovering new 3D TIs [22,23]. However, in this thesis, we shall restrict ourselves to 2D systems.

Motivated by the above discussion, we took a chance to explore these novel phenomena in our 2D system. This thesis is essentially focused on the study of quantum transport phenomena in the presence of spin-orbit couplings and the magnetic field. The band structures of the Dirac and the semi-Dirac systems play a crucial role in transport properties that leads to new insights. The newly developed approaches serve as a useful method of describing the low energy impacts of new physics for a very large system.

Before going to the main content, we give a more elaborate introduction of two important phenomena that we have explored in our systems. They are the quantum Hall effect and quantum spin Hall effect. Later, we shall describe the Landauer approach and the Kernel Polynomial Method based on Chebyshev expansion which we have used to solve our problems numerically.

1.2 Topological phases of matter: quantum Hall and quantum spin Hall phases

1980s were marked by the remarkable discovery of the integer quantum Hall effects, and the first experiment was performed by von Klitzing, using the samples prepared by Dorda and Pepper [5]. A similar experimental set-up has been used for the integer quantum Hall effect to the classical case. Consider a 2DEG that can be formed from a semiconductor heterostructure, for example, a Gallium Arsenide (GaAs) structure is sandwiched between two Aluminium Arsenide (AlAs) semiconductors. When this 2DEG is subjected to a large perpendicular magnetic field, the QH effect is observed. The magnetic field causes the electrons to travel along circular cyclotron orbits, and the radii get smaller with the increasing value of the magnetic field. In the case of larger magnetic fields, the electrons move in a closed cyclotron orbit in the bulk of the sample and hence cannot conduct, whereas they can skip along the edges of the sample forming open orbits.

At low temperatures, two important quantum effects happen. First, the electrons moving in closed orbits in bulk become localized, and the bulk turns into an insulator. The second is the formation of extended one-dimensional channels with a quantized conductance of e^2/h per channel from the skipping edge orbits. At low temperatures ($T < 4\text{K}$) and strong magnetic fields (of the order of several Teslas), the longitudinal resistivity is zero whenever the Hall resistivity, ρ_{xy} shows a sharp plateau over a range of magnetic fields, and spikes are observed when ρ_{xy} jumps from one plateau to the next plateau. The experimental result is

depicted in Fig. (1.1). The quantized value of ρ_{xy} is given by,

$$\rho_{xy} = \frac{2\pi\hbar}{e^2} \frac{1}{\nu} \quad (1.2.1)$$

The integer, ν known as the filling factor, is measured to an extraordinary accuracy which is of the order of 1 part in a billion. The Hall conductivity can be obtained from the inverse of the Hall resistivity, namely $\sigma_{xy} = \frac{e^2}{2\pi\hbar} \nu$.

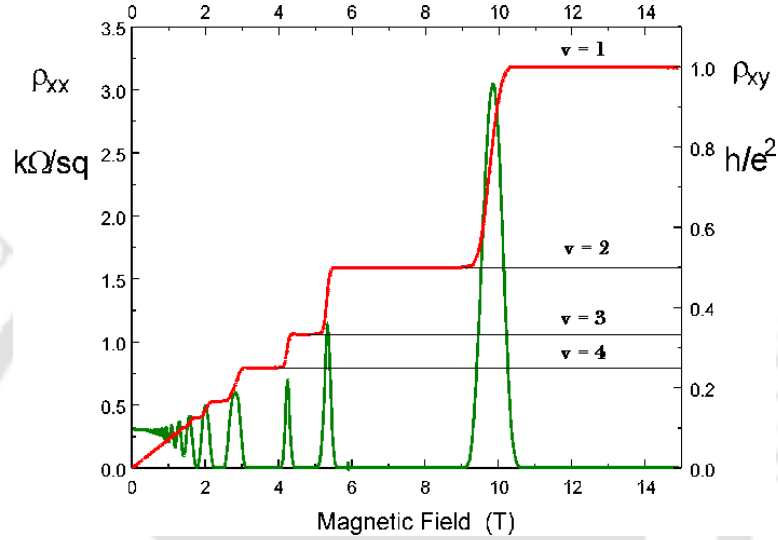


Figure 1.1. (Color online) The longitudinal and the Hall resistivities (ρ_{xx} and ρ_{xy}) are shown as a function of the magnetic field. The green line shows the longitudinal resistivity, ρ_{xx} and the red line denotes the Hall resistivity, ρ_{xy} . The Hall resistivity shows quantized plateaus in multiples of h/e^2 . This image is reproduced from Ref. [24].

Let us analyze deep into the phenomena that occur in the presence of large magnetic fields [25, 26]. The energy levels lose direct dependence on the momentum vector, \mathbf{K} . Consequently, the energy levels which are still quantized are called Landau levels. In normal metals and in 2DEGs, these levels are equally spaced due to their linear dependence on n through $E_n \sim (n + 1/2)\hbar\omega$, where ω denotes the cyclotron frequency that depends on the magnetic field ($\omega = eB/m$). However, in graphene, the velocity of the charge carrier is independent of their energy which leads to the unequal spacing between the LL energies, including a $n = 0$ LL zero-energy state. Experimentally, the discrete and non-equally spaced energy level spectrum of LLs, including the hallmark zero-energy state of graphene, was observed directly using the scanning tunneling spectroscopy of graphene grown on silicon carbide [27].

The QH state indeed denotes a new state of matter where the bulk of the sample behaves very distinctly compared to the edges. After the discovery of the QH effect, a new topolog-

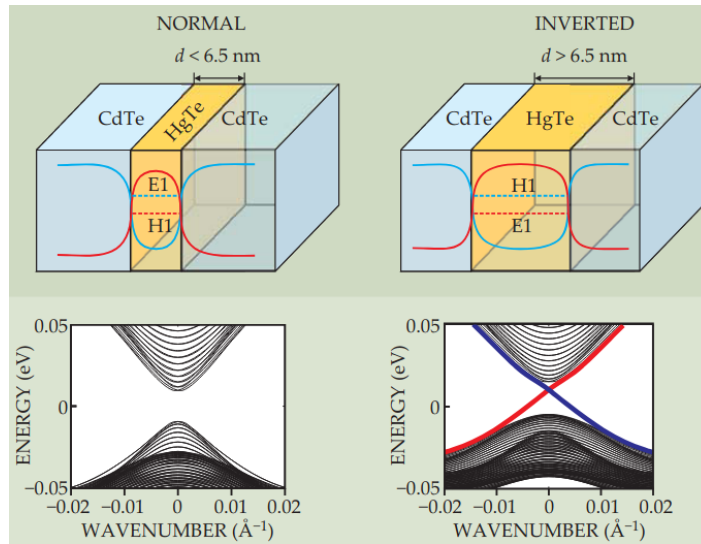


Figure 1.2. (Color online) In the upper left panel, for a thin quantum well (that is, when $d < d_c$, d being the width of HgTe layer), the energy of the lowest-energy conduction subband, denoted by E1, is higher than that of the highest-energy valence band, denoted by H1. In the upper right panel, for a thick quantum well (that is when $d > d_c$), the band inversion occurs. In the lower two panels, the energy spectra are shown for a HgTe quantum well for both cases, respectively. The thin quantum well has an insulating energy gap (lower left panel), whereas the edge states are shown by the red and the blue line for the thick quantum well (lower right panel). This image is taken from Ref. [28].

ical state of matter was found in 2006, known as the QSH effect which holds the different qualitative behavior to the QH effect and becomes the key element for the development of an emerging field of spintronics. In 2007, the QSH effect was experimentally observed in CdTe/HgTe/CdTe quantum wells [20] in the absence of zero external magnetic fields. The SOC in CdTe/HgTe/CdTe quantum wells can be increased by increasing the thickness d of the HgTe layer. Hence, for a thin quantum well, the CdTe has the dominant effect (s -like conduction subband denoted as E1 is located above the p -like valence subband H1), whereas in a thick quantum well, there is a critical thickness d_c (around 6.5 nm) for which the band inversion occurs as shown in Fig. (1.2). Consequently, one pair of edge states is observed for $d > d_c$ in the inverted regime and no edge states in the $d < d_c$ regime. The crossing of the dispersive bands is preserved by the TRS symmetry, which denotes the topological signatures of a QSH insulator. Quite contrary to the QH effect, which is responsible for breaking the TRS in the presence of an applied magnetic field, the QSH system respects the TRS. In the QSH effect, instead of charge accumulation, accumulation of spin occurs at the edges of a current-carrying conductor with opposite spins at the opposite edges. If an electric field is applied in the y direction, the transverse spin current flows in the x direction. The SOC played a role in the QSH effect as the role played by the magnetic field in the charge Hall

effect. More specifically, the SOC acts as a “spin-dependent magnetic field” that leads to the spin-dependent QH effect. The counterpropagating edge states at different edges of the sample with opposite spins evolve from this SOC, which can perceive a topological invariant.

Let us now focus on the Kane-Mele (KM) model [15, 29] which is studied extensively in this thesis. Kane and Mele proposed that two copies of the QH system with opposite spins (one with Haldane flux $\frac{\pi}{2}$, and the other with $-\frac{\pi}{2}$) preserve the TRS. The main idea was to achieve the topological insulation respecting the TRS. Before discussing the said topic, it is convenient to explore the Haldane model, which is denoted as a Chern insulator (owing to a non-zero Chern number) in the absence of a magnetic field. Haldane proposed a model which breaks the TRS by introducing a magnetic phase ϕ to the next-nearest neighbor hopping (complex hopping) amplitude. The Haldane Hamiltonian on a honeycomb lattice can be written as,

$$H = -t \sum_{\langle ij \rangle} c_i^\dagger c_j + t_2 \sum_{\langle\langle ij \rangle\rangle} e^{-iv_{ij}\phi} c_i^\dagger c_j + M \sum_i \epsilon_i c_i^\dagger c_j, \quad (1.2.2)$$

where t_2 is the next-nearest neighbor hopping amplitude, M is an on-site mass term and the parameter $\epsilon_i = \pm 1$ depends on $i = A$ or B sublattice. The t_2 term breaks the TRS, whereas the M term breaks the inversion symmetry. Both the terms open a bandgap in the spectrum, but they correspond to be of different topological nature. In particular, the effect of M in lifting a gap is trivial in nature (does not yield edge modes), while that of t_2 is topological where edge modes are observed. Now, there may arise a question of whether the breaking of TRS is the only way to realize a topological phase. The answer was given by Kane and Mele by introducing the intrinsic SOC whose low-energy expansion yields a term such as $\tau_z \sigma_z s_z$. The main idea that leads to the realization of another topological state while preserving the TRS is to add a spin degree of freedom (which is a natural choice anyway) by stacking two copies of the Haldane model. The tight-binding Hamiltonian for a KM model reads,

$$H = -t \sum_{\langle ij \rangle} c_i^\dagger c_j + i\lambda_{SO} \sum_{\langle\langle ij \rangle\rangle} e^{iv_{ij}\phi} c_i^\dagger s_z c_j \quad (1.2.3)$$

The second term in Eq. (1.2.3) is the intrinsic SOC term, which respects all of the symmetries of graphene, and s_z is also conserved. This new term can be written in the low energy limit as,

$$H_{\text{ISOC}} = \Delta_{\text{SO}} \int_{\mathbf{k}} c_{\mathbf{k}}^\dagger [\tau_z \sigma_z s_z] c_{\mathbf{k}}, \quad \Delta_{\text{SO}} = 3\sqrt{3}\lambda_{\text{SO}}. \quad (1.2.4)$$

The term σ_z corresponds to the sublattice degree of freedom, τ_z denotes the valley degree of freedom, and s_z represents the real spin. The combined term ' $\sigma_z\tau_z$ ' remains odd under time-reversal. In this case, the corresponding bulk energy spectrum has a gap at the Dirac points with a pair of counterpropagating edge modes on a graphene strip with open boundary conditions. Another SOC term that may be relevant for 2D systems with broken inversion symmetry leads to the spin mixing can be described as,

$$H_R = \lambda_R \int_{\mathbf{k}} c_{\mathbf{k}}^\dagger [\sigma_x \tau_z s_y - \sigma_y s_x] c_{\mathbf{k}}. \quad (1.2.5)$$

This type of SOC can be realized and found in experiments [30–32]. It also respects the TRS but breaks the structural inversion symmetry. The s_z quantum number is no longer conserved. Naturally, one can ask whether the topology still exists in the presence of Rashba SOC. The Kane-Mele model with Rashba SOC gives a clear picture to this question. When $\lambda_{SO} \neq 0$ and $\lambda_R = 0$, the system acquires a topologically nontrivial gap, but as we turn on λ_R , the gap (topological) slowly decreases. Hence, the key ingredient of realizing the QSH effect on graphene is SOC, especially the intrinsic SOC.

1.3 Two-dimensional (2D) systems

1.3.1 Dirac system (graphene)

Graphene is made of carbon atoms distributed at the edges of hexagons, as shown in Fig. (1.3). Each carbon atom is joined by sigma covalent bonds with three neighbors. The honeycomb lattice is not a Bravais lattice because the two neighboring sites are not equivalent. The electronic configuration of carbon is $(1s)^2 (2s)^2 (2p)^2$, however, mixed states of these orbitals exist due to the energy difference between the $2s$ and $2p$ orbitals. The $1s$ electrons become more or less inert, whereas orbital hybridization occurs between the $2s$ and $2p$ electrons in a solid-state condition. There is one possibility to form four sp^3 orbitals which form a tetrahedral bonding pattern in solid form of C, namely diamond, which is a well-known insulator. Another possibility is to form three sp^2 orbitals. The sp^2 orbitals arrange themselves in a plane at 120° angles and thus form the honeycomb lattice structure.

The structure can be seen as a triangular lattice with two inequivalent sublattices, here

labelled as A and B as shown in Fig. (1.3). The primitive lattice vectors can be written as,

$$\mathbf{a}_1 = \frac{a}{2}(3, \sqrt{3}), \quad \mathbf{a}_2 = \frac{a}{2}(3, -\sqrt{3}), \quad (1.3.1)$$

where $a \approx 1.42 \text{ \AA}$ is the spacing between the nearest neighbor carbon atoms. The reciprocal lattice vectors $\mathbf{b}_1, \mathbf{b}_2$ are defined by,

$$\mathbf{b}_1 = \frac{2\pi}{3a}(1, \sqrt{3}), \quad \mathbf{b}_2 = \frac{2\pi}{3a}(1, -\sqrt{3}). \quad (1.3.2)$$

The first Brillouin zone (BZ) of the reciprocal lattice is bounded by the planes bisecting the

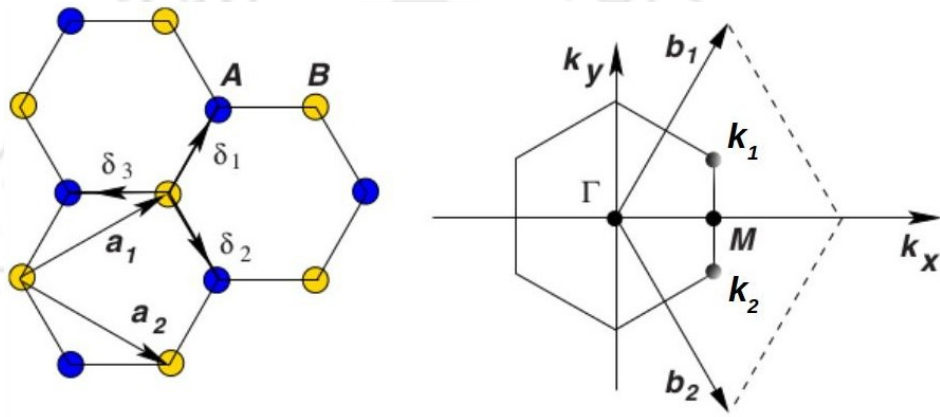


Figure 1.3. (Color online) A schematic diagram of honeycomb lattice structure (left panel) and its Brillouin zone (right panel) of graphene is shown. \mathbf{a}_1 and \mathbf{a}_2 are the lattice unit vectors, and $\delta_i, (i = 1, 2, 3)$ are the three nearest neighbor vectors. \mathbf{k}_1 and \mathbf{k}_2 are the two non-equivalent Dirac points. This image is reproduced from Ref. [33].

vectors to the nearest reciprocal lattice points. The six points are located at the corners of the FBZ where only two are of importance, that is, \mathbf{k}_1 and \mathbf{k}_2 . They are called Dirac points, owing to the Dirac-like low energy dispersion of the electrons, and their positions in the momentum space are given by,

$$\mathbf{k}_1 = \left(\frac{2\pi}{3a}, \frac{2\pi}{3\sqrt{3}a} \right), \quad \mathbf{k}_2 = \left(\frac{2\pi}{3a}, -\frac{2\pi}{3\sqrt{3}a} \right). \quad (1.3.3)$$

Also the three nearest neighbor vectors in real space are defined as, $\delta_1 = \frac{a}{2}(1, \sqrt{3})$, $\delta_2 = \frac{a}{2}(1, -\sqrt{3})$, $\delta_3 = -a(1, 0)$.

The tight-binding Hamiltonian for electrons in graphene considering the nearest neighbor hopping can be written as,

$$H = -t \sum_{\langle i,j \rangle, \sigma} (a_{\sigma,i}^\dagger b_{\sigma,j} + \text{h.c.}), \quad (1.3.4)$$

where $a_{\sigma,i}^\dagger$ ($a_{\sigma,i}$) creates (annihilates) an electron with spin σ ($\sigma = \uparrow, \downarrow$) on site R_i and sublattice A . b operators denote similar things for B sublattice. t (≈ 2.8 eV) is the nearest neighbor hopping amplitude between different sublattices. The energy dispersion of Eq. (1.3.4) have the form [34],

$$E_{\pm}(\mathbf{k}) = \pm t \sqrt{3 + f(\mathbf{k})}, \quad (1.3.5)$$

where

$$f(\mathbf{k}) = 2 \cos(\sqrt{3}k_y a) + 4 \cos\left(\frac{\sqrt{3}}{2}k_y a\right) \cos\left(\frac{3}{2}k_x a\right). \quad (1.3.6)$$

The ‘+’ (‘-’) sign refers to the upper (lower) band in Eq. (1.3.5). The electron-hole symmetry is present, and the spectrum is symmetric around zero energy. The band structure has been presented and discussed in Chapter 2.

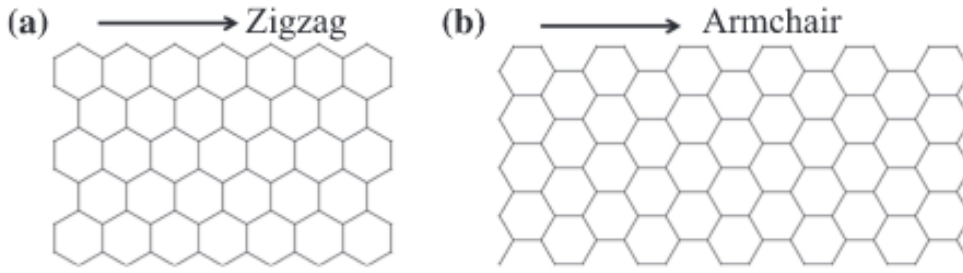


Figure 1.4. (Color online) A schematic sketch of (a) zigzag graphene nanoribbon and (b) armchair graphene nanoribbon is shown respectively. The direction of arrows denotes the zigzag and armchair edges as mentioned. This image is reproduced from Ref. [35].

For some of our studies on conductivity, finite size systems are necessary. Graphene sheets in the form of ribbons which are very large (practically infinite) in one spatial direction and finite in the other, are ideal for our purpose and are called graphene nanoribbon (GNR). These ribbons can be prepared by cutting a graphene sheet in a certain direction. Depending upon their edge orientation and termination type, there are different types of graphene, namely zigzag graphene nanoribbon (ZGNR), armchair graphene nanoribbon (AGNR), or random edge GNRs. Random edge GNRs can be characterized as a combination of zigzag and armchair sites. Two out of them are mostly studied, namely, the ZGNR and the AGNR. GNRs can be fabricated by lithography [36] and etching techniques of exfoliated graphene flakes, chemical vapor deposition (CVD) technique [37] etc. In the left and right panel of Fig. (1.4), the edge orientation types are shown by the arrow directions for zigzag and armchair edges, respectively. The transport properties of GNRs greatly depend on the edge termination and based on the different edge geometries and have gathered intense research

interest. Also, the electronic properties depend strongly on the size and the geometry of the GNRs theoretically [38,39]. In our thesis, we mainly deal with the zigzag orientation, which is formed by atoms that belong to the same sublattice A or B . The partly flat band, first analyzed by Fujita *et al.* [38] using tight-binding band calculations, is of great relevance to study the properties of ZGNRs.

1.3.2 Semi-Dirac system

Since over a decade, graphene has been known for its linear dispersion at the Dirac points. Subsequently, new features in the band structure have been discovered where the quasiparticle dispersion is known as the semi-Dirac dispersion. Pardo *et al.* [40,41] found that such kind of dispersion in ultrathin (001) VO_2 layers embedded in TiO_2 . This hybrid system is a combination of linear (“massless”, Dirac-Weyl) in one of the directions and is quadratic (“massive”, Dirac) in the other orthogonal direction [42,43]. Such a dispersion has also been obtained by Volovik at the point node in the A -phase of superfluid He^3 [44]. In a simple approximation, such dispersion can be obtained in a model that has an anisotropic Hamiltonian where hopping to two of the nearest neighbors (say t) is the same, however to the third neighbor (say t_2) is different as shown in Fig. (2.1) (see Chapter 2). In this situation, the “Dirac points” of graphene merge, which results in the semi-Dirac spectrum. The semi-Dirac point $t_2 = 2t$ is special where one can observe a topological phase transition between a semimetallic phase (for $t_2 < 2t$) with a pair of Dirac cones and a band insulator (for $t_2 > 2t$) [42,45,46]. Such hybrid semi-Dirac points that hold linear-parabolic dispersion relation are inaccessible in graphene since it requires large strains [47]. However, such dispersion may found in other physical systems such as cold atoms in optical lattices [48–51], the quasi-2D organic material α -(BEDT-TTF) $_2\text{I}_3$ (where BEDT-TTF is bis ethylenedithio tetrathiafulvalene) [52,53], VO_2/TiO_2 heterostructures [43] etc. In the former example, the possibility of the moving Dirac points by changing the intensity of the laser fields has been shown extensively [54]. More elaborate discussions can be found in Chapter 2.

1.4 Conductivity of 2D systems: formalism

The quantum transport phenomena represent the features of the orbital dynamics of electrons in a confined system. Drude-Sommerfeld model of transport was one of the first models for charge and energy transport by electrons in metals, proposed by Paul Drude in 1900

[55]. Later on, there have been several proposals for different approaches such as semi-classical Boltzmann transport [56], random matrix theory to study the quantum transport properties. Transport is a dissipative phenomenon, where energy gets exchanged either with the reservoirs at the ends of a sample or with the environment at the bulk of the sample. Importantly, Landauer formalism, which is extensively used by us, is based on this principle where one considers the system along with the presence of leads.

1.4.1 Landauer-Büttiker formalism

Landauer-Büttiker Formula has been very useful in describing the mesoscopic transport in an elegant way using Green's function formalism. For a 2D conductor, the conductance is given by,

$$G = \sigma W/L, \quad (1.4.1)$$

where W and L are the width and length of the conductor, respectively. σ denotes the conductivity, which is independent of the dimensions of the sample. According to this ohmic law (Eq. (1.4.1)), the conductance will increase indefinitely with the decrease of the length of the conductor. However, in the ballistic regime (that is when $L \ll l_e$), it was found experimentally that the conductance has a limiting value. This way the corrected formula, known as the Landauer formula, takes the form,

$$G = \frac{2e^2}{h} MT, \quad (1.4.2)$$

where M is the number of the transverse modes, and T represents the average probability of an electron to be injected from one end and transmitted to the other end of the conductor. Later, Büttiker improved the formula following Eq. (1.4.2), where the current flow occurs in the electrochemical potential between μ_1 and μ_2 at zero temperature, then the linear response formula for two-terminal becomes,

$$I = \frac{2e}{h} \bar{T} [\mu_1 - \mu_2], \quad (1.4.3)$$

where \bar{T} involves the product of the transmission probability per mode T at the Fermi energy and the number of modes M . Eq. (1.4.3) can be written by combining all the terminals as

(considering all the probes on the same footing),

$$I_p = \frac{2e}{h} \sum_q [\bar{T}_{q \leftarrow p} \mu_p - \bar{T}_{p \leftarrow q} \mu_q]. \quad (1.4.4)$$

These arrows tell us that there is a backward electron transfer from the second subscript to the first one (we shall drop it afterwards). Let $V_i = \mu_i/e$, and the Eq. (1.4.4) becomes

$$I_p = \sum_q [G_{qp} V_p - G_{pq} V_q], \quad (1.4.5)$$

where, $G_{qp} = \frac{2e^2}{h} \bar{T}_{q \leftarrow p}$. To ensure that the current becomes zero when the values of the chemical potential are equal [2], the transmission coefficient G satisfy the sum rules as follows,

$$\sum_q G_{qp} = \sum_q G_{pq}. \quad (1.4.6)$$

According to Eq. (1.4.6), Eq. (1.4.5) can be written as,

$$I_p = \sum_q G_{pq} [V_p - V_q]. \quad (1.4.7)$$

The above equation (Eq. (1.4.7)) is known as Landauer-Büttiker formula. If the coupling to the leads is strong and the electrons in the system can be treated to be noninteracting (that is, by a single particle Hamiltonian), the Landauer-Büttiker formalism turns out to be an extremely successful tool in describing quantum transport.

1.4.1.a Transmission function, scattering matrix, and Green's function

To find the relation between the scattering matrix (also called as the S -matrix) and the transmission coefficient, we consider a device as shown in Fig. (1.5) for coherent conductor. S -matrix relates the outgoing wave amplitudes (b) to the incoming wave amplitudes (a) at different leads. A coherent conductor can be described by an S -matrix at each value of energy. We can write considering total of three modes in the leads in matrix notation as (which can be shown schematically in Fig. (1.5)),

$$\begin{pmatrix} b_1 \\ b_2 \\ b_3 \end{pmatrix} = \begin{pmatrix} S_{11} & S_{12} & S_{13} \\ S_{21} & S_{22} & S_{23} \\ S_{31} & S_{32} & S_{33} \end{pmatrix} \begin{pmatrix} a_1 \\ a_2 \\ a_3 \end{pmatrix}. \quad (1.4.8)$$

. We can write the above Eq. (1.4.8) as,

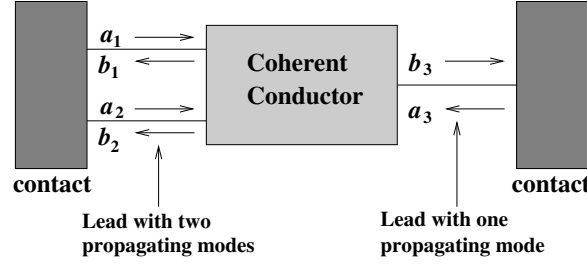


Figure 1.5. (Color online) A coherent conductor is connected to two contacts on both sides of the sample and can be characterized by a scattering matrix at each value of the propagating energy mode. The scattering matrix relates the outgoing mode amplitudes b to the incoming mode amplitudes a . This image is taken for illustration from Ref. [57].

$$\{b\} = [S]\{a\} \quad (1.4.9)$$

where the S -matrix must satisfy the following unitarity condition,

$$[S]^\dagger [S] = [S][S]^\dagger = I \quad (1.4.10)$$

In general, the S -matrix can be calculated if the Hamiltonian is known. Thus one can define and compute an S -matrix for a coherent conductor. To obtain the transmission probability between two modes m (outgoing modes) and n (incoming modes), one needs the squared magnitude of matrix elements of S -matrix is taken as,

$$T_{m \leftarrow n} = |S_{m \leftarrow n}|^2. \quad (1.4.11)$$

Thus, the transmission function $\bar{T}_{pq}(E)$ at an energy E can be derived by summing the transmission probability T_{nm} over all modes m in lead q and all modes n in lead p as follows,

$$\bar{T}_{p \leftarrow q} = \sum_{m \in q} \sum_{n \in p} T_{n \leftarrow m} = \sum_{m \in q} \sum_{n \in p} |S_{n \leftarrow m}|^2. \quad (1.4.12)$$

In a simplified notation, we can write $\bar{T}_{p \leftarrow q}$ as T_{pq} . Next, we will see how the transmission coefficient and Green's function are related. In the Landauer-Büttiker formalism, a central region is connected to leads on both sides. These transmission coefficients are related to the Green's function of the central device via [58, 59],

$$T_{pq} = \text{Tr}[\Gamma_p G^R \Gamma_q G^A]. \quad (1.4.13)$$

$G^{R(A)}$ is the retarded (advanced) Green's function of the central region. The coupling matrices Γ_p and Γ_q are the imaginary parts representing the coupling between the central region and the leads. Γ_p can be defined as [2],

$$\Gamma_p = i \left[\Sigma_p - (\Sigma_p)^\dagger \right], \quad (1.4.14)$$

where Σ_p represents the retarded self-energy associated with lead p . Also, the retarded Green's function can be written as [2],

$$G^R = \left(E - H - \sum_p \Sigma_p \right)^{-1}, \quad (1.4.15)$$

where E is the Fermi energy of electrons and H is the Hamiltonian for the central region. The advanced Green's function can be calculated in terms of the retarded Green's function via, $G^A = (G^R)^\dagger$.

1.4.2 The recursive Green's function

The theoretical description of mesoscopic electronic transport has been developed within the Landauer formalism [60]. This formalism states that there is a direct relation between the conductance of a mesoscopic sample and the probability that an electron will transmit through it. Among several numerical techniques, the recursive Green's function (RGF) method is one of the most efficient approaches to tackle the coherent ballistic electron transport. In order to calculate the conductance through the sample and the local particle densities within the nanodevices, the retarded Green's function is needed to calculate. The main focus of the recursive algorithm is to find either the diagonal blocks or the selected block columns of an inverted block tridiagonal matrix [61]. Also, a parallel algorithm has been developed for the computation of the electronic transmission probability within the framework of the RGF approach. The parallelization aids to perform calculations on very large systems with millions of degrees of freedom and will be particularly efficient to handle highly complex modular scattering structures.

In this section, we shall describe the two-terminal RGF method [61] briefly. The retarded Green's function can be calculated using the RGF method after the discretized Hamiltonian matrix has been properly partitioned.

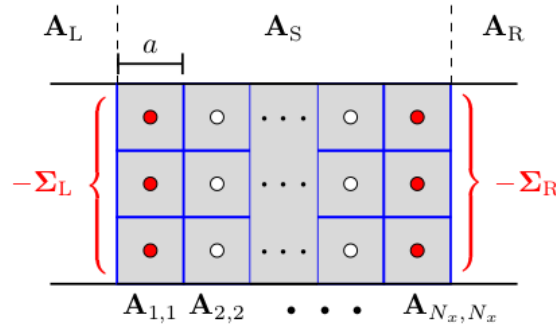


Figure 1.6. (Color online) A schematic diagram of a two-terminal system discretized on a grid. The size of the mesh is denoted by a . The system has a central region denoted by the matrix \mathbf{A}_S and two semi-infinite leads on both sides of the central region denoted by the matrices \mathbf{A}_L and \mathbf{A}_R . A block tridiagonal matrix is formed by \mathbf{A}_S by grouping the discretized points into vertical slices. Slice ' i ' is represented by the block $\mathbf{A}_{i,i}$. Σ_L and Σ_R (denoted by red color) are the self-energies of the semi-infinite leads. This image is taken from Ref. [61].

1.4.2.a Discretization of the system Hamiltonian

Here, we particularly focus on 2D systems though the method can be extended to 3D systems as well. We consider a system with two-terminals as shown in Fig. (1.6). The retarded Green's function G^R of a Hamiltonian H can be calculated from the inverse of

$$\mathbf{A} = E\mathbf{I} - \mathbf{H}, \quad (1.4.16)$$

where \mathbf{A} is an infinite matrix (since the leads are semi-infinite) that describes the whole system consisting the central region and the leads. The central scattering region being of our main interest, we divide the Hamiltonian and the Green's function for the whole system into three major parts: the scattering region, denoted by \mathbf{A}_S and the left and right leads denoted by \mathbf{A}_L and \mathbf{A}_R respectively as shown in Fig. (1.6). Hence we can write,

$$\begin{bmatrix} \mathbf{A}_L & \mathbf{A}_{LS} & 0 \\ \mathbf{A}_{SL} & \mathbf{A}_S & \mathbf{A}_{SR} \\ 0 & \mathbf{A}_{RS} & \mathbf{A}_R \end{bmatrix} \begin{bmatrix} \mathbf{G}_L^R & \mathbf{G}_{LS}^R & \mathbf{G}_{LR}^R \\ \mathbf{G}_{SL}^R & \mathbf{G}_S^R & \mathbf{G}_{SR}^R \\ \mathbf{G}_{RL}^R & \mathbf{G}_{RS}^R & \mathbf{G}_R^R \end{bmatrix} = \begin{bmatrix} \mathbf{I}_L & 0 & 0 \\ 0 & \mathbf{I}_S & 0 \\ 0 & 0 & \mathbf{I}_R \end{bmatrix}. \quad (1.4.17)$$

It is to be noted that the coupling between the left and right leads is zero, that is, $\mathbf{A}_{LR} = 0$ and $\mathbf{A}_{RL} = 0$. We have $\mathbf{A}_{Sj} = \mathbf{A}_{jS}^\dagger = -\mathbf{H}_{Sj} = t\mathbf{I}$. This result from the discretization process couples the scattering region to the left lead ($j = L$) and right lead ($j = R$) together. We can

separately write a finite matrix equation for G_S^R from Eq. (1.4.17) as,

$$\left(\mathbf{A}_S - \sum_j \Sigma_j \right) \mathbf{G}_S^R = \mathbf{I}, \quad (1.4.18)$$

whose dimension is the number of spatial points in the scattering region. Here, the self-energy contribution that comes from lead j is given by,

$$\Sigma_j = \mathbf{A}_{Sj} \mathbf{A}_j^{-1} \mathbf{A}_{js}. \quad (1.4.19)$$

This procedure can be used for any lead connected to the device. Also, the leads are supposed to be translationally invariant, which means that the self-energy matrix Σ_j can be solved analytically [2] and numerically using a convergent iteration method [62].

In our thesis, to perform numerical calculations on tight-binding models efficiently, we have used the Kwant package [63]. We have used the two-terminal RGF method via Kwant. However, this method is also applicable for multi-terminal systems. Kwant is an open-source software based on Python language, and in particular, focused on studying the quantum transport phenomena. It is easy to implement and very user-friendly. Kwant calculates the transmission coefficients through the RGF technique as described. This package solves the scattering problem in a robust and highly efficient way. Kwant takes as an input a finite-dimensional matrix representing a tight-binding model, which can, for instance, originate from an atomic description where each site corresponds to an atom. Kwant allows to compute a variety of features of tight-binding systems, for instance, wave functions, the dispersion relation, the current density, the local density of states (LDOS), the scattering matrix, the conductance, and many more. The details are available in Ref. [63].

1.4.3 The kernel polynomial method

The computation of eigenvalues of large matrices in real space is expensive in condensed matter physics. Recently, an efficient numerical method, known as the kernel polynomial method (KPM) based on the Chebyshev expansion [64] has attracted attention due to its powerful applications for solving the Hamiltonian in large Hilbert spaces. The Chebyshev expansion has aroused deep interest in numerical quantum simulations due to the high performance in parallelization since the matrix operation involves the product of sparse matrices and vectors. Also, the advantage of this method relies on the parallelizability and the linear scaling of the computational cost with the system size, which allows us to simulate very large

systems (with dimensions larger than a million). The KPM is frequently used to calculate spectral quantities in real-space basis [64–66]. In our thesis, we have used this method to simulate very large systems in the presence of a magnetic field.

1.4.4 The Chebyshev polynomials

The Chebyshev polynomials are considered as two sets of orthogonal polynomials that are solutions of ordinary differential equations [67]. There are two kinds of Chebyshev polynomials, namely the first kind and the second kind of polynomials. The first kind polynomials $T_n(x)$ are bounded, whereas the second kind diverges at the boundaries. Hence the first kind is commonly used for polynomial expansions, while the latter may lead to poor convergence of the approximation. Hence, the methods in this thesis will be presented in terms of the first kind of Chebyshev polynomials.

The Chebyshev polynomials of the first kind $T_n(x)$ can be defined in terms of trigonometric functions as,

$$T_m(x) \equiv \cos(m \theta(x)) = \cos(m \arccos(x)), \quad x \in [-1, 1], \quad (1.4.20)$$

where $\theta(x) \equiv \arccos(x)$. A complete basis can be formed for continuous functions on the interval $[-1, 1]$ and can be expressed through its closure relation,

$$\delta(x-y) = \frac{2}{\pi \sqrt{1-x^2}} \left(\frac{1}{2} + \sum_{m=1}^{\infty} T_m(x) T_m(y) \right). \quad (1.4.21)$$

Hence, if $f(x)$ is defined in this interval, it can be expressed in terms of Chebyshev expansion using,

$$f(x) = \frac{2}{\pi \sqrt{1-x^2}} \left(\frac{\mu_0}{2} + \sum_{m=1}^{\infty} \mu_m T_m(x) \right), \quad (1.4.22)$$

where μ_m represents the expansion coefficients (also known as Chebyshev moments). The orthogonality of the Chebyshev polynomials appear as,

$$\int_{-1}^1 T_m(x) T_n(x) w(x) dx = \begin{cases} 0 & m \neq n \\ 1 & m = n \neq 0, \quad w(x) \equiv \frac{1}{\sqrt{1-x^2}} \\ \frac{1}{2} & m = n = 0 \end{cases}. \quad (1.4.23)$$

Then the moments of the Chebyshev polynomials, which are called as the Chebyshev mo-

ments, can be calculated using,

$$\mu_m = \int_{-1}^1 \frac{f(x)T_m(x)}{\sqrt{1-x^2}} dx. \quad (1.4.24)$$

The Chebyshev polynomials aid in very efficient numerical approximations and can be described through recursive relation,

$$\begin{aligned} T_0(x) &= 1, \\ T_1(x) &= x, \\ T_{m+1}(x) &= 2xT_m(x) - T_{m-1}(x). \end{aligned} \quad (1.4.25)$$

Also, the truncation errors can be minimized by the usage of a kernel that is highly efficient in eliminating the Gibbs oscillations.

1.4.5 Chebyshev expansion in terms of Green's function

In this subsection, we shall address the Chebyshev expansion in terms of Green's function. In the case of non-interacting electrons, two kinds of Green's function contribute: the retarded $G^-(H, E)$ and advanced $G^+(H, E)$ Green's functions. They are defined by the relation,

$$G^\pm(H, \varepsilon) = \lim_{\eta \rightarrow 0} \frac{1}{\varepsilon - H \mp i\eta}, \quad (1.4.26)$$

where H is Hamiltonian of the system. Using Eq. (1.4.26), the Green's function can be calculated by performing an inversion of the Hamiltonian. The KPM helps to approximate the Green's functions for very large systems with reasonable accuracy and moderate computational cost.

At first, to approximate the Green's function, we need to rescale the energy spectra into the domain of the polynomials $[-1, 1]$. To avoid the approximation near the edges of the interval, the Hamiltonian is being rescaled within the interval $[-\alpha, \alpha]$, where $\alpha \in (0, 1)$ being a positive parameter. The rescaled Hamiltonian and energy can be written as,

$$\tilde{H} = \frac{2\alpha}{\Delta E} \left(H - \frac{E^+ + E^-}{2} \right), \quad \tilde{\varepsilon} = \frac{2\alpha}{\Delta E} \left(\varepsilon - \frac{E^+ + E^-}{2} \right), \quad (1.4.27)$$

where $\Delta E \equiv E^+ - E^-$ and E^+ and E^- are the maximum and minimum eigenvalue of the spectrum. α is chosen to be 0.9 for the transport calculation. The Green's function can be

written in terms of rescaled \tilde{H} and $\tilde{\varepsilon}$ as,

$$G^\pm(\tilde{H}, \tilde{\varepsilon}) = \frac{2\alpha}{\Delta E} \tilde{G}^\pm(\tilde{H}, \tilde{\varepsilon}), \quad \tilde{G}^\pm(\tilde{H}, \tilde{\varepsilon}) = \lim_{\eta \rightarrow 0} \frac{1}{\tilde{\varepsilon} - \tilde{H} \mp i\eta}, \quad (1.4.28)$$

where $\tilde{G}^\pm(\tilde{H}, \tilde{\varepsilon})$ are the rescaled Green's function. In the following we shall write the Green's function in terms of the Hamiltonian's eigenvectors $|E_k\rangle$ and the Green's functions eigenvalues $G^\pm(\tilde{E}_k, \tilde{\varepsilon})$ using the spectral theorem as [68],

$$\tilde{G}^\pm(\tilde{H}, \tilde{\varepsilon}) = \sum_k \tilde{G}^\pm(\tilde{E}_k, \tilde{\varepsilon}) |\tilde{E}_k\rangle \langle \tilde{E}_k|. \quad (1.4.29)$$

Now each of the eigenvalues can be expanded in terms of the Chebyshev polynomials as,

$$\tilde{G}^\pm(\tilde{E}_k, \tilde{\varepsilon}) = \sum_{m=0}^M \Gamma_m^\pm(\tilde{\varepsilon}) g_m T_m(\tilde{E}_k), \quad (1.4.30)$$

where,

$$\Gamma_m^\pm(\tilde{\varepsilon}) \equiv \frac{2}{\delta_{m,0} + 1} \int_{-\alpha}^{\alpha} \frac{\tilde{G}^\pm(\lambda, \tilde{\varepsilon}) T_m(\lambda)}{\pi \sqrt{1 - \lambda^2}} d\lambda. \quad (1.4.31)$$

The total rescaled Green's functions can be written as in the following,

$$\begin{aligned} \tilde{G}^\pm(\tilde{H}, \tilde{\varepsilon}) &= \sum_{m=0}^M \frac{\mp 2i}{(\delta_{m,0} + 1) \sqrt{1 - \tilde{\varepsilon}^2}} g_m \Gamma_m^\pm(\tilde{\varepsilon}) \sum_k T_m(\tilde{E}_k) |\tilde{E}_k\rangle \langle \tilde{E}_k| \\ \tilde{G}^\pm(\tilde{H}, \tilde{\varepsilon}) &= \sum_{m=0}^M \frac{\mp 2i}{(\delta_{m,0} + 1) \sqrt{1 - \tilde{\varepsilon}^2}} g_m \Gamma_m^\pm(\tilde{\varepsilon}) T_m(\tilde{H}). \end{aligned} \quad (1.4.32)$$

The Sokhotski-Plemelj [69] identity can be used to calculate $\Gamma_m^\pm(\tilde{\varepsilon})$,

$$\tilde{G}^\pm(\lambda, \tilde{\varepsilon}) = \mp i\pi \delta(\lambda - \tilde{\varepsilon}) + \mathcal{P} \left(\frac{1}{\lambda - \tilde{\varepsilon}} \right). \quad (1.4.33)$$

From which one can write,

$$\Gamma_m^\pm(\tilde{\varepsilon}) = \frac{2}{\delta_{m,0} + 1} \left(\mp i \frac{T_m(\tilde{\varepsilon})}{\sqrt{1 - \tilde{\varepsilon}^2}} + \mathcal{P} \int_{-\alpha}^{\alpha} \frac{T_m(\lambda)}{\pi(\lambda - \tilde{\varepsilon}) \sqrt{1 - \lambda^2}} d\lambda \right), \quad (1.4.34)$$

where \mathcal{P} denotes the principal value of the integral. The last part of the integral can be solved using the trigonometric definition of the Chebyshev functions as,

$$\Gamma_m^\pm(\tilde{\varepsilon}) = \mp \frac{2ie^{\mp im \arccos(\tilde{\varepsilon})}}{(\delta_{m,0} + 1) \sqrt{1 - \tilde{\varepsilon}^2}}. \quad (1.4.35)$$

The basic advantage of the Green's function formalism is that a few matrix elements of the Green's functions are required for the calculation of a given observable. In the following we shall see that one can calculate the matrix elements of Green's functions independently using Eq. (1.4.32).

In the real space basis, the eigenvectors of the position operator can be written as, $\hat{\mathbf{R}}|\mathbf{R}_i\rangle = \mathbf{R}_i|\mathbf{R}_i\rangle$. similarly, one can compute the matrix elements of the Green's functions $G_{i,j}^\pm(H, \varepsilon)$ as,

$$G_{i,j}^\pm(H, \varepsilon) = \langle \mathbf{R}_i | G^\pm(H, \varepsilon) | \mathbf{R}_j \rangle. \quad (1.4.36)$$

Also the approximation can be obtained through the following expansion as,

$$\tilde{G}_{i,j}^\pm(\tilde{H}, \tilde{\varepsilon}) = \sum_{m=0}^M g_m \mu_m^{i,j} \Gamma_m^\pm(\tilde{\varepsilon}), \quad \mu_m^{i,j} = \langle \mathbf{R}_i | T_m(\tilde{H}) | \mathbf{R}_j \rangle, \quad (1.4.37)$$

where $\mu_{i,j}$ are the expansion moments of the series. Finally, the result is an expansion on a basis defined by the Γ -functions and hence the Green's function acquires the form of Eq. (1.4.35).

It is not necessary to calculate the matrices $T_m(\tilde{H})$ for obtaining these moments. One can define the vectors as,

$$|\Phi_0^i\rangle = |\mathbf{R}_i\rangle, \quad |\Phi_1^i\rangle = \tilde{H}|\mathbf{R}_i\rangle, \quad (1.4.38)$$

and obtain all the subsequent vectors using the recursive relation in Eq. (1.4.25) as,

$$T_m(\tilde{H})|\mathbf{R}_i\rangle = |\Phi_m^i\rangle = 2\tilde{H}|\Phi_{m-1}^i\rangle - |\Phi_{m-2}^i\rangle. \quad (1.4.39)$$

The Chebyshev moments can be calculated,

$$\mu_m^{i,j} = \langle \mathbf{R}_i | \Phi_m^i \rangle. \quad (1.4.40)$$

The diagonal elements of the Green's functions are directly related to the LDOS which can be considered as the number of available states for a given energy at a given lattice site. This can be defined as,

$$\rho_i(\varepsilon) \equiv \langle \mathbf{R}_i | \delta(\varepsilon - H) | \mathbf{R}_i \rangle = \mp \frac{1}{\pi} \text{Im}[G_{i,i}^\mp(\varepsilon)]. \quad (1.4.41)$$

In a Chebyshev series expansion, the LDOS can be expressed as,

$$\tilde{\rho}_i(\tilde{\varepsilon}) = \sum_{m=0}^M g_m \mu_m^{i,i} \text{Im}[\Gamma^\pm(\tilde{\varepsilon})] \quad (1.4.42)$$

$$\tilde{\rho}_i(\tilde{\varepsilon}) = \frac{2}{\pi \sqrt{1 - \tilde{\varepsilon}^2}} \left(\frac{g_0}{2} + \sum_{m=0}^M g_m \mu_m^{i,i} T_m(\tilde{\varepsilon}) \right) \quad (1.4.43)$$

Also the density of states (DOS) $\rho(\varepsilon)$ at an energy can be defined as the trace of the imaginary part of the Green's function as,

$$\rho(\varepsilon) = \text{Tr}[\text{Im}[G(H, \varepsilon)]]. \quad (1.4.44)$$

Using Eq. (1.4.39), one can find

$$\tilde{\rho}(\tilde{\varepsilon}) = \frac{1}{\pi \sqrt{1 - \tilde{\varepsilon}^2}} \left(\frac{g_0}{2} + \sum_{m=1}^M g_m \text{Tr}[T_m(\tilde{H})] \right). \quad (1.4.45)$$

This is the expression for DOS in terms of Chebyshev expansion. The trace can be calculated using a stochastic method.

1.4.6 The Kubo-Bastin formula

The linear response theory implies that the effective motion or velocity of the charge carriers are proportional to the external perturbation, such as mechanical perturbations (perturbation of Hamiltonian) or thermal perturbations (perturbation of boundary conditions), and the transport behavior can be quantified by the proportionality constant. The linear response theory is the most standard method to study the bulk Hall conductivities, which was developed by R. Kubo [70]. This method was applied to the QH effect by Aoki and Ando [71] for the first time. The standard Kubo's formula for the conductivity tensor is a current-current correlation function that can be written as [70, 72],

$$\sigma_{\alpha\beta}(\mu, T) = \frac{1}{\Omega} \int_0^\infty dt \int_0^\infty d\lambda \langle f(\mu, T, H) j_\alpha j_\beta(t + i\hbar\lambda) \rangle. \quad (1.4.46)$$

where Ω is the volume of the system, j_α is the current operator and $f(\mu, T, H) \equiv 1/(1 + e^{-(\mu-H)/kT})$ is the Fermi-Dirac distribution function for a given temperature, T and the chemical potential, μ . Eq. (1.4.46) can be rewritten in the non-interacting electron approximation

as,

$$\sigma_{\alpha\beta}(\mu, T) = \frac{ie^2\hbar}{A} \int_{E^-}^{E^+} d\varepsilon f(\varepsilon) \text{Tr} \left\langle v_\alpha \delta(\varepsilon - H) v_\beta \frac{dG^+(\varepsilon)}{d\varepsilon} - v_\alpha \frac{dG^-(\varepsilon)}{d\varepsilon} v_\beta \delta(\varepsilon - H) \right\rangle. \quad (1.4.47)$$

This is known as the Kubo-Bastin formula. H and v_α denote the non-interacting Hamiltonian and velocity operators respectively. Using the Heisenberg relation, the velocity operator v can be expressed in terms of the eigenvalues of the position operator $|\mathbf{R}_i\rangle$, $i = 1, \dots, D$ and the Hamiltonian's matrix elements as,

$$v = \frac{1}{i\hbar} [\mathbf{R}, H] = \frac{1}{i\hbar} \sum_{i,j=1}^D (\mathbf{R}_i - \mathbf{R}_j) H_{i,j} |\mathbf{R}_i\rangle \langle \mathbf{R}_j|. \quad (1.4.48)$$

Now the Kubo-Bastin formula can be expressed in terms of a Chebyshev expansion as described earlier. We can rescale the Hamiltonian's spectrum into the interval $[-\alpha, \alpha]$. Hence the rescaled conductivity in terms of rescaled Green's function and δ -function becomes,

$$\sigma_{\alpha\beta}(\mu, T) = \frac{4\alpha^2}{\Delta E^2} \tilde{\sigma}_{\alpha\beta}(\tilde{\mu}, \tilde{T}) \quad (1.4.49)$$

$$\tilde{\sigma}_{\alpha\beta}(\tilde{\mu}, \tilde{T}) = \frac{ie^2\hbar}{A} \int_{-\alpha}^{\alpha} d\varepsilon f(\varepsilon) \text{Tr} \left\langle v_\alpha \tilde{\delta}(\varepsilon - H) v_\beta \frac{d\tilde{G}^+(\varepsilon)}{d\varepsilon} - v_\alpha \frac{d\tilde{G}^-(\varepsilon)}{d\varepsilon} v_\beta \delta(\varepsilon - H) \right\rangle. \quad (1.4.50)$$

In terms of the Chebyshev polynomials the rescaled δ -function and the Green's function can be expressed as,

$$\begin{aligned} \tilde{\delta}(\varepsilon - \tilde{H}) &= \frac{2}{\pi \sqrt{1 - \varepsilon^2}} \sum_{m=0}^M g_m \frac{T_m(\varepsilon)}{\delta_{m,0} + 1} T_m(\tilde{H}), \\ \tilde{G}^\pm(\varepsilon, \tilde{H}) &= \mp \frac{2i}{\sqrt{1 - \varepsilon^2}} \sum_{m=0}^M g_m \frac{e^{\pm im \arccos(\varepsilon)}}{\delta_{m,0} + 1} T_m(\tilde{H}), \\ \frac{d\tilde{G}^\pm(\varepsilon, \tilde{H})}{d\varepsilon} &= \mp 2i \sum_{m=0}^M \frac{g_m}{\delta_{m,0} + 1} \frac{d}{d\varepsilon} \left(\frac{e^{\pm im \arccos(\varepsilon)}}{\sqrt{1 - \varepsilon^2}} \right) T_m(\tilde{H}) \end{aligned} \quad (1.4.51)$$

Using Eq. (1.4.51) in Eq. (1.4.50), the following expression can be found as,

$$\sigma_{\alpha\beta}(\mu, T) = \frac{4e^2\hbar}{\pi A} \frac{4}{(\Delta E)^2} \int_{-1}^1 d\tilde{\varepsilon} \frac{f(\tilde{\varepsilon})}{(1 - \tilde{\varepsilon}^2)^2} \sum_{m,n} \Gamma_{nm}(\tilde{\varepsilon}) \mu_{nm}^{\alpha\beta}(\tilde{H}) \quad (1.4.52)$$

where we have,

$$\Gamma_{nm}(\tilde{\varepsilon}) \equiv (\tilde{\varepsilon} - in \sqrt{1 - \tilde{\varepsilon}^2}) e^{in \arccos(\tilde{\varepsilon})} T_m(\tilde{\varepsilon}) + (\tilde{\varepsilon} + im \sqrt{1 - \tilde{\varepsilon}^2}) e^{-im \arccos(\tilde{\varepsilon})} T_n(\tilde{\varepsilon})$$

$$\mu_{nm}^{\alpha\beta}(\tilde{H}) \equiv \frac{g_m g_n}{(1 + \delta_{n0})(1 + \delta_{m0})} \text{Tr}[v_\alpha T_m(\tilde{H}) v_\beta T_n(\tilde{H})]. \quad (1.4.53)$$

Here $\Gamma_{mn}(\tilde{\epsilon})$ are the expansion functions and $\mu_{mn}(\tilde{H})$ are the expansion moments of the polynomial expansion. It is to be noted that the numerical integration of spectral functions in Eq. (1.4.52) can be efficiently computed in terms of convergence by performing the integration first and then expand the function in terms of the Chebyshev polynomials. The analytical solution for the integration of Kubo-Bastin formula at temperature $T = 0$ is known as Kubo-Streda formula. Two types of contributions comes from the Kubo-Streda formula,

$$\tilde{\sigma}_{\alpha,\beta}^I = \frac{ie^2\hbar}{2} \text{Tr} \left\langle \delta(\epsilon_f - H) [v_\alpha G^+(\epsilon_f) v_\beta - v_\beta G^-(\epsilon_f) v_\alpha] \right\rangle \quad (1.4.54)$$

$$\tilde{\sigma}_{\alpha,\beta}^{II} = -\frac{e^2}{2} \text{Tr} \left\langle \delta(\epsilon_f - H) (r_\alpha v_\beta - r_\beta v_\alpha) \right\rangle. \quad (1.4.55)$$

The first one contributes to the longitudinal conductivity, while the second has a contribution to the Hall conductivity.

In this thesis, we have used both these efficient techniques, as described above, to compute the various quantum transport phenomena in semi-Dirac and Dirac systems. Mainly, we have computed the Landauer conductance in the presence of SOCs and have used the Kubo-Bastin formula for dealing with the transport features in the presence of a magnetic field.

1.5 Outline of the thesis

The main goal of this thesis lies in studying the transport properties of a 2D semi-Dirac system within the framework of a tight-binding model on a honeycomb lattice in the presence of SOC and magnetic field, B (SOC \rightarrow no TRS breaking, $B \rightarrow$ TRS breaking). We also took a chance to compare systematically each of these results with those obtained for the Dirac case. We have a total of seven chapters in the thesis. We organize the thesis as follows.

In the *first chapter*, we start with the basic introduction to mesoscopic physics and its relevance to transport properties. We have introduced SOCs, such as the Rashba SOC, and discussed the effects of an external magnetic field. We have discussed the two important topological phases of matter elaborately mostly studied in our thesis, that is quantum Hall and quantum spin Hall phases. We have introduced the 2D Dirac (graphene) and semi-Dirac systems with examples of the experimental background of these systems and their applications in real materials. Further, we present the formalism for calculating transport properties

relevant for the thesis, namely, the RGF implemented via Landauer-Büttiker formula [3, 73] that we have used to study both charge and spin conductivities. The formalism employs the usage of Kwant, for which we provide an overview. For the latter part of the thesis, we have used the Kubo formula, which we discussed for computing transport based on the KPM via KITE [74]. The rationale for using these methods is illustrated via the merits that lie therein.

In the *second chapter*, we compute the eigenvalue equations for the zero-energy edge modes using a tight-binding Hamiltonian of 2D Dirac (such as single layer and bilayer graphene) and semi-Dirac nanoribbons. We solved these equations numerically to observe the nature of the edge states and the band structures of the zigzag nanoribbon. We have numerically computed the LDOS results, which provide robust support of our results on the edge states derived analytically. We also calculated the charge conductance for both these cases and explored the transport properties.

In the *third chapter*, we compute the analytical expressions for the localized edge states for a KM Hamiltonian corresponding to the Dirac and the semi-Dirac cases. We elaborately study the zero-energy edge modes, band dispersion, and charge conductance for several different cases, such as in the presence of only intrinsic SOC, both the SOCs (that is, intrinsic and Rashba), etc. Next, we have extended the above study for a bilayer graphene nanoribbon using the KM model and observed the interplay of the Rashba and the intrinsic SOCs with the edge states, band structures, charge and spin transport in detail. A study of spin transport has been done in bilayer graphene by tuning the Rashba SOC that relates to spintronic applications. To make a connection with experiments, we have computed the effective mass and have shown that it can be tuned by the inclusion of Rashba SOC. The corresponding scenarios for a semi-Dirac nanoribbon have also been investigated, which provide the distinct feature of the edge states, along with different transport characteristics as compared to the Dirac case.

In the *fourth chapter*, we turn our attention to the effects of an external magnetic field, where we study the different physical properties of a semi-Dirac nanoribbon in the presence of a field within the framework of a tight-binding model of a honeycomb lattice. In order to compare with a Dirac system, such as graphene, we present our results for both cases. We have also focused on several physical properties that have ramifications in experiments, such as the nature of the LLs, Fractal spectra observed in the Hofstadter butterfly, etc.

In the *fifth chapter*, we study the quantum Hall transport properties of a semi-Dirac nanoribbon in the presence of an external magnetic field using the same tight-binding model as described in the fourth chapter. For comparison, we also present our results for the Dirac

case. We investigate the density of states in the absence and presence of a magnetic field. We numerically explore the magneto-transport properties (such as the longitudinal and the Hall conductivities) using the Kubo formula based on the KPM.

In the *sixth chapter*, we have investigated the magneto-optical (MO) transport properties of a semi-Dirac system subjected to an external magnetic field and compared them to those of the Dirac systems. Selection rules, various transitions, and their presence from the peaks in the absorption spectra are investigated. Moreover, we have studied the effect of electron filling on the absorption spectra by tuning the chemical potential between the consecutive LLs. Also, to explore the interplay of the polarization of the incident radiation with MO transport, we consider the light of different polarization, namely, a circularly polarized light. Finally, to ascertain the MO activity of the semi-Dirac systems and to make a connection with experiments, we study Faraday rotation for the semi-Dirac case, which should be possible to be realized in the experiments.

We conclude in the *seventh chapter* by summarizing the important results obtained in our thesis. We also include a brief outlook on the possible extension of the thesis work.

2 Transport properties of 2D Dirac and semi-Dirac nanoribbons: Role of edge states

Contents

2.1 Landauer formula used for computing transport	32
2.2 Dirac and semi-Dirac systems.	32
2.3 Tight-binding model of Dirac nanoribbon	35
2.3.1 Edge states and band structure	35
2.3.2 LDOS and conductivity	39
2.3.3 Bilayer graphene	40
2.4 Tight-binding model of semi-Dirac nanoribbon	47
2.4.1 Edge states and band structure	49
2.4.2 LDOS and conductivity	50
2.5 Summary	51

Since the discovery of graphene [75], Dirac materials in two dimensions have generated intense research activities to study the electronic properties of these novel 2D electronic systems. The valence and the conduction bands of graphene touch each other at two non-equivalent Dirac points, namely K_1 and K_2 , which have opposite chiralities and form a time-reversed pair. The band structure around those points has the form of massless Dirac fermions, that is, $E_{\vec{k}} = \hbar v |\vec{k}|$, where v ($\approx 10^6$ ms $^{-1}$) is the Fermi velocity. The Dirac nature of the electrons [34] is responsible for many interesting properties of graphene [33], such

as unconventional quantum Hall effect [75–77], half metallicity [78, 79], Klein tunneling through a barrier [80], high carrier mobility [81, 82] and many more. Owing to these features, graphene is recognized as one of the promising materials for realizing next-generation electronic devices.

After the successful fabrication of graphene [75], it was observed that bilayer graphene too shows a variety of striking phenomena [83, 84]. Many of the properties of bilayer graphene are analogous to those of a monolayer, such as high thermal conductivity [85, 86], high electrical conductivity [87], mechanical strength, and flexibility [88, 89]. However, bilayer graphene has some additional features that make it distinct from monolayer graphene. Monolayer graphene has a linear dispersion near the Dirac points [34], whereas, in bilayer graphene, the band shows parabolic dispersion with massive chiral quasiparticles [84, 90]. In the absence of an external electric field, the system comprises four bands, two of them touch each other at zero energy and the other two are separated by an amount equal to the magnitude of the interlayer tunneling, t_{\perp} . Moreover, the bandgap in bilayer graphene can be opened and tuned by applying a gate voltage externally [33, 91]. In general, bilayer graphene can be synthesized in two different configurations, one with carbon (C) atoms of the *A* sublattice in one layer being stacked directly over that of *A* sublattice of the other layer (*AA* stacking), or in another, C atoms of *A* sublattice is stacked over C atoms of *B* sublattice (*AB* stacking).

Recently, a close variant of the 2D Dirac materials termed as the semi-Dirac materials have been discovered. In a tight-binding model for a 2D Dirac system, such as graphene, consider that one of the three nearest neighbors hopping energies is tuned (say, t_2) with respect to the other two (say, t), the two Dirac points with opposite chiralities move in the BZ. Eventually, when t_2 becomes equal to $2t$, the two cones merge into one at the so-called semi-Dirac point. Such materials possess unique band dispersion, which simultaneously shows massless Dirac (linear) along one direction and massive fermionic (quadratic) features in other directions. Such dispersion are found in phosphorene under pressure and doping [92, 93], electric fields [94, 95], α -(BEDT-TTF)₂I₃ salt under pressure [96, 97], and many more as described earlier in Chapter 1.

The existence of the edge states in a graphene sheet is one of the interesting features in condensed matter physics. The properties of the edge states are different than those of the bulk states and play important roles in transport. When the valence and the conduction bands are separated by an energy gap, one either gets a semiconductor (when the energy gap is of the order of an eV) or an insulator (for the gap to be around 4 to 6 eV). However, this does

not guarantee that the system is a simple insulator (assuming a large gap) since conduction may still be allowed via the edge modes. These new types of insulators are fundamentally different from the trivial insulators due to their unique gapless edge states protected by the time-reversal symmetry. They have been attributed the name topological insulators (TIs). Thus TIs represent a new quantum state. The phenomena associated with the TIs are the well-known QH effect and the QSH effect (see Chapter 1). It has been found that the gapless chiral (for QH) or helical (for QSH) edge states are robust channels with quantized conductance accompanied by non-vanishing values at zero-bias voltage [15, 18, 19, 29, 98–101]. Moreover, the study of the edge states in graphene has ramifications in many aspects, such as magnetism [102], superconductivity [103], spintronics [104], quantum topological phases [105], and many more.

On the other hand, graphene nanoribbons (GNRs) have also drawn huge attention due to their striking physical properties and practical applications in nano-devices [33, 106, 107]. There are mainly two kinds of GNRs, AGNRs and ZGNRs (see Fig. 1.4). The two edges have 30° difference in their cutting direction. The ZGNRs are always metallic with zero bandgaps, while the AGNRs are metallic when the lateral width $N = 3M - 1$ (M is an integer), else the AGNRs are semiconducting in nature [39] with a finite bandgap. The ZGNRs possess localized edge states with energies close to the Fermi level, which are absent for AGNRs. It was shown that a monolayer ZGNR supports zero-energy edge states and is dispersionless (flat band) near the Fermi energy [38, 39, 108]. Later, it was also shown that a bilayer ZGNR also supports edge states at zero Fermi energy [109].

In the following section, we discuss the method to calculate the transport properties of GNRs with Dirac and semi-Dirac band structure based on the Landauer-Büttiker formalism (details are given in Chapter 1 and the essential steps are outlined in the next section). We compute the analytical expressions for the zero-energy edge modes using a tight-binding honeycomb lattice of the 2D Dirac system (graphene), bilayer graphene, and semi-Dirac system. We specifically show the band dispersion using the ribbon geometry that holds the property of translational invariance along the longitudinal direction. To confirm the behavior of the edge states, we have calculated the local density of states (LDOS) near the Fermi energy. Further, the conductance properties are explored using Landauer-Büttiker formalism. For our numerical calculation on the LDOS and conductance, we have used Kwant [63].

2.1 Landauer formula used for computing transport

To study the electron conductance, we investigate the transport characteristics using Landauer-Büttiker formula [3, 73] that relates the scattering matrix to the conductance via,

$$G = \frac{e^2}{h} T(E), \quad (2.1.1)$$

where e is the electronic charge, h is the Planck's constant and $T(E)$ is the transmission coefficient at a given value of the biasing energy, E . The transmission coefficient is defined as [58, 59],

$$T = \text{Tr}[\Gamma_R G^R \Gamma_L G^A]. \quad (2.1.2)$$

$G^{R(A)}$ is the retarded(advanced) Green's function of the scattering region. The coupling matrices $\Gamma_{L(R)}$ are the imaginary parts representing the coupling between the scattering region and the left(right) lead (see Fig. 1.5 in Chapter 1). They are defined by [2],

$$\Gamma_{L(R)} = i[\Sigma_{L(R)} - (\Sigma_{L(R)})^\dagger]. \quad (2.1.3)$$

Here $\Sigma_{L(R)}$ is the retarded self-energy associated with the left(right) lead. The self-energy contribution is computed by modelling each terminal as a semi-infinite perfect wire [110]. From Green's function, the LDOS can be found using [2],

$$\rho(E) = -\frac{1}{\pi} \text{Im}[G^R(E)]. \quad (2.1.4)$$

To compute the LDOS maps, the retarded Green's function can be used for the system is written as [2],

$$G^R = \frac{1}{EI - H + i\eta}, \quad (2.1.5)$$

where H is the Hamiltonian for the system and η is a small positive number.

2.2 Dirac and semi-Dirac systems

In this section, we describe the tight-binding model on the honeycomb lattice with anisotropic hopping that leads to semi-Dirac electronic spectra at low energies. More precisely, the hopping energy to one of the nearest neighbors (t_2) is different than the other two (t) as shown in Fig. (2.1). It is also instructive to look at the full dispersion with the following three nearest

neighbor vectors in real space, $\vec{\delta}_1 = (0, a)$; $\vec{\delta}_2 = \left(\frac{\sqrt{3}a}{2}, -\frac{a}{2}\right)$ and $\vec{\delta}_3 = \left(-\frac{\sqrt{3}a}{2}, -\frac{a}{2}\right)$, where a is the distance between two nearest neighbor carbon atoms. The dispersion relation for a semi-Dirac system can be written as,

$$E(k) = \pm \sqrt{2t^2 + t_2^2 + 2t^2 \cos \sqrt{3}k_x a + 4t_2 t \cos(3k_y a/2) \cos(\sqrt{3}k_x a/2)}. \quad (2.2.1)$$

The above expression can be used for both Dirac and semi-Dirac depending upon the choice

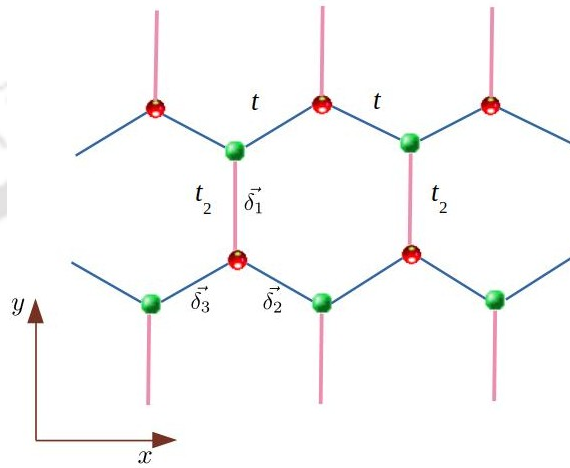


Figure 2.1. (color online) A schematic sketch of lattice geometry of a semi-Dirac system with different hopping parameters, t (denoted by blue) and t_2 (denoted by pink) is shown. Two sublattices are denoted by two different colors, that is, red and green. $\vec{\delta}_1$, $\vec{\delta}_2$, $\vec{\delta}_3$ are the real space nearest neighbor vectors mentioned in the text.

of t_2 value as shown in Eq. (2.2.1). When $t_2 = t$ or $2t$, we have the 3D tight-binding band-structure for the Dirac or semi-Dirac as shown in Fig. (2.2a) and Fig. (2.2b) respectively. The band dispersion within the BZ along the high-symmetry points is also shown in Fig. (2.2c) and Fig. (2.2d) for both cases. For the Dirac case (that is, $t_2 = t$), the dispersion shows that the Dirac points touch at the K_1 and K_2 points at the BZ corners as shown in Fig. (2.2c). With increasing the strength of the parameter t_2 , the two Dirac points originally located at $K_1 \left(\frac{2\pi}{3\sqrt{3}a}, \frac{2\pi}{3a}\right)$ and $K_2 \left(-\frac{2\pi}{3\sqrt{3}a}, \frac{2\pi}{3a}\right)$ move closer till they merge at the M point resulting in a semi-Dirac spectrum (see Fig. (2.2d)). As mentioned earlier, such manipulation of the Dirac points and their eventual merger have been achieved in honeycomb optical lattices [51]. Thus by fixing $t_2 = 2t$ and focusing on the M point $(0, \frac{2\pi}{3a})$, the low-energy effective Hamiltonian based on the tight-binding model for a semi-Dirac system, apart from a constant term, can be written as [111–113],

$$H_0 = \frac{p_x^2 \sigma_x}{2m^*} + v_F p_y \sigma_y, \quad (2.2.2)$$

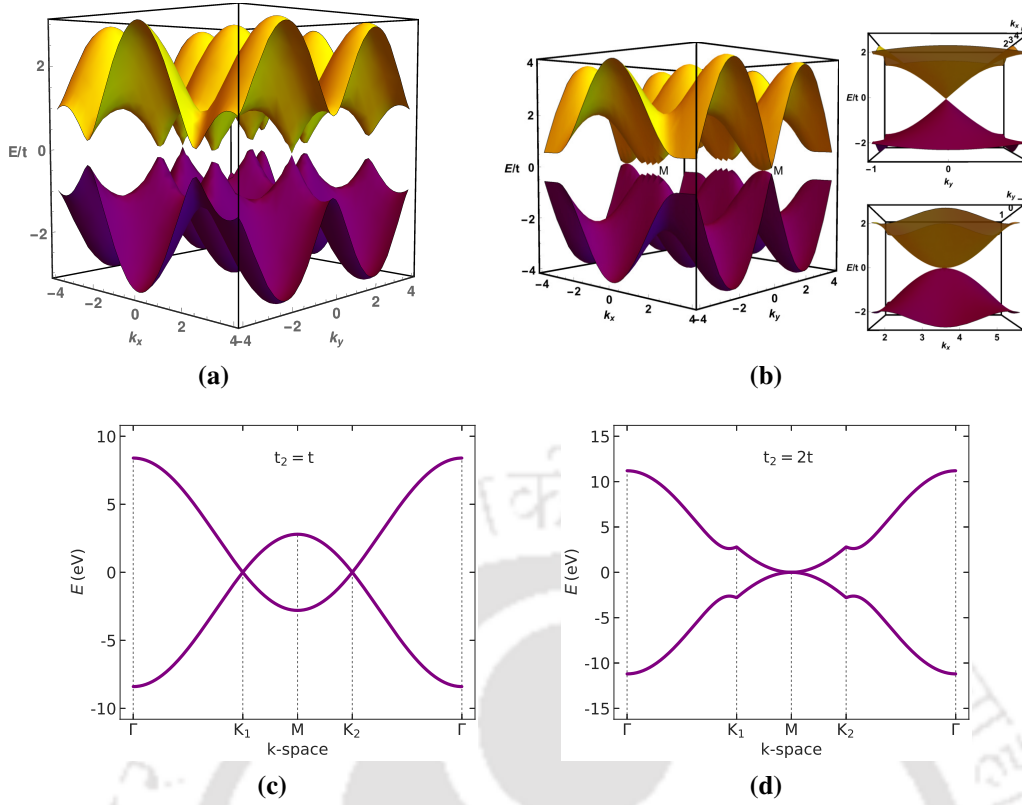


Figure 2.2. (Color online) Energy band dispersion of a (a) Dirac system and (b) semi-Dirac system is shown. The anisotropic band dispersion is observed for the semi-Dirac case. In the side panel of (b), we zoom the region near the M point along the k_y and the k_x directions. The dispersion is linear along the y -direction and quadratic along the x -direction. Here a is set to be unity. The dispersion along the high symmetry points $\Gamma \rightarrow K_1 \rightarrow M \rightarrow K_2 \rightarrow \Gamma$ for different strength of hopping parameters (c) $t_2 = t$ (Dirac) and (d) $t_2 = 2t$ (semi-Dirac) respectively. Here we taken $t = 2.8\text{eV}$.

where p_x and p_y are the momenta along the x and the y directions respectively. σ_x and σ_y are the Pauli spin matrices in the pseudospin space. The velocity along the p_y direction, v_F , and the effective mass, m^* corresponding to the parabolic dispersion along p_x are expressed as $v_F = 3ta/\hbar$ and $m^* = 2\hbar/3ta^2$. Henceforth we set $a = 1$. The dispersion relation corresponding to Eq. (2.2.2) ignoring a constant shift in energy can be written as,

$$E = \pm \sqrt{(\hbar v_F k_y)^2 + \left(\frac{\hbar^2 k_x^2}{2m^*}\right)^2}, \quad (2.2.3)$$

where ‘+’ denotes for the conduction band and ‘-’ stands for the valence band. Eq. (2.2.3) shows that the dispersion is linear (Dirac-like) along y -direction, whereas the dispersion along the x -direction is quadratic (non-relativistic), the combination of which results in the semi-Dirac dispersion. In the following, we shall work with a semi-infinite Dirac and semi-Dirac nanoribbon for our purpose as described earlier.

2.3 Tight-binding model of Dirac nanoribbon

To begin our discussion of a Dirac material, such as graphene, we consider a 2D semi-infinite graphene sheet which consists of two sublattices A and B connected to the three nearest neighbors vectors in real space via,

$$\vec{\delta}_1 = (0, a); \quad \vec{\delta}_2 = \left(\frac{\sqrt{3}a}{2}, -\frac{a}{2}\right); \quad \vec{\delta}_3 = \left(-\frac{\sqrt{3}a}{2}, -\frac{a}{2}\right), \quad (2.3.1)$$

where $a \approx 1.42\text{\AA}$ is the distance between two consecutive carbon atoms. In order to study the nature of the edge states and transport properties of graphene, we consider the following tight-binding Hamiltonian written as,

$$H = -t \sum_{\langle ij \rangle \sigma} (c_{i\sigma}^\dagger c_{j\sigma} + h.c.). \quad (2.3.2)$$

Here $c_{i\sigma}^\dagger$ and $c_{j\sigma}$ are creation and annihilation operators for π -electron with spin σ on site i and j . The $\langle ij \rangle$ term describes the hopping between nearest neighbors i and j on a honeycomb lattice and the hopping amplitude is $t \simeq 2.8$ eV. $h.c.$ denotes the hermitian conjugate. Though we used the spin index σ , however, the results are identical for both $\sigma = \uparrow$ and \downarrow (except that it includes the degeneracy factor), and hence not shown them separately in this chapter. In the following, we shall derive the edge modes for a ZGNR and compute the corresponding band structure.

2.3.1 Edge states and band structure

In this subsection, in order to study the properties of the band structure and the edge states, we consider a ribbon geometry with zigzag edges which are infinite along the x -axis (longitudinal direction), and all the atoms of the zigzag edges belong to the same sublattice as shown in Fig. (2.3). Keeping in mind that all the dangling bonds at graphene edges are terminated by hydrogen atoms, we do not consider any contribution to the electronic states near the Fermi energy. The ribbon width is such that it has N unit cells in the y -axis (transverse direction). We rewrite the equation (2.3.2) in terms of m, n which labels the unit cell (see Fig. (2.3)), is given by [33],

$$H = -t \sum_{\langle mn \rangle \sigma} [a_\sigma^\dagger(m, n)b_\sigma(m, n) + a_\sigma^\dagger(m, n)b_\sigma(m, n-1) + a_\sigma^\dagger(m, n)b_\sigma(m-1, n) + h.c.], \quad (2.3.3)$$

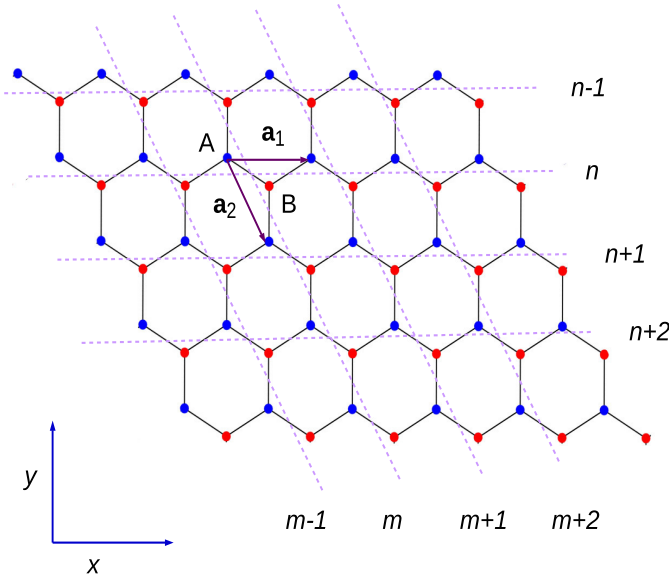


Figure 2.3. (Color online) Graphene nanoribbon geometry with zigzag edges. The blue and the red circles represent A and B sublattices of the ribbon. \vec{a}_1 and \vec{a}_2 are the primitive vectors. (m, n) labels the unit cell. m increases along the positive x -direction, whereas n increases along the negative y -direction.

where $\langle \rangle$ denotes nearest neighbors and σ represents the \uparrow, \downarrow spin for both sublattices A and B . The translational symmetry exists along the x -axis, but there is no translational symmetry along the y -direction due to the existence of a boundary. Hence, only the momentum along x , namely k_x is a good quantum number. Now we can use a momentum representation of the electron operator due to the periodicity in the x -direction, which is,

$$c_i = \frac{1}{\sqrt{N}} \sum_{k_x} e^{ik_x X_i} c_{\mathbf{k}}, \quad (2.3.4)$$

where X_i represents the coordinate of the site A in the unit cell (m, n) and N denotes the number of unit cells. Using Schrödinger equation $H|\psi\rangle = E|\psi\rangle$, we get the following eigenvalue equations for sites in A and B sublattices as,

$$\begin{aligned} E\alpha(k_x, n) &= -t \left[2 \cos\left(\frac{\sqrt{3}k_x}{2}\right) \beta(k_x, n) + \beta(k_x, n-1) \right] \\ E\beta(k_x, n) &= -t \left[2 \cos\left(\frac{\sqrt{3}k_x}{2}\right) \alpha(k_x, n) + \alpha(k_x, n+1) \right], \end{aligned} \quad (2.3.5)$$

where we have chosen the basis as,

$$|\psi_k\rangle = \sum_{n, \sigma} \alpha(k, n, \sigma) |a, k, n, \sigma\rangle + \beta(k, n, \sigma) |b, k, n, \sigma\rangle, \quad (2.3.6)$$

where α , β are the coefficients corresponding to A and the B sublattices respectively. Since we have taken zigzag edges and the ribbon exists only between 0 to $N - 1$ (the edges are passivated), and thus the boundary condition can be written as,

$$\alpha(k_x, N) = \beta(k_x, -1) = 0. \quad (2.3.7)$$

Applying this boundary condition to Eq. (2.3.5), we get

$$\begin{aligned} E\alpha(k_x, 0) &= -t \left[2 \cos \left(\frac{\sqrt{3}k_x}{2} \right) \beta(k_x, 0) \right] \\ E\beta(k_x, N-1) &= -t \left[2 \cos \left(\frac{\sqrt{3}k_x}{2} \right) \alpha(k_x, N-1) \right]. \end{aligned} \quad (2.3.8)$$

Now we consider the zero-energy modes (close to the Fermi energy), namely $E = 0$ and put it in Eqs. (2.3.5) and (2.3.8) to get the solutions for the edge states. Thus, we obtain the following equations,

$$0 = \left[2 \cos \left(\frac{\sqrt{3}k_x}{2} \right) \beta(k_x, n) + \beta(k_x, n-1) \right] \quad (2.3.9)$$

$$0 = \left[2 \cos \left(\frac{\sqrt{3}k_x}{2} \right) \alpha(k_x, n) + \alpha(k_x, n+1) \right] \quad (2.3.10)$$

$$0 = \beta(k_x, 0) \quad (2.3.11)$$

$$0 = \alpha(k_x, N-1). \quad (2.3.12)$$

Solving Eqs. (2.3.9) and (2.3.10), we finally get,

$$E\alpha(k_x, n) = \left[-2 \cos \left(\frac{\sqrt{3}k_x}{2} \right) \right]^n \alpha(k_x, 0) \quad (2.3.13)$$

$$E\beta(k_x, n) = \left[-2 \cos \left(\frac{\sqrt{3}k_x}{2} \right) \right]^{(N-1-n)} \beta(k_x, N-1). \quad (2.3.14)$$

These are the solutions that we have used to capture the behavior of the wave functions along both edges. It can be seen that the charge density shows an exponential decay as one deviates from the edges [38], implying the presence of localized edge states.

In our calculation, we have made k_x to be a dimensionless quantity by absorbing the lattice spacing a into the definition of k_x . Also, we have taken $N = 100$ unit cells in the y -direction (see Fig. (2.3)). To see how the states at the edges look like, we have plotted the probability density, $|\psi|^2$ as a function of site index, n by solving Eqs. (2.3.13) and (2.3.14)

in Fig. (2.4a). It shows that the wave function has maximum amplitude at the edges and gradually decays as one moves inwards into the bulk. Moreover, it is completely localized at the edge, when $k_x = 2\pi/3 \sqrt{3}$ and penetrate into the bulk as k_x deviates from this value. Afterwards, they become extended between $k_x = 2\pi/3 \sqrt{3}$ and $4\pi/3 \sqrt{3}$. The lack of a gap in the spectrum in graphene turns the $E = 0$ state whose amplitude is maximum at the two edges and decays as one moves inward [114]. We have to set a convergence condition which is $|-2 \cos(\frac{\sqrt{3}k_x}{2})| \leq 1$, in order to solve Eq. (2.3.13) and Eq. (2.3.14) iteratively. Without this condition, the wave function will not be square-integrable in the semi-infinite graphene sheet. This convergence condition defines the region in the momentum space given by, $2\pi/3 \sqrt{3} \leq k_x \leq 4\pi/3 \sqrt{3}$ where the $E = 0$ band is dispersionless.

To calculate the band structure we use Eq. (2.3.3) and the tight-binding parameter t is set to be 1. Also, we have considered the lattice spacing, $a = 1$. All the energies are measured in units of t . The computed band structure is presented in Fig. (2.4b). It can be easily observed that the flat band exists at exactly zero energy lying between the values $k_x = -4\pi/3 \sqrt{3}$ and $-2\pi/3 \sqrt{3}$ and between $k_x = 2\pi/3 \sqrt{3}$ and $4\pi/3 \sqrt{3}$ [115]. These bands represent that the states are completely localized at the edges of the ribbon for these special k_x values. These states which correspond to dispersionless band are the peculiar edge states which eventually contribute to the transport properties. We shall see interesting phenomena in the conductance owing to the presence of edge states in the following subsection.

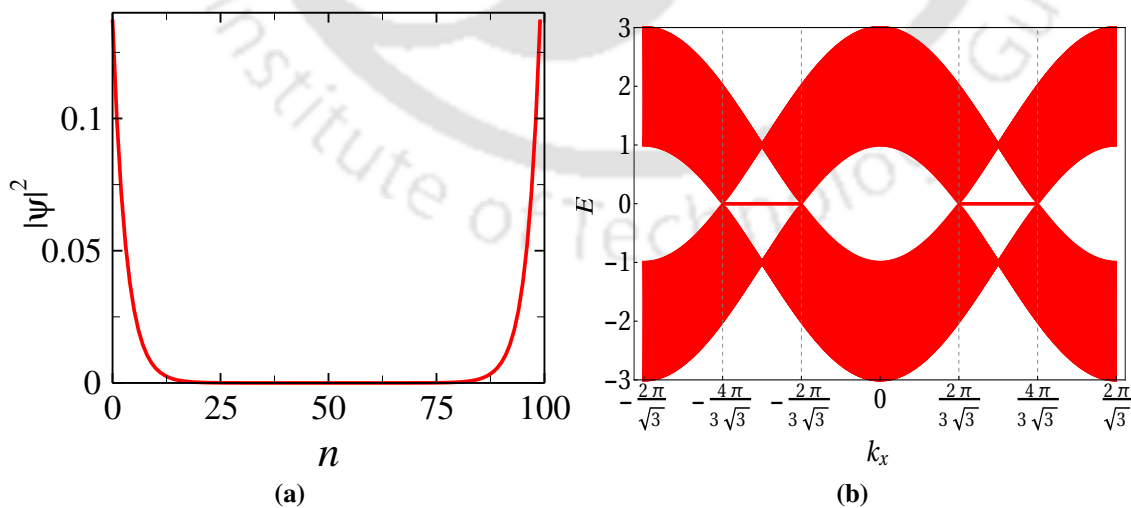


Figure 2.4. (color online) (a) Probability density of the wavefunction, $|\psi|^2$ as a function of site index, n at $k_x = \frac{2\pi}{3\sqrt{3}}$ and (b) the Band structure is shown for $N = 100$ for a Dirac system (zigzag graphene ribbon).

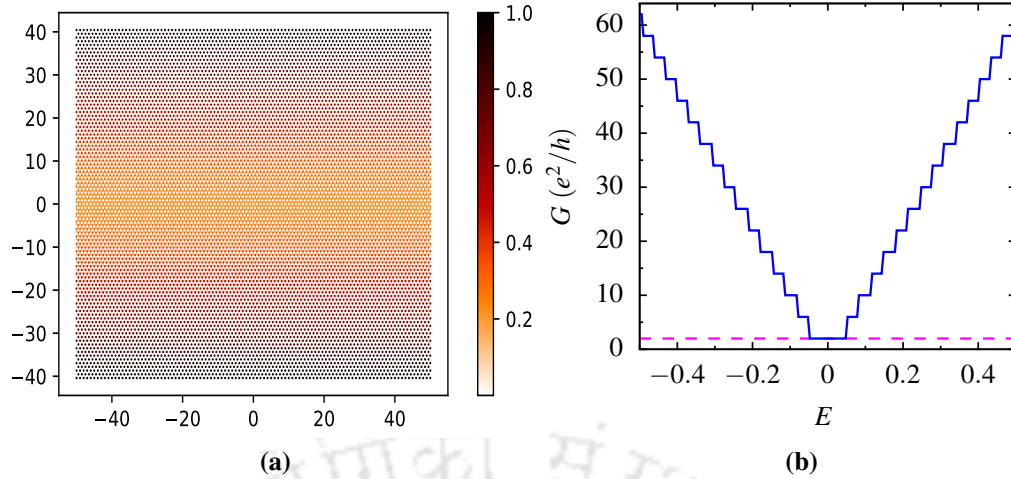


Figure 2.5. (color online) (a) The LDOS is plotted near Fermi energy and (b) the charge conductance, G (in units of e^2/h) is plotted as a function of Fermi energy, E (in units of t) of zigzag nanoribbon for a Dirac system. The value of the quantized conductance is shown by the pink dashed line.

2.3.2 LDOS and conductivity

In this subsection, we numerically compute the LDOS and the charge conductance using the tight-binding model to compare with the analytical expressions (see Eqs. (2.3.13) and (2.3.14)). The size of the ribbon in our numeric computation is taken as 201Z-94A ($L_x \sim 25$ nm and $L_y \sim 20$ nm) [116] with zigzag edges. All the energies are measured in units of t . We have plotted the LDOS for energy value close to zero in Fig. (2.5a). The color bar on the right-hand side suggests that the LDOS is largest at the edges and falls off gradually into the bulk. Thus these edge states are conducting in nature, whereas deep inside the bulk, they remain insulating owing to their decaying amplitude. To ascertain the effects of the edge modes on the conductance properties of a ZGNR, we have further computed the conductance of zigzag graphene as shown in Fig. (2.5b). We can see that the conductance follows a step-like behavior as one goes away from zero of the Fermi energy.

It is well-known that the conductance quantization in graphene ribbon has a strong dependency on the edge termination. Since the geometry of our ribbon holds the zigzag edge termination, the conductance quantization becomes even multiples (2, 6, 10, 14, ...) in units of e^2/h , where the spin and valley degeneracies both are considered. The conductance behavior also confirms that a $2e^2/h$ (e is the electronic charge, h is the Planck's constant, and the factor '2' comes due to the spin degeneracy) plateau exists around the zero of the Fermi energy (zero-bias), which is shown by the pink dashed line. This is because of the presence of the two conducting zero-energy modes, which contribute to the zero bias conductivity.

The value of the conductance depends on the number of transverse modes present in the system. This special feature of conductance holds as long as the electron-hole symmetry is present in the system. However, this plateau is fragile owing to the absence of ‘protected’ edge states.

2.3.3 Bilayer graphene

We consider a AB -stacked bilayer graphene sheet with zigzag edges which consists of two coupled monolayers of carbon (C) atoms and hence involves four sublattices labelled by A_i and B_i (where $i = 1$ and 2 denote top and bottom layer respectively). The three nearest neighbors vectors in real space are defined by, $\vec{\delta}_1 = (0, a)$; $\vec{\delta}_2 = \left(\frac{\sqrt{3}a}{2}, -\frac{a}{2}\right)$ and $\vec{\delta}_3 = \left(-\frac{\sqrt{3}a}{2}, -\frac{a}{2}\right)$, where a represent the vectors from sublattice sites A to its three nearest sublattice sites B . The tight-binding model of a bilayer graphene can be written as,

$$\begin{aligned} H &= H^T + H^B + H^{T-B} \\ &= H^T + H^B - t_{\perp} \sum_{i \in (T,A), j \in (B,B), \sigma} (c_{i\sigma}^{\dagger} c_{j\sigma} + h.c.), \end{aligned} \quad (2.3.15)$$

where H^T and H^B refer to the Hamiltonians for the top and the bottom graphene layers respectively. H^{T-B} includes coupling between the top and bottom layers. Since the form of the Hamiltonian depends on the stacking geometry of the layers, we have considered only the hopping between the A site of the top layer and the nearest B site of the bottom layer which is represented by the third term. The subscripts i, j label the lattice sites and σ denotes the spin index. The interlayer hopping amplitude is denoted by t_{\perp} , where $t_{\perp} \approx 0.4$ eV ($t_{\perp} \ll t$). We can write $H_{T(B)}$ as,

$$H_{T(B)} = -t \sum_{\langle ij \rangle \sigma} c_{i\sigma}^{\dagger} c_{j\sigma}. \quad (2.3.16)$$

The term $H_{T(B)}$ describes the hopping between nearest neighbors with hopping energy t . The other quantities have been already described in the previous section.

2.3.3.a Edge states and band structure

Here, we first study the edge state properties of a AB -stacked zigzag bilayer graphene nanoribbon. We focus on the bilayer graphene ribbon geometry with zigzag edges where the translational invariance exists along the x -axis (horizontal direction). Similar to monolayer graphene, we have also considered that the ribbon has N unit cells along the y -axis (where $n \in 0$ to $N - 1$). We begin with the tight-binding model where Eq. (2.3.15) can be written in

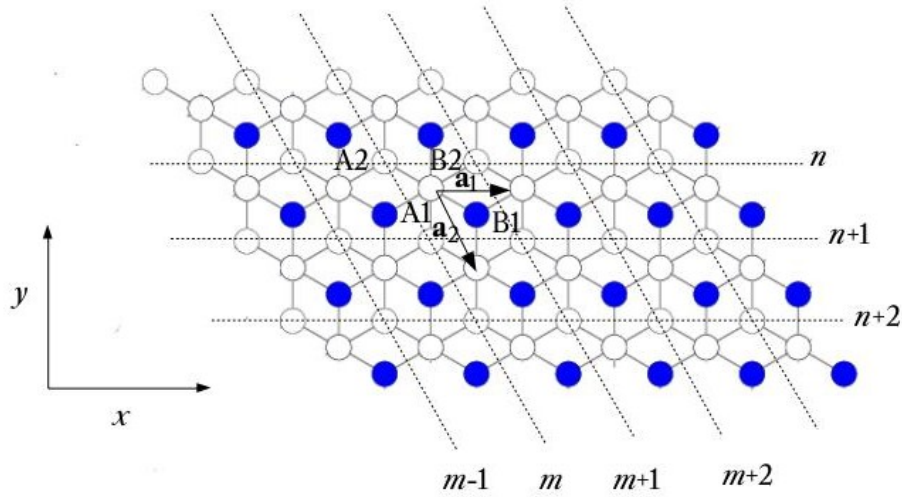


Figure 2.6. (Color online) Bilayer graphene nanoribbon geometry with zigzag edges. The white and the blue circles represent A and B sublattices of the ribbon respectively. \mathbf{a}_1 and \mathbf{a}_2 are the primitive vectors. (m, n) labels the unit cell along the x and the y direction.

terms of m and n that label the unit cell as shown in Fig. (2.6) as [109],

$$\begin{aligned}
 H = & -t \sum_{i=1}^2 \sum_{mn\sigma} \left[a_{\sigma i}^\dagger(m, n) \{ b_{\sigma i}(m, n) + b_{\sigma i}(m, n-1) + b_{\sigma i}(m-1, n) \} + h.c. \right] \\
 & - t_\perp \sum_{mn\sigma} \left[a_{\sigma 1}^\dagger(m, n) b_{\sigma 2}(m, n) + h.c. \right].
 \end{aligned} \tag{2.3.17}$$

We use periodic boundary conditions along the x -direction. Using the momentum representation of the electron operators and solving the time-independent Schrödinger equation $H\psi = E\psi$, we get the following set of four eigenvalue equations corresponding to the A and the B sublattices as,

$$\begin{aligned}
 E\alpha_1(k_x, n) &= -t \left[D_k \beta_1(k_x, n) + \beta_1(k_x, n-1) \right] - t_\perp \beta_2(k_x, n) \\
 E\alpha_2(k_x, n) &= -t \left[D_k \beta_2(k_x, n) + \beta_2(k_x, n-1) \right] \\
 E\beta_1(k_x, n) &= -t \left[D_k \alpha_1(k_x, n) + \alpha_1(k_x, n+1) \right] \\
 E\beta_2(k_x, n) &= -t \left[D_k \alpha_2(k_x, n) + \alpha_2(k_x, n+1) \right] - t_\perp \alpha_1(k_x, n),
 \end{aligned} \tag{2.3.18}$$

where $D_k = -2 \cos\left(\frac{\sqrt{3}k_x}{2}\right)$. We have chosen the basis as,

$$|\psi_k\rangle = \sum_{n,\sigma} \sum_{i=1}^2 \left[\alpha_i(k, n, \sigma) |a_i, k, n, \sigma\rangle + \beta_i(k, n, \sigma) |b_i, k, n, \sigma\rangle \right], \tag{2.3.19}$$

where α_i, β_i refer to the amplitudes corresponding to the A and B sublattices. Since we are interested to see the edge modes which is close to zero energy, we further put $E = 0$ in Eq. (2.3.18) and simply get,

$$0 = -t[D_k\beta_1(k_x, n) + \beta_1(k_x, n-1)] - t_\perp\beta_2(k_x, n) \quad (2.3.20)$$

$$0 = -t[D_k\beta_2(k_x, n) + \beta_2(k_x, n-1)] \quad (2.3.21)$$

$$0 = -t[D_k\alpha_1(k_x, n) + \alpha_1(k_x, n+1)] \quad (2.3.22)$$

$$0 = -t[D_k\alpha_2(k_x, n) + \alpha_2(k_x, n+1)] - t_\perp\alpha_1(k_x, n). \quad (2.3.23)$$

From Eq. (2.3.20)-(2.3.23), we get the following matrix forms,

$$\begin{bmatrix} \alpha_1(k_x, n+1) \\ \alpha_2(k_x, n+1) \end{bmatrix} = \begin{bmatrix} D_k & 0 \\ -\frac{t_\perp}{t} & D_k \end{bmatrix} \begin{bmatrix} \alpha_1(k_x, n) \\ \alpha_2(k_x, n) \end{bmatrix} \quad (2.3.24)$$

and

$$\begin{bmatrix} \beta_2(k_x, n-1) \\ \beta_1(k_x, n-1) \end{bmatrix} = \begin{bmatrix} D_k & 0 \\ -\frac{t_\perp}{t} & D_k \end{bmatrix} \begin{bmatrix} \beta_2(k_x, n) \\ \beta_1(k_x, n) \end{bmatrix}. \quad (2.3.25)$$

Since we choose to solve the above equations (Eq. (2.3.24) and (2.3.25)) in an iterative way, we need the 2×2 matrix multiplication. For that, we use the following property which is in general,

$$\begin{bmatrix} D_k & 0 \\ u_k & D_k \end{bmatrix}^n = \begin{bmatrix} D_k^n & 0 \\ u_k n D_k^{n-1} & D_k^n \end{bmatrix}. \quad (2.3.26)$$

In our case, we have

$$\begin{bmatrix} D_k & 0 \\ -\frac{t_\perp}{t} & D_k \end{bmatrix}^n = \begin{bmatrix} D_k^n & 0 \\ -n\frac{t_\perp}{t}D_k^{n-1} & D_k^n \end{bmatrix}. \quad (2.3.27)$$

In case of a bilayer nanoribbon, the boundary condition is,

$$\alpha_1(k_x, N) = \alpha_2(k_x, N) = \beta_1(k_x, -1) = \beta_2(k_x, -1) = 0. \quad (2.3.28)$$

To make k_x a dimensionless quantity, again we have absorbed the lattice spacing a into the definition of k_x . Using the above boundary condition mentioned in Eq. (2.3.28)) and applying

the induction method, we finally obtain the following matrix equations for the amplitudes of the wavefunction at A and B sublattices as,

$$\begin{bmatrix} \alpha_1(k_x, n) \\ \alpha_2(k_x, n) \end{bmatrix} = \begin{bmatrix} D_k^n & 0 \\ -nD_k^{n-1} \frac{t_\perp}{t} & D_k^n \end{bmatrix} \begin{bmatrix} \alpha_1(k_x, 0) \\ \alpha_2(k_x, 0) \end{bmatrix} \quad (2.3.29)$$

and

$$\begin{bmatrix} \beta_2(k_x, N-n-1) \\ \beta_1(k_x, N-n-1) \end{bmatrix} = \begin{bmatrix} D_k^n & 0 \\ -nD_k^{n-1} \frac{t_\perp}{t} & D_k^n \end{bmatrix} \begin{bmatrix} \beta_2(k_x, N-1) \\ \beta_1(k_x, N-1) \end{bmatrix}. \quad (2.3.30)$$

Similar to the monolayer graphene, the convergence conditions remain the same in the case of bilayer graphene. Hence, the range of momentum for the edge states is analogous to monolayer, which we will see in the following sections. The number of edge modes will differ due to the presence of an extra layer compared to a single one. To see this, we choose two linearly independent initial vectors $[\alpha_1(k_x, 0), 0]$ and $[0, \alpha_2(k_x, 0)]$ to compute the edge states. Using this in Eq. (2.3.29), we get two equations for α ,

$$\begin{bmatrix} \alpha_1(k_x, n) \\ \alpha_2(k_x, n) \end{bmatrix} = \begin{bmatrix} D_k^n & 0 \\ -nD_k^{n-1} \frac{t_\perp}{t} & D_k^n \end{bmatrix} \begin{bmatrix} \alpha_1(k_x, 0) \\ 0 \end{bmatrix} \quad (2.3.31)$$

and

$$\begin{bmatrix} \alpha_1(k_x, n) \\ \alpha_2(k_x, n) \end{bmatrix} = \begin{bmatrix} D_k^n & 0 \\ -nD_k^{n-1} \frac{t_\perp}{t} & D_k^n \end{bmatrix} \begin{bmatrix} 0 \\ \alpha_2(k_x, 0) \end{bmatrix}, \quad (2.3.32)$$

which implies

$$\alpha_1(k_x, n) = D_k^n \alpha_1(k_x, 0) \quad (2.3.33)$$

$$\alpha_2(k_x, n) = -nD_k^{n-1} \frac{t_\perp}{t} \alpha_1(k_x, 0) \quad (2.3.34)$$

and

$$\alpha_1(k_x, n) = 0 \quad (2.3.35)$$

$$\alpha_2(k_x, n) = D_k^n \alpha_2(k_x, 0). \quad (2.3.36)$$

Similarly, we can have the solutions for β as well which follows as,

$$\beta_2(k_x, N-n-1) = D_k^n \beta_2(k_x, N-1) \quad (2.3.37)$$

$$\beta_1(k_x, N-n-1) = -n D_k^{n-1} \frac{t_\perp}{t} \beta_2(k_x, N-1) \quad (2.3.38)$$

and

$$\beta_2(k_x, N-n-1) = 0 \quad (2.3.39)$$

$$\beta_1(k_x, N-n-1) = D_k^n \beta_1(k_x, N-1). \quad (2.3.40)$$

These equations (Eq. (2.3.34) and Eq. (2.3.36) for A sublattice) are the possible edges states but not orthogonal to each other (except at $k_x = \pi$). Hence we use the Gram-Schmidt orthogonalization process (taking $N \rightarrow \infty$), we finally obtain for the amplitudes at A as,

$$\begin{aligned} \alpha_1(k_x, n) &= 0 \\ \alpha_2(k_x, n) &= D_k^n \alpha_2(k_x, 0) \end{aligned} \quad (2.3.41)$$

and

$$\begin{aligned} \alpha_1(k_x, n) &= \alpha_1(k_x, 0) D_k^n \\ \alpha_2(k_x, n) &= -\alpha_1(k_x, 0) D_k^{n-1} \frac{t_\perp}{t} \left(n - \frac{D_k^2}{1 - D_k^2} \right), \end{aligned} \quad (2.3.42)$$

and for B sublattice,

$$\begin{aligned} \beta_2(k_x, N-n-1) &= 0 \\ \beta_1(k_x, N-n-1) &= D_k^n \beta_1(k_x, N-1) \end{aligned} \quad (2.3.43)$$

and

$$\begin{aligned} \beta_2(k_x, N-n-1) &= \beta_2(k_x, N-1) D_k^n \\ \beta_1(k_x, N-n-1) &= -\beta_2(k_x, N-1) D_k^{n-1} \frac{t_\perp}{t} \left(n - \frac{D_k^2}{1 - D_k^2} \right), \end{aligned} \quad (2.3.44)$$

which represent the orthonormalized zero-energy edge states for a bilayer graphene. From Eq. (2.3.41), we can see that the amplitudes corresponding to the sites belonging to the A

sublattices of layer 1 vanish and that of layer 2 are finite. This implies that the corresponding equations and hence their solutions are applicable for a monolayer graphene, whereas Eq. (2.3.42) refers to the respective solutions for a bilayer graphene. Here, the sites for both the layers are found to have non-vanishing amplitudes and that the amplitudes in layer 2 are connected to those in layer 1 via t_{\perp} . Similarly, the same applies for the B sublattice through Eq. (2.3.43) and (2.3.44) (in case if we increase the sheet from the other side of the ribbon).

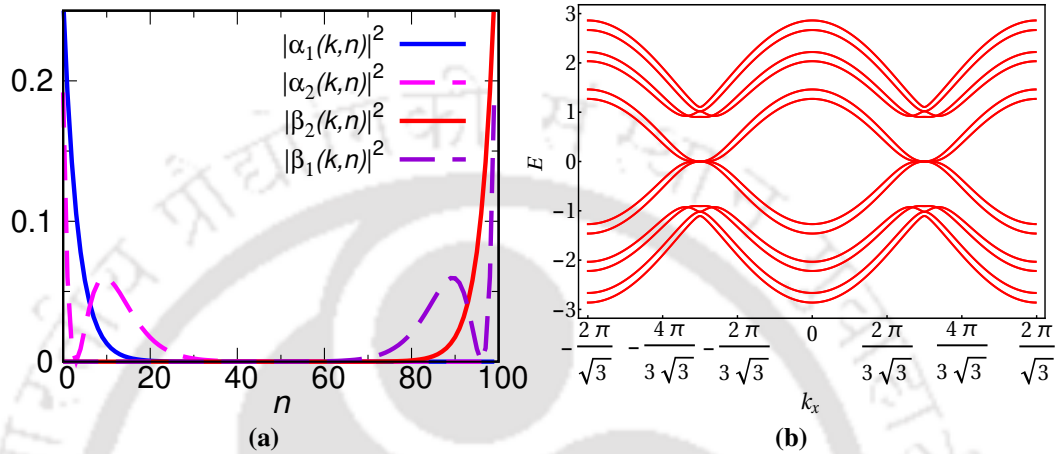


Figure 2.7. (color online) (a) Charge density is plotted as a function of site index, n at $k_x = \frac{2.15\pi}{3\sqrt{3}}$ and (b) the band dispersion is shown for $N = 3$ for a zigzag bilayer graphene nanoribbon. Here, we set $t_{\perp} = 0.2$.

To study the surface (or edge) state properties for different sublattices, we have plotted the charge densities as a function of n (n being the site index) for different cases in Fig. (2.7) using Eq. (2.3.42) and Eq. (2.3.44) for the top and the bottom layers. It yields that the edge states exist at the zigzag edges at zero energy and they are strictly localized at the edges. The amplitude at the sublattices α_1 and β_2 fall off gradually at both the edges of the ribbon, whereas α_2 and β_1 show different nature than these two, namely, α_1 and β_2 . It can also be seen that the penetration depth of the amplitudes into the bulk gets enhanced because of the linear dependence of α_2 on n .

We have also computed the electronic energy dispersion to provide support to the corresponding results for the edge states for a few orbitals, that is, corresponding to small values of N . In Fig. (2.7b), we have plotted the band structure for $N = 3$ by solving the tight-binding Hamiltonian shown in Eq. (2.3.17). Although the flat band is observed at $E = 0$ at the momentum intervals given by $-\frac{4\pi}{3\sqrt{3}} \leq k_x \leq -\frac{2\pi}{3\sqrt{3}}$ and $\frac{2\pi}{3\sqrt{3}} \leq k_x \leq \frac{4\pi}{3\sqrt{3}}$, in contrast to a monolayer, there are four flat bands in the above mentioned range of k_x which correspond to the four edge states for the bilayer and they remain dispersionless. The particle-hole symmetry is conserved and the energy spectrum remains spin-degenerate.

Next we present our numerical results for the charge conductances and the LDOS using Eq. ((2.1.1) and (2.1.4)). We have taken $L_x = 15$ and $L_y = 10$ for zigzag bilayer ribbon to calculate both the LDOS and charge conductances. The LDOS behavior is depicted in

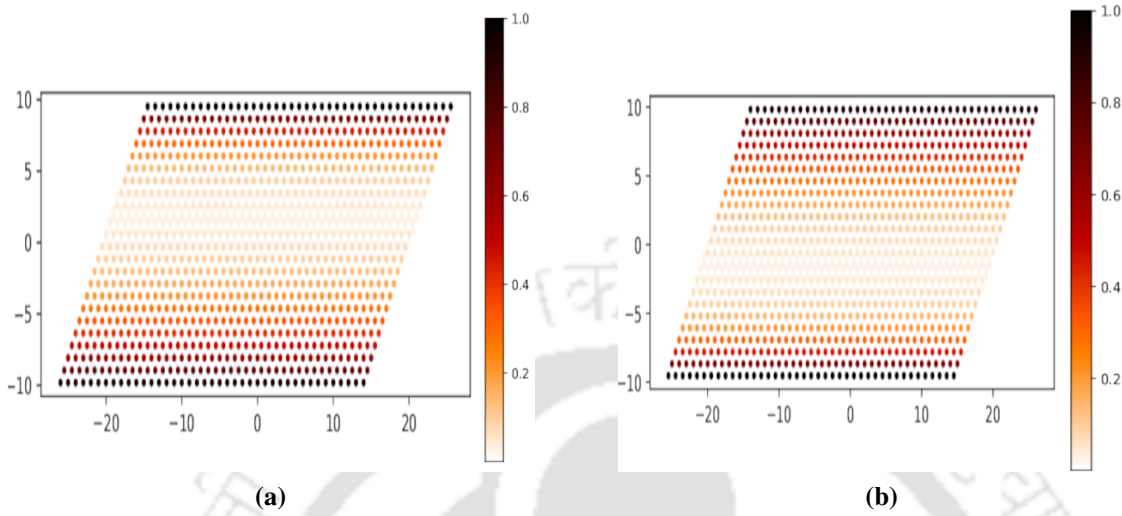


Figure 2.8. (color online) The LDOS for a bilayer graphene nanoribbon is plotted for (a) bottom layer and (b) top layer respectively. Here, we set $t_{\perp} = 0.2$.

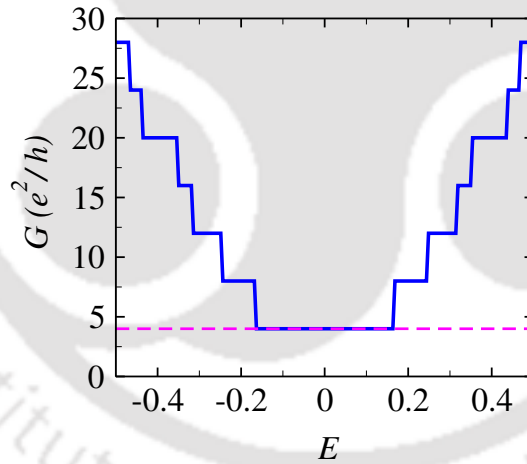


Figure 2.9. (color online) The charge conductance, G (in units of e^2/h) is plotted as a function of Fermi energy E (in units of t) for a bilayer graphene nanoribbon. The value of the quantized conductance is shown by the pink dashed line. Here, we set $t_{\perp} = 0.2$.

Fig. (2.8a) and (2.8b) for the bottom layer and the top layer respectively. It can be seen that the probability density for the bottom layer decays more quickly than that of the top layer near the Fermi energy corresponding to one edge of the ribbon. The reverse happens for the other edge.

We have computed the charge conductance of a bilayer graphene as shown in Fig. (2.9). It can be easily observed that for a bilayer nanoribbon, though the conductance plot shows step-like behavior emphasizing the basic features of quantum transport phenomena at discrete

energy values, the plateau in the vicinity of zero Fermi energy now acquires a new value $4e^2/h$ (shown by a pink dashed line in Fig. (2.9)) instead of $2e^2/h$ as observed in monolayer graphene. The presence of the edge states is confirmed by the existence of this plateau. The conductance steps are not equidistant along the Fermi energy axis as seen from Fig. (2.9). The width of these steps depends on the ribbon width and the energy intervals [117].

2.4 Tight-binding model of semi-Dirac nanoribbon

In this section, we consider a semi-Dirac nanoribbon with zigzag edges, which consists of two sublattices A and B (similar to Dirac one) and the three nearest neighbors vectors in real space remain analogous to graphene (see Eq. (2.3.1)). The only difference is that we have tuned one of the nearest neighbors hopping parameters, say t_2 which denotes hopping along the y -direction in the case of semi-Dirac systems as shown in Fig. (2.1) (denoted by the solid pink line). The modified parameter t_2 can take any value $t \leq t_2 \leq 2t$. In our case we have considered two values of t_2 , that is $t_2 = 1.5t$ and $2t$ (semi-Dirac). The tight-binding

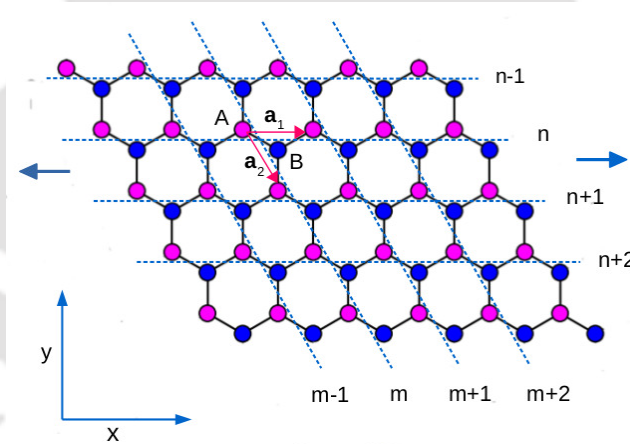


Figure 2.10. (color online) Zigzag nanoribbon of a honeycomb lattice for a semi-Dirac system is shown. The magenta and blue circles represent the A and B sublattices respectively. \mathbf{a}_1 and \mathbf{a}_2 are the primitive vectors. (m, n) labels the positions of the unit cells along x and y directions. The ribbon is infinite along the x -direction shown by the arrow on both side.

Hamiltonian for the semi-Dirac nanoribbon can be written as,

$$H = -t \sum_{\langle ij \rangle \sigma} (c_{i\sigma}^\dagger c_{j\sigma} + h.c.). \quad (2.4.1)$$

Now, as mentioned earlier we have modified one of the parameter t by t_2 for a pair of C atoms as shown in Fig. (2.1) and thus, we can write the above Hamiltonian in terms of m and

n as from Fig. (2.10),

$$H = - \sum_{\langle mn \rangle \sigma} \left[t a_{\sigma}^{\dagger}(m, n) b_{\sigma}(m, n) + t_2 a_{\sigma}^{\dagger}(m, n) b_{\sigma}(m, n - 1) + t a_{\sigma}^{\dagger}(m, n) b_{\sigma}(m - 1, n) + h.c. \right], \quad (2.4.2)$$

where $\langle \rangle$ denotes nearest neighbors and σ denotes the spin index with \uparrow and \downarrow spin for both sublattices A and B . Keeping in mind that the translational symmetry exists along the x -axis, we are allowed to use the momentum k_x as a good quantum number. Due to the periodicity in the x -direction and using Schrödinger equation $H|\psi\rangle = E|\psi\rangle$, we arrive at the following eigenvalue equations for sites in A and B sublattices using the same basis as mentioned in Eq. (2.3.6),

$$\begin{aligned} E\alpha(k_x, n) &= - \left[2t \cos\left(\frac{\sqrt{3}k_x}{2}\right) \beta(k_x, n) + t_2 \beta(k_x, n - 1) \right] \\ E\beta(k_x, n) &= - \left[2t \cos\left(\frac{\sqrt{3}k_x}{2}\right) \alpha(k_x, n) + t_2 \alpha(k_x, n + 1) \right]. \end{aligned} \quad (2.4.3)$$

Now, we may apply the same boundary condition (Eq. (2.3.7)) to Eq. (2.4.3), thus we get

$$\begin{aligned} E\alpha(k_x, 0) &= - \left[2t \cos\left(\frac{\sqrt{3}k_x}{2}\right) \beta(k_x, 0) \right] \\ E\beta(k_x, N - 1) &= - \left[2t \cos\left(\frac{\sqrt{3}k_x}{2}\right) \alpha(k_x, N - 1) \right]. \end{aligned} \quad (2.4.4)$$

To obtain the zero-energy modes, we again apply $E = 0$ in Eqs. (2.4.3) and (2.4.4). Thus, we obtain the following equations,

$$0 = - \left[2t \cos\left(\frac{\sqrt{3}k_x}{2}\right) \beta(k_x, n) + t_2 \beta(k_x, n - 1) \right] \quad (2.4.5)$$

$$0 = - \left[2t \cos\left(\frac{\sqrt{3}k_x}{2}\right) \alpha(k_x, n) + t_2 \alpha(k_x, n + 1) \right] \quad (2.4.6)$$

$$0 = \beta(k_x, 0) \quad (2.4.7)$$

$$0 = \alpha(k_x, N - 1). \quad (2.4.8)$$

Now we solved the above equations (Eq. (2.4.5) and Eq. (2.4.6)) iteratively and finally get as the following,

$$E\alpha(k_x, n) = \left[-\frac{t}{t_2} 2 \cos\left(\frac{\sqrt{3}k_x}{2}\right) \right]^n \alpha(k_x, 0) \quad (2.4.9)$$

$$E\beta(k_x, n) = \left[-\frac{t}{t_2} 2 \cos\left(\frac{\sqrt{3}k_x}{2}\right) \right]^{(N-1-n)} \beta(k_x, N-1). \quad (2.4.10)$$

These equations represent the edge state solutions for the zigzag semi-Dirac nanoribbons when t_2 has been set to $2t$. In the following, we numerically solve these equations to see how the evolution of the edge states and the band dispersion occurs when one goes from t to $2t$ via $1.5t$. Since we have already shown the results for $t_2 = t$, that is, when all the three nearest neighbor hopping amplitudes are the same in the Sec. (2.3), we only described the other two cases in this section.

2.4.1 Edge states and band structure

We first plotted the charge density, $|\psi|^2$ as a function of site index, n at $k_x = \frac{2.15\pi}{3\sqrt{3}}$ for two different values of t_2 , say $t_2 = 1.5t$ and $2t$ (semi-Dirac case) as shown in Fig. (2.11a) and (2.11b). It can be seen that the charge density depends on the $\frac{t}{t_2}$ ratio for these cases, which somewhat differs from the Dirac one. As compared to the Dirac case, we assert that the wave functions now decay faster from both sides of the edges due to the ratio of t/t_2 , which is always less than 1 and in particular, for the semi-Dirac case, it is equal to $1/2$. Moreover, the amplitude of the wave function get increases for both cases with the increasing values of t_2 . This indicates that the zero energy states are more localized at the edges for the semi-Dirac case.

To have the essence of the edge state on the band dispersion, we have also plotted the band structure for $N = 100$ in fig. (2.11) using the Hamiltonian as shown in Eq. (2.4.2). For Dirac case ($t_2 = t$), we observed that the flat band exists in the momentum intervals $\pm \frac{2\pi}{3\sqrt{3}} \leq k_x \leq \pm \frac{4\pi}{3\sqrt{3}}$. With the increase of t_2 (that is when $t_2 = 1.5t$), the momentum interval of the flat band gets enhanced at zero energy, which can be easily seen from Fig. (2.11c) and these bands also correspond to two edge modes. Eventually, the flat bands get more enhanced beyond the k_x range (shown by the grey dashed line), and the edge modes are completely separated from the bulk in the case of semi-Dirac ($t_2 = 2t$) as shown in Fig. (2.11d). The contribution from these zero-energy edge modes affects the conductance properties of semi-Dirac nanoribbon at zero-bias, which we will see in the next subsection.

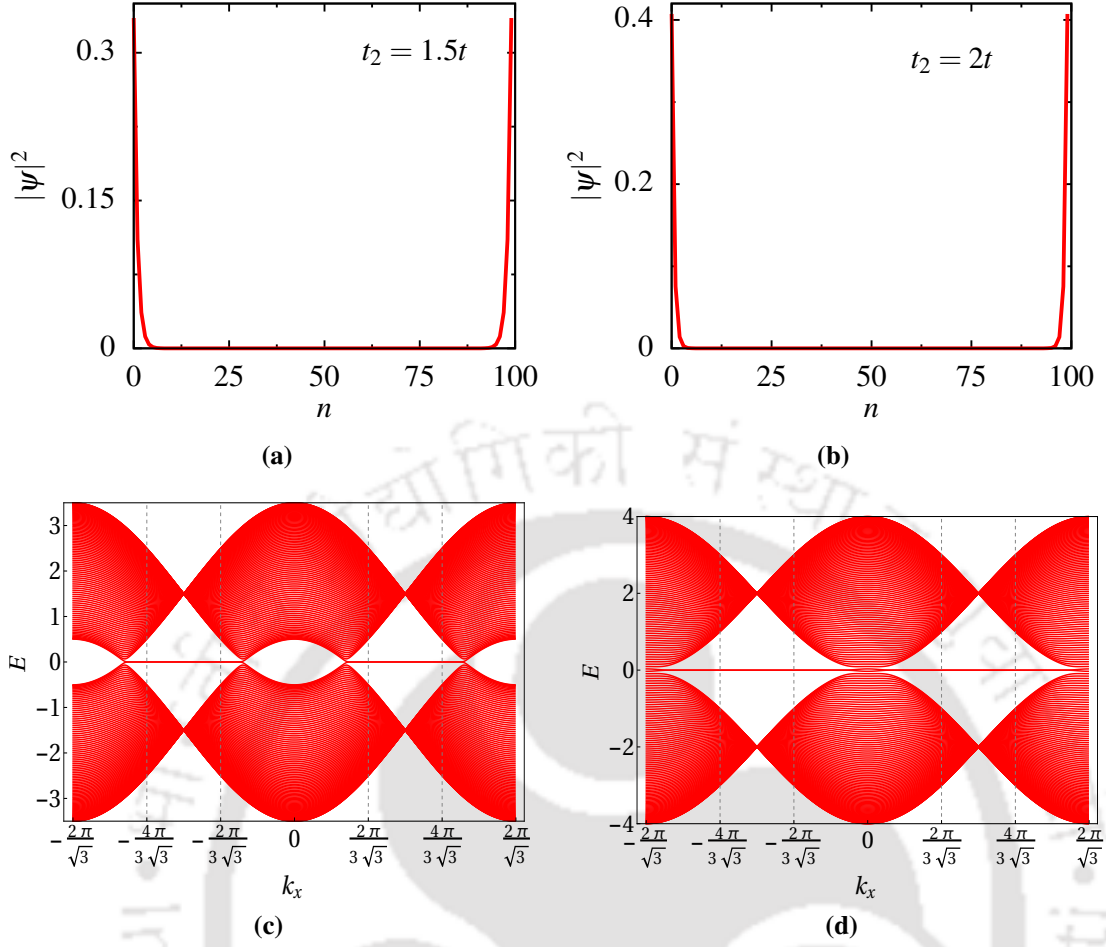


Figure 2.11. (color online) Charge density as a function of site index, n at $k_x = \frac{2.15\pi}{3\sqrt{3}}$ and (b) the band structure for $N = 100$ for a semi-Dirac nanoribbon with zigzag edges. Here, we set $t_2 = 2t$. The vertical line (grey dashed) indicates that the flat band gets enhanced in case of semi-Dirac nanoribbon.

2.4.2 LDOS and conductivity

To confirm the edge state behavior, we have plotted the LDOS considering the same size of the ribbon as mentioned earlier in sec. (2.3.2). The LDOS behavior is depicted in Figs. (2.12a) and (2.12b) for $t_2 = 1.5t$ and $2t$ respectively. When $t_2 = 2t$, we can see that the electron probability density vanishes faster than the situation when $t_2 = 1.5t$ as one move from edge to the bulk from Figs. (2.12a) and (2.12b). Hence, we can argue that our analytical results match with the numerical ones for both cases. Finally, to explore the transport properties we calculated the charge conductance, G as a function of Fermi energy, E for the corresponding values of t_2 as shown in Figs. (2.12c) and (2.12d). For the intermediate value of t_2 (that is, when $t_2 = 1.5t$), the charge conductance still acquires the same value ($2e^2/h$) near the Fermi energy but the magnitude decreased as seen from Fig. (2.12c). For the semi-Dirac case, We also observed a well-known conductance plateau at $2e^2/h$ near zero Fermi energy, similar to

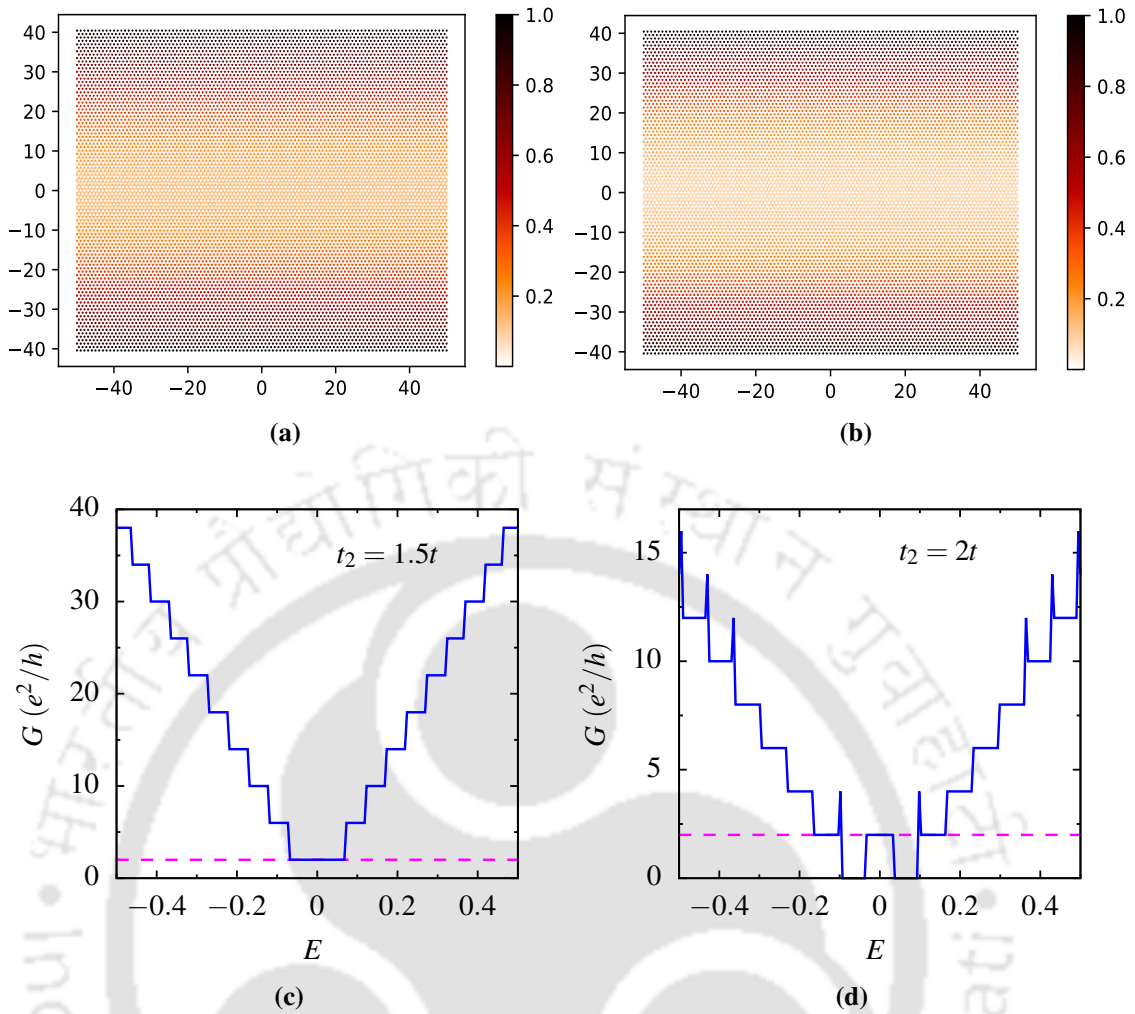


Figure 2.12. (color online) (a) The local density of states (LDOS) is plotted near Fermi energy and (b) the charge conductance, G (in units of e^2/h) is plotted as a function of Fermi energy, E (in units of t) of zigzag nanoribbon for a semi-Dirac system. The value of the quantized conductance is shown by the pink dashed line.

the Dirac case where $t_2 = t$. The width of the plateau now decreased. In the case of semi-Dirac ($t_2 = 2t$), the conductance corresponding to the edge modes is separated from the bulk conductance, which confirms the complete isolation of the edge modes from the bulk as seen from the band dispersion (Fig. (2.11d)).

2.5 Summary

In this chapter, we have computed the analytical expressions for the edge modes using a tight-binding Hamiltonian for 2D Dirac (graphene) and semi-Dirac systems. We solved these equations numerically to observe the nature of the edge states of the ribbon. For the Dirac case (graphene), we see the exponentially decaying amplitude of the wave functions which indicates that the edge states are localized at the edges and decay into the bulk. We also

compute the band structure, where we observe the flat bands between a finite range of momentum that corresponds to the two edge modes and are gapless in bulk. The transport properties are explored by calculating the charge conductance. The conductance spectra show a plateau at a non-zero value $2e^2/h$ near the zero of the Fermi energy due to the presence of the edge modes. To continue the study in graphene, we have also looked into the bilayer graphene nanoribbon. The analytic results show that the behavior of the edge states of a bilayer graphene is quite different than that of a monolayer graphene. For the band structure, the four bands correspond to four edge states which implies that there exist two edge modes per edge. Moreover, the charge conductance spectrum shows plateaus at $4e^2/h$ for bilayer graphene near the zero of the Fermi energy. For the semi-Dirac case, the edge states are more localized at both edges and decay faster inside the ribbon than the Dirac one. It can also be seen from the band dispersion that the edge modes are completely separated from the bulk ones. Also, the flat band gets enhanced in the case of semi-Dirac one. The conductance plateau is quantized with the same value ($2e^2/h$) as observed for the Dirac case, but the width of the plateau has diminished. For all the cases, we have shown LDOS results that support well our edge states derived analytically.

3 Transport properties of a Kane-Mele Dirac and semi-Dirac nanoribbon

Contents

3.1 Kane-Mele model in a Dirac system	55
3.1.1 Edge states: Analytical expressions	56
3.1.2 Results and discussion	59
3.1.3 Intrinsic SOC	60
3.1.4 Rashba SOC	62
3.1.5 Intrinsic and Rashba SOC	63
3.1.6 Bilayer system	66
3.2 Kane-Mele model in semi-Dirac system	79
3.2.1 Edge states: Analytical expressions	80
3.2.2 Results and discussion	82
3.2.3 Intrinsic SOC	82
3.2.4 Intrinsic and Rashba SOC	83
3.3 Summary	86

Recently, the study of the effects of spin-orbit coupling (SOC) has become one of the most important topics, especially in systems that do not have surface or bulk inversion symmetry. Some of these systems assumably have exciting prospects of spintronic applications [118–120] where spin current can be used to transmit dissipationless information.

On the other hand, it has been realized that SOC can lead to a new quantum state of matter that supports gapless edge (or surface) states protected by the TRS, while the bulk remains insulating. It is named as a topological insulator (TI) [22, 23] or more specifically, as the QSH insulator. There may be different kinds of SOC present in the system due to different physical origins. Mainly, two kinds of SOCs are thought to be relevant in the context of graphene, namely the intrinsic SOC and the Rashba SOC [15, 29]. Kane and Mele [15, 29] predicted that a QSH state could be observed in the presence of a complex next-nearest neighbor hopping, the so-called intrinsic SOC, which triggered an enormous study on topologically nontrivial electronic materials [18, 22, 23, 121]. Unfortunately, the QSH phase in pristine graphene is still not observed experimentally owing to its vanishingly small intrinsic SOC strength (typically $\sim 0.01 - 0.05$ meV) [122, 123], whereas, in strong SOC materials, such as CdTe/HgTe quantum wells, the QSH phase has been observed [20]. From different first-principles studies [122, 123], the strength of the intrinsic SOC emerges that is of the order of 10^{-3} meV. This value is much weaker than the value predicted by Kane-Mele compared to what is needed to realize the topological phase. Nevertheless, owing to its vast and potential applications as spintronic devices, several experimental studies could yield enhanced SOC values which are realized by doping with heavy adatoms, such as Indium or Thallium [124], using the proximity to a three-dimensional topological insulator, such as Bi₂Se₃ [125, 126], by functionalization with methyl [127] etc. Recently, many other 2D materials have been found with prospects of a tunable SOC, such as silicene, germanene, and stanene [128–132] etc. From the first-principles calculation, it is reported that Rashba SOC can be enhanced via doping with 3d or 5d transition-metal atoms [133, 134]. Recent observations showed that the strength of the Rashba SOC can also be enhanced up to 100 meV from Gold (Au) intercalation at the graphene-Ni interface [135]. A Rashba splitting of about 225 meV in epitaxial graphene layers grown on the surface of Ni [136] and a giant Rashba SOC (~ 600 meV) from Pb intercalation at the graphene-Ir surface [137] are also observed in experiments.

There are only very few studies on the effects of SOC in a bilayer graphene so far. Intrinsically, the magnitude of the SOC in a bilayer graphene is about one order of magnitude larger than that in monolayer graphene due to mixing of the π and σ bands via interlayer hoppings (typically $\sim 0.01 - 0.1$ meV) [138]. A bulk energy gap can be opened by breaking the inversion symmetry via the staggered sublattice potential term, and it plays a similar role in a monolayer graphene as that played by the gate bias in a bilayer graphene [139, 140]. It has also been studied that the bias voltage may reduce the bulk energy gap induced by

the intrinsic SOC [141]. The topological phases of a bilayer Kane-Mele model have been studied in detail in the presence of both the SOCs [142, 143]. The main findings are that a \mathbb{Z}_2 -metallic phase can be achieved with nontrivial \mathbb{Z}_2 invariant, which gives rise to spin helical edge states in the presence of the TRS, whereas a Chern metallic phase can be achieved with nontrivial Chern invariant. The latter gives rise to chiral edge states due to breaking of the TRS by a Zeeman-like coupling term [143]. A stable topological insulator phase can be achieved in gated bilayer graphene in the presence of large Rashba SOC [144]. Further, the study of the band structure reveals that a *Mexican-hat* feature appears in the vicinity of the Dirac points in the presence of SOC and without any bias voltage [145]. Moreover, the conventional charge transport in bilayer graphene has been studied earlier [146], but a systematic study of charge and spin transport in a spin-orbit coupled bilayer graphene is still new and hence needs to be explored.

In this chapter, we explore the roles of different SOCs in a Kane-Mele Dirac and semi-Dirac nanoribbon and emphasize its various physical properties. We show the effects of SOC on the edge states and the band structure. To see the interplay between these two types of SOC on the band structure and the edge states with a view to understand the data on charge conductances, we consider a Kane-Mele model. We write the Kane-Mele model for a nanoribbon and perform an analytical investigation of the edge states for a few choices of intrinsic SOC and Rashba SOC. We derive the fundamental eigenvalue equations that form the backbone of our results for the discussion on the edge states and the band structure. On the other hand, the transport properties are investigated in order to understand charge conductance. For our numerical calculation on the LDOS and conductance, we have used Kwant [63].

3.1 Kane-Mele model in a Dirac system

We consider a graphene sheet consisting of two sublattices A and B and the nearest neighbor vectors in real space are given by, $\vec{\delta}_1 = (0, a)$; $\vec{\delta}_2 = \left(\frac{\sqrt{3}a}{2}, -\frac{a}{2}\right)$ and $\vec{\delta}_3 = \left(-\frac{\sqrt{3}a}{2}, -\frac{a}{2}\right)$, where $a \approx 1.42\text{\AA}$ is the distance between two consecutive carbon atoms. In presence of the SOC term, the Kane-Mele (KM) [15, 29] Hamiltonian can be written as,

$$H = -t \sum_{\langle ij \rangle \sigma} c_{i\sigma}^\dagger c_{j\sigma} + i\lambda_{SO} \sum_{\langle\langle ij \rangle\rangle \sigma\sigma'} v_{ij} c_{i\sigma}^\dagger s_{\sigma\sigma'}^z c_{j\sigma'} + i\lambda_R \sum_{\langle ij \rangle \sigma\sigma'} c_{i\sigma}^\dagger \left(\mathbf{s}_{\sigma\sigma'} \times \hat{\mathbf{d}}_{ij} \right)_z c_{j\sigma'}. \quad (3.1.1)$$

The first term describes the electron hopping between the nearest neighbors sites i and j on a honeycomb lattice with a hopping strength t . The operators $c_{i\sigma}^\dagger = (c_{i\uparrow}^\dagger, c_{i\downarrow}^\dagger)$ and $c_{i\sigma} = (c_{i\uparrow}, c_{i\downarrow})^T$ are the creation and the annihilation operators for site i of the lattice. The second term is the mirror-symmetric intrinsic SOC which involves spin-dependent second neighbor hopping between the same sublattices with a coupling strength λ_{SO} . s^z is the z -component of the Pauli spin matrix, and it is conserved here. The parameter $\nu_{ij} = +1(-1)$ if the electron makes a left(right) turn to go from site j to i through their common nearest neighbor. The third term is the nearest neighbor Rashba term with coupling strength λ_R , which arises due to the broken surface inversion symmetry. This term preserves TRS, but s^z is no longer conserved due to broken inversion symmetry. The unit vector $\hat{\mathbf{d}}_{ij}$ points from site i to site j and corresponds to the nearest neighbor vectors. The SOC term λ_{SO} breaks the $SU(2)$ symmetry down to $U(1)$ symmetry, the Rashba term λ_R breaks the $U(1)$ symmetry down to \mathbb{Z}_2 [147]. Due to the small atomic number of carbon, the intrinsic SOC is usually weak [122, 148]. However, the Rashba coupling strength can be tuned by applying an external gate voltage.

3.1.1 Edge states: Analytical expressions

In this section, we analytically derive the solutions for the edge states considering the tight-binding KM Hamiltonian in the presence of both SOC that is the intrinsic SOC and the Rashba SOC. We focus on a graphene nanoribbon (GNR) geometry with zigzag edges via the KM model, which is infinite along the x -direction and finite along the y -direction. We prefer to call the GNR in the presence of SOC as Kane-Mele nanoribbon (KMNR), and we shall deal with the zigzag variant. All the atoms of the zigzag edges belong to the same sublattice as shown in Fig. (2.3) (see Chapter 2). The ribbon width is such that it has N unit cells in the y -direction. We rewrite the Eq. (3.1.1) in presence of only intrinsic SOC term (with $t = \lambda_R = 0$) in terms of (m, n) as shown in Fig. (2.3) considering the hopping only between A to A sublattices (hopping between B to B sublattices not shown here),

$$\begin{aligned}
H_{\text{ISOC}} = i\lambda_{SO} & \left[\sum_{\langle\langle mn \rangle\rangle} \left(a_{\uparrow}^\dagger(m, n) a_{\uparrow}(m, n-1) - a_{\downarrow}^\dagger(m, n) a_{\downarrow}(m, n-1) \right) \right. \\
& - \left(a_{\uparrow}^\dagger(m, n) a_{\uparrow}(m+1, n-1) - a_{\downarrow}^\dagger(m, n) a_{\downarrow}(m+1, n-1) \right) \\
& - \left(a_{\uparrow}^\dagger(m, n) a_{\uparrow}(m-1, n) - a_{\downarrow}^\dagger(m, n) a_{\downarrow}(m-1, n) \right) \\
& + \left(a_{\uparrow}^\dagger(m, n) a_{\uparrow}(m+1, n) - a_{\downarrow}^\dagger(m, n) a_{\downarrow}(m+1, n) \right) \\
& \left. + \left(a_{\uparrow}^\dagger(m, n) a_{\uparrow}(m-1, n+1) - a_{\downarrow}^\dagger(m, n) a_{\downarrow}(m-1, n+1) \right) \right]
\end{aligned}$$

$$-\left(a_{\uparrow}^{\dagger}(m,n)a_{\uparrow}(m,n+1)-a_{\downarrow}^{\dagger}(m,n)a_{\downarrow}(m,n+1)\right)\Big]+h.c.. \quad (3.1.2)$$

Similarly, the Hamiltonian in Eq. (3.1.1), in presence of only nearest neighbor Rashba SOC term (with $t = \lambda_{SO} = 0$), can be written in terms of (m,n) as,

$$\begin{aligned} H_{\text{RSOC}} = & i\lambda_R \left[\sum_{\langle mn \rangle} \left\{ a_{\uparrow}^{\dagger}(m,n) \left(-\frac{a}{2} + \frac{i\sqrt{3}a}{2} \right) b_{\downarrow}(m,n) + a_{\downarrow}^{\dagger}(m,n) \left(-\frac{a}{2} - \frac{i\sqrt{3}a}{2} \right) b_{\uparrow}(m,n) \right. \right. \\ & + a_{\uparrow}^{\dagger}(m,n) a b_{\downarrow}(m,n-1) + a_{\downarrow}^{\dagger}(m,n) a b_{\uparrow}(m,n-1) \\ & \left. \left. + a_{\uparrow}^{\dagger}(m,n) \left(-\frac{a}{2} - \frac{i\sqrt{3}a}{2} \right) b_{\downarrow}(m-1,n) + a_{\downarrow}^{\dagger}(m,n) \left(-\frac{a}{2} + \frac{i\sqrt{3}a}{2} \right) b_{\uparrow}(m-1,n) \right\} \right] + h.c.. \end{aligned} \quad (3.1.3)$$

Since the translational symmetry exists along the x -direction, we can consider the momentum k_x to be a good quantum number. Similar to the tight-binding model, we can use a momentum representation of the electron operator as given in Eq. (2.3.4). We have chosen the basis as,

$$|\psi_k\rangle = \sum_{n,\sigma} \alpha(k,n,\sigma) |a,k,n,\sigma\rangle + \beta(k,n,\sigma) |b,k,n,\sigma\rangle, \quad (3.1.4)$$

where α, β are the coefficients for the A and B sublattices. Using the Schrödinger equation, $H|\psi\rangle = E|\psi\rangle$ and including the spin degrees of freedom we get four eigenvalue equations for spins up and down in presence of intrinsic SOC and for A and B sublattice points which are written as [149],

$$\begin{aligned} E\alpha_{\uparrow}(k_x,n) = & -t \left[2\cos\left(\frac{\sqrt{3}k_x}{2}\right) \beta_{\uparrow}(k_x,n) + \beta_{\uparrow}(k_x,n-1) \right] \\ & - 2\lambda_{SO} \left[\sin(\sqrt{3}k_x) \alpha_{\uparrow}(k_x,n) - \sin\left(\frac{\sqrt{3}k_x}{2}\right) (\alpha_{\uparrow}(k_x,n-1) + \alpha_{\uparrow}(k_x,n+1)) \right], \\ E\alpha_{\downarrow}(k_x,n) = & -t \left[2\cos\left(\frac{\sqrt{3}k_x}{2}\right) \beta_{\downarrow}(k_x,n) + \beta_{\downarrow}(k_x,n-1) \right] \\ & + 2\lambda_{SO} \left[\sin(\sqrt{3}k_x) \alpha_{\downarrow}(k_x,n) - \sin\left(\frac{\sqrt{3}k_x}{2}\right) (\alpha_{\downarrow}(k_x,n-1) + \alpha_{\downarrow}(k_x,n+1)) \right], \\ E\beta_{\uparrow}(k_x,n) = & -t \left[2\cos\left(\frac{\sqrt{3}k_x}{2}\right) \alpha_{\uparrow}(k_x,n) + \alpha_{\uparrow}(k_x,n+1) \right] \\ & + 2\lambda_{SO} \left[\sin(\sqrt{3}k_x) \beta_{\uparrow}(k_x,n) - \sin\left(\frac{\sqrt{3}k_x}{2}\right) (\beta_{\uparrow}(k_x,n-1) + \beta_{\uparrow}(k_x,n+1)) \right], \\ E\beta_{\downarrow}(k_x,n) = & -t \left[2\cos\left(\frac{\sqrt{3}k_x}{2}\right) \alpha_{\downarrow}(k_x,n) + \alpha_{\downarrow}(k_x,n+1) \right] \end{aligned}$$

$$-2\lambda_{SO} \left[\sin(\sqrt{3}k_x)\beta_{\downarrow}(k_x, n) - \sin\left(\frac{\sqrt{3}k_x}{2}\right)(\beta_{\downarrow}(k_x, n-1) + \beta_{\downarrow}(k_x, n+1)) \right], \quad (3.1.5)$$

where $\alpha_{\uparrow, \downarrow}$ and $\beta_{\uparrow, \downarrow}$ correspond to the spin resolved eigenstates for the A and B sublattices respectively.

Next, we turn on the other SOC, namely the Rashba SOC. This yields the new set of equations given by [150],

$$\begin{aligned} E\alpha_{\uparrow}(k_x, n) &= -t \left[2 \cos\left(\frac{\sqrt{3}k_x}{2}\right) \beta_{\uparrow}(k_x, n) + \beta_{\uparrow}(k_x, n-1) \right] \\ &\quad - 2\lambda_{SO} \left[\sin(\sqrt{3}k_x)\alpha_{\uparrow}(k_x, n) - \sin\left(\frac{\sqrt{3}k_x}{2}\right)(\alpha_{\uparrow}(k_x, n-1) + \alpha_{\uparrow}(k_x, n+1)) \right] \\ &\quad + i\lambda_R \left[\left(\cos\left(\frac{\sqrt{3}k_x}{2}\right) + \sqrt{3} \sin\left(\frac{\sqrt{3}k_x}{2}\right) \right) \beta_{\downarrow}(k_x, n) - \beta_{\downarrow}(k_x, n-1) \right], \\ E\alpha_{\downarrow}(k_x, n) &= -t \left[2 \cos\left(\frac{\sqrt{3}k_x}{2}\right) \beta_{\downarrow}(k_x, n) + \beta_{\downarrow}(k_x, n-1) \right] \\ &\quad + 2\lambda_{SO} \left[\sin(\sqrt{3}k_x)\alpha_{\downarrow}(k_x, n) - \sin\left(\frac{\sqrt{3}k_x}{2}\right)(\alpha_{\downarrow}(k_x, n-1) + \alpha_{\downarrow}(k_x, n+1)) \right] \\ &\quad + i\lambda_R \left[\left(\cos\left(\frac{\sqrt{3}k_x}{2}\right) - \sqrt{3} \sin\left(\frac{\sqrt{3}k_x}{2}\right) \right) \beta_{\uparrow}(k_x, n) - \beta_{\uparrow}(k_x, n-1) \right], \\ E\beta_{\uparrow}(k_x, n) &= -t \left[2 \cos\left(\frac{\sqrt{3}k_x}{2}\right) \alpha_{\uparrow}(k_x, n) + \alpha_{\uparrow}(k_x, n+1) \right] \\ &\quad + 2\lambda_{SO} \left[\sin(\sqrt{3}k_x)\beta_{\uparrow}(k_x, n) - \sin\left(\frac{\sqrt{3}k_x}{2}\right)(\beta_{\uparrow}(k_x, n-1) + \beta_{\uparrow}(k_x, n+1)) \right] \\ &\quad - i\lambda_R \left[\left(\cos\left(\frac{\sqrt{3}k_x}{2}\right) - \sqrt{3} \sin\left(\frac{\sqrt{3}k_x}{2}\right) \right) \alpha_{\downarrow}(k_x, n) - \alpha_{\downarrow}(k_x, n+1) \right], \\ E\beta_{\downarrow}(k_x, n) &= -t \left[2 \cos\left(\frac{\sqrt{3}k_x}{2}\right) \alpha_{\downarrow}(k_x, n) + \alpha_{\downarrow}(k_x, n+1) \right] \\ &\quad - 2\lambda_{SO} \left[\sin(\sqrt{3}k_x)\beta_{\downarrow}(k_x, n) - \sin\left(\frac{\sqrt{3}k_x}{2}\right)(\beta_{\downarrow}(k_x, n-1) + \beta_{\downarrow}(k_x, n+1)) \right] \\ &\quad - i\lambda_R \left[\left(\cos\left(\frac{\sqrt{3}k_x}{2}\right) + \sqrt{3} \sin\left(\frac{\sqrt{3}k_x}{2}\right) \right) \alpha_{\uparrow}(k_x, n) - \alpha_{\uparrow}(k_x, n+1) \right]. \quad (3.1.6) \end{aligned}$$

It can be checked that for $\lambda_R = 0$, we retrieve Eq. (3.1.5). It is clear from the above equations that s_z is not conserved and the spin of the edges can be rotated [151]. We define the total probability as,

$$|\psi|^2 = \sum_{\sigma} |\psi_{A\sigma}|^2 + |\psi_{B\sigma}|^2. \quad (3.1.7)$$

The probability of finding an electron in the spin-up state that is, $|\psi_{A\uparrow}|^2 + |\psi_{B\uparrow}|^2$ is equal to the probability of finding an electron in the spin-down state that is, $|\psi_{A\downarrow}|^2 + |\psi_{B\downarrow}|^2$. This provides an evidence that the Rashba SOC does not break TRS [152].

Since we have taken zigzag edges and the ribbon exists only between 0 to $N - 1$, and thus the boundary condition is,

$$\alpha(k_x, n) = \beta(k_x, -1) = 0 \quad (3.1.8)$$

and we impose $E = 0$ here as the plateau in the conductance spectrum is observed at $E \simeq 0$. We have made k_x as a dimensionless quantity by absorbing the lattice spacing a into the definition of k_x . For a comprehensible solution, we turn to a numerical computation of the above set of equations. Here we have used $k_x = \frac{\pi}{\sqrt{3}}$ which particularly renders simple forms for the equations. Solving the above set of equations (Eq. (3.1.5) and Eq. (3.1.6)) numerically (with $t = 1$) and following the boundary conditions (as given in Eq. (3.1.8)), we shall see how the probability densities of the wavefunctions decay, thereby ascertaining whether edge states exist in our system.

3.1.2 Results and discussion

To begin with, let us discuss the values of the SOC's used in our work. Ideally, the strengths of both kinds of SOC are too weak to observe perceptible effects. For example, gold (Au) and Thallium (Tl) decorated GNRs yield the following values for the SOC, namely $\lambda_{SO} = 0.007$, $\lambda_R = 0.0165$ and $\lambda_{SO} = 0.02$, $\lambda_R = 0$ respectively (all quoted in units of hopping, t). However, in our work, without much trepidation, we take λ_R and λ_{SO} as parameters. Here we have taken $\lambda_{SO} = 0.1$ and 0.5 and considered different values of λ_R in the range $[0.01 : 0.5]$. We have also examined other values of λ_{SO} and λ_R , however, they do not produce any qualitatively new results than the ones already presented in this work.

Our focus is to understand the nature of the edge states via both analytic and numeric computations and their effects on the conductance spectra of a KMNR. To distinguish between the various cases, we have considered (a) KMNR with only intrinsic SOC, that is, $\lambda_{SO} \neq 0$ and $\lambda_R = 0$ (as is the case for Tl decorated GNR, albeit with an overestimated λ_{SO}), (b) KMNR with only Rashba SOC, $\lambda_{SO} = 0$, $\lambda_R \neq 0$, and (c) KMNR with $\lambda_{SO} \neq 0$, $\lambda_R \neq 0$. Further, to have a lucid visualization of the existence of edge states and compare them with the results obtained above, we plot the band structure in each of these cases.

A bit of detail on our numeric computation can be given as follows. We have taken $N = 100$ unit cells in the y -direction and thus the Hamiltonian in Eq. (3.1.1) is a 400×400

matrix owing to both spin and sublattice degrees of freedom. We have set the tight-binding parameter, $t = 1$ and the lattice spacing, $a = 1$. All the energies are measured in units of t . The size of the KMNR in numeric computation is taken as 201Z-94A ($L_x \sim 25$ nm and $L_y \sim 20$ nm) with zigzag edges.

3.1.3 Intrinsic SOC

In this subsection, we shall discuss the results for an intrinsic SOC added to a pristine graphene. Fig. (3.1) shows the band structure for two different intrinsic SOC strengths, namely $\lambda_{SO} = 0.1$ and 0.5 . In Fig. (3.1a) when $\lambda_{SO} = 0.1$, we see a bulk gap has opened at the Dirac points, which gives rise to non-trivial edge states with a finite value for the slope. Instead of flat bands (as observed in the tight-binding model), there is a crossing of two edge modes which indicates that the system is in a QSH phase [153]. As we increase the value of λ_{SO} (say, $\lambda_{SO} = 0.5$), a larger bulk gap than the previous case is observed as shown in Fig. (3.1b). To confirm the existence of edge modes, we have also plotted the probability density as a function of site index, n and the LDOS as shown in Fig. (3.2).

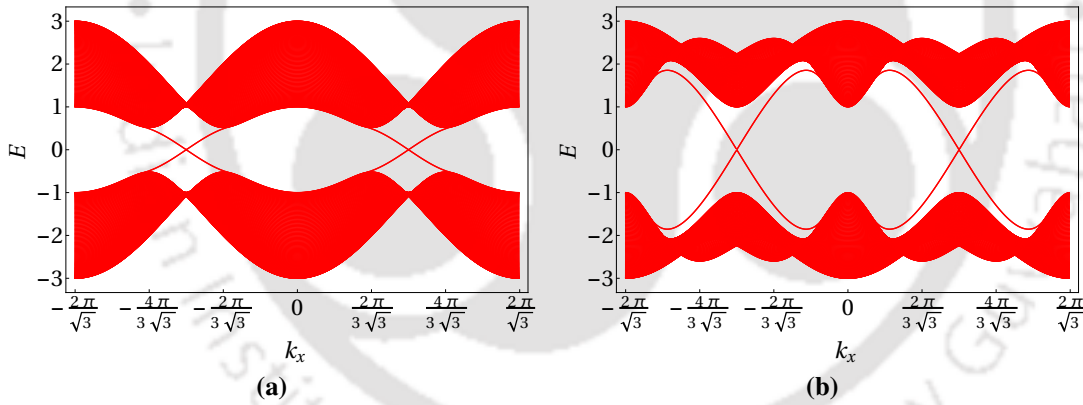


Figure 3.1. (color online) Band structure of a zigzag graphene nanoribbon is shown for different values of intrinsic spin-orbit coupling parameter (a) $\lambda_{SO} = 0.1$ and (b) $\lambda_{SO} = 0.5$. Here we put $\lambda_R = 0$.

We have plotted the probability density for the edge states with the strength of the intrinsic coupling, $\lambda_{SO} = 0.1$ as shown in Fig. (3.2a). We see that the edge states fall off sharply at both edges of the sample. We have also plotted the LDOS for a comparison. The corresponding Fig. (3.2b) implies that the electronic states are highly localized at the edges and vanish immediately inside the ribbon. However, with the inclusion of the intrinsic SOC, which respects the TRS of the KM Hamiltonian, these edge states should be protected by topological invariance. We have also plotted the probability density in Fig. (3.2c) and the LDOS in Fig. (3.2d) for a large value of intrinsic SOC, namely $\lambda_{SO} = 0.5$. The probability

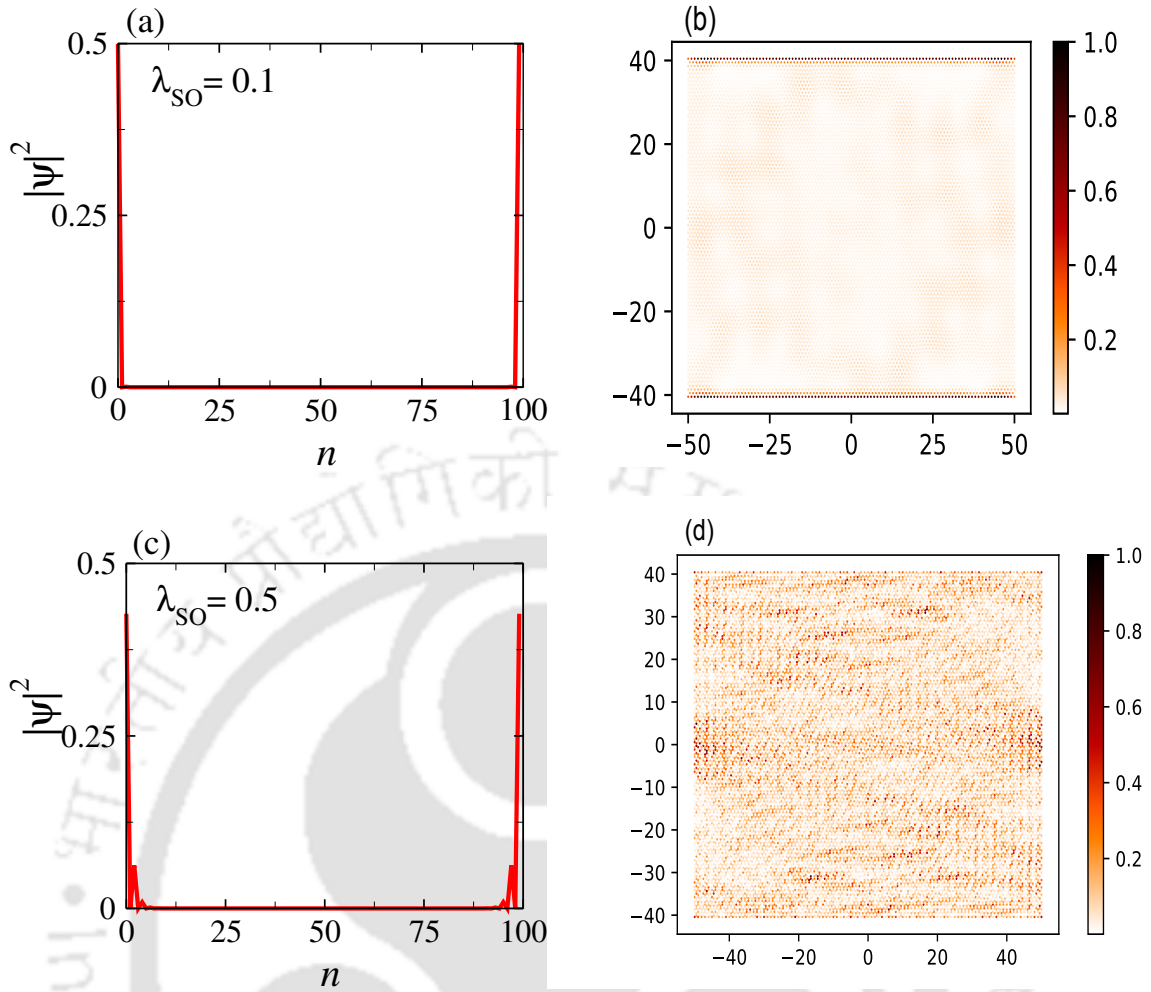


Figure 3.2. (Color online) Probability density of the wave-function, $|\psi|^2$ is plotted as a function of site index, n for (a) $\lambda_{SO} = 0.1$ and (c) $\lambda_{SO} = 0.5$. The LDOS is plotted for (b) $\lambda_{SO} = 0.1$ and (d) $\lambda_{SO} = 0.5$. Here we put $\lambda_R = 0$.

amplitude now does not decay sharply as that for $\lambda_{SO} = 0.1$ and also, this result is in agreement with the LDOS plot where the states are not localized at the edges of the sample rather show an oscillating nature. The localized edge states as seen from Fig. (3.2a) and Fig. (3.2b) conduct and should yield a non-zero conductance value at the zero bias condition.

To explore further, we have plotted the charge conductance, G as a function of Fermi energy, E in presence of the intrinsic SOC as shown in Fig. (3.3). Although the step-like behavior is absent, unlike that of pristine graphene, a $2e^2/h$ plateau is still observed for the case of $\lambda_{SO} = 0.1$ shown by the pink dotted line in Fig. (3.3a). However, for $\lambda_{SO} = 0.5$ as shown in Fig. (3.3b), there is no sharp $2e^2/h$ plateau near the zero of the Fermi energy. It is also important to note that the maximum value of the conductance, that is at $|E| \simeq 0.3$ is higher for a larger value of the intrinsic SOC (see Fig. (3.3b)).

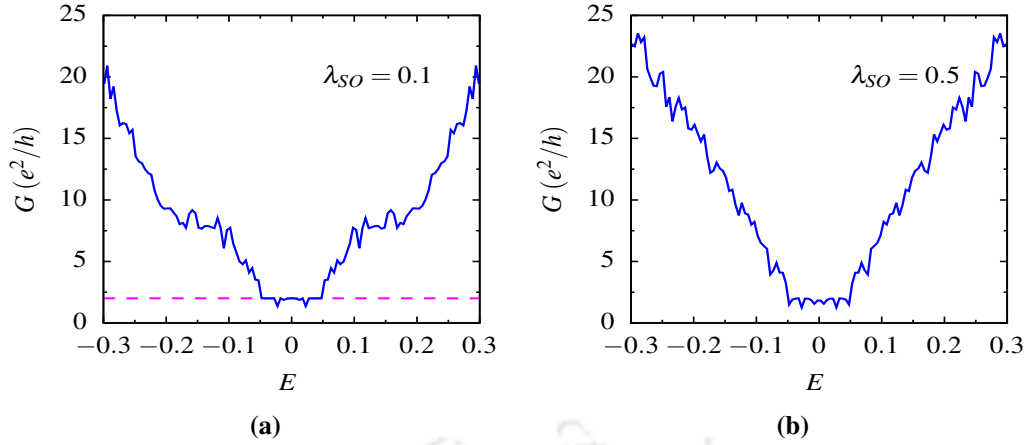


Figure 3.3. (color online) The charge conductance, G (in units of e^2/h) is plotted as a function of energy, E (in units of t) for (a) $\lambda_{SO} = 0.1$ and (b) $\lambda_{SO} = 0.5$. Here we have considered $\lambda_R = 0$.

3.1.4 Rashba SOC

Next, we add a Rashba SOC to a pristine graphene. Thus we have $\lambda_{SO} = 0$, but $\lambda_R \neq 0$ here. For a small value of λ_R ($\lambda_R = 0.1$), the flat band is observed in Fig. (3.4a) as we have already seen for the pristine graphene case. However, if we enhance λ_R , the flat band reduces as shown in Fig. (3.4b) for a large value of λ_R , namely $\lambda_R = 0.5$, where the flat bands have almost vanished and in the $|k_x|$ range of $\left[\frac{2\pi}{3\sqrt{3}}; \frac{4\pi}{3\sqrt{3}}\right]$. The above features are

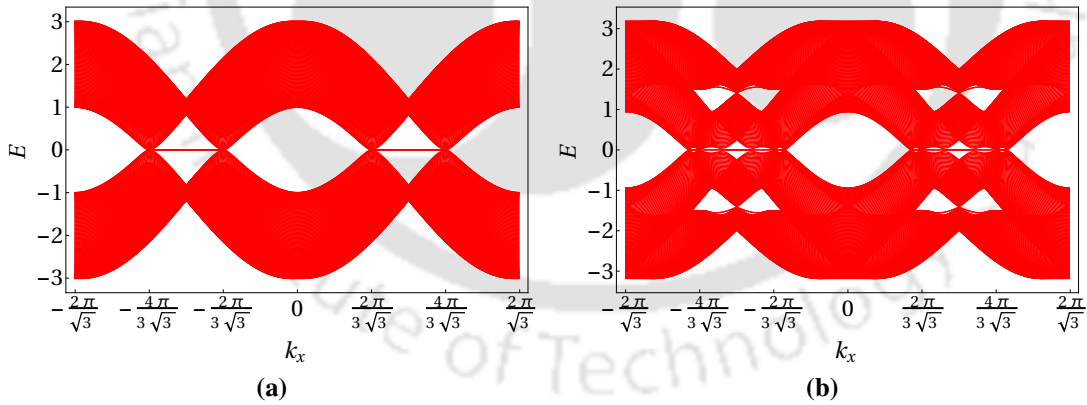


Figure 3.4. (color online) Band structure of a zigzag graphene nanoribbon for different values of Rashba spin-orbit coupling strength (a) $\lambda_R = 0.1$ and (b) $\lambda_R = 0.5$. Here we put $\lambda_{SO} = 0$.

appropriately justified by the analytic behavior (obtained by solving Eq. (3.1.6) by putting $\lambda_{SO} = 0$) as shown in Fig. (3.5). For small values of λ_R (say, $\lambda_R = 0.1$), there is no oscillation, and the probability density decay quickly as one move inward as shown in Fig. (3.5a). The corresponding LDOS plot in Fig. (3.5b) shows the same behavior. For large values of λ_R , the probability densities show damped oscillations as one moves inside the bulk and remain finite till quite a few lattice spacings inside the sample (see Fig. (3.5c)). The LDOS plots

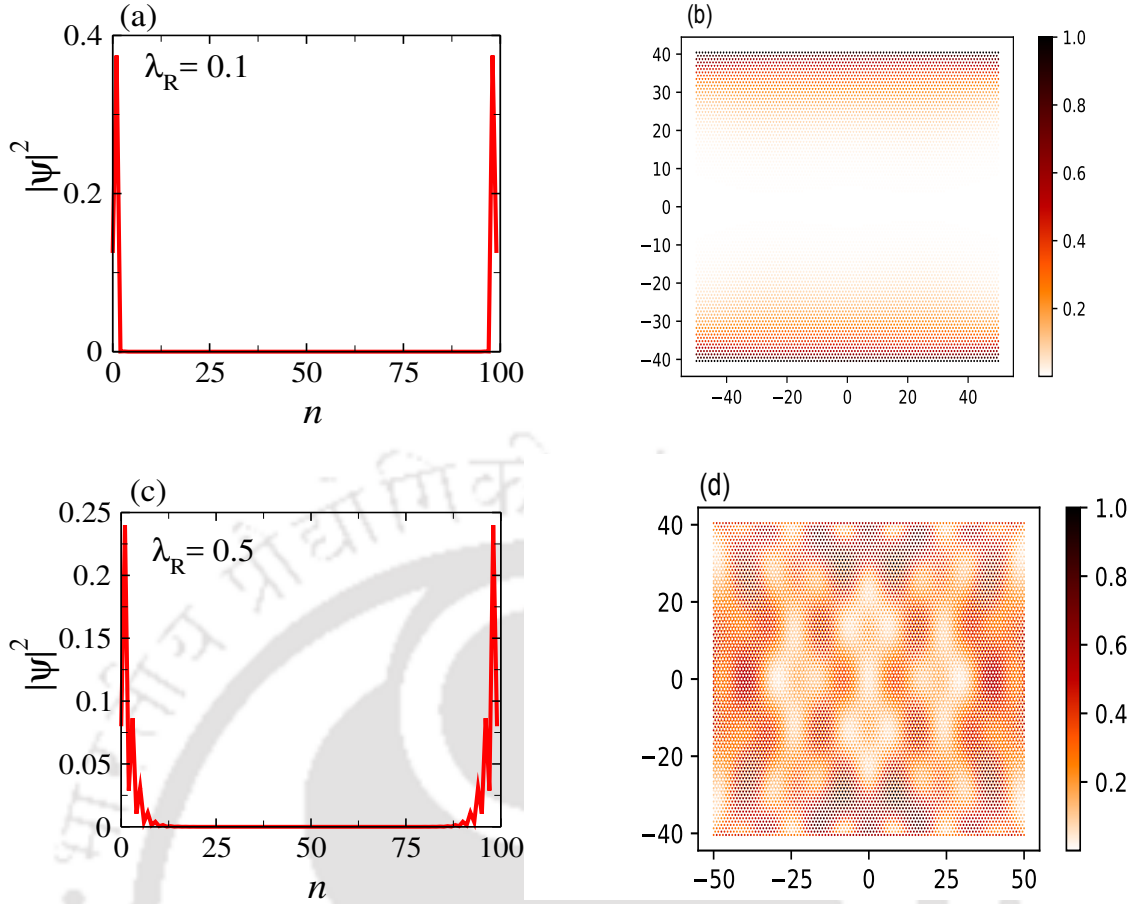


Figure 3.5. (Color online) Probability density of the wave-function, $|\psi|^2$ is plotted as a function of site index, n for (a) $\lambda_R = 0.1$ and (c) $\lambda_R = 0.5$. The LDOS is shown for (b) $\lambda_R = 0.1$ and (d) $\lambda_R = 0.5$. The oscillatory pattern is seen in Fig. (c) and (d). Here we put $\lambda_{SO} = 0$.

in Fig. (3.5d) provide ample support for this oscillatory behavior and non-vanishing weights inside the bulk.

Finally, we have plotted the charge conductance as shown in Fig. (3.6). For $\lambda_R = 0.1$, there is a $2e^2/h$ plateau near the zero of the Fermi energy as shown in Fig. (3.6a). However, this $2e^2/h$ value is not associated with a topological phase, as is evident from Fig. (3.5). For $\lambda_R = 0.5$, the conductance plot shows the absence of plateau at a $2e^2/h$ and closing of gaps is observed near the zero of the Fermi energy as shown in Fig. (3.6b). These results signify the absence of edge modes and, subsequently, any topologically non-trivial behavior in the conductance data.

3.1.5 Intrinsic and Rashba SOC

In this section, we include both the intrinsic and the Rashba SOC in the graphene nanoribbon call this as Kane-Mele nanoribbon (KMNR) with zigzag edges. It is sensible to ask what happens to the edge state when both of these are present. The KM Hamiltonian is P - T

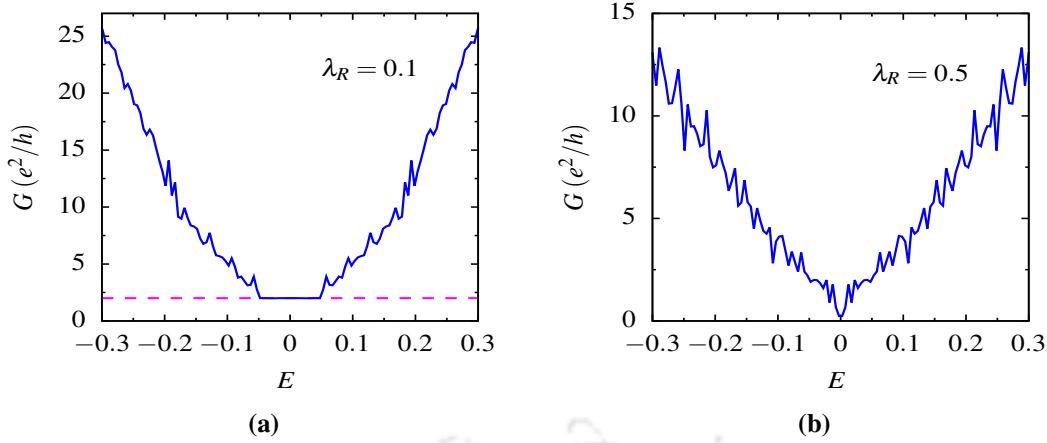


Figure 3.6. (color online) The charge conductance, G (in units of e^2/h) is plotted as a function of energy, E (in units of t) for (a) $\lambda_R = 0.1$ and (b) $\lambda_R = 0.5$. Here we put $\lambda_{SO} = 0$.

symmetric and hence the Kramer's doublet must enjoy topological protection. However, the existence of edge states still needs to be ascertained and the implications on the conductance spectra thereof.

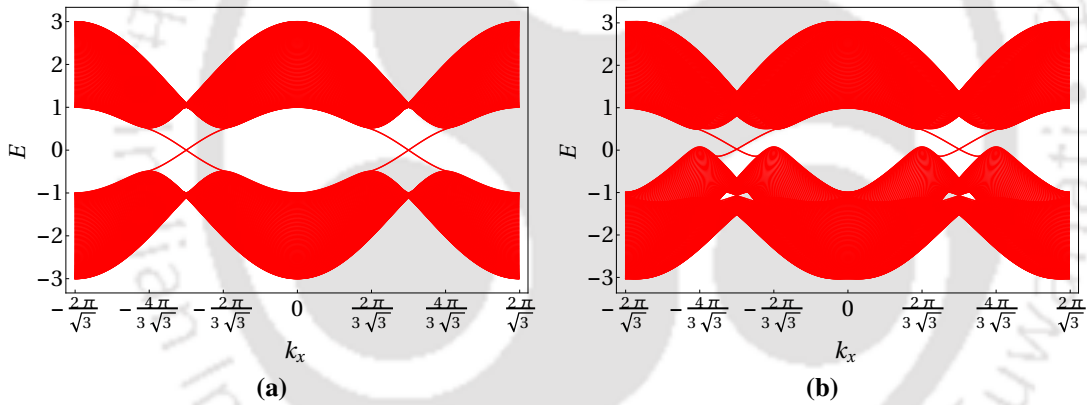


Figure 3.7. (color online) The band structure of zigzag Kane-Mele nanoribbon with (a) $\lambda_{SO} = 0.1$, $\lambda_R = 0.01$ and (b) $\lambda_{SO} = 0.1$, $\lambda_R = 0.2$.

We keep $\lambda_{SO} = 0.1$ and explore two different values of Rashba SOC, namely $\lambda_R = 0.01$ and $\lambda_R = 0.2$. The former corresponds to $\lambda_R < \lambda_{SO} (< t)$ and the latter denotes $\lambda_R > \lambda_{SO} (< t)$. The band structures for the corresponding cases are shown in Fig. (3.7). When the strength of the Rashba SOC is weak, the band structure for $\lambda_{SO} = 0.1$ is almost similar (shown in Fig. (3.7a)) to the band structure for the same value of the intrinsic SOC in the absence of Rashba SOC (Fig. (3.1a)). However, for a larger value of λ_R (Fig. (3.7b)), the band gap in bulk gets smaller than the previous case. The results corresponding to these two cases are not much different with regard to the existence of the edge states. The behavior of the edge states is depicted in Fig. (3.8a) and Fig. (3.8c). The only (minor) difference is that the analytic form yields a non-zero value for $n = 2$ corresponding to the larger value of λ_R , that

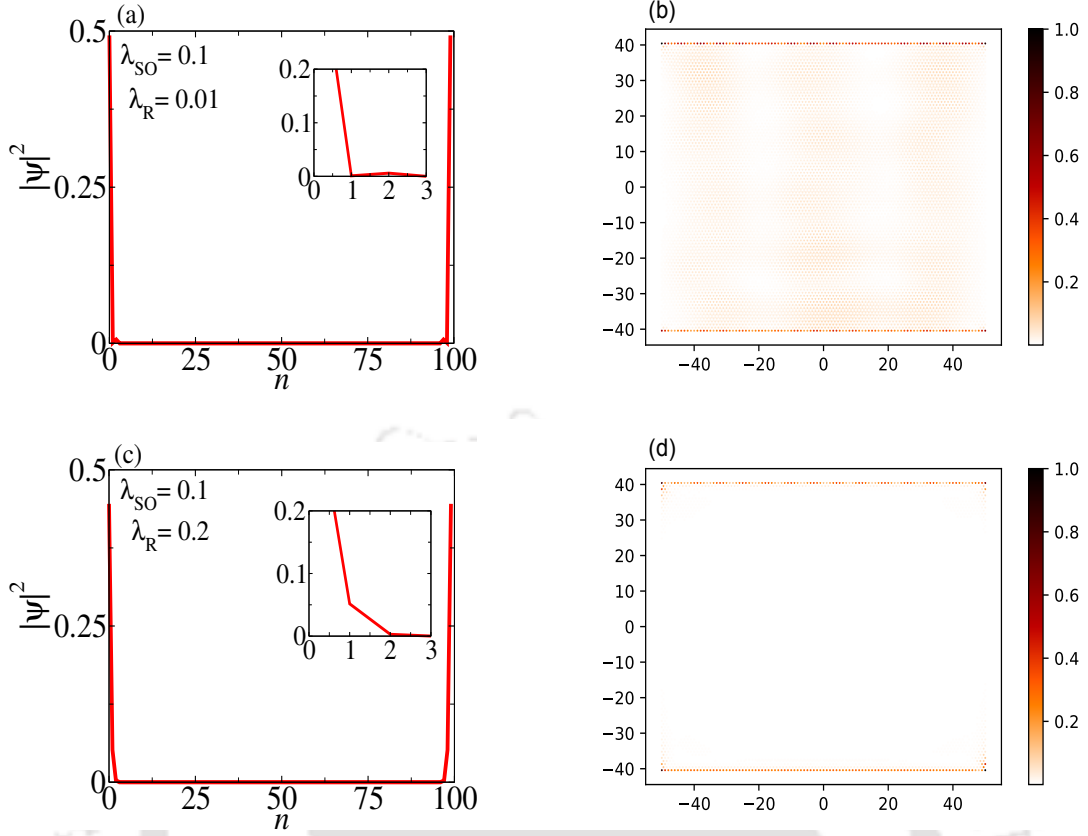


Figure 3.8. (color online) Probability density of the wave-function, $|\psi|^2$ as a function of site index, n for (a) $\lambda_{SO} = 0.1$, $\lambda_R = 0.01$ and (c) $\lambda_{SO} = 0.1$ and $\lambda_R = 0.2$. The corresponding LDOS is plotted for (b) $\lambda_{SO} = 0.1$, $\lambda_R = 0.01$ and (d) $\lambda_{SO} = 0.1$, $\lambda_R = 0.2$.

is, $\lambda_R = 0.2$. The LDOS maps corroborate the existence of the edge modes (see Fig. (3.8b) and Fig. (3.8d)) as is evident for Fig. (3.8a) and Fig. (3.8c). The conductance spectra is

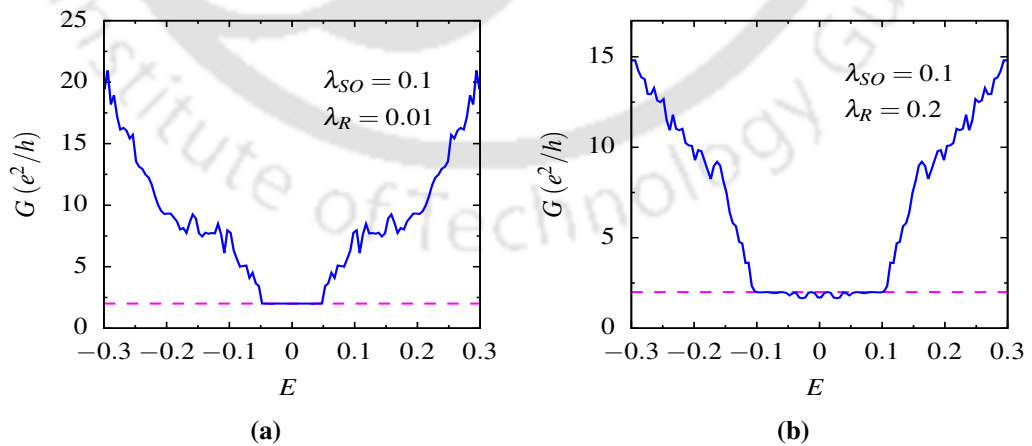


Figure 3.9. (color online) The charge conductance, G (in units of e^2/h) is plotted as a function of energy E (in units of t) for different values of λ_R (a) $\lambda_R = 0.01$ and (b) $\lambda_R = 0.2$. Here, we have fixed $\lambda_{SO} = 0.1$.

plotted as a function of the Fermi energy for different values of λ_R , keeping the $\lambda_{SO} = 0.1$ as shown in Fig. (3.9a) and Fig. (3.9b). Fig. (3.9a) shows the existence of a $2e^2/h$ plateau,

which is topologically protected and corresponds to a QSH insulating phase. However, when $\lambda_{SO} < \lambda_R$ (Fig. (3.9b)), the topological gap tends to vanish, destroying the existence of the $2e^2/h$ plateau. It may be noted that we have presented plots only for two sets of parameter values, namely $(\lambda_{SO}, \lambda_R) = (0.1, 0.01)$ and $(0.1, 0.2)$. However, the same inferences can be drawn for other sets, such as larger values of λ_{SO} and λ_R , which we have explicitly checked but have not shown the data for brevity.

3.1.6 Bilayer system

3.1.6.a Model Hamiltonian

We consider the same AB -stacked bilayer graphene sheet with zigzag edges, which consists of two coupled monolayers of C atoms as shown in Fig. (2.6). The KM model of a bilayer graphene in the presence of a biasing voltage V can be written as,

$$\begin{aligned}
 H &= H^T + H^B + H^{T-B} + V \left(\sum_{i \in T, \sigma} c_{i\sigma}^\dagger c_{i\sigma} - \sum_{i \in B, \sigma} c_{i\sigma}^\dagger c_{i\sigma} \right) \\
 &= H^T + H^B - t_\perp \sum_{i \in (T,A), j \in (B,B), \sigma} (c_{i\sigma}^\dagger c_{j\sigma} + h.c.) - i\lambda_R^\perp \sum_{i \in (T,A), j \in (B,B), \sigma\sigma'} \left(c_{i\sigma}^\dagger (\mathbf{s}_{\sigma\sigma'} \times \hat{\mathbf{d}}_{ij})_z c_{j\sigma'} + h.c. \right) \\
 &\quad + V \left(\sum_{i \in T, \sigma} c_{i\sigma}^\dagger c_{i\sigma} - \sum_{i \in B, \sigma} c_{i\sigma}^\dagger c_{i\sigma} \right), \tag{3.1.9}
 \end{aligned}$$

where H^T and H^B refer to the Hamiltonians for the top and the bottom layers, respectively. H^{T-B} includes coupling between the top and bottom layers. Since the form of the Hamiltonian depends on the stacking geometry of the layers, we have considered only the hopping between the A site of the top layer and the nearest B site of the bottom layer, which is represented by the third term. The subscripts i, j label the lattice sites and σ denotes the spin index. The interlayer hopping amplitude is denoted by t_\perp , where $t_\perp \simeq 0.4$ eV. The fourth term represents the interlayer Rashba coupling arising in the presence of a tilted electric field [145]. The negative sign in the fourth term indicates that the A site of the top layer and nearest B site of the bottom layer are connected by a unit vector $-\hat{\mathbf{z}}$. The last term is the interlayer bias potential with strength V . The KM [15, 29] Hamiltonian contains the following terms for each of the single layers, namely,

$$H^{T(B)} = H_{\text{hop}} + H_{\text{ISOC}} + H_{\text{RSOC}}, \tag{3.1.10}$$

where

$$\begin{aligned}
 H_{\text{hop}} &= -t \sum_{\langle ij \rangle \sigma} c_{i\sigma}^\dagger c_{j\sigma} \\
 H_{\text{ISOC}} &= i\lambda_{SO} \sum_{\langle\langle ij \rangle\rangle \sigma \sigma'} v_{ij} c_{i\sigma}^\dagger s_{\sigma\sigma'}^z c_{j\sigma'} \\
 H_{\text{RSOC}} &= i\lambda_R \sum_{\langle ij \rangle \sigma \sigma'} c_{i\sigma}^\dagger \left(\mathbf{s}_{\sigma\sigma'} \times \hat{\mathbf{d}}_{ij} \right)_z c_{j\sigma'}.
 \end{aligned}$$

The first term H_{hop} describes the hopping between nearest neighbors with hopping energy t ($t \approx 2.7$ eV). The second term H_{ISOC} is the mirror-symmetric intrinsic SOC term with a coupling strength λ_{SO} . $v_{ij} = +1(-1)$ if the electron makes a left (right) move to go from site j to a next neighbor i through their common nearest neighbor. The vector $\hat{\mathbf{d}}$ points from site i to site j and corresponds to the nearest neighbor vectors. s^z is the z -component of the Pauli spin matrix. The third term is the nearest neighbor Rashba term which arises due to the perpendicular electric field or interaction with a substrate with a coupling strength λ_R .

3.1.6.b Edge states and band structure

In the following, we show the edge states and the band structure plots for several choices of parameters both in the absence and the presence of a bias voltage [154]. Initially, we study the model by switching off the biasing term ($V = 0$).

3.1.6.c Zero bias ($V = 0$)

In this section, we study the edge state properties of a bilayer graphene in the presence of SOCs. We focus on the bilayer graphene ribbon geometry with zigzag edges where the translational invariance exists along the x -axis as shown in Fig. (2.6). The ribbon width is such that it has N unit cells along the y -axis (where $n \in 0$ to $N - 1$). We use periodic boundary conditions along the x -direction. Since intrinsic SOC involves next to nearest neighbor coupling in a plane, it does not affect the interlayer Hamiltonian. Using the momentum representation of the electron operators and solving the time-independent Schrödinger equation, we get eight eigenvalue equations corresponding to the spin up and spin down states for A_i and B_i ($i = 1, 2$). They are,

$$\begin{aligned}
 E\alpha_{1\pm}(k_x, n) &= -t \left[D_k \beta_{1\pm}(k_x, n) + \beta_{1\pm}(k_x, n-1) \right] - t_\perp \beta_{2\pm}(k_x, n) \\
 &\mp 2\lambda_{SO} \left[P_k \alpha_{1\pm}(k_x, n) - M_k \{ \alpha_{1\pm}(k_x, n-1) + \alpha_{1\pm}(k_x, n+1) \} \right]
 \end{aligned}$$

$$\begin{aligned}
E\alpha_{2\pm}(k_x, n) &= -t \left[D_k \beta_{2\pm}(k_x, n) + \beta_{2\pm}(k_x, n-1) \right] \\
&\mp 2\lambda_S O \left[P_k \alpha_{2\pm}(k_x, n) - M_k \{ \alpha_{2\pm}(k_x, n-1) + \alpha_{2\pm}(k_x, n+1) \} \right] \\
E\beta_{1\pm}(k_x, n) &= -t \left[D_k \alpha_{1\pm}(k_x, n) + \alpha_{1\pm}(k_x, n+1) \right] \\
&\pm 2\lambda_S O \left[P_k \beta_{1\pm}(k_x, n) - M_k \{ \beta_{1\pm}(k_x, n-1) + \beta_{1\pm}(k_x, n+1) \} \right] \\
E\beta_{2\pm}(k_x, n) &= -t \left[D_k \alpha_{2\pm}(k_x, n) + \alpha_{2\pm}(k_x, n+1) \right] - t_{\perp} \alpha_{1\pm}(k_x, n) \\
&\pm 2\lambda_S O \left[P_k \beta_{2\pm}(k_x, n) - M_k \{ \beta_{2\pm}(k_x, n-1) + \beta_{2\pm}(k_x, n+1) \} \right], \quad (3.1.11)
\end{aligned}$$

where the ‘ \pm ’ sign in the subscripts denote the up and down spins for both the sublattices in each layer and $D_k = 2 \cos\left(\frac{\sqrt{3}k_x}{2}\right)$; $P_k = \sin\left(\sqrt{3}k_x\right)$; $M_k = \sin\left(\frac{\sqrt{3}k_x}{2}\right)$. Here α_i, β_i refer to the amplitudes corresponding to the A and B sublattices. We have chosen the basis as,

$$|\psi_k\rangle = \sum_{n,\sigma} \sum_{i=1}^2 \left[\alpha_i(k, n, \sigma) |a_i, k, n, \sigma\rangle + \beta_i(k, n, \sigma) |b_i, k, n, \sigma\rangle \right]. \quad (3.1.12)$$

Next, we consider the Rashba SOC, which leads to spin mixing in the presence of a tilted electric field. The intralayer and the interlayer Rashba couplings can now be included, and hence the amplitudes, $\alpha_{i\pm}$ and $\beta_{i\pm}$ are obtained from the following sets of equations.

$$\begin{aligned}
E\alpha_{1\pm}(k_x, n) &= -t \left[D_k \beta_{1\pm}(k_x, n) + \beta_{1\pm}(k_x, n-1) \right] - t_{\perp} \beta_{2\pm}(k_x, n) \\
&\mp 2\lambda_S O \left[P_k \alpha_{1\pm}(k_x, n) - M_k \{ \alpha_{1\pm}(k_x, n-1) + \alpha_{1\pm}(k_x, n+1) \} \right] \\
&+ i\lambda_R \left[N_{\pm} \beta_{1\mp}(k_x, n) - \beta_{1\mp}(k_x, n-1) \right] \mp \lambda_R^{\perp} \beta_{2\mp}(k_x, n) \\
E\alpha_{2\pm}(k_x, n) &= -t \left[D_k \beta_{2\pm}(k_x, n) + \beta_{2\pm}(k_x, n-1) \right] \\
&\mp 2\lambda_S O \left[P_k \alpha_{2\pm}(k_x, n) - M_k \{ \alpha_{2\pm}(k_x, n-1) + \alpha_{2\pm}(k_x, n+1) \} \right] \\
&+ i\lambda_R \left[N_{\pm} \beta_{2\mp}(k_x, n) - \beta_{2\mp}(k_x, n-1) \right] \\
E\beta_{1\pm}(k_x, n) &= -t \left[D_k \alpha_{1\pm}(k_x, n) + \alpha_{1\pm}(k_x, n+1) \right] \\
&\pm 2\lambda_S O \left[P_k \beta_{1\pm}(k_x, n) - M_k \{ \beta_{1\pm}(k_x, n-1) + \beta_{1\pm}(k_x, n+1) \} \right] \\
&- i\lambda_R \left[N_{\mp} \alpha_{1\mp}(k_x, n) - \alpha_{1\mp}(k_x, n+1) \right] \\
E\beta_{2\pm}(k_x, n) &= -t \left[D_k \alpha_{2\pm}(k_x, n) + \alpha_{2\pm}(k_x, n+1) \right] - t_{\perp} \alpha_{1\pm}(k_x, n) \\
&\pm 2\lambda_S O \left[P_k \beta_{2\pm}(k_x, n) - M_k \{ \beta_{2\pm}(k_x, n-1) + \beta_{2\pm}(k_x, n+1) \} \right] \\
&- i\lambda_R \left[N_{\mp} \alpha_{2\mp}(k_x, n) - \alpha_{2\mp}(k_x, n+1) \right] \pm \lambda_R^{\perp} \alpha_{1\mp}(k_x, n), \quad (3.1.13)
\end{aligned}$$

where $N_{\pm} = \left[\cos\left(\frac{\sqrt{3}k_x}{2}\right) \pm \sqrt{3} \sin\left(\frac{\sqrt{3}k_x}{2}\right) \right]$. We have solved these equations (namely, Eq. (3.1.11) and Eq. (3.1.13)) numerically using the boundary condition given in Eq. (2.3.28) (see Chap-

ter 1) for our purpose. These equations become particularly simple corresponding to $k_x = \frac{\pi}{\sqrt{3}}$ where D_k and P_k (see their definition above) vanish.

Next we discuss the results obtained via solving the eigenvalue equations, namely (3.1.11) and (3.1.13). All the energies are measured in units of inplane hopping t . We have fixed our interlayer tight binding coupling parameter, $t_{\perp} = 0.2$ and have considered different parameter values for the intralayer intrinsic SOC, λ_{SO} and the inplane and interlayer Rashba couplings, namely λ_R and λ_R^{\perp} respectively. Nevertheless, the SOC parameters considered by us are indeed higher (usually one or two order) compared to the actual values. But then, as we said earlier, these SOC values can be enhanced by using heavily adatoms [155], we proceed with the values without trepidation.

To study the surface (or edge) state properties for different sublattices, we have plotted the charge densities as a function of n (n being the site index) for different values of SOCs. We have also computed the electronic energy dispersion to provide support to the corresponding results for the edge states for a few orbitals, that is, corresponding to small values of N .

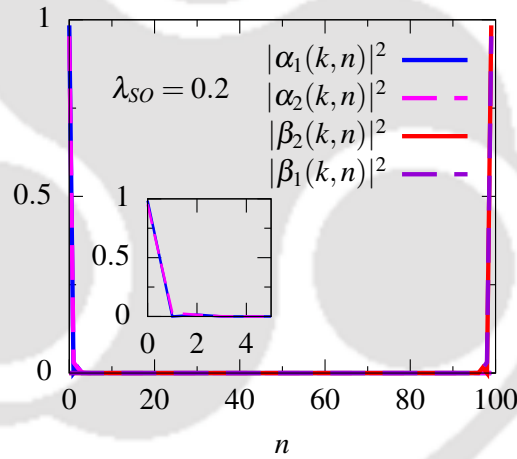


Figure 3.10. (color online) Charge density as a function of site index, n at $k_x = \frac{\pi}{\sqrt{3}}$. Here, we set $t_{\perp} = 0.2$ and $\lambda_{SO} = 0.2$.

We have considered only the intralayer intrinsic SOC as given in Eq. (3.1.9). Fig. (3.10) shows the charge density plot at the Dirac point for intrinsic SOC strength $\lambda_{SO} = 0.2$ at an energy close to zero. As compared to a pristine bilayer, the amplitudes for the A sublattice in layer 1 and the B sublattice in layer 2 fall off sharply at the two opposite edges of the ribbon, while the amplitudes for the A sublattice in layer 2 and the B sublattice in layer 1 fall off more gradually as is shown in the inset plot. However, these edge states are topologically protected by the TRS.

Fig. (3.11) shows the band structure for different values of N , namely an even N ($N = 4$) and an odd N ($N = 5$) for $\lambda_{SO} = 0.2$. It can be seen that there is an odd-even asymmetry in

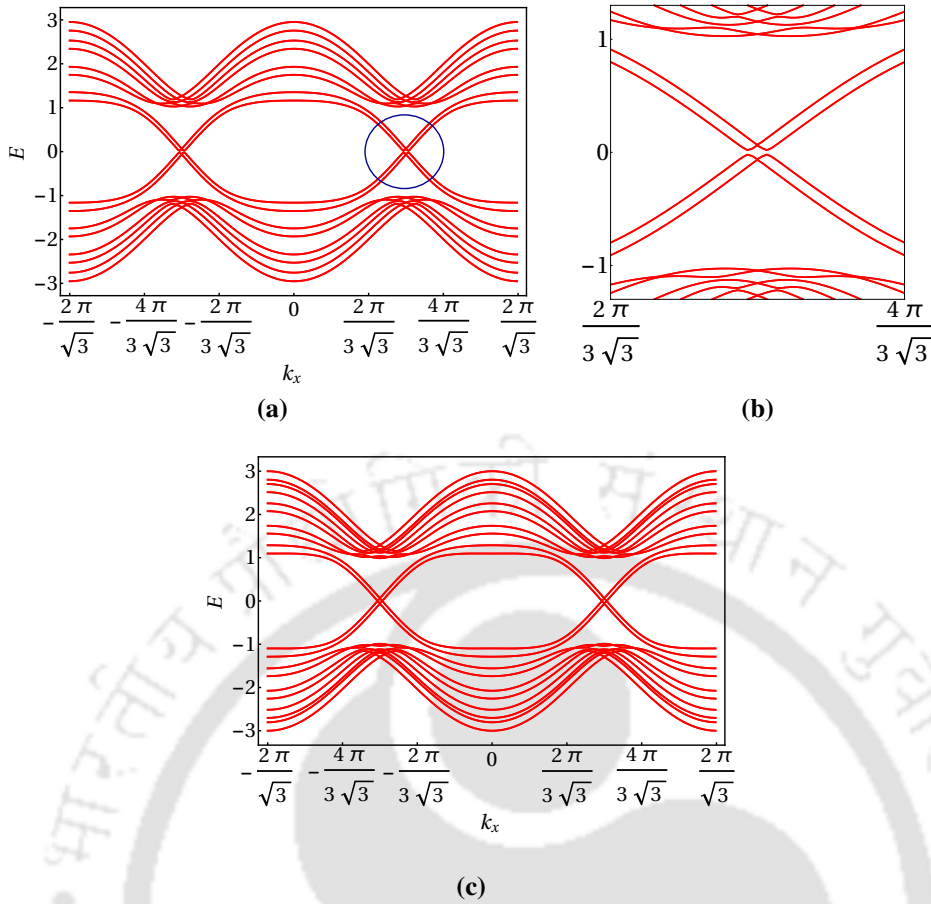


Figure 3.11. (color online) The band structure for different values of N (a) $N = 4$, (b) zoomed view of the region encircled by blue as shown in (a) and (c) $N = 5$. Here, we set $t_{\perp} = 0.2$ and $\lambda_{SO} = 0.2$.

presence of the intrinsic SOC. Fig. (3.11a) shows that there is an opening of the band gap of small magnitude at the two Dirac points for $N = 4$. It is well-known that backscattering is forbidden between the time-reversed pairs in a QSH state. Due to the finite-size effects, backscattering still may be possible, which demonstrates that though the TRS is trying to keep a gapless edge state, a small gap may open up. However, for $N = 5$ (Fig. (3.11c)), one sees the closing of the gap for the same values of the intrinsic coupling constant. The above odd-even scenario depends on the ribbon width. For larger values of N , such discrepancies will cease to exist. This asymmetry occurs only for a ZGNR may be attributed due to its configuration in the sense that the even ZGNRs ($N = \text{even}$) are in "zigzag/zigzag" configuration, while the odd ZGNRs ($N = \text{odd}$) are in "zigzag/antizigzag" configuration [156] where the gap in the former case appears owing to a lack of sublattice translational invariance which renders an effective interedge tunneling.

Next we have considered intralayer intrinsic SOC and Rashba SOC in and between the layers. Here we have all non-zero values of the coupling parameters, namely, $\lambda_{SO} \neq 0$, $\lambda_R \neq 0$

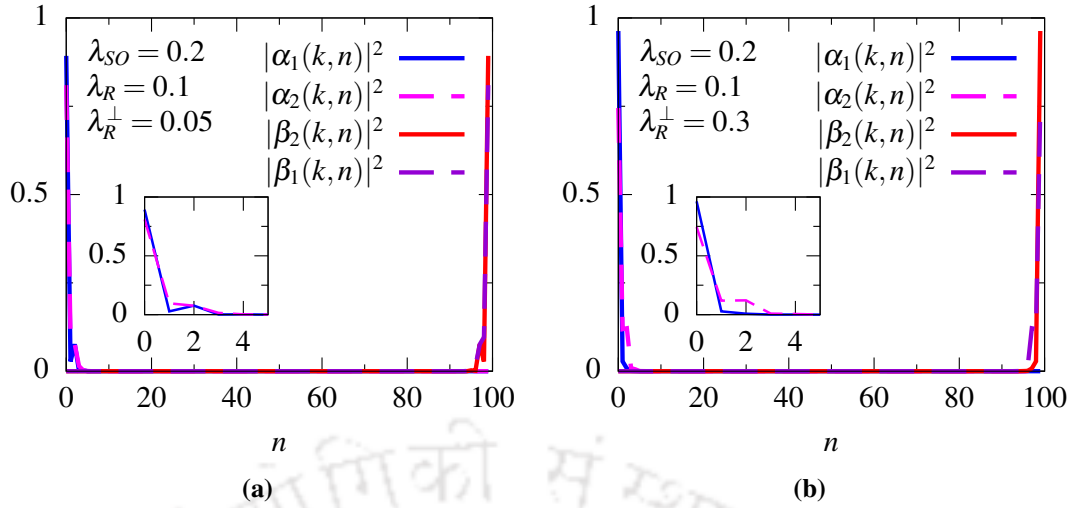


Figure 3.12. (color online) Charge density as a function of site index, n at $k_x = \frac{\pi}{\sqrt{3}}$ for different values of λ_R^\perp (a) $\lambda_R^\perp = 0.05$ (b) $\lambda_R^\perp = 0.3$. Here, we set $t_\perp = 0.2$, $\lambda_{SO} = 0.2$ and $\lambda_R = 0.1$.

and $\lambda_R^\perp \neq 0$. To see the effects of interlayer Rashba coupling, we have fixed the intralayer intrinsic SOC ($\lambda_{SO} = 0.2$) and intralayer Rashba SOC ($\lambda_R = 0.1$). We have plotted the charge density as shown in Fig. (3.12) for two different values of the interlayer Rashba SOC, namely $\lambda_R^\perp = 0.05$ and 0.3 . It can be seen from Fig. (3.12a) that for a small value of λ_R^\perp , the amplitudes of the A and B sublattices penetrate somewhat gradually into the bulk for a fixed value of intralayer intrinsic SOC and Rashba SOC, while for large values of λ_R^\perp the penetration depth is enhanced where the fall off of the amplitudes become even more gradual (see Fig. (3.12b)). The amplitudes in either of the cases do not exhibit any sharp fall off.

We have also plotted the band structure for the above mentioned values of parameter for $N = 5$ (Fig. (3.13a) and Fig. (3.13b)). It can be seen that for a small value of λ_R^\perp , there exists a band gap which is vanishingly small (shown in Fig. (3.13a)), and the spin degeneracy is lifted. However, for large values of λ_R^\perp , the band gap increases, and it varies almost linearly with the interlayer Rashba SOC (Fig. (3.13b)). This indicates that the topological properties of the QSH phase are destroyed in the presence of both intralayer and interlayer Rashba coupling along with intralayer intrinsic SOC. For both the above cases, we have fixed the other parameters $t_\perp = 0.2$, $\lambda_{SO} = 0.2$ and $\lambda_R = 0.1$. It is interesting to note that the edge modes can be seen in the presence of intrinsic SOC only, while the inclusion of the interlayer Rashba coupling along with the intralayer Rashba SOC destroys the edge modes.

To distinguish between the effects of intralayer and interlayer Rashba SOC on the energy spectrum, we have also plotted Fig. (3.13c) and Fig. (3.13d). For $\lambda_R = 0.1$ and $\lambda_R^\perp = 0$, the crossing of the bands in the k_x range as observed before in the presence of only intrinsic SOC

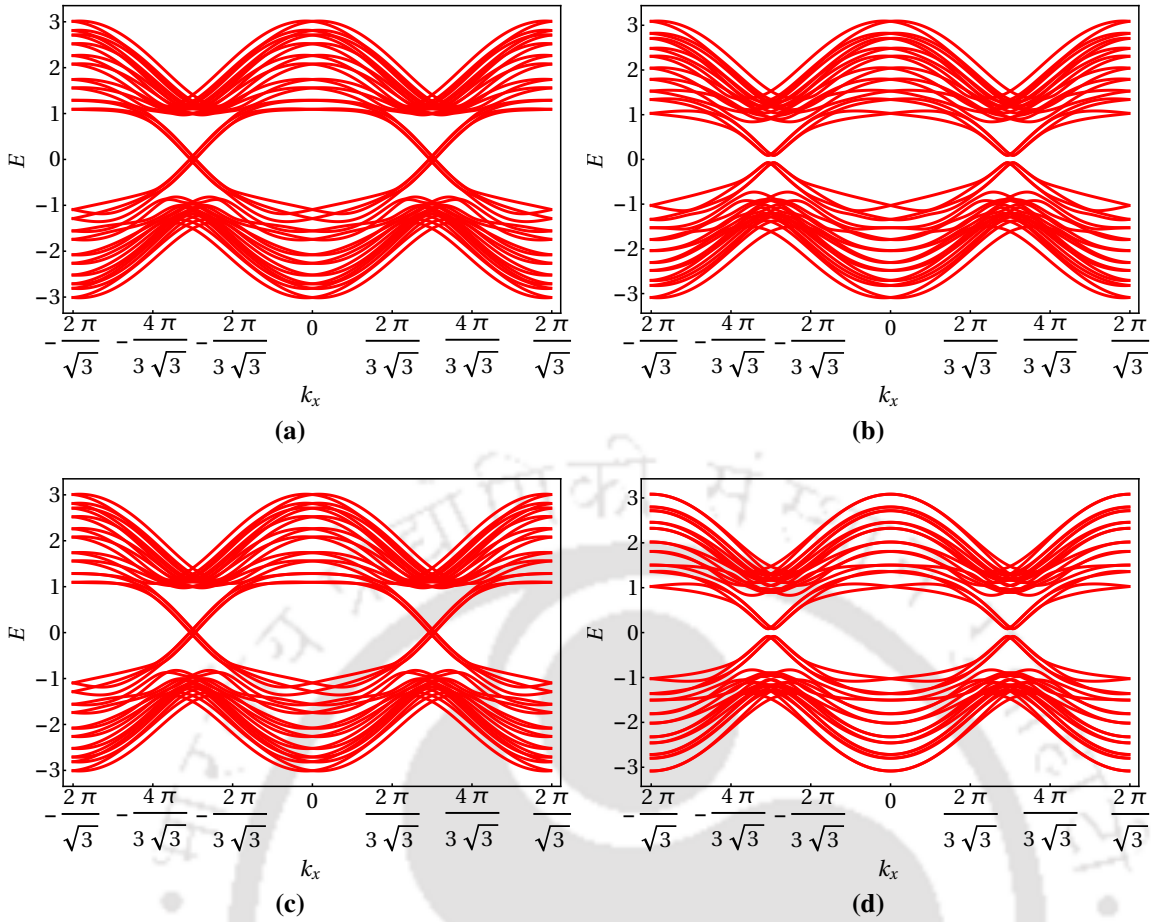


Figure 3.13. (color online) The band structure for (a) $\lambda_R = 0.1$ and $\lambda_R^\perp = 0.05$ (b) $\lambda_R = 0.1$ and $\lambda_R^\perp = 0.3$ (c) $\lambda_R = 0.1$ and $\lambda_R^\perp = 0$ (d) $\lambda_R = 0$ and $\lambda_R^\perp = 0.3$. Here, we set $t_\perp = 0.2$, $\lambda_{SO} = 0.2$ and $N = 5$.

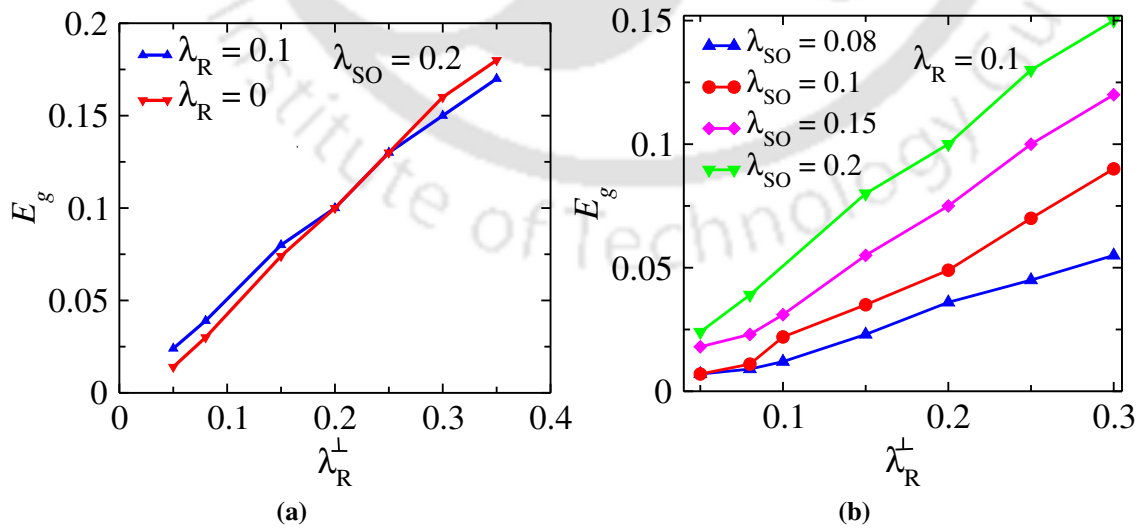


Figure 3.14. (color online) Energy gap, E_g as a function of interlayer Rashba SOC parameter, λ_R^\perp for (a) two different values of λ_R , namely $\lambda_R = 0$ and 0.1 with fixed λ_{SO} (namely $\lambda_{SO} = 0.2$) (b) different values of λ_{SO} with fixed λ_R (namely $\lambda_R = 0.1$). Here, we set $t_\perp = 0.2$.

remains as it is (as shown in Fig. (3.13c)), while for $\lambda_R = 0$ and $\lambda_R^\perp = 0.3$, band gap opens up, thereby altering the scenario of having crossed edge modes (see Fig. (3.13d)). For a lucid visualization, we have plotted the band gap, E_g as a function of interlayer Rashba coupling, λ_R^\perp for two different cases. Fig. (3.14a) shows that although the band gap, E_g varies linearly for the $\lambda_R = 0$ and $\lambda_R = 0.1$ for a fixed λ_{SO} , the gap increases more sharply for $\lambda_R = 0$ than the other one, while Fig. (3.14b) shows the same plot for different values of λ_{SO} . Thus the energy gap at the Dirac points is affected by the interlayer Rashba SOC in a roughly linear fashion predominantly.

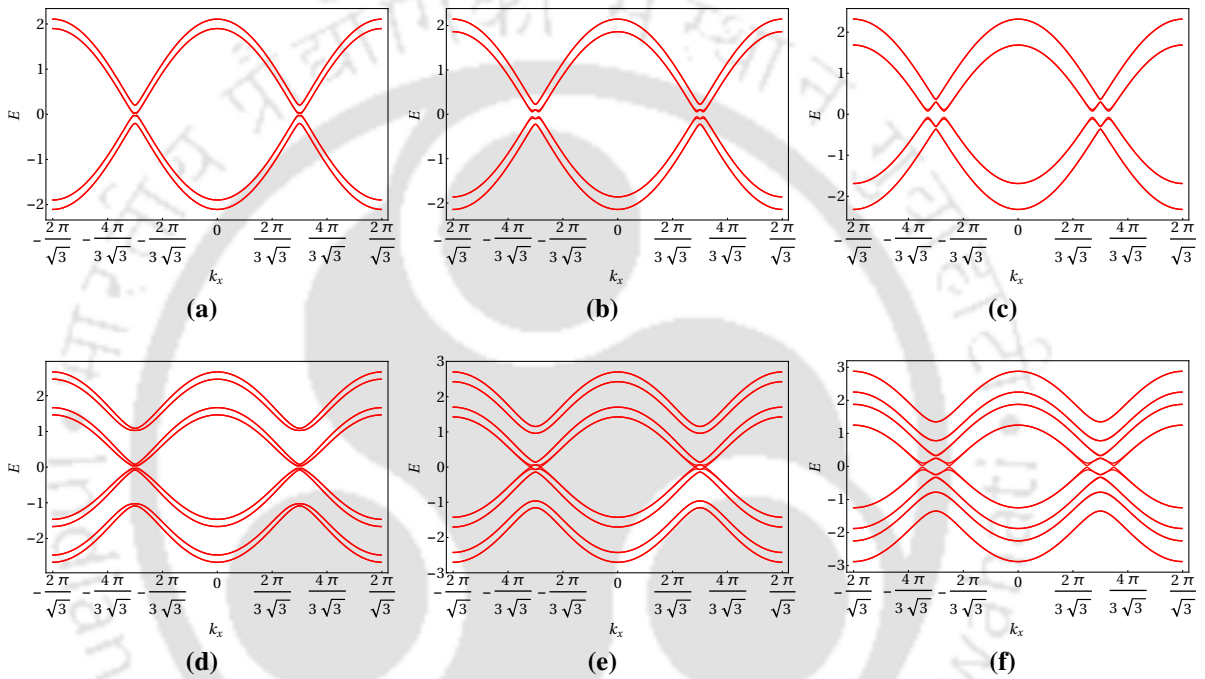


Figure 3.15. (color online) The band structure for different values of bias voltage $V = 0.03, 0.1, 0.3$ for $N = \text{odd}$ (a-c) and $N = \text{even}$ (d-f) respectively. Here, we set $t_\perp = 0.2$ and $\lambda_{SO} = 0.1$. We also put $\lambda_R = \lambda_R^\perp = 0$.

3.1.6.d Turning on the bias voltage ($V \neq 0$)

In this section, we include a biasing term V (such that a constant potential difference $2V$ exists between the layers) and study the effect of this bias voltage in the presence of spin-orbit interactions. It is well-known that if we add a bias voltage to bilayer graphene, it will open a gap and a *Mexican-hat* like feature can be observed in the lowest energy band around the Dirac points [91]. In our previous study, we have seen that there is an odd-even asymmetry in the energy spectrum in the presence of an intrinsic SOC for very small values of N with no bias voltage ($V = 0$). For $V \neq 0$, the odd-even asymmetry still can be observed in the energy spectrum as the bias voltage is tuned. In particular, we have considered three

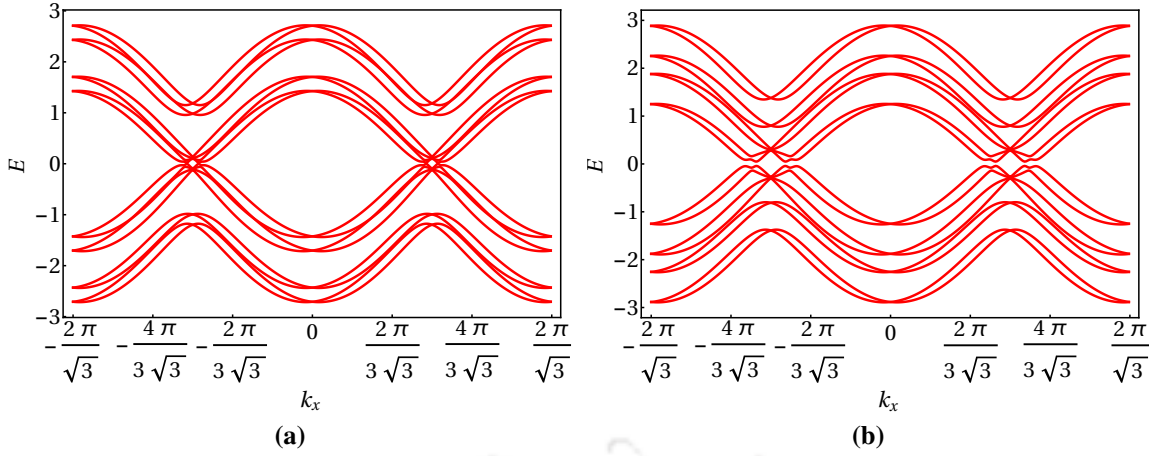


Figure 3.16. (color online) The band structure for two different values of bias voltage, V (a) $V = 0.1$ and (b) $V = 0.3$. Here, we set $t_{\perp} = 0.2$, $\lambda_{SO} = 0.1$ and $\lambda_R = 0.1$. We put $\lambda_R^{\perp} = 0$.

different values of V , namely $V = 0.03, 0.1$ and 0.3 (in units of t). For $N = \text{odd}$, the energy gap in the spectrum increases with increasing bias voltage and the spin degeneracy is lifted only around $k_x = \frac{\pi}{\sqrt{3}}$ (as shown in Fig. (3.15a-3.15c)). The intrinsic SOC alone cannot result in a spin-lifting spectrum which is observed from Fig. (3.11). The evolution of the *Mexican-hat* feature is also observed with increasing bias voltage. The scenario is very different for even values of N , for which, when V is small, an energy gap is noted with a small magnitude (see Fig. (3.15d)). The value of this energy gap is, however, less than that for $V = 0$. With a large value of V , namely, $V = 0.1$, the *Mexican-hat* type of feature starts developing with the closing of the gap, which eventually becomes more prominent at $V = 0.3$ with an energy gap opening at the Dirac points (see Fig. (3.15e) and Fig. (3.15f)). It can be seen that the band transforms from a parabolic nature to a *Mexican-hat* like nature with increasing the bias voltage.

We also investigate the effect of a non-zero bias voltage of V , that is, $V \neq 0$ with finite λ_{SO} and λ_R . Here we keep $\lambda_R^{\perp} = 0$. Without any bias voltage, the intrinsic SOC tends to open a gap in the bulk, whereas the Rashba SOC tends to close it. If we add a bias voltage, the gap increases with increasing of the bias voltage for a fixed λ_{SO} and λ_R (as shown in Fig. (3.16)). The particle-hole symmetry no longer exists and the spin degeneracy is lifted except at $k_x = 0$ and $k_x = \pi/\sqrt{3}$ due to the Rashba SOC. Intrinsic SOC destroys the *Mexican-hat* like feature and turns it into a parabolic one (not shown in fig), while the *Mexican-hat* feature resurfaces with the increasing bias voltage (as shown in Fig. (3.16)). We have checked the results with finite λ_R^{\perp} along with λ_{SO} and λ_R . However, no significant change is observed.

3.1.6.e Transport properties

The transport properties of a bilayer KM model can be affected by the presence of their edge states. The electron conductance can be calculated using Landauer-Büttiker formula [3, 73] as mentioned in Sec. (2.1). Also the spin polarized conductance is defined as [157],

$$G_\gamma^s = \frac{e^2}{h} \text{Tr} [\hat{\sigma}_\gamma \Gamma_R G^R \Gamma_L G^A], \quad (3.1.14)$$

where $\gamma = x, y, z$ and σ denote the Pauli matrices.

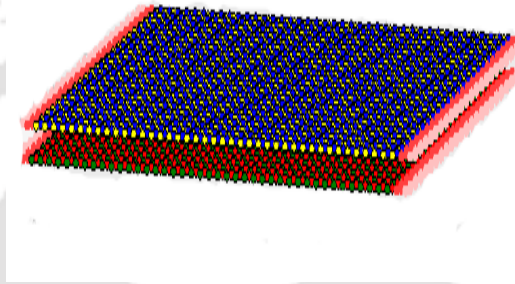


Figure 3.17. (color online) A schematic view of zigzag bilayer graphene sheet which consists of a central region, left and right semi-infinite leads (denoted by the red at the both end of the sample). In the central region, blue and yellow circles denote the A_2 and B_2 sublattices in the top layer, whereas red and green denotes A_1 and B_1 sublattices in the bottom layer.

We present our numerical results for the charge and the spin conductances using Eqs. (2.1.1) and (3.1.14). We have taken $L_x = 15$ and $L_y = 10$ for zigzag bilayer ribbon to calculate both the charge and spin conductances. We have computed the charge conductance of a

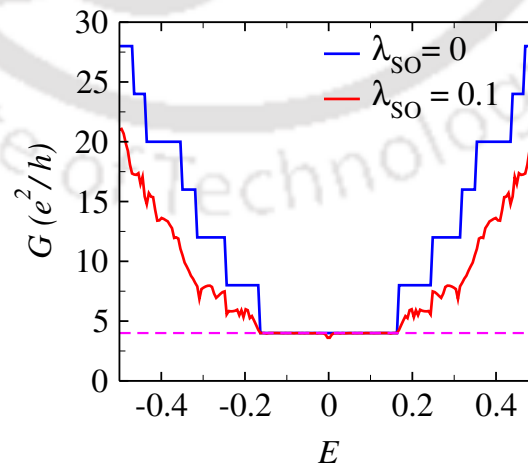


Figure 3.18. (color online) The charge conductance, G (in units of e^2/h) as a function of Fermi energy, E (in units of t) without intralayer intrinsic SOC (denoted the blue curve) and with intralayer intrinsic SOC for $\lambda_{SO} = 0.1$ (denoted the red curve). Here, we set $t_\perp = 0.2$.

bilayer graphene with and without intrinsic SOC as shown in Fig. (3.18). As compared to

the $\lambda_{SO} = 0$ (pristine bilayer graphene), we see that the conductance spectra record lesser magnitude at $E = 0.5$ for $\lambda_{SO} = 0.1$ (shown by the red curve). Although a plateau is roughly observed at $4e^2/h$ (shown by the pink dashed curve), there is an interruption by the presence of dips around the zero of the Fermi energy in the presence of intrinsic SOC. We have also

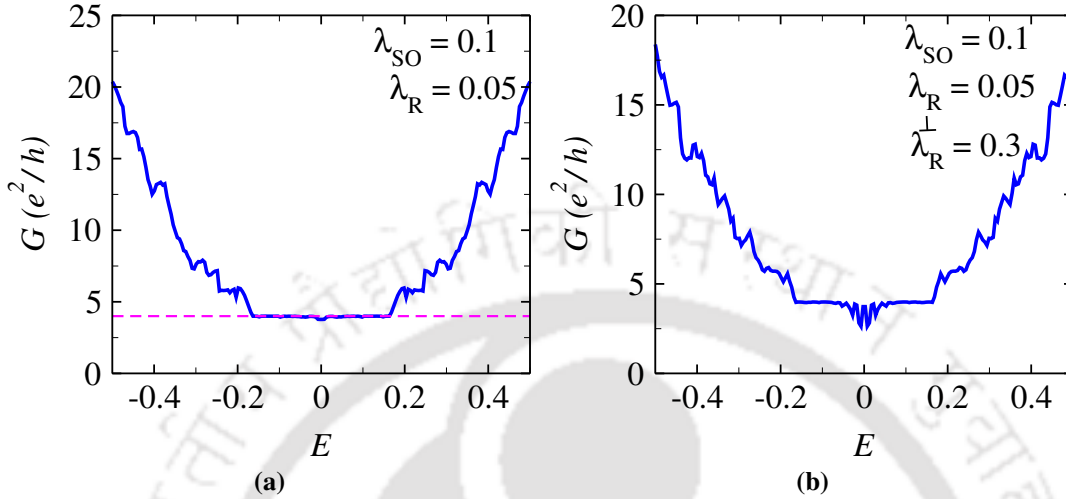


Figure 3.19. (color online) The charge conductance, G (in units of e^2/h) as a function of Fermi energy E (in units of t) for (a) $\lambda_R^\perp = 0$ (b) $\lambda_R^\perp = 0.3$. Here, we set $t_\perp = 0.2$, $\lambda_{SO} = 0.1$ and $\lambda_R = 0.05$.

computed the charge conductance in the presence of intralayer Rashba coupling and both intra and interlayer Rashba coupling as shown in Fig. (3.19a) and Fig. (3.19b) respectively. Fig. (3.19a) confirms the existence of the edge modes (as shown by the pink dashed line), whereas Fig. (3.19b) shows that the dip is quite sharp around zero Fermi energy and confirms the absence of the edge modes, thereby making the zero-bias conductance to vanish.

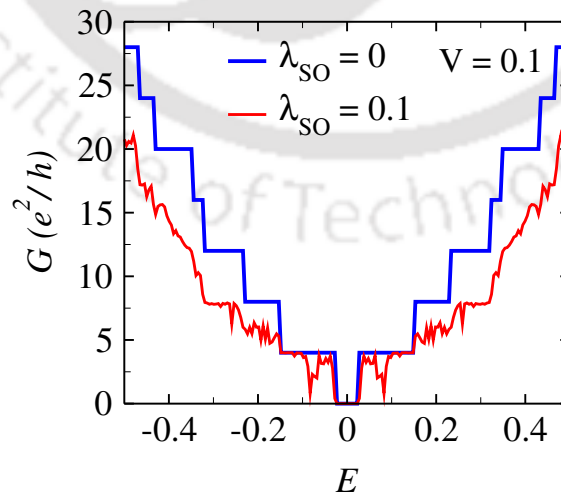


Figure 3.20. (color online) The charge conductance, G (in units of e^2/h) as a function of Fermi energy E (in units of t) for $\lambda_{SO} = 0$ (blue curve) and $\lambda_{SO} = 0.1$ (red curve). Here we set $t_\perp = 0.2$, $V = 0.1$.

To see the effect of a bias voltage on the conductance properties, we have included a

potential $+V$ on the top layer and $-V$ on the bottom layer as given in Eq. (3.1.9). Fig. (3.20) shows the behavior of the charge conductance as a function of the Fermi energy for a biased bilayer system where we have used $V = 0.1$. The blue and the red curves correspond to biased bilayer graphene in the absence and the presence of the intrinsic SOC, respectively. As compared to Fig. (3.18), the $4e^2/h$ plateau near the zero of the Fermi energy turns out to be zero for both the cases. The conductance steps still remain unaltered, but the width of the plateau becomes smaller (as shown in Fig. (3.20) by the blue and red curve). The value of the conductance becomes zero due to the opening of the gap between the valence band and conduction band.

We further investigated the spin-polarized transport in zigzag bilayer graphene. Spin-polarized conductance results due to the presence of Rashba SOC. It was also shown by Zhang *et al.* [158, 159] that the spin polarization components for x and z are zero for an ideal graphene nanoribbon because of the longitudinal mirror symmetry of an infinite system. The spin polarization component corresponding to the y -direction is finite and is found to be around 40% polarized for both the armchair and the zigzag nanoribbon [158]. However, for a bilayer graphene, we get finite values for all the components of spin polarization. This ensures larger net spin-polarized conductance than that of a single layer, and hence a bilayer graphene should be a more efficient candidate for spintronic applications.

All the three components of the spin polarization, namely, G_x^s , G_y^s and G_z^s are plotted as a function of the Fermi energy in Fig. (3.21a), (3.21b) and (3.21c) for three different values of λ_R , namely, 0.05, 0.08 and 0.1 with $\lambda_{SO} = \lambda_R^\perp = 0$. The magnitudes of the x and z components are one order smaller than that of the y component. It can be seen that the spin polarization vanishes in the low energy range and is anti-symmetric in nature around the zero of the Fermi energy for all the three components due to the electron-hole symmetry present in the Hamiltonian. The nature of the spin polarization for different values of λ_R qualitatively remains the same, but the magnitude gets larger as we increase the strength of the intralayer Rashba parameter, λ_R . In addition, we have included both the intralayer intrinsic SOC and the interlayer Rashba SOC in our model and have plotted the three components of the spin polarization for three different values of λ_R as a function of energy as shown in Fig. (3.21d), (3.21e) and (3.21f) corresponding to fixed values of the other SOC parameters, namely, $\lambda_{SO} = 0.1$, $\lambda_R^\perp = 0.3$. Though the magnitude of y component of the spin polarization gets smaller (as shown in Fig. (3.21e)), the magnitudes for the x and the z components grow larger (as shown in Fig. (3.21d) and Fig. (3.21f)) compared to a scenario where only intralayer Rashba SOC (λ_R) exists (Fig. (3.21a)-(3.21c)). Importantly, the spin polarization

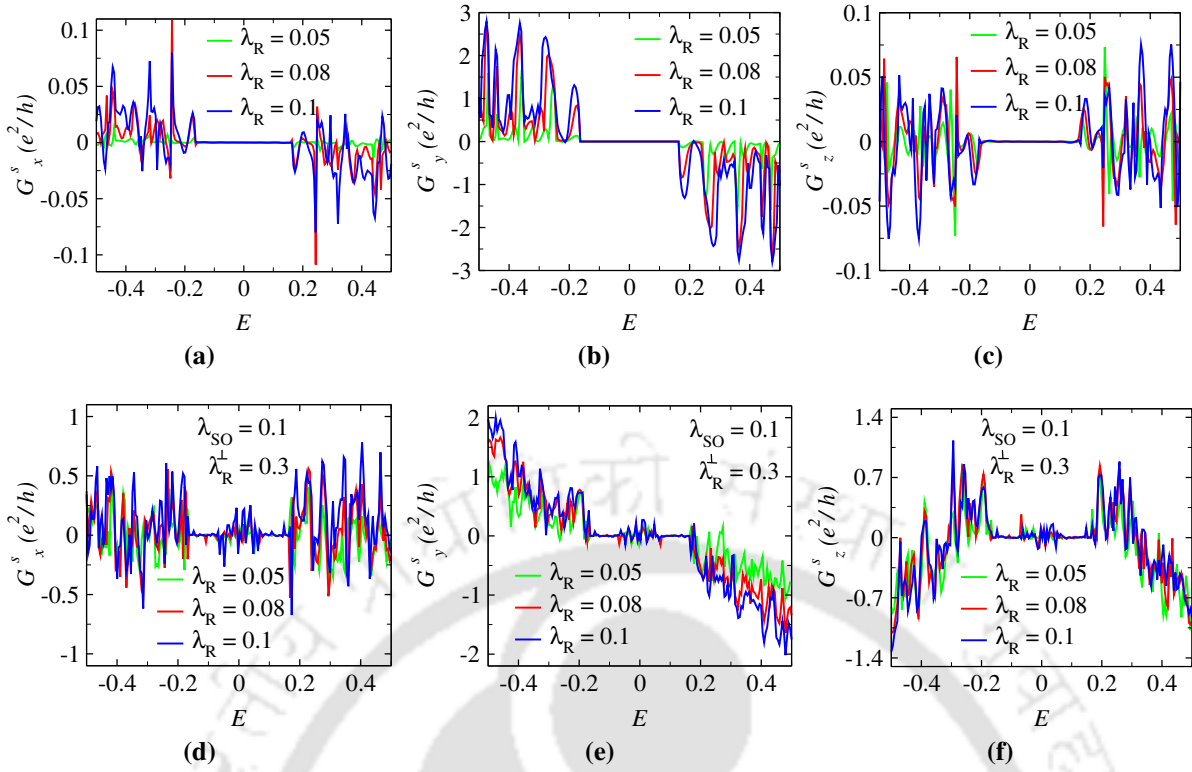


Figure 3.21. (color online) The spin polarized conductance, G_γ^s ($\gamma = x, y, z$) (in units of e^2/h) as a function of Fermi energy E (in units of t) for (a-c) $\lambda_R = 0.05, 0.08$ and 0.1 (Other parameters $t_\perp = 0.2$, $\lambda_{SO} = 0$ and $\lambda_R^\perp = 0$) and (d-f) $\lambda_R = 0.05, 0.08$ and 0.1 (Other parameters $t_\perp = 0.2$, $\lambda_{SO} = 0.1$ and $\lambda_R^\perp = 0.3$).

is finite for $E \approx 0$. The y component is anti-symmetric as a function of Fermi energy E , while the same does not hold for the x and the z components.

3.1.6.f Connection with experiments

In order to connect with the experimental data, we have computed the effective mass, m^* and investigated its variation with the intralayer Rashba SOC parameter, λ_R for a bilayer graphene. The definition of the effective mass and the group velocity can be given as, $m^* = \hbar^2 k / [dE(k)/dk]$ and $v_g = \frac{1}{\hbar} \frac{dE}{dk}$ (where k is the crystal momentum). Thus $m^* = \hbar k / v_g$ and hence depends upon the slope of the dispersion near the Dirac points. The measurement of effective mass m^* for a large range of carrier densities in a bilayer graphene was performed using Shubnikov-de Haas (SdH) oscillations [160]. From the first principles study, it was reported that the effective mass in bilayer graphene is approximately $0.022m_e$ (m_e being the bare mass) and also the value increases with the increase in number of layers [161]. Alternatively, the carrier transport properties in a bilayer graphene can also be tuned by the presence of Rashba SOC which could be enhanced by metal-atom adsorption or using an external gate voltage.

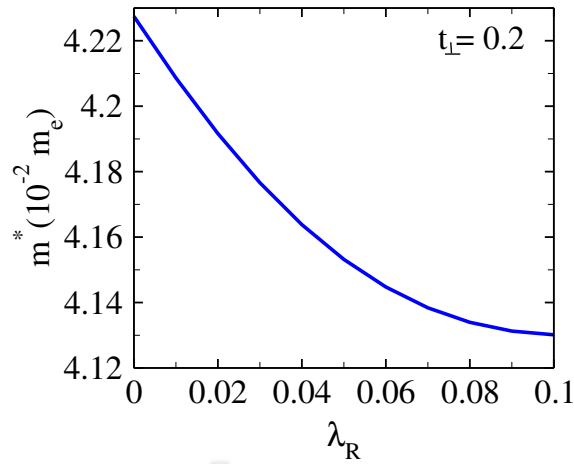


Figure 3.22. (color online) Effective mass, m^* as a function of intralayer Rashba SOC parameter, λ_R for zigzag bilayer graphene. Here, we set $t_{\perp} = 0.2$, λ_{SO} and λ_R^{\perp} both are zero.

In Fig. (3.22), we have calculated the effective mass as a function of the intralayer Rashba SOC parameter, λ_R for the lowest-lying energy band (closest to the Fermi level $E = 0$ and $N = 10$) in the vicinity of a Dirac point. We have considered the inplane hopping, $t = 2.7$ eV and the lattice constant, $a_0 = 2.46\text{\AA}$. The energies are measured in units of t . We have not incorporated any intrinsic SOC and interlayer Rashba coupling here. The effective mass is seen to decrease with the increase of the Rashba SOC. For $\lambda_R = 0$, we have obtained some overestimated value of effective mass ($0.043m_e$) which may be due to the artifact of the behavior of the band structure of bilayer graphene. Consequently, the electrons will have a larger group velocity for the corresponding band. As a result, the mobility of the electrons, which varies inversely with m^* ($\mu \sim |m^*|^{-3/2}$), increases [162].

3.2 Kane-Mele model in semi-Dirac system

To study the KM model in a semi-Dirac system, we consider a semi-Dirac sheet with zigzag edges consisting of two sublattices A and B and the nearest neighbors vectors in real space are chosen as, $\vec{\delta}_1 = (0, a)$; $\vec{\delta}_2 = \left(\frac{\sqrt{3}a}{2}, -\frac{a}{2}\right)$ and $\vec{\delta}_3 = \left(-\frac{\sqrt{3}a}{2}, -\frac{a}{2}\right)$, where $a \approx 1.42\text{\AA}$ is the distance between two consecutive carbon atoms. The KM Hamiltonian can be written as [15, 29],

$$H = -t \sum_{\langle ij \rangle \sigma} c_{i\sigma}^{\dagger} c_{j\sigma} + i\lambda_{SO} \sum_{\langle\langle ij \rangle\rangle \sigma \sigma'} v_{ij} c_{i\sigma}^{\dagger} s_{\sigma\sigma'}^z c_{j\sigma'} + i\lambda_R \sum_{\langle ij \rangle \sigma \sigma'} c_{i\sigma}^{\dagger} (\mathbf{s}_{\sigma\sigma'} \times \hat{\mathbf{d}}_{ij})_z c_{j\sigma'} \quad (3.2.1)$$

Here the nearest neighbor hopping amplitude in the first term, t may take t or t_2 value depending upon the direction of the hoppings between the A and B sublattices. The individual terms in the above Eq. (3.2.1) have already been mentioned earlier.

3.2.1 Edge states: Analytical expressions

Here we compute the analytical solutions for the edge states considering the tight-binding KM Hamiltonian as given in Eq. (3.2.1) in presence of intrinsic SOC and Rashba SOC. We consider a ribbon geometry with zigzag edges which is infinite along the x -direction and it has finite width along the y -direction as shown in Fig. (2.10) (see Chapter 2). Considering the hopping only between A to A sublattices for the next nearest neighbor, Eq. (3.2.1) in terms of (m, n) becomes (with $\lambda_R = 0$),

$$\begin{aligned}
H_{\text{TB}} + H_{\text{ISOC}} = & - \sum_{\langle mn \rangle} \left[t a_{\uparrow}^{\dagger}(m, n) b_{\uparrow}(m, n) + t_2 a_{\uparrow}^{\dagger}(m, n) b_{\uparrow}(m, n-1) + t a_{\uparrow}^{\dagger}(m, n) b_{\uparrow}(m-1, n) \right. \\
& + t a_{\downarrow}^{\dagger}(m, n) b_{\downarrow}(m, n) + t_2 a_{\downarrow}^{\dagger}(m, n) b_{\downarrow}(m, n-1) + t a_{\downarrow}^{\dagger}(m, n) b_{\downarrow}(m-1, n) \left. \right] + h.c. \\
& + i \lambda_{\text{SO}} \left[\sum_{\langle\langle mn \rangle\rangle} \left(a_{\uparrow}^{\dagger}(m, n) a_{\uparrow}(m, n-1) - a_{\downarrow}^{\dagger}(m, n) a_{\downarrow}(m, n-1) \right) \right. \\
& - \left(a_{\uparrow}^{\dagger}(m, n) a_{\uparrow}(m+1, n-1) - a_{\downarrow}^{\dagger}(m, n) a_{\downarrow}(m+1, n-1) \right) \\
& - \left(a_{\uparrow}^{\dagger}(m, n) a_{\uparrow}(m-1, n) - a_{\downarrow}^{\dagger}(m, n) a_{\downarrow}(m-1, n) \right) \\
& + \left(a_{\uparrow}^{\dagger}(m, n) a_{\uparrow}(m+1, n) - a_{\downarrow}^{\dagger}(m, n) a_{\downarrow}(m+1, n) \right) \\
& + \left(a_{\uparrow}^{\dagger}(m, n) a_{\uparrow}(m-1, n+1) - a_{\downarrow}^{\dagger}(m, n) a_{\downarrow}(m-1, n+1) \right) \\
& \left. - \left(a_{\uparrow}^{\dagger}(m, n) a_{\uparrow}(m, n+1) - a_{\downarrow}^{\dagger}(m, n) a_{\downarrow}(m, n+1) \right) \right] + h.c. . \quad (3.2.2)
\end{aligned}$$

Using the same method (as described in Sec. (3.1)), we get four eigenvalue equations for spin up and spin down corresponding to A and B sublattice points which are written as,

$$\begin{aligned}
E \alpha_{\uparrow}(k_x, n) = & - \left[2t \cos\left(\frac{\sqrt{3}k_x}{2}\right) \beta_{\uparrow}(k_x, n) + t_2 \beta_{\uparrow}(k_x, n-1) \right] \\
& - 2\lambda_{\text{SO}} \left[\sin(\sqrt{3}k_x) \alpha_{\uparrow}(k_x, n) - \sin\left(\frac{\sqrt{3}k_x}{2}\right) (\alpha_{\uparrow}(k_x, n-1) + \alpha_{\uparrow}(k_x, n+1)) \right], \\
E \alpha_{\downarrow}(k_x, n) = & - \left[2t \cos\left(\frac{\sqrt{3}k_x}{2}\right) \beta_{\downarrow}(k_x, n) + t_2 \beta_{\downarrow}(k_x, n-1) \right] \\
& + 2\lambda_{\text{SO}} \left[\sin(\sqrt{3}k_x) \alpha_{\downarrow}(k_x, n) - \sin\left(\frac{\sqrt{3}k_x}{2}\right) (\alpha_{\downarrow}(k_x, n-1) + \alpha_{\downarrow}(k_x, n+1)) \right], \\
E \beta_{\uparrow}(k_x, n) = & - \left[2t \cos\left(\frac{\sqrt{3}k_x}{2}\right) \alpha_{\uparrow}(k_x, n) + t_2 \alpha_{\uparrow}(k_x, n+1) \right] \\
& + 2\lambda_{\text{SO}} \left[\sin(\sqrt{3}k_x) \beta_{\uparrow}(k_x, n) - \sin\left(\frac{\sqrt{3}k_x}{2}\right) (\beta_{\uparrow}(k_x, n-1) + \beta_{\uparrow}(k_x, n+1)) \right], \\
E \beta_{\downarrow}(k_x, n) = & - \left[2t \cos\left(\frac{\sqrt{3}k_x}{2}\right) \alpha_{\downarrow}(k_x, n) + t_2 \alpha_{\downarrow}(k_x, n+1) \right]
\end{aligned}$$

$$-2\lambda_{SO} \left[\sin(\sqrt{3}k_x)\beta_{\downarrow}(k_x, n) - \sin\left(\frac{\sqrt{3}k_x}{2}\right)(\beta_{\downarrow}(k_x, n-1) + \beta_{\downarrow}(k_x, n+1)) \right], \quad (3.2.3)$$

where $\alpha_{\uparrow, \downarrow}$ and $\beta_{\uparrow, \downarrow}$ are the spin resolved coefficients for the A and B sublattices respectively.

Next, we calculate the eigenvalue equations for the edge states considering the Rashba SOC along with the intrinsic SOC. These equations which lead to the spin mixing are,

$$\begin{aligned} E\alpha_{\uparrow}(k_x, n) &= - \left[2t \cos\left(\frac{\sqrt{3}k_x}{2}\right)\beta_{\uparrow}(k_x, n) + t_2\beta_{\uparrow}(k_x, n-1) \right] \\ &\quad - 2\lambda_{SO} \left[\sin(\sqrt{3}k_x)\alpha_{\uparrow}(k_x, n) - \sin\left(\frac{\sqrt{3}k_x}{2}\right)(\alpha_{\uparrow}(k_x, n-1) + \alpha_{\uparrow}(k_x, n+1)) \right] \\ &\quad + i\lambda_R \left[\left(\cos\left(\frac{\sqrt{3}k_x}{2}\right) + \sqrt{3} \sin\left(\frac{\sqrt{3}k_x}{2}\right) \right) \beta_{\downarrow}(k_x, n) - \beta_{\downarrow}(k_x, n-1) \right], \\ E\alpha_{\downarrow}(k_x, n) &= - \left[2t \cos\left(\frac{\sqrt{3}k_x}{2}\right)\beta_{\downarrow}(k_x, n) + t_2\beta_{\downarrow}(k_x, n-1) \right] \\ &\quad + 2\lambda_{SO} \left[\sin(\sqrt{3}k_x)\alpha_{\downarrow}(k_x, n) - \sin\left(\frac{\sqrt{3}k_x}{2}\right)(\alpha_{\downarrow}(k_x, n-1) + \alpha_{\downarrow}(k_x, n+1)) \right] \\ &\quad + i\lambda_R \left[\left(\cos\left(\frac{\sqrt{3}k_x}{2}\right) - \sqrt{3} \sin\left(\frac{\sqrt{3}k_x}{2}\right) \right) \beta_{\uparrow}(k_x, n) - \beta_{\uparrow}(k_x, n-1) \right], \\ E\beta_{\uparrow}(k_x, n) &= - \left[2t \cos\left(\frac{\sqrt{3}k_x}{2}\right)\alpha_{\uparrow}(k_x, n) + t_2\alpha_{\uparrow}(k_x, n+1) \right] \\ &\quad + 2\lambda_{SO} \left[\sin(\sqrt{3}k_x)\beta_{\uparrow}(k_x, n) - \sin\left(\frac{\sqrt{3}k_x}{2}\right)(\beta_{\uparrow}(k_x, n-1) + \beta_{\uparrow}(k_x, n+1)) \right] \\ &\quad - i\lambda_R \left[\left(\cos\left(\frac{\sqrt{3}k_x}{2}\right) - \sqrt{3} \sin\left(\frac{\sqrt{3}k_x}{2}\right) \right) \alpha_{\downarrow}(k_x, n) - \alpha_{\downarrow}(k_x, n+1) \right], \\ E\beta_{\downarrow}(k_x, n) &= - \left[2t \cos\left(\frac{\sqrt{3}k_x}{2}\right)\alpha_{\downarrow}(k_x, n) + t_2\alpha_{\downarrow}(k_x, n+1) \right] \\ &\quad - 2\lambda_{SO} \left[\sin(\sqrt{3}k_x)\beta_{\downarrow}(k_x, n) - \sin\left(\frac{\sqrt{3}k_x}{2}\right)(\beta_{\downarrow}(k_x, n-1) + \beta_{\downarrow}(k_x, n+1)) \right] \\ &\quad - i\lambda_R \left[\left(\cos\left(\frac{\sqrt{3}k_x}{2}\right) + \sqrt{3} \sin\left(\frac{\sqrt{3}k_x}{2}\right) \right) \alpha_{\uparrow}(k_x, n) - \alpha_{\uparrow}(k_x, n+1) \right]. \quad (3.2.4) \end{aligned}$$

Similar to the Dirac one, we have used $k_x = \frac{\pi}{\sqrt{3}}$ for the numerical solutions. Also the boundary condition remains same, that is, $\alpha(k_x, n) = \beta(k_x, -1) = 0$ and again we consider $E = 0$.

3.2.2 Results and discussion

To solve the above equations (Eq. (3.2.3) and Eq. (3.2.4)), we have taken $N = 100$ unit cells in the y -direction. We have considered the intrinsic SOC and Rashba SOC parameter values as discussed in the sec. (3.1.2). We have set the tight-binding parameter, $t = 1$ and the lattice spacing, $a = 1$. All the energies are measured in units of t . The size of the semi-Dirac nanoribbon in numeric computation is taken as 201Z-94A ($L_x \sim 25$ nm and $L_y \sim 20$ nm) with zigzag edges.

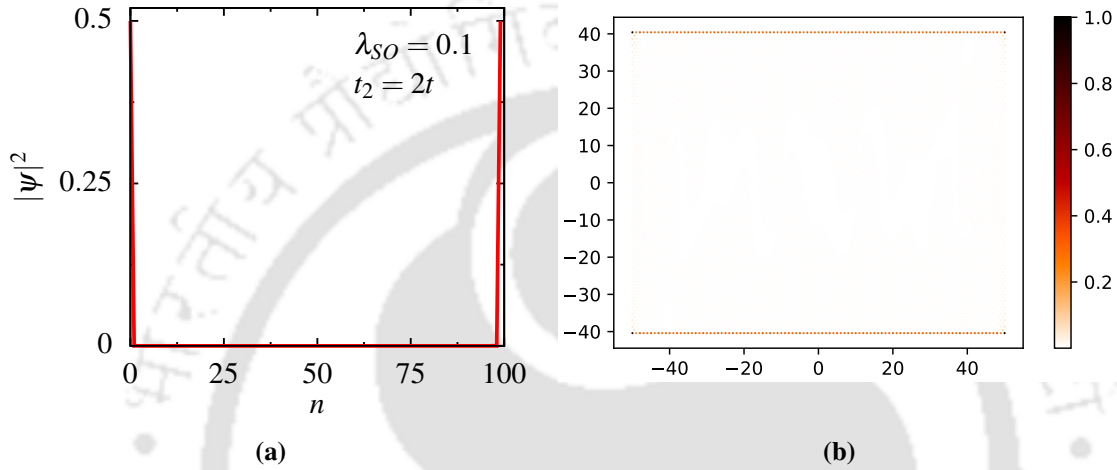


Figure 3.23. (color online) (a) Probability density, $|\psi|^2$ is plotted as a function of site index, n at $k_x = \frac{\pi}{\sqrt{3}}$ (b) the LDOS is plotted for a semi-Dirac nanoribbon. Here we put $\lambda_{SO} = 0.1$ and $\lambda_R = 0$.

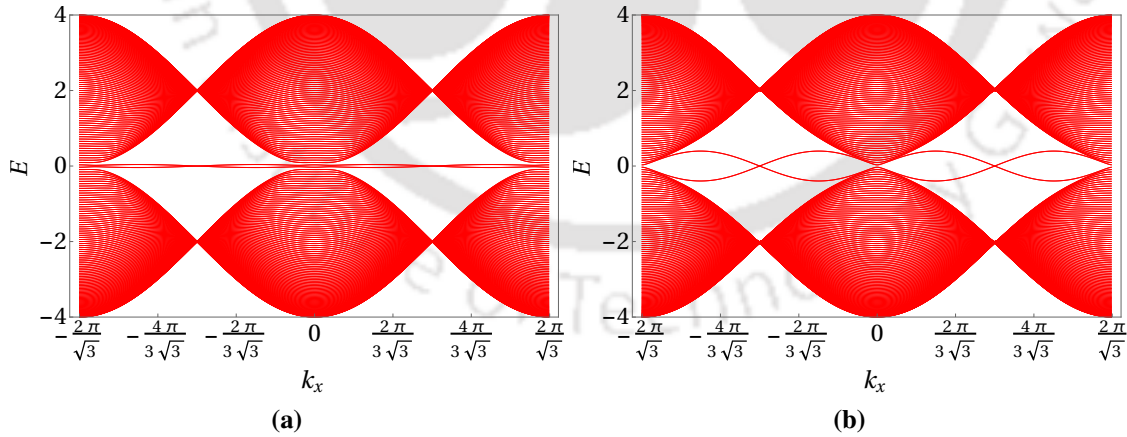


Figure 3.24. (color online) The band structure for a semi-Dirac nanoribbon in presence of intrinsic SOC with coupling strength, λ_{SO} (a) $\lambda_{SO} = 0.01$ and (b) $\lambda_{SO} = 0.1$. Here we put $\lambda_R = 0$.

3.2.3 Intrinsic SOC

We start with the case where the intrinsic SOC is considered in our model (Eq. (3.2.1)) and the Rashba SOC is initially turned off. Fig. (3.23a) shows the probability density, $|\psi|^2$ as a

function of site index, n in presence of an intrinsic SOC with coupling strength $\lambda_{SO} = 0.1$ for the semi-Dirac case ($t_2 = 2t$). The probability density has its maximum amplitude at the edges and it becomes immediately zero inwards the ribbon. To compare with the numerical one, we have also plotted the LDOS for the same coupling strength in Fig. (3.23b). The LDOS plot also shows the maximum electron density at the edges of the sample confirming the presence of edge states.

Next, we have plotted the electronic dispersion as a function of k_x for two different values of $\lambda_{SO} = 0.01$ and 0.1 in Figs. (3.24a) and (3.24b) respectively. The flat bands, as was observed in the tight binding band structure (Fig. (2.11d)), now become dispersive and there are crossing of two edge modes between the k_x value $\left[0 : \pm \frac{2\pi}{\sqrt{3}}\right]$ which becomes more prominent in Fig. (3.24b). Also a finite gap is observed at $k_x = 0$ for the both cases. These edge modes are completely separated from the bulk.

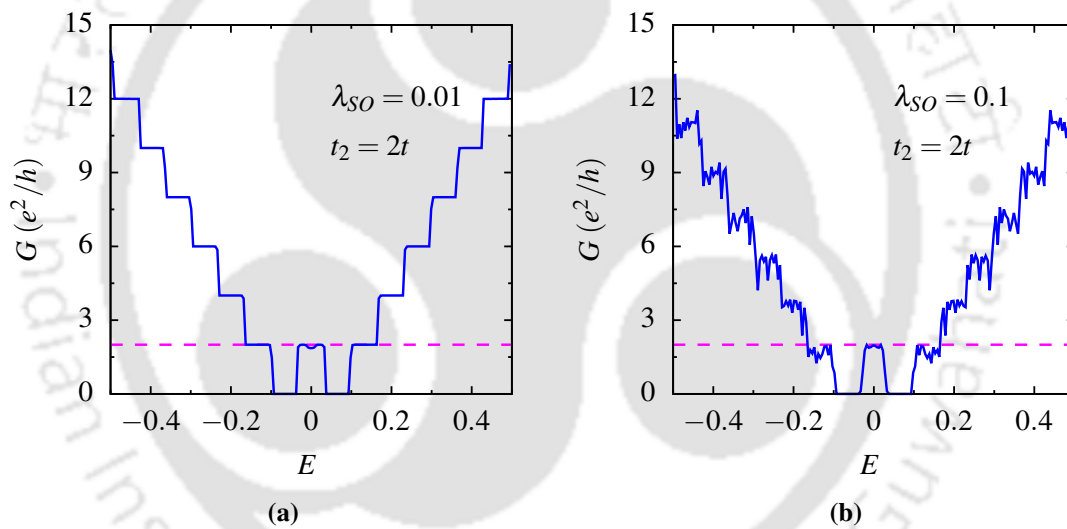


Figure 3.25. (color online) The charge conductance, G (in units of e^2/h) as a function of Fermi energy, E (in units of t) for (a) $\lambda_{SO} = 0.01$ and $\lambda_{SO} = 0.1$. Here we put $\lambda_R = 0$.

To see the conductance property, we have also plotted the charge conductance as a function of Fermi energy for $\lambda_{SO} = 0.01$ and 0.1 in Fig. (3.25a) and Fig. (3.25b). Although there is a change in the step behavior, the charge conductance shows a narrow $2e^2/h$ plateau for both the cases (as shown by the pink dashed line). The behavior of the plateau confirms that it is separated from the bulk even in the presence of intrinsic SOC.

3.2.4 Intrinsic and Rashba SOC

Next, we have considered the Rashba SOC in our model along with the intrinsic SOC. In Figs. (3.26a) and (3.26c), we have plotted the probability density as a function of site index

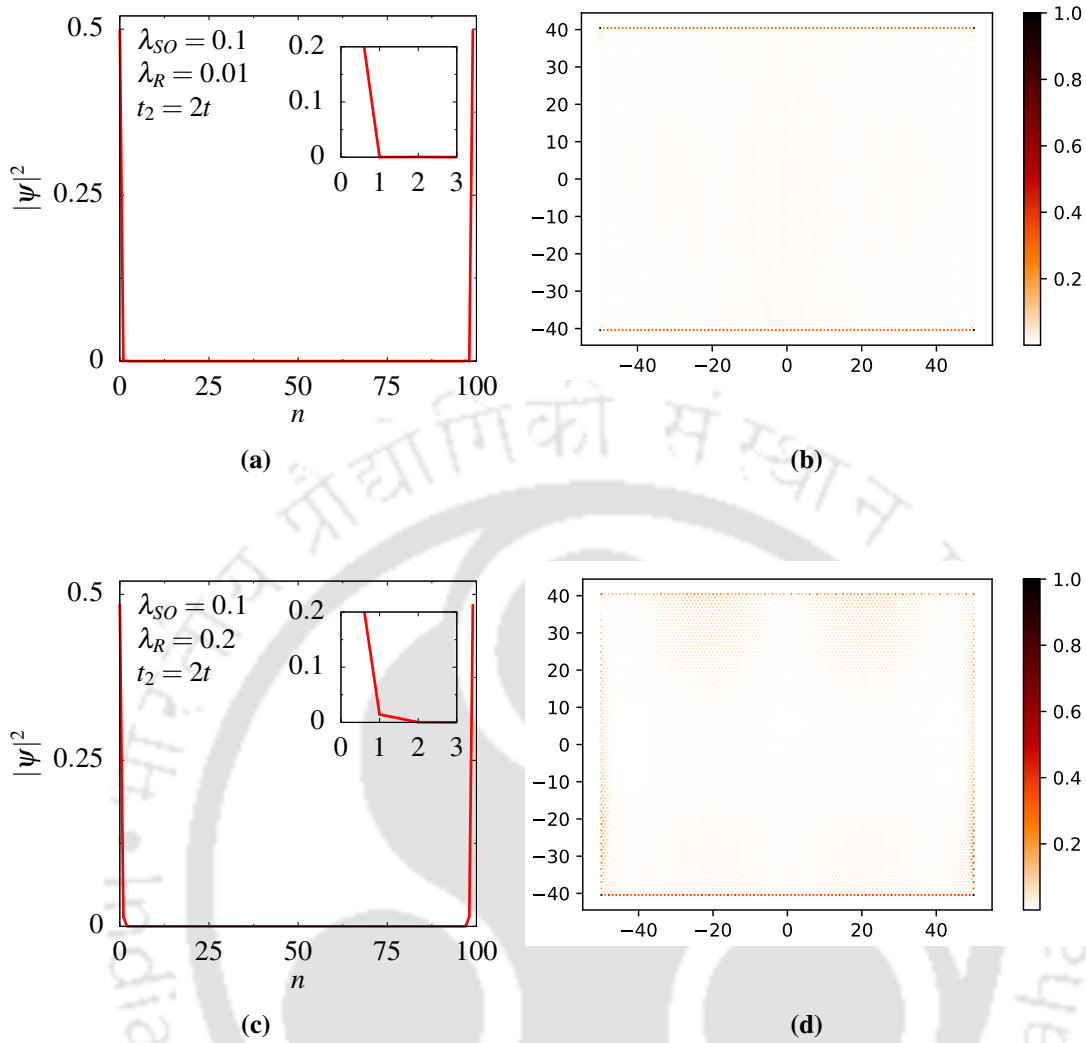


Figure 3.26. (color online) Probability density, $|\psi|^2$ is plotted as a function of site index, n at $k_x = \frac{\pi}{\sqrt{3}}$ for (a) $\lambda_R = 0.01$ and (c) $\lambda_R = 0.2$. The LDOS is plotted for (b) $\lambda_R = 0.01$ and (d) $\lambda_R = 0.2$ for a semi-Dirac nanoribbon. Here we fixed $\lambda_{SO} = 0.1$.

for two different values of Rashba SOC. For both the cases, we have considered a fixed intrinsic SOC, namely $\lambda_{SO} = 0.1$ and tuned the other SOC, that is, Rashba SOC, namely $\lambda_R = 0.01$ and 0.1 . For a small value of λ_R ($\lambda_R = 0.01$), the probability density shows the same behavior as observed from Fig. (3.23a). For a larger value of Rashba SOC ($\lambda_R = 0.2$), the penetration depth enhances upto sites with index $n = 2$. To confirm the presence of edge states, we have also shown the LDOS plot in Fig. (3.26b) and (3.26d). In Fig. (3.27a) and (3.27b), we have plotted the band structure in presence of both the SOC's. For a small value of λ_R ($\lambda_R = 0.01$), the band dispersion shows the crossing of the two edge modes per edge in the vicinity of $[0 : \pm \frac{2\pi}{\sqrt{3}}]$ and a finite bulk gap is present at $k_x = 0$ as seen from Fig. (3.27a). Now, as we increase the Rashba SOC (say, $\lambda_R = 0.2$), there is crossing of the edge modes even in the vicinity of $k_x = 0$ instead of a bulk gap (see Fig. (3.27b)). In addition, we have

observed the band splitting due to the presence of the Rashba SOC.

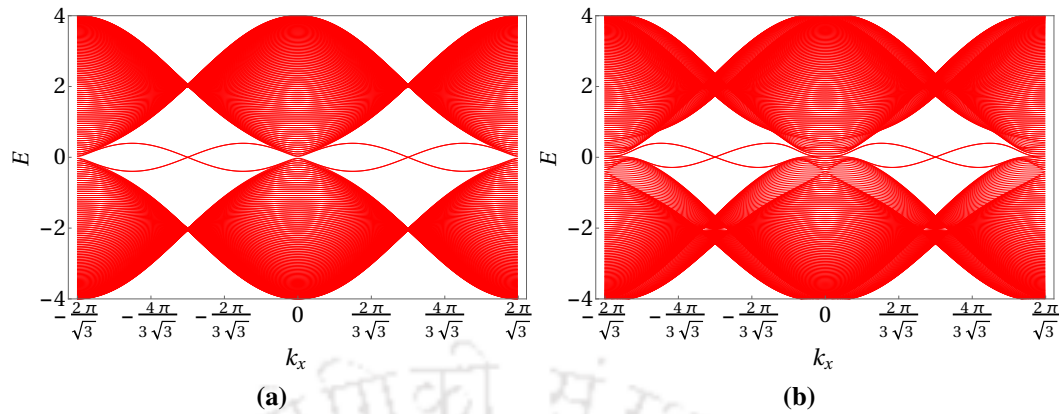


Figure 3.27. (color online) The band structure for a semi-Dirac nanoribbon in the presence of intrinsic and Rashba SOC with coupling strength (a) $\lambda_{SO} = 0.1$, $\lambda_R = 0.01$ and (b) $\lambda_{SO} = 0.1$, $\lambda_R = 0.2$.

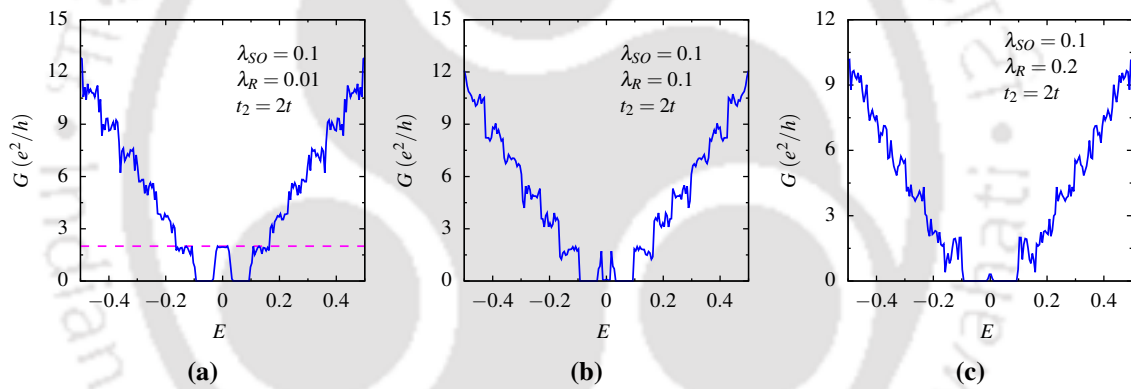


Figure 3.28. (color online) The charge conductance, G (in units of e^2/h) as a function of Fermi energy, E (in units of t) for (a) $\lambda_R = 0.01$, (b) $\lambda_R = 0.1$ and (c) $\lambda_R = 0.2$. Here we have fixed $\lambda_{SO} = 0.1$.

The conductance property is also observed via calculating the charge conductance. In Figs. (3.28a), (3.28b) and (3.28c), we have plotted the charge conductance, G as a function of Fermi energy, E for three different values of Rashba SOC, namely $\lambda_R = 0.01$, 0.1 and 0.2 . When $\lambda_{SO} = 0.1$ and $\lambda_R = 0.01$, the charge conductance shows similar behavior as observed from Fig. (3.25b). As we increase the value of λ_R , the quantized ($2e^2/h$) plateau vanishes and the charge conductance becomes zero for $\lambda_{SO} = \lambda_R = 0.1$ as seen from Fig. (3.28b). It is to be noted that the bulk mode is still separated from the edge modes. When we further increase the Rashba SOC (say, $\lambda_R = 0.2$), the conductance still remains zero with the vanishing plateau (see Fig. (3.28c)). This is owing to closing of the gap between the bulk and the edge modes or in other words, the edge modes disappear into the bulk.

3.3 Summary

In this chapter, we have analytically computed the expressions for the localized edge states in the presence of two kinds of SOCs via the KM model for the Dirac and the semi-Dirac nanoribbons. The analytic results are supported by LDOS obtained using Kwant. We consider the intrinsic SOC as well as the Rashba SOC and study the zero-energy edge modes, the band dispersion, and the charge conductance for each of these cases. For the Dirac case, the probability density of the wave function falls off sharply at both edges of the sample and becomes zero inside the bulk in the presence of intrinsic SOC, which also can be seen from the LDOS plots. The band structure plots show that bulk gaps open up at the Dirac points, and the edge modes cross each other. The charge conductance still acquires a quantized value same as that of pristine graphene with a vanishing step-like behavior. In presence of both the SOCs, we observed that crossing of the edge modes still exists in the system but depends on the strength of the coupling parameter. We show the existence of topologically protected edge states owing to the presence of parity and TRS of the Hamiltonian. Further, we derive analytical expressions for the edge modes for a bilayer KM model in the presence of intralayer intrinsic, intralayer and interlayer Rashba SOCs. We have solved the analytical expressions to capture the nature of the surface states in presence of both the SOCs for a bilayer Dirac system. An asymmetry in a finite-size ribbon is also observed in presence of intrinsic SOC, which is otherwise absent for pure tight-binding dispersion. This asymmetry is present both in the presence and the absence of a bias voltage that may be included in addition between the layers. With the inclusion of Rashba SOC, the band structure plots reveal that the QSH phase is destroyed in the presence of an interlayer Rashba SOC. Moreover, the charge conductance spectra show the emergence of a dip near the zero of the Fermi energy in presence of intralayer intrinsic, intra and interlayer Rashba SOCs. The interlayer Rashba SOC, along with the intralayer intrinsic SOC and intralayer Rashba SOC, seem to destroy the QSH phase. The QSH phase is identified by the presence of a conductance plateau in the vicinity of zero Fermi energy. The plateau is sensitive to the values of the SOC parameters. Studies on spin transport reveal bilayer graphene should be a positive input for spintronic applications. We have also computed the effective mass and have shown that it can be tuned by the inclusion of Rashba SOC. For the semi-Dirac case, we have shown the analytic expressions for the edge modes in presence of both the SOCs. We find that the edge modes are completely separated from the bulk modes in the presence of intrinsic SOC, similar to the tight-binding case. This feature is also provided by the charge conductance plot. With the

inclusion of Rashba SOC, the $2e^2/h$ plateau vanishes at some critical value when both the parameter values become equal, and the charge conductance eventually becomes zero. The same was also found to be true for higher values of Rashba SOC.





4 Hofstadter butterfly spectra and Landau levels for a semi-Dirac nanoribbon

Contents

4.1 Magnetic field: Peierls coupling	92
4.2 Hofstadter butterfly spectra in semi-Dirac and Dirac system	93
4.3 Landau levels	96
4.4 Summary	97

Over the years, the two-dimensional electron gas (2DEG) has promoted intense research interest owing to a completely new area of physics which includes the quantum Hall effect, the Hofstadter butterfly, etc. When a 2DEG is subjected to a magnetic field at very low temperatures, it shows quantized plateaus of Hall resistance [5]. Consequently, the energy spectrum of electrons changes from a continuous spectrum to discrete energy levels. The presence of a periodic potential has added excitement to the ongoing research. The 2D electron system shows a fractal structure when the flux passing per unit cell is plotted with respect to the single-particle energy spectrum in the presence of a magnetic field and periodic potential.

The Hamiltonian in presence of a magnetic field for free electrons can be written as,

$$\hat{H} = \frac{(\hat{\mathbf{P}} - e\mathbf{A})^2}{2m} \quad (4.0.1)$$

where $\hat{\mathbf{P}}$ is the momentum operator, e denotes the electronic charge, m being the mass of the electron and \mathbf{A} is the vector potential. Now the Schrödinger equation for this Hamiltonian can

be solved and the energy levels (called as Landau Levels (LLs)) of those electrons get quantized with a relevant length scale, known as the magnetic length, $l_B = \sqrt{\frac{\hbar}{eB}} \approx 25.7\text{nm}/\sqrt{B}$, where \hbar is the Planck's constant divided by 2π , e is the charge of electrons and B is the magnetic field (of the order of Tesla). The energy of the n^{th} LLs is $E_n = (n + 1/2)\hbar\omega_c$, where ω_c is the cyclotron frequency. On the other hand, the Hamiltonian in a periodic potential for electrons can be written as,

$$\hat{H} = \frac{\hat{\mathbf{P}}^2}{2m} + \hat{U}(\mathbf{r}), \quad (4.0.2)$$

where $U(\mathbf{r}) = U(\mathbf{r} + a)$ is the periodic potential with lattice periodicity a . Hence, in a periodic lattice geometry, the electrons are described by Bloch wavefunctions and the relevant length scale is expressed in terms of a lattice constant, a . In presence of magnetic field, the Bloch electrons obey the Hamiltonian,

$$\hat{H} = \frac{(\hat{\mathbf{p}} - e\mathbf{A})^2}{2m} + \hat{U}(\mathbf{r}). \quad (4.0.3)$$

Each Bloch band divides further into subbands gives rise to fractal spectra exactly when these two length scales, that is, a and l_B , become commensurate. This complex energy spectrum known as Hofstadter butterfly [163] arises from the delicate interplay between these two length scales associated with the two quantizing fields [7, 164] and this particular regime is called the Hofstadter regime.

This phenomenon was first predicted by D. Hofstadter in 1976, where he solved the Harper's equation [165]. Hofstadter showed that the single-particle Bloch bands split into q subbands (which are p -fold degenerate) for the commensurate field, corresponding to rational values of $\phi/\phi_0 = p/q$ (ϕ and ϕ_0 being the magnetic flux and the magnetic flux quantum, respectively) in a two-dimensional square lattice. p and q are co-prime integers. Consequently, one can observe a quasi-continuous distribution of incommensurate quantum states that form a self-similar recursive structure (butterfly-like). Schlösser *et al.*, have observed the existence of the Hofstadter spectrum in an artificial semiconductor superlattice [166] for the first time. Later on, many researchers took the initiative to realize the spectra in supercells such that the lattice constant is enlarged and becomes comparable with the magnetic length. Afterward, there are a few highlighted works that present the signature of the butterfly in such supercells [167, 168]. On the other hand, the cold atom systems offer different lattice geometries consisting of various types of particles and controllable interactions. Laser assisted tunneling [169, 170] was the first technique with cold atoms where one can generate

an artificial effective magnetic field controlling the phase of the Fourier decomposed Bloch waves. The second one was developed by the Zurich group [171, 172]. An optical lattice was created such that it can adiabatically change its geometry (for example, from triangle to dimer, dimer to honeycomb, and other lattice geometries).

As we have emphasized, in recent years, graphene has attracted more attention owing to the peculiar low energy electronic dispersion. The dispersion shows linear behavior at the two special points K_1 and K_2 in the BZ. The density of states also varies linearly near these points [34]. The presence of a magnetic field [75] in graphene and the study of transport properties have boosted further progress in research. In a conventional 2DEG (non-relativistic), the quantized LLs denote equidistant energy levels due to a simple harmonic oscillator like spectrum for the free electrons. In graphene, the electrons follow the relativistic dispersion law at low energies, which modifies the Landau quantization of the energy and the spacing between the levels. The largest energy gap is between the zero and the first LL, which allows one to observe the QH effect in graphene, even at room temperature. The LLs in graphene have been observed experimentally by measuring cyclotron resonances in infrared spectroscopy [173] and tunneling current in scanning tunneling spectroscopy [174]. The LLs follow a square root dependence on the magnetic field in graphene, which affects the Hofstadter butterfly of graphene. The deviation from the square-root dependencies in the LL spectrum for the semi-Dirac system has a consequence on the Hofstadter spectrum.

Topology also plays a role where the quantization of the Hall conductance $\sigma_{xy} = Ce^2/h$ in Hofstadter butterfly is determined by a topological quantum number C (also called as Chern number), computed as an integral of Bloch states over the BZ. In the presence of a magnetic field, 2D electron systems support topologically ordered states, in which the coexistence of an insulating bulk with conducting one-dimensional chiral edge states gives rise to the QH effect. The presence of the edge states contributes to the transport properties of a two-dimensional system where these localized states provide the current-carrying channels despite having a bulk gap. For a two-dimensional electron gas, the Hall conductance can be affected by the presence of edge states at the Fermi level [98]. Monolayer graphene with zigzag edges supports the dispersionless zero-energy edge states as described in earlier chapters, which is also true in the presence of a magnetic field. The peculiar dispersion is responsible for the appearance of the $n = 0$ LL around energy $E = 0$ in a magnetic field. In graphene QH effect has an edge mode at $E = 0$ that resides exactly at the $n = 0$ LL as protected by the chiral symmetry. The charge accumulation along zigzag edges only occurs for the $E = 0$ edge mode in the $n = 0$ LL.

In this chapter, we have explored the influence of a perpendicular magnetic field on the physical properties of a semi-Dirac system using a tight-binding Hamiltonian on a honeycomb lattice. We have studied the Hofstadter butterfly spectra and characteristics of the LL spectra for semi-Dirac and Dirac nanoribbons in the presence of an external magnetic field in order to show that the semi-Dirac system has quite distinct properties as compared to the Dirac systems.

It may be noted that the Dirac systems were discussed ahead of the semi-Dirac cases in the preceding chapters. From this chapter onwards (and also for the remaining), we shall give emphasis to the semi-Dirac system which is the main focus of our thesis.

4.1 Magnetic field: Peierls coupling

To include a magnetic field, we shall work with a semi-Dirac nanoribbon which is infinitely long along the x direction but has a finite width along the y direction. We apply a uniform magnetic field, $\mathbf{B} = B\hat{z}$ perpendicular to the plane of the ribbon. Owing to the presence of the vector potential \vec{A} , each tight-binding wavefunction picks up an extra phase term. We have chosen the Landau gauge as $\vec{A} = (-By, 0, 0)$ such that the translational invariance along the x -direction remains unaltered under the choice of the gauge. Hence, the momentum along the x -direction is conserved and can be taken as a good quantum number. We make k_x a dimensionless quantity by absorbing the lattice spacing a into the definition of k_x . The ribbon width is such that it has N unit cells along the y -axis (where the index n for the unit cells takes $\in 0, \dots, N-1$) as shown in Fig. (2.10) (see Chapter 2). The tight-binding Hamiltonian in the presence of magnetic field thus has the form,

$$H = - \sum_{\langle ij \rangle} (t_{ij} a_i^\dagger b_j + h.c.) \quad (4.1.1)$$

where a_i^\dagger (b_j) creates (annihilates) an electron on sublattice A (B). t_{ij} is the hopping amplitude between nearest neighbor sites, which obtain a phase due to the magnetic field by the Peierls substitution, namely, $t_{ij} = t \rightarrow te^{2i\pi\phi_{ij}}$ (here t denotes both t or t_2). ϕ_{ij} is the magnetic flux and is given by the line integral of the vector potential from a site i to a site j , namely, $\phi_{ij} = \frac{e}{h} \int_i^j \vec{A} \cdot d\vec{l}$. The flux is usually denoted in terms of the flux quantum $\phi_0 = h/e$ (h is Planck's constant and e is the magnitude of the electron charge). In the case of electrons on a lattice, the Peierls substitution, remains valid as long as the lattice spacing, a_0 is much smaller than the magnetic length l_B .

Thus the tight-binding Hamiltonian in presence of the perpendicular magnetic field can be written in terms of m and n (where m increases along the x -direction and n increases along the negative y -direction) (see Fig. (2.10)) [91],

$$H = - \sum_{\langle mn \rangle} \left[t e^{i\pi(\phi/\phi_0)n[(1+\alpha)/2]} a^\dagger(m,n)b(m,n) + t e^{-i\pi(\phi/\phi_0)n} a^\dagger(m,n)b(m-1,n-(1-\alpha)/2) \right. \\ \left. + t_2 e^{i\pi(\phi/\phi_0)n[(\alpha-1)/2]} a^\dagger(m,n)b(m,n-\alpha) + h.c. \right] \quad (4.1.2)$$

where the summation $\langle mn \rangle$ is over the nearest neighbors. $a^\dagger(m,n)$ and $b(m,n)$ denote the creation and annihilation operators at the (m,n) site, respectively. Eq. (4.1.2) for a zigzag semi-Dirac ribbon ($\alpha = 1$) reduces to

$$H = - \sum_{\langle mn \rangle} \left[t e^{i\pi(\phi/\phi_0)n} a^\dagger(m,n)b(m,n) + t e^{-i\pi(\phi/\phi_0)n} a^\dagger(m,n)b(m-1,n) \right. \\ \left. + t_2 a^\dagger(m,n)b(m,n-1) + h.c. \right]. \quad (4.1.3)$$

In the following, we solve the above equation (Eq. (4.1.3)) to observe the influence of the magnetic field on the fractal spectrum as well as the LL spectrum. The consequences of the different LLs properties for the Dirac and the semi-Dirac systems are described below.

4.2 Hofstadter butterfly spectra in semi-Dirac and Dirac system

We have numerically calculated the Hofstadter butterfly [175] for the number of unit cells to be $N = 100$. The butterfly is plotted for different values of the parameter, ϕ/ϕ_0 ranging from 0 to 1. In Fig. (4.1), we have shown the evolution of the fractal spectra in a zigzag ribbon geometry by tuning the parameter t_2 from $2t$ to t . We have taken two intermediate values of t_2 (namely $t_2 = 1.8t$ and $1.5t$) between $2t$ and t to study the evolution of the fractal structure as we move from the semi-Dirac to the Dirac limit. Fig. (4.1a) shows the fractal spectra plotted as a function of magnetic flux, ϕ/ϕ_0 for a semi-Dirac nanoribbon ($t_2 = 2t$). It can be seen clearly that there occurs opening of a central gap around the zero energy. Also, a flat band is observed exactly at zero energy. This butterfly pattern originates from the splitting of LL energies into many minibands. The energy gap gets smaller along with the two identical spectra that emerge from the conduction and the valence bands as t_2 is tuned. These are as well true corresponding to $t_2 = 1.8t$ and $t_2 = 1.5t$ as shown in Figs. (4.1b) and

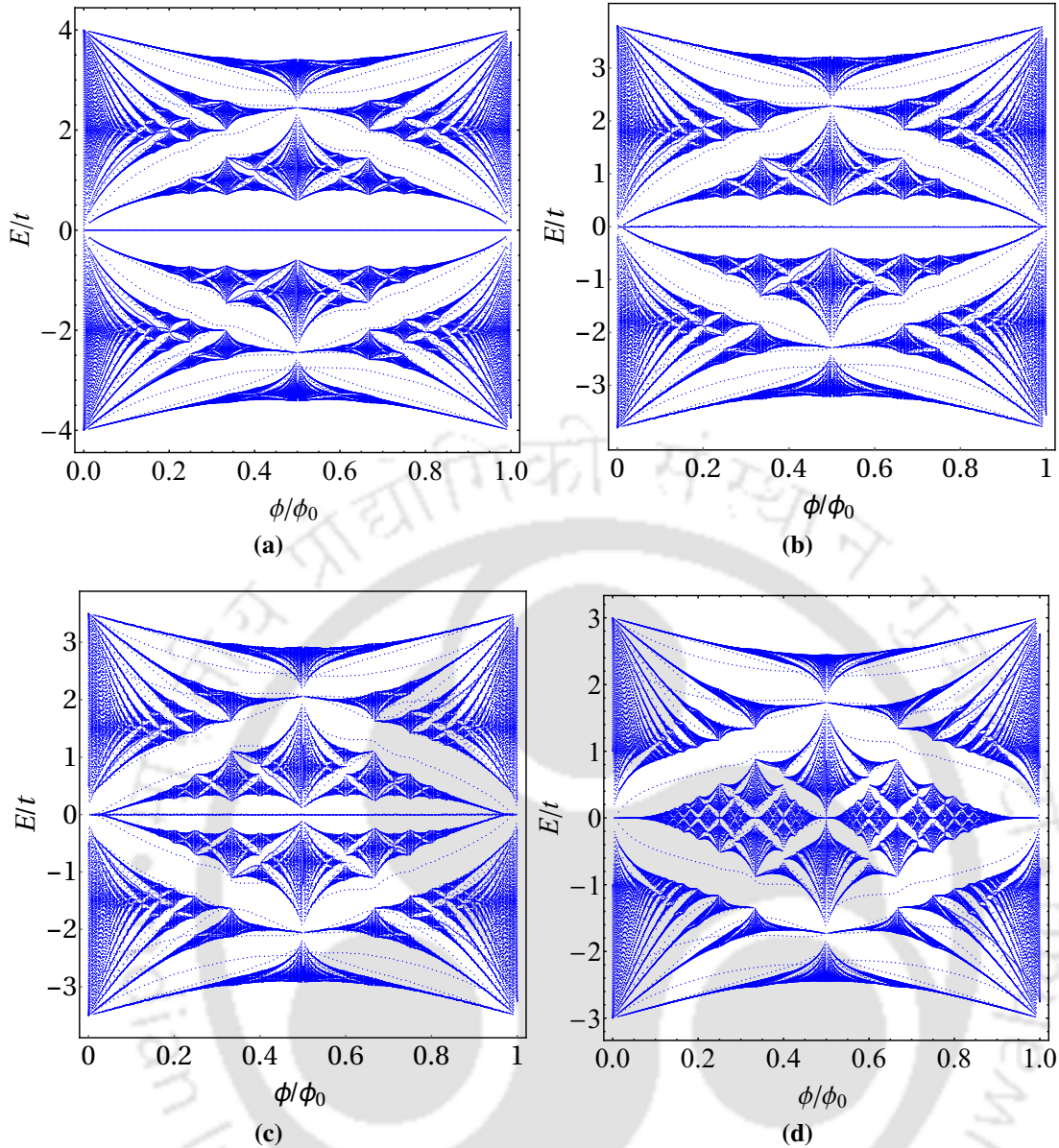


Figure 4.1. (Color online) Evolution of the Hofstadter butterfly spectrum is shown as a function of ϕ/ϕ_0 for (a) $t_2 = 2t$ (semi-Dirac), (b) $t_2 = 1.8t$, (c) $t_2 = 1.5t$ and (d) $t_2 = t$ (Dirac).

(4.1c) respectively. The zero-energy flat band still exists for both cases.

The same is also plotted for the Dirac system ($t_2 = t$) as shown in Fig. (4.1d). We can see that the gap completely closes around the zero energy with the flat band persisting for $t_2 = t$. The central LLs (around zero energy) have the characteristic of square-root behavior as a function of the magnetic field in graphene, whereas the upper and lower LLs at low values of the field, linearly vary with the magnetic field. The reason is obvious that the electrons far away from the zero energy no longer remain Dirac fermions. The Hall conductivity can be determined using the Hofstadter spectrum via the well-known Diophantine equation. However, we have not taken that route, and in the next chapter, we have calculated the Hall

conductivity using the Kubo formula.

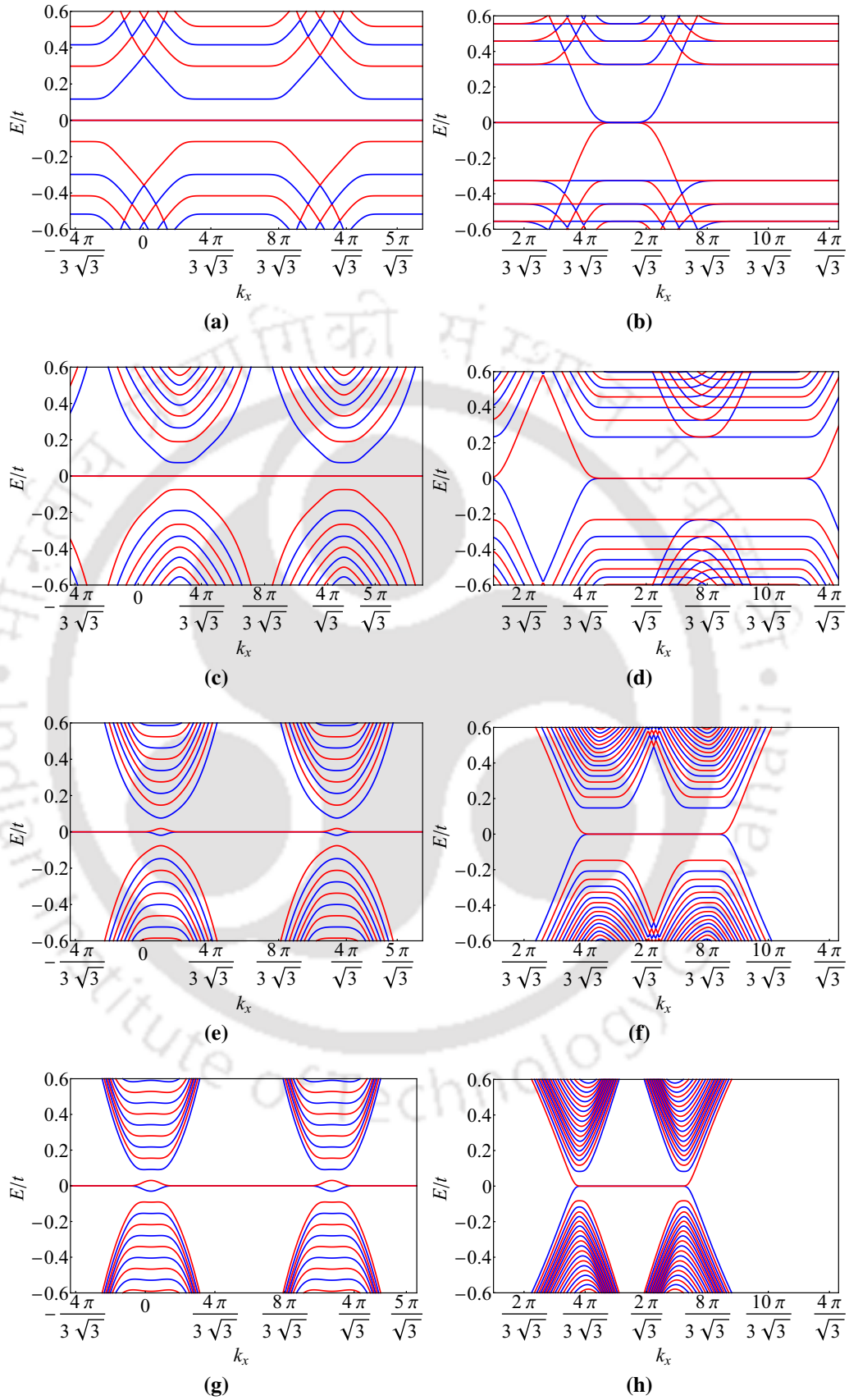


Figure 4.2. (Color online) Evolution of Landau levels for a finite strip with $N = 100$ unit cells in the presence of a magnetic flux (a and b) $\phi = \frac{\phi_0}{100}$, (c and d) $\frac{\phi_0}{200}$, (e and f) $\frac{\phi_0}{500}$ and (g and h) $\frac{\phi_0}{1600}$ is shown for $t_2 = 2t$ (semi-Dirac) in left panel and $t_2 = t$ (Dirac) in right panel.

4.3 Landau levels

Next, we have plotted the LLs spectra using a ribbon geometry in the presence of a magnetic field. Fig. (4.2) shows the LL spectra for different values of the magnetic flux (such as $\phi/\phi_0 = 1/100, 1/200, 1/500, 1/1600$) for the semi-Dirac and the Dirac systems with regard to the size of the ribbon, here we have chosen $N = 100$. Fig. (4.2a), (4.2c), (4.2e) and (4.2g) show the dispersion of the energy levels in presence of the magnetic field for a semi-Dirac nanoribbon ($t_2 = 2t$) as a function of the momentum in the x direction, namely k_x . For comparison, we have also plotted the LL spectrum for the Dirac case ($t_2 = t$) using the same values of the magnetic flux as shown in Fig. (4.2b), (4.2d), (4.2f) and (4.2h). It is to be noted that in a semi-Dirac system, there is no zero energy bulk state, which implies that the zero energy state in Fig. (4.2) is an edge state. On the other hand, zero energy bulk states exist in a Dirac system. Further, for $t_2 = 2t$, the LLs are not equidistant, since their energies vary as $(n + \frac{1}{2})^{2/3}$ (n being the LL index) [43] which lies intermediate to the behavior of the Dirac system and the conventional 2DEG. As a consequence, the gaps between the consecutive LLs shrink as one considers a larger value of n . In the case of a Dirac system, since the energies of the LLs vary as \sqrt{n} , its non-equidistant Landau spectra can have different quantitative behavior from that of a semi-Dirac system. For a large value of the flux, ϕ such as $\phi = \phi_0/100$, the flatness of the energy bands is observed for both the semi-Dirac and the Dirac systems owing to the shrinking of the cyclotron radius as shown in Figs. (4.2a) and (4.2b) respectively. For a different value of the magnetic flux $\phi = \phi_0/200$, the energy bands become parabolic as seen from Fig. (4.2c) for the semi-Dirac case. The flatness of the Landau spectrum in bulk completely vanishes in the semi-Dirac system as compared to a Dirac one (see Fig. (4.2d)). With lower values of ϕ/ϕ_0 , the LLs demonstrate a dispersive behavior and start getting flatter for large values of n for $t_2 = 2t$ (see Fig. (4.2e)). In the case of a Dirac system ($t_2 = t$), the LLs show quite a distinct behavior, where the flat bands become dispersive in the bulk corresponding to larger values of n and lower values of ϕ/ϕ_0 (see Fig. (4.2f)). For a small value of the magnetic field, such that the flux is given by, $\phi = \phi_0/1600$, the energy bands eventually become flat in bulk for the semi-Dirac case as shown in Fig. (4.2g). This is not the case for a Dirac system (see Fig. (4.2h)). For all values of ϕ/ϕ_0 , the zero-energy mode is completely separated from the bulk bands for a semi-Dirac system as compared to the Dirac case (see any of Fig. (4.2)).

4.4 Summary

In this work, we have studied the influence of a perpendicular magnetic field with a semi-Dirac dispersion within the framework of a tight-binding model of a honeycomb lattice. In order to compare and contrast with a prototype Dirac material, such as graphene, we have presented our results for both cases. We consider a semi-Dirac nanoribbon with finite width and study the Hofstadter butterfly and properties of the LL spectra. We have observed two identical gapped spectra symmetrically placed above and below $E = 0$ and along with a zero-energy mode in the Hofstadter butterfly spectrum in contrast to what is observed for a Dirac system. For the intermediate values, the gapped spectra are still observed with a flat band. For a semi-Dirac system, the absence of a zero-energy bulk state implies that the zero energy state is an edge state. On the other hand, zero energy bulk states exist in a Dirac system. The non-equidistant LLs are observed for both cases. The LL becomes fully dispersive in bulk for moderate values of the magnetic flux, which is not true for the Dirac case. For all values of the flux $\frac{\phi}{\phi_0}$, the zero-energy mode is completely separated from the bulk bands for a semi-Dirac system as compared to the Dirac case.



5 Quantum Hall studies of a semi-Dirac nanoribbon

Contents

5.1 Transport properties	100
5.1.1 Methodology	101
5.1.2 Numerical details	102
5.1.3 Density of states	102
5.1.4 Hall conductivity	104
5.1.5 Longitudinal conductivity	107
5.2 Summary	108

Graphene has attracted huge attention in the scientific community since its discovery, owing to its several unique properties. The behavior of electrons in graphene, exposed to a strong perpendicular magnetic field, played an important role not only for the discovery of room-temperature half-integer quantum Hall effect [76, 77, 176–178] but also for supporting the existence of massless Dirac particles [179]. The unconventional Hall conductivity was found to be quantized as $\sigma_{xy} = 4(n + 1/2)e^2/h$ [76, 179], where both the spin (2 for spin) and the valley (2 for valley) degeneracies are taken into account. Experimental measurements confirm that the LLs of a monolayer graphene obey the relation, $E_n = \text{sgn}(n) \sqrt{2\hbar v_F^2 e|n|B}$, where $v_F = 10^6$ m/s is the Fermi velocity, B is the magnetic field and n denote LL indices [180, 181]. In contrast to the observed LLs obtained in conventional 2DEGs where $E_n = \hbar\omega_c(n + 1/2)$, there is a distinctive new energy LL at $E = 0$, which is a consequence of the electron-hole symmetry in graphene. The zero energy LL, which is formed due to equal

contributions from the electron and the hole states, leads to a half-integer shift in the number of flux quanta needed to fill an integer number of LLs. Thus the well-known integer quantum Hall effect [5] observed in conventional 2D electron systems transforms into a relativistic half-integer (anomalous) quantum Hall effect in graphene.

The distinct LL behavior for the semi-Dirac dispersion leads to different quantization than a Dirac-like case. As told earlier, semi-Dirac dispersion has been observed in a few-layer black phosphorene by means of the in situ deposition of potassium atoms in experiments [182]. Recently, quite a few studies on LLs and transport properties in the presence of a magnetic field in phosphorene have been reported [183, 184]. More precisely, they have found that the anisotropic band structure that leads to Hall quantization in the presence of a perpendicular magnetic field is similar to that of a conventional 2DEG. Since phosphorene may be considered as a realistic material that possesses semi-Dirac properties, it is necessary to pursue QH studies on the semi-Dirac systems. As discussed above, the energy dispersion of phosphorene is similar to that of the semi-Dirac systems, and it is thus likely that other properties too show similar characteristics.

In this chapter, we have explored the transport properties in the presence of a magnetic field for a semi-Dirac system using a tight-binding Hamiltonian on a honeycomb lattice. We calculate the DOS via the tight-binding propagation method [185, 186], which is a sophisticated numerical tool used in large-scale calculations for any real system. We have implemented the recently developed real-space order- N quantum transport approach to calculate the Kubo conductivities as a function of the Fermi energy for moderate as well as very high values of the magnetic field [66]. The Hall conductivity in a semi-Dirac system shows the *standard* quantization, namely, $\sigma_{xy} \propto n$ as compared to the previously observed *anomalous* quantization, that is, $\sigma_{xy} \propto 2(n + 1/2)$ for a Dirac system. The degeneracy factor ‘2’ can be accounted for a spin. The longitudinal conductivities show highly anisotropic behavior in one direction compared to the other, which is obviously absent for Dirac systems.

5.1 Transport properties

To study the transport properties in the presence of a perpendicular magnetic field, we consider a large sample of a lattice model of the semi-Dirac system consisting of millions of atoms. The contribution in transport comes from both the off-diagonal and the diagonal terms as appear in the Kubo formula [70]. The former contributes to the Hall conductivity (σ_{xy}), whereas the latter leads to individual longitudinal conductivity in different directions

(σ_{xx} and σ_{yy}).

5.1.1 Methodology

In this section, we shall describe the numerical approach, developed by Garcia and his co-workers [66] which is based on a real-space implementation of the Kubo formalism, where both the diagonal and the off-diagonal conductivities are treated on the same footing. It is known that in the momentum space, the Hall conductivity can be easily obtained in terms of the Berry curvature associated with the bands [7]. The Kubo formalism can be implemented in real space for obtaining the Hall conductivity [66] which uses Chebyshev expansions to compute the conductivities. The components of the dc conductivity tensor ($\omega \rightarrow 0$ limit of the ac conductivity) for the non-interacting electrons are given by the Kubo-Bastin formula [70, 187] which can be written as [66, 188, 189],

$$\sigma_{\alpha\beta}(\mu, T) = \frac{ie^2\hbar}{A} \int_{-\infty}^{\infty} d\varepsilon f(\varepsilon) \text{Tr} \left\langle v_{\alpha} \delta(\varepsilon - H) v_{\beta} \frac{dG^{+}(\varepsilon)}{d\varepsilon} - v_{\alpha} \frac{dG^{-}(\varepsilon)}{d\varepsilon} v_{\beta} \delta(\varepsilon - H) \right\rangle \quad (5.1.1)$$

where T is the temperature, μ is the chemical potential, v_{α} is the α component of the velocity operator, A is the area of the sample, $f(\varepsilon)$ is the Fermi-Dirac distribution and $G^{\pm}(\varepsilon, H) = \frac{1}{\varepsilon - H \pm i\eta}$ are the advanced (+) and retarded (-) Green's functions. Using the KPM [64], the rescaled delta and Green's function can be expanded in terms of the Chebyshev polynomials, whence Eq. (5.1.1) becomes,

$$\sigma_{\alpha\beta}(\mu, T) = \frac{4e^2\hbar}{\pi A} \frac{4}{(\Delta E)^2} \int_{-1}^1 d\tilde{\varepsilon} \frac{f(\tilde{\varepsilon})}{(1 - \tilde{\varepsilon}^2)^2} \sum_{m,n} \Gamma_{nm}(\tilde{\varepsilon}) \mu_{nm}^{\alpha\beta}(\tilde{H}) \quad (5.1.2)$$

where ΔE is the range of the energy spectrum, $\tilde{\varepsilon}$ is the rescaled energy whose upper and lower bounds are +1 and -1 respectively and \tilde{H} is the rescaled Hamiltonian (see Chapter 1 for details). $\Gamma_{nm}(\tilde{\varepsilon})$ and $\mu_{nm}^{\alpha\beta}(\tilde{H})$ are the functions of the rescaled energy and the rescaled Hamiltonian respectively. The energy dependent scalar function, $\Gamma_{nm}(\tilde{\varepsilon})$ can be written as,

$$\Gamma_{nm}(\tilde{\varepsilon}) \equiv (\tilde{\varepsilon} - in \sqrt{1 - \tilde{\varepsilon}^2}) e^{in \arccos(\tilde{\varepsilon})} T_m(\tilde{\varepsilon}) + (\tilde{\varepsilon} + im \sqrt{1 - \tilde{\varepsilon}^2}) e^{-im \arccos(\tilde{\varepsilon})} T_n(\tilde{\varepsilon}) \quad (5.1.3)$$

and the Hamiltonian-dependent term which involves products of polynomial expansions can be written as,

$$\mu_{nm}^{\alpha\beta}(\tilde{H}) = \frac{g_m g_n}{(1 + \delta_{n0})(1 + \delta_{m0})} \text{Tr} [v_{\alpha} T_m(\tilde{H}) v_{\beta} T_n(\tilde{H})] \quad (5.1.4)$$

where the Chebyshev polynomials, $T_m(x)$ obey the recurrence relation (see Chapter 1 for a detailed discussion),

$$T_m(x) = 2xT_{m-1}(x) - T_{m-2}(x) \quad (5.1.5)$$

The Jackson kernel, g_m is used to smoothen out the Gibbs oscillations which arise due to the truncation of the expansion in Eq. (5.1.2) [64].

The DOS can be calculated using an efficient algorithm based on the evolution of the time-dependent Schrödinger equation. We use a random superposition of all basis states as an initial state $|\phi(0)\rangle$,

$$|\phi(0)\rangle = \sum_i a_i |i\rangle \quad (5.1.6)$$

where $|i\rangle$ denote the basis states and a_i are the normalized random complex numbers. Applying the Fourier transformation to the correlation function, $\langle \phi(0) | e^{-iHt} | \phi(0) \rangle$ we get the DOS as [185],

$$\text{DOS} = \frac{1}{2\pi} \int_{-\infty}^{\infty} e^{i\epsilon t} \langle \phi(0) | e^{-iHt} | \phi(0) \rangle dt \quad (5.1.7)$$

where t denotes time.

5.1.2 Numerical details

Using the above mentioned efficient numerical approach, we calculate the DOS in the absence and the presence of a magnetic field, the longitudinal conductivity in both x (σ_{xx}) and y (σ_{yy}) directions and the Hall conductivity (σ_{xy}) for the semi-Dirac system ($t_2 = 2t$). To compare between the Dirac and the semi-Dirac systems, we have also shown results for the Dirac ($t_2 = t$) case simultaneously. In our simulation, we consider a lattice of 5120 unit cells in each of the x and y directions (that is, a sample size denoted by (L_x, L_y) to be (5120, 5120)). We apply periodic boundary conditions for all our numerical results. We set the nearest-neighbor hopping parameter $t = 2.8\text{eV}$. We adopt a large number of Chebyshev moments, M , since the energy resolution of the KPM and the convergence of the peaks of σ_{xx} depend on M . We have used $M = 6144$ here [66]. The system size and the truncation order can be enhanced to reduce the fluctuations.

5.1.3 Density of states

To get a feel for the evolution of the single-particle properties between the Dirac and the semi-Dirac limits, we have plotted the DOS in the absence of a magnetic field for different

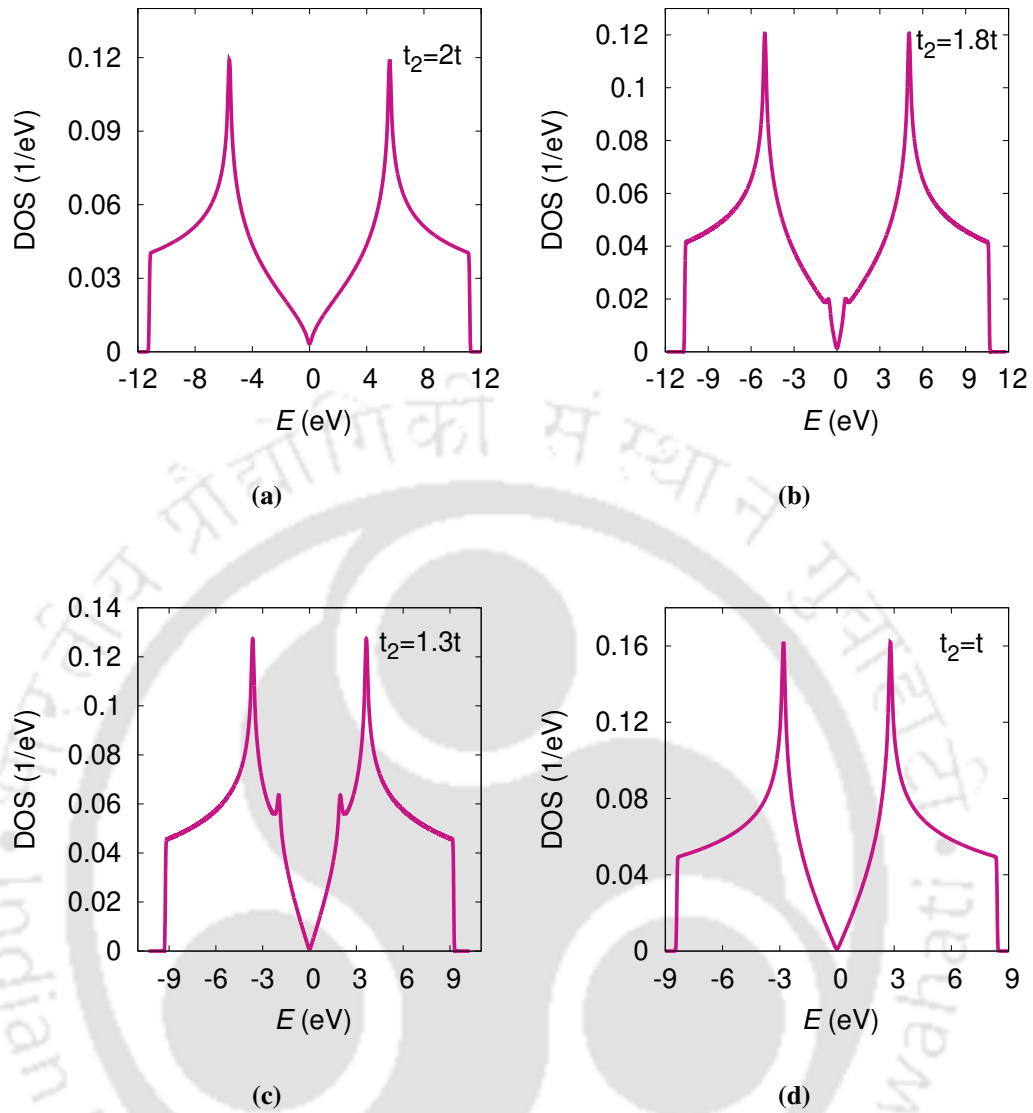


Figure 5.1. (Color online) Density of states (in units of $1/\text{eV}$) is plotted as a function of energy, E (in units of eV) for (a) $t_2 = 2t$ (semi-Dirac), (b) $t_2 = 1.8t$, (c) $t_2 = 1.3t$ and (d) $t_2 = t$ (Dirac). We put $t = 2.8\text{eV}$ in the calculation.

values of t_2 in Fig. (5.1). In the case of a semi-Dirac system ($t_2 = 2t$), the DOS is proportional to $\sqrt{|E|}$ near $E \simeq 0$ (see Fig. (5.1a)), while for the Dirac case ($t_2 = t$), again near the zero energy the DOS varies as $|E|$ as shown in Fig. (5.1d). The energy range for the semi-Dirac case gets enhanced as we go from Dirac to semi-Dirac. Thus apart from broadening the energy range in the semi-Dirac case, the low energy behavior is different in the Dirac and the semi-Dirac systems. It is well-known that a saddle point in the electronic band structure leads to a divergence in the density of states which is known as a Van Hove singularity (VHS). In the two intermediate values of t_2 , namely, $t_2 = 1.8t$ and $t_2 = 1.3t$ (as shown in Fig. (5.1b) and Fig. (5.1c)), a kink related to VHS is visible near $E = 0$ which disappears for both the

semi-Dirac and the Dirac cases.

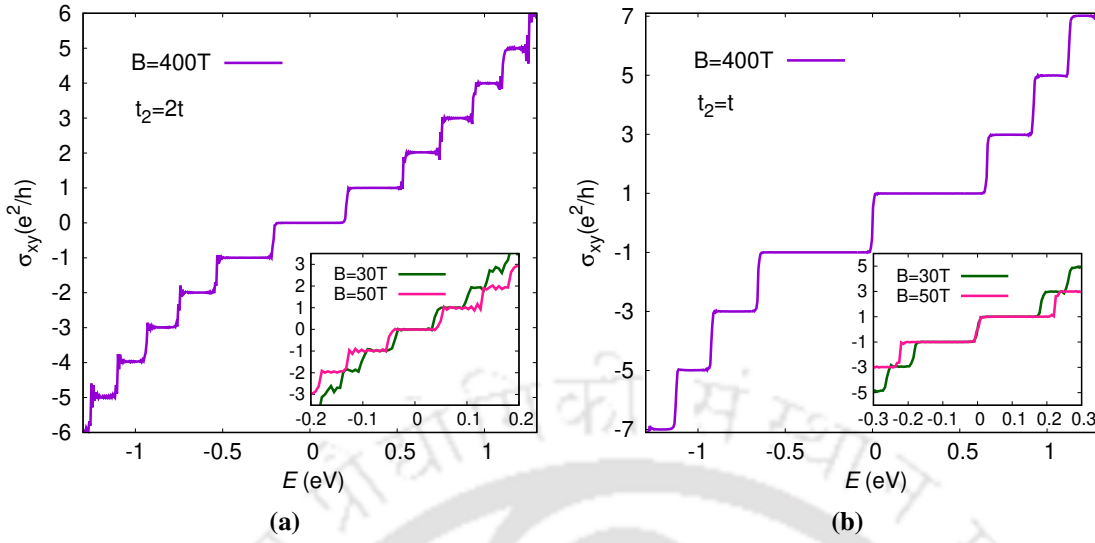


Figure 5.2. (Color online) Hall conductivity, σ_{xy} (in units of $2e^2/h$) is plotted as a function of Fermi energy, E (in units of eV) for (a) $t_2 = 2t$ (semi-Dirac) and (b) $t_2 = t$ (Dirac) for a very high field (400T) and two moderate fields namely, 30T and 50T. Here t is taken as 2.8eV.

5.1.4 Hall conductivity

In this subsection, we have shown the results for Hall conductivity (σ_{xy}) for moderate values of the magnetic field as well as extremely high fields in Fig. (5.2). Generally, higher values of the magnetic field require smaller system sizes, and hence a fewer number of Chebyshev moments are sufficient to be computed for realistic results. This yields faster convergence of the Hall conductivity in the limit of large magnetic fields. For $t_2 = 2t$ (semi-Dirac), the Hall conductivity (σ_{xy}) is plotted as a function of Fermi energy, E for the large value of the field $B = 400T$ (as shown in the main frame of Fig. (5.2a)). To relate this result to the recent experiments [87, 190, 191] performed for realistic values of magnetic field on a Dirac system, we have also plotted the Hall conductivity for moderate values of the field, namely 30T (green curve) and 50T (pink curve) as shown in the inset of Fig. (5.2a). The quantization of the plateaus is similar to that of a conventional 2DEG with a parabolic band dispersion in a sense that the conductance quantization happens at $\sigma_{xy} = ne^2/h$ where n takes integer values $0, \pm 1, \pm 2, \pm 3, \pm 4, \dots$ in units of e^2/h . The plot in the inset shows that the plateau step can be obtained with good accuracy, even in the case of realistic values of the magnetic field. The difference between the semi-Dirac and the Dirac cases lies in the fact that the fluctuations in the plateau step become prominent with lowering the strength of the field, especially at higher values of the Fermi energy. Further lowering of the magnetic field will

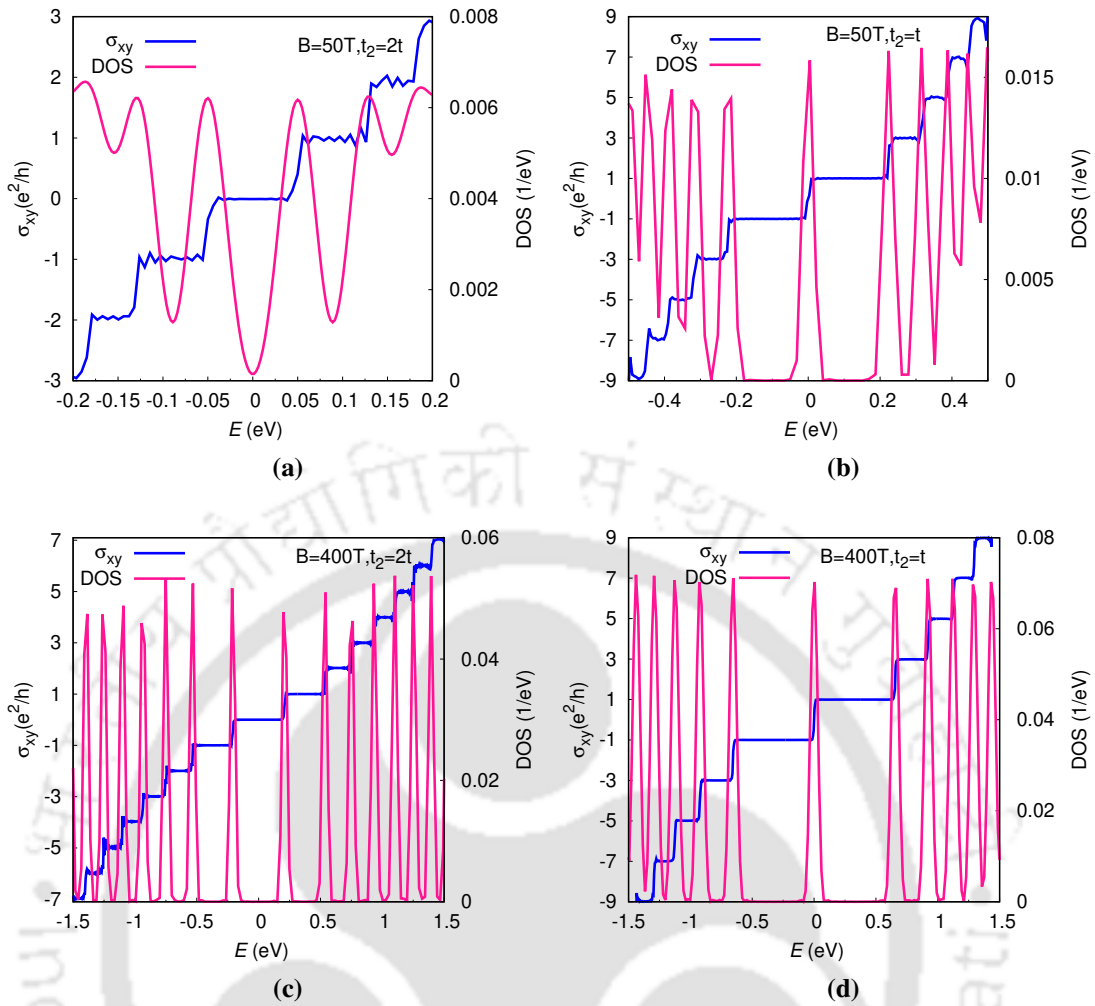


Figure 5.3. (Color online) Hall conductivity, σ_{xy} (in units of $2e^2/h$) and the DOS (in units of $1/eV$) is plotted as a function of Fermi energy, E (in units of eV) for different cases (a) $t_2 = 2t$, $B = 50T$ (b) $t_2 = t$, $B = 50T$ (c) $t_2 = 2t$, $B = 400T$ and (d) $t_2 = t$, $B = 400T$.

reduce the sharpness of the plateaus due to the effect of finite energy resolution and the finite size of the sample. These are the artifacts of the method used here. In the Dirac system ($t_2 = t$), the well-known Hall quantization at $\sigma_{xy} = (2n + 1)e^2/h$ is observed for very high magnetic field, namely $B = 400T$ as shown in the main frame of Fig. (5.2b). The degeneracy factor ‘2’ can be accounted for a spin. The inset shows the same for realistic values of the magnetic field. The Hall conductivity plot ensures that there is a transition from a half-integer to an integer quantum Hall effect as we go from a Dirac to a semi-Dirac system by tuning t_2 (Fig. (5.2a) and (5.2b)). The reason can be drawn from the fact that although the band dispersion in a semi-Dirac system is linear in one direction, the quadratic behavior in the other direction seemingly dominates over the linear term, which results in a similar characteristic of conductance quantization of a 2DEG.

In Fig. (5.3), we have shown the Hall conductivity, σ_{xy} and the DOS for $B = 50T$ and

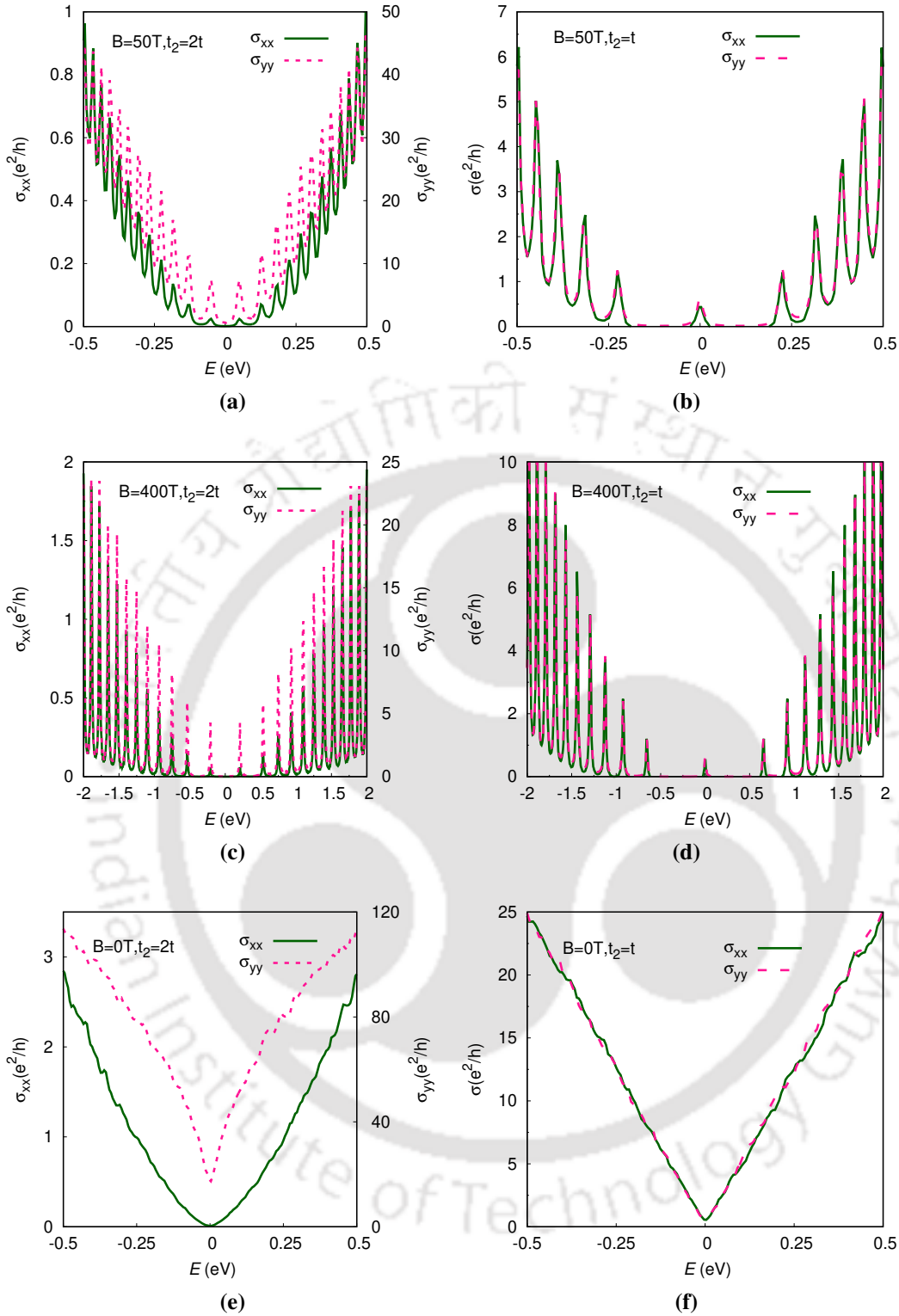


Figure 5.4. (Color online) Longitudinal conductivities, σ_{xx} and σ_{yy} (in units of $2e^2/h$) are plotted as a function of Fermi energy, E (in units of eV) for different cases (a) $t_2 = 2t$, $B = 50T$ (b) $t_2 = t$, $B = 50T$ (c) $t_2 = 2t$, $B = 400T$ (d) $t_2 = t$, $B = 400T$ (e) $t_2 = 2t$, $B = 0T$ and (f) $t_2 = t$, $B = 0T$.

400T in the same frame. In the presence of the magnetic field, the DOS consists of peaks of discrete energy levels (LLs) as shown in Fig. (5.3). The DOS vanishes in the plateau region and shows a sharp peak corresponding to a LL when the Hall conductivity goes through a

transition from one plateau to another. However, we get broad DOS peaks at lower values of the magnetic field ($B = 50\text{T}$) which is particularly visible for the semi-Dirac case owing to the small energy separation between the LLs (less than 3 meV). Sharper peaks will require the computation of a very large number of Chebyshev moments. Fig. (5.3a) shows that there is no LL peak at zero energy for $t_2 = 2t$ which is also characteristic of a conventional 2DEG in contrast to $t_2 = t$ case, where the zero-energy peak is well-observed (see Fig. 5.3b). The presence of a zero-energy peak for the Dirac case is related to the chiral anomaly present there. Figs. (5.3c) and (5.3d) show that several LLs can be observed with the same qualitative behavior for a very high magnetic field $B = 400\text{T}$ for both the semi-Dirac and the Dirac systems. The Hall conductance is quantized due to the quantized LL. It is interesting to note that although the energy does not depend linearly on the LL index, n and magnetic field, B in the case of a semi-Dirac system, as said earlier, the quantized value of σ_{xy} of a semi-Dirac material is analogous to that of a 2DEG. It is once again pertinent to mention that the LL spectra in phosphorene in a perpendicular magnetic field depending on the index, n (an additional factor of '2' will appear for spin degeneracy) have connections with the semi-Dirac physics [157, 184].

5.1.5 Longitudinal conductivity

To investigate the magneto-transport, we further calculate the longitudinal conductivities, that is σ_{xx} and σ_{yy} along the x and y directions. Figs. (5.4a) and (5.4b) show the longitudinal conductivity, σ_{xx} (green curve) and σ_{yy} (magenta curve) as a function of the Fermi energy, E for moderate values of the B field $B=50\text{T}$ for a semi-Dirac and a Dirac system respectively. The longitudinal conductivity reveals largely anisotropic behavior owing to the presence of anisotropy in the dispersion for $t_2 = 2t$. The component of σ in the x (σ_{xx}) and y (σ_{yy}) directions are quantitatively different in nature. The magnitude of σ_{yy} is larger than that of σ_{xx} . This is definitely a contrasting feature compared to the case of a Dirac system where the magnitudes of σ_{xx} and σ_{yy} are the same as shown in Fig. (5.4b). Moreover, the absence of a zero-energy peak also supports our discussion on the LL results (see Fig. (5.3c)) for the semi-Dirac material. Figures (5.4c) and (5.4d) show similar results for very high values of the magnetic field, namely, $B = 400\text{T}$ with the well-observed sharp peaks at larger values of energy. The amplitudes increase at large values of the Fermi energy owing to the increase in the scattering rate of the LLs as one goes to higher values of n for both the semi-Dirac and the Dirac systems. Since the LLs are not equidistant for both of these cases, the interval

between the peaks is not spaced equally. It can be seen that the longitudinal conductivity is non-vanishing only when the Fermi energy is within a Landau band where the backscattering processes are present.

To compare and contrast further between the two cases, we plot the longitudinal conductivities (σ_{xx} and σ_{yy}) in the absence of any magnetic field ($B = 0$) in Figs. (5.4e) and (5.4f) for the semi-Dirac and the Dirac systems respectively. Apart from the suppression of the conductivities by one order of magnitude by the magnetic field, one can take a note of the linear dependence of the conductivity on the Fermi energy, E for the Dirac case [179, 192], while they appear with different exponents for the semi-Dirac one. The feature is qualitatively the same as that observed for $B \neq 0$. However, the peaks in the conductance spectra vanish at $B = 0$ owing to the absence of LLs.

5.2 Summary

In this chapter, we have studied the magneto-transport properties for a semi-Dirac nanoribbon in the presence of a perpendicular magnetic field within the framework of a tight-binding model of a honeycomb lattice. For comparison, we have also discussed the result for a Dirac system, such as graphene. We have used the recently developed real space calculation based on the KPM method. We observed that the Hall conductivity shows standard quantization similar to that of a conventional semiconductor 2DEG with a parabolic band, which is highly contrasted with respect to a Dirac system. The zero LL peak is absent in the case of a semi-Dirac system. The longitudinal conductivities, σ_{xx} and σ_{yy} , show anisotropic behavior due to the distinct dispersion in two longitudinal directions. The linear dependence of the conductivity on the Fermi energy, E for the Dirac case turns into different exponents for the semi-Dirac one.

6 Magneto-optical properties of a semi-Dirac system in the near ultraviolet-visible frequency regime

Contents

6.1 Keldysh formalism	112
6.2 Results	115
6.2.1 Zero magnetic field	115
6.2.2 Magneto-transport	117
6.2.3 Electron filling	124
6.2.4 Circular polarization	125
6.2.5 Faraday rotation	127
6.3 Summary	128

Over the past few years, the discovery of graphene [33, 193] as well as other 2D materials, such as silicene [194], phosphorene [81, 195], MoS₂ [196–198], 8-pmmn borophene [199] etc. have enriched our knowledge on many of the experimental and theoretical aspects [83, 200, 201] of these materials owing to their low-energy physics being governed by massless Dirac particles. Also, a close variant of the 2D Dirac materials termed as the semi-Dirac materials that hold the unique band dispersion gives rise to many exciting phenomena. Several properties of the semi-Dirac system have been discussed in literature [43, 202] including the effect of the merging Dirac points on the emergence of a Chern insulating state [111], the presence of Chern insulating state including spin-orbit coupling [203], the

topological phase transition driven by disorder [204], the Floquet topological transition in graphene by an ac electric field [205], and the orbital susceptibility in dice lattice [206] etc.

Further, the behavior of the Dirac fermions in graphene has been studied in the presence of an external magnetic field, which facilitated the realization of half-integer quantum Hall effect at room temperature [75, 77]. When an external magnetic field B is applied perpendicularly to the plane of the sample, the energy spectrum transforms into discrete LLs and the level energies, E_n takes the form, $E_n \propto \sqrt{|n|B}$, where B is the magnetic field and n denotes LL indices [180, 181]. The dependence of the LL energy deviates from \sqrt{B} for semi-Dirac systems [43] and it varies as $((n + \frac{1}{2})B)^{2/3}$. Very recently, the study of LLs has been done extensively where the quantization of the conductance plateaus shows the integer quantum Hall effect for semi-Dirac system [207].

Usage of an optical probe for the Dirac materials has gathered momentum on a parallel ground in recent years. The vector potential of the incident photons couple to the band electrons via Peierls' coupling. The situation becomes more complicated in the presence of an external magnetic field where the kinetic energy of the carriers transforms into macroscopically degenerate LLs. The magneto-optical (MO) transport properties of these materials are gradually studied in the linear regime using the Kubo formula. However, evaluating the effects of deformation of the band structure on the transitions induced by optical means for the carriers from one LL to another is a harder task. In the following, we present a systematic exploration of the MO transport for a semi-Dirac system in the visible frequency range.

In the context of MO transitions, near ultraviolet-visible (UV-VIS) (energy of the order of a few eV) frequencies are extensively used in emerging fields such as spectroscopy, communication, and imaging [208, 209]. Many interesting MO phenomena, such as giant Faraday rotation [210], gate-tunable magneto-plasmons [211], non-linear transport driven by the light radiation [212] have been discovered with graphene exposed to radiation at the UV-VIS frequencies. At these particular frequencies, graphene supports the propagation of plasmon-polaritons [213–215] that can be tuned by the external gate voltage. Parallely, it helps for the basic studies of the interaction of radiation with the matter at nanoscale dimensions [216]. Here, we show the emergence of strong magneto-absorption in the UV-VIS regime where the absorption peaks are well-observed. Also, optical conductivity has always yielded very useful information on the electronic transitions in presence of a time-varying driving field. This facilitates observing frequency-dependent (ac) conductivity. The real part of the longitudinal MO conductivity gives information on the absorption properties as a function of photon energy, while the imaginary part contains the information about the transmis-

sion. In the case of the optical conductivity, a photon can induce a transition between these LLs, and the optical frequency matches with the energy level difference of the LLs [217] resulting in the absorption peaks. The characteristics of the band dispersion and the energy gap can be found from these absorption lines in the experiments [180, 218, 219]. In the presence of an external magnetic field, similar information emerges for the system, except that now the energy spectrum comprises LLs, as opposed to single-particle energies. MO properties of graphene have been studied both theoretically and experimentally and the result shows good agreement between the theoretical findings and the experiments [220, 221]. Also, MO properties of topological insulators [222] and other two-dimensional materials, such as MoS₂ [223] and silicene [224], phosphorene [225] have been studied. A recent study on the MO conductivity in three-dimensional materials has provided valuable information on quasicrystals, as well as on Dirac [132] and Weyl semimetals [226–228]. It is well known that the LL spacings are proportional to the magnetic field, B when a quadratic term in Hamiltonian is alone there (for example, a 2DEG), while the linear term alone yields spacings as the square root of B (for example, graphene) which are quite different. This has important implications for the optical absorption in a situation when both terms are present. Very few studies on optical conductivity in semi-Dirac materials have been done and hence the anisotropy in the spectra corresponding to the different planar directions (x and y) remain largely unexplored [229–231]. Very recently, the MO properties of a semi-Dirac system have been studied [232]. A detailed and systematic study is indeed needed on the MO transport properties of the semi-Dirac materials to enhance our understanding of these systems.

In this chapter, we study the MO conductivity in a perpendicular magnetic field of a semi-Dirac system using a tight-binding Hamiltonian on a honeycomb lattice. We use a numerical tool based on the Keldysh formalism for large-scale calculations for any realistic system [74]. First, we study the optical conductivity in the absence of a magnetic field of a semi-Dirac nanoribbon. To include a magnetic field, we shall apply a perpendicular magnetic field and look for the possible optical transitions that occur between the LLs by absorption of photons. We further calculate the longitudinal MO as well as the (MO) Hall conductivities as a function of the photon energy for moderate as well as very high values of the magnetic field in the UV-VIS regime [233]. We also explore the effects of the carrier concentration of the LLs on the optical spectra by varying the chemical potential. Further, we report the MO conductivity for a different polarization of the incident light, such as circularly polarized radiation. Moreover, we study the effects of Faraday rotation for the semi-Dirac as well as the Dirac systems. The Faraday rotation occurs in an active MO medium where the plane

of polarization of the transmitted radiation is rotated with respect to that of the incident radiation. The effect is characterized by the angle by which the plane of polarization is rotated and is called the Faraday angle [210,234,235] which we compute for the semi-Dirac and the Dirac cases.

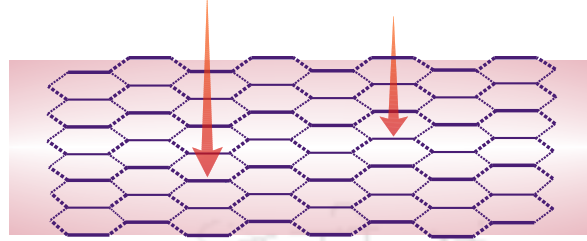


Figure 6.1. (Color online) A schematic diagram of hexagonal ribbon geometry of a semi-Dirac system irradiated by light is shown. The incident photon energies are of the order of a few eV.

6.1 Keldysh formalism

To obtain the MO conductivity we use a general perturbation method, known as the Keldysh formalism [236], which describes the quantum mechanical time evolution of non-equilibrium and even interacting systems at finite temperatures. A few relevant quantities that we needed are the time-ordered (T), anti-time-ordered (\tilde{T}), lesser ($G^<$) and greater ($G^>$) Green's functions which are defined as,

$$\begin{aligned}
 iG_{ab}^T(t, t') &= \left\langle T [c_a(t) c_b^\dagger(t')] \right\rangle \\
 iG_{ab}^<(t, t') &= - \left\langle c_b^\dagger(t') c_a(t) \right\rangle \\
 iG_{ab}^>(t, t') &= \left\langle c_a(t) c_b^\dagger(t') \right\rangle \\
 iG_{ab}^{\tilde{T}}(t, t') &= \left\langle \tilde{T} [c_a(t) c_b^\dagger(t')] \right\rangle.
 \end{aligned} \tag{6.1.1}$$

The time-ordering operator and the anti-time-ordering operator are denoted by T and \tilde{T} . The creation and the annihilation operators are in the Heisenberg picture and the labels a and b denote the indices for the single-particle states. The retarded and the advanced Green's functions can be written with the combination of the Green's functions in Eq. (6.1.1) as,

$$G^R = G^T - G^< \tag{6.1.2}$$

$$G^A = -G^{\tilde{T}} + G^<. \quad (6.1.3)$$

The tight-binding Hamiltonian can be expressed as,

$$H_0 = \sum_{\mathbf{R}_i, \mathbf{R}_j} \sum_{\sigma_1, \sigma_2} t_{\sigma_1 \sigma_2}(\mathbf{R}_i, \mathbf{R}_j) c_{\sigma_1}^\dagger(\mathbf{R}_i) c_{\sigma_2}(\mathbf{R}_j), \quad (6.1.4)$$

where the operator $c_{\sigma_1}^\dagger(\mathbf{R}_i)$ creates an electron in the carbon atoms at lattice site \mathbf{R}_i , whereas $c_{\sigma_2}(\mathbf{R}_j)$ annihilates an electron at lattice site \mathbf{R}_j with t as connecting the nearest neighbors. We have performed all our numerical calculations by using $t = 2.8$ eV which corresponds to electron hopping in graphene. In a 2D Dirac system, this value may be different. The σ_1 and σ_2 are the orbitals degrees of freedom. The electromagnetic field can be introduced through Peierls' substitution as,

$$t_{\sigma_1 \sigma_2}(\mathbf{R}_i, \mathbf{R}_j) \rightarrow e^{\frac{-ie}{\hbar} \int_{\mathbf{R}_j}^{\mathbf{R}_i} \mathbf{A}(\mathbf{r}', t) \cdot d\mathbf{r}'} t_{\sigma_1 \sigma_2}(\mathbf{R}_i, \mathbf{R}_j). \quad (6.1.5)$$

The following vector potential can be used to introduce both a static magnetic field and a uniform electric field,

$$\mathbf{A}(\mathbf{r}, t) = \mathbf{A}_1(\mathbf{r}) + \mathbf{A}_2(t). \quad (6.1.6)$$

The electric and magnetic fields are obtained via $\mathbf{E}(t) = -\partial_t \mathbf{A}_2(t)$ and $\mathbf{B}(r) = \nabla \times \mathbf{A}_1(r)$. Accordingly, $t_{\sigma_1 \sigma_2}(\mathbf{R}_i, \mathbf{R}_j)$ gets modified by the introduction of the magnetic field only. The many-particle time-dependent Hamiltonian can be described by

$$H(t) = H_0 + H_{ext}(t), \quad (6.1.7)$$

where H_0 is an unperturbed Hamiltonian and $H_{ext}(t)$ is the time-dependent external perturbation. The exponential in Eq. (6.1.5) can be expanded, which results in an infinite series of operators for the full Hamiltonian, $H(t)$ as,

$$H(t) = H_0 + eA^\alpha(t)\hat{h}^\alpha + \frac{1}{2!}e^2A^\alpha(t)A^\beta(t)\hat{h}^{\alpha\beta} + \dots. \quad (6.1.8)$$

From the above equation, we can write the $H_{ext}(t)$ as,

$$H_{ext}(t) = eA^\alpha(t)\hat{h}^\alpha + \frac{1}{2!}e^2A^\alpha(t)A^\beta(t)\hat{h}^{\alpha\beta} + \dots. \quad (6.1.9)$$

Now, we are defining $V(t) = (i\hbar)^{-1}H_{ext}$ and $A(t) = \int_{-\infty}^{\infty} \frac{d\omega}{2\pi} \tilde{A}(\omega)e^{-i\omega t}$. After a Fourier transform we get (dropping the spatial dependence),

$$\tilde{V}(\omega) = \frac{e}{i\hbar} \hat{h}^\alpha \tilde{A}^\alpha(\omega) + \frac{e^2}{i\hbar} \frac{\hat{h}^{\alpha\beta}}{2!} \int \frac{d\omega'}{2\pi} \int \frac{d\omega''}{2\pi} \times \tilde{A}^\alpha(\omega') \tilde{A}^\beta(\omega'') 2\pi \delta(\omega' + \omega'' - \omega) + \dots, \quad (6.1.10)$$

where $\hat{h}^\alpha = \frac{1}{i\hbar} [r^\alpha, H]$ and $\hat{h}^{\alpha\beta} = \frac{1}{(i\hbar)^2} [r^\alpha, [r^\beta, H]]$. Now we define in a general sense,

$$\hat{h}^{\alpha_1 \dots \alpha_n} = \frac{1}{(i\hbar)^n} [\hat{r}^{\alpha_1}, \dots, [\hat{r}^{\alpha_n}, H]], \quad (6.1.11)$$

where \hat{h}^α is the single-particle velocity operator at the first-order, and \hat{r} is the position operator. In the presence of periodic boundary conditions, the position operator is ill-defined, but its commutator with the Hamiltonian continues to be a well-defined quantity. In the real space, this commutator yields the matrix element of the Hamiltonian connecting the two sites i and j multiplied by the distance vector, \mathbf{d}_{ij} between them. \mathbf{d}_{ij} will be a well defined quantity in case of a periodic boundary condition if we define this quantity as the distance between the neighbors, instead of the difference between the two positions. Hence, \hat{h} operators can be defined in position space by multiplying the Hamiltonian matrix elements with the required product of the difference vectors. The current operator can be calculated from the Hamiltonian, via $\hat{J}^\alpha = -\frac{1}{\Omega} \left(\frac{\partial H}{\partial A^\alpha} \right)$ (where Ω denotes the volume of the sample). \hat{J}^α also follows a series expansion due to the presence of an infinite number of $A(t)$ terms in presence of an external perturbation, namely,

$$\hat{J}^\alpha(t) = -\frac{e}{\Omega} \left(\hat{h}^\alpha + e \hat{h}^{\alpha\beta} A^\beta(t) + \frac{e^2}{2!} \hat{h}^{\alpha\beta\gamma} A^\beta(t) A^\gamma(t) + \dots \right), \quad (6.1.12)$$

and the first-order optical conductivity is found to be [74],

$$\sigma^{\alpha\beta}(\omega) = \frac{ie^2}{\Omega\omega} \int_{-\infty}^{\infty} d\epsilon f(\epsilon) \text{Tr} \left[\hat{h}^{\alpha\beta} \delta(\epsilon - H_0) + \frac{1}{\hbar} \hat{h}^\alpha g^R(\epsilon/\hbar + \omega) \hat{h}^\beta \delta(\epsilon - H_0) + \frac{1}{\hbar} \hat{h}^\alpha \delta(\epsilon - H_0) \hat{h}^\beta g^A(\epsilon/\hbar - \omega) \right]. \quad (6.1.13)$$

The retarded and the advanced Green's functions, Dirac deltas and the generalized velocity operators are written in the position basis which are expanded in a truncated series of Chebyshev polynomials [237] (See appendix A).

6.2 Results

We have taken a ribbon of size 6144×6144 , that is, the number of unit cells in each of the x and y directions is 6144. We further use periodic boundary conditions in our calculations. The modified hopping parameter t_2 may take values t and $2t$. The convergence of the peaks depends on the number of Chebyshev moments, M . For reasonable accuracy, we choose a large number of Chebyshev moments, $M = 4096$ [66]. The value of the magnetic field B is taken 400T for all the purposes. It may be noted that the value of B chosen here is very high, however, computations with a lower B demands a larger size of the nanoribbon. Thus a compromise is made between the system size and value of B for keeping our computations numerically feasible. Nevertheless, in some situations, we have used more moderate values of B , namely $B = 100\text{T}$. We have also checked that the value of M used by us serves our purpose. However, the system size and the number of the Chebyshev moments can further be enhanced in order to minimize the fluctuations and to achieve greater accuracy.

6.2.1 Zero magnetic field

In this subsection, we study the optical conductivity of a semi-Dirac material ($t_2 = 2t$) in the absence of a magnetic field for a fixed value of the chemical potential. Here, we have taken $\mu = 0.4$ eV. However, we also vary the chemical potential and see its effect later. To compare the results with that of the Dirac systems, we simultaneously show results corresponding to $t_2 = t$.

Let us look at the longitudinal conductivities, namely, σ_{xx} and σ_{yy} . In Fig. (6.2a)-(6.2d), we have shown the real and imaginary part of σ_{xx} and σ_{yy} as a function of the incident photon energy for the semi-Dirac ($t_2 = 2t$) systems (denoted by the green dotted line). The corresponding scenario for the Dirac system is included for comparisons with a solid line (denoted by the dark-pink color). Both the real and the imaginary parts contain the zero-frequency Drude peak at $\mu = 0.4$ eV. The real part of σ_{xx} shows a sharp absorption peak at $\omega = 2t_2$ (where $t_2 = t = 2.8\text{eV}$ for Dirac) for the Dirac system, whereas a peak with lesser magnitude at $\omega = 2t_2$ (where $t_2 = 2t = 5.6\text{eV}$ for semi-Dirac) over a broad frequency range is observed for the semi-Dirac one. The Dirac case ($t_2 = t$) of course fails to distinguish between the real part of σ_{xx} and σ_{yy} as shown in Fig. (6.2a) and (6.2b) (this is also true for the imaginary part of σ_{xx} and σ_{yy}). Since the symmetry of the Dirac cone changes when the particle hopping is different along one direction of the lattice (here it is $t_2 = 2t$), the absorption

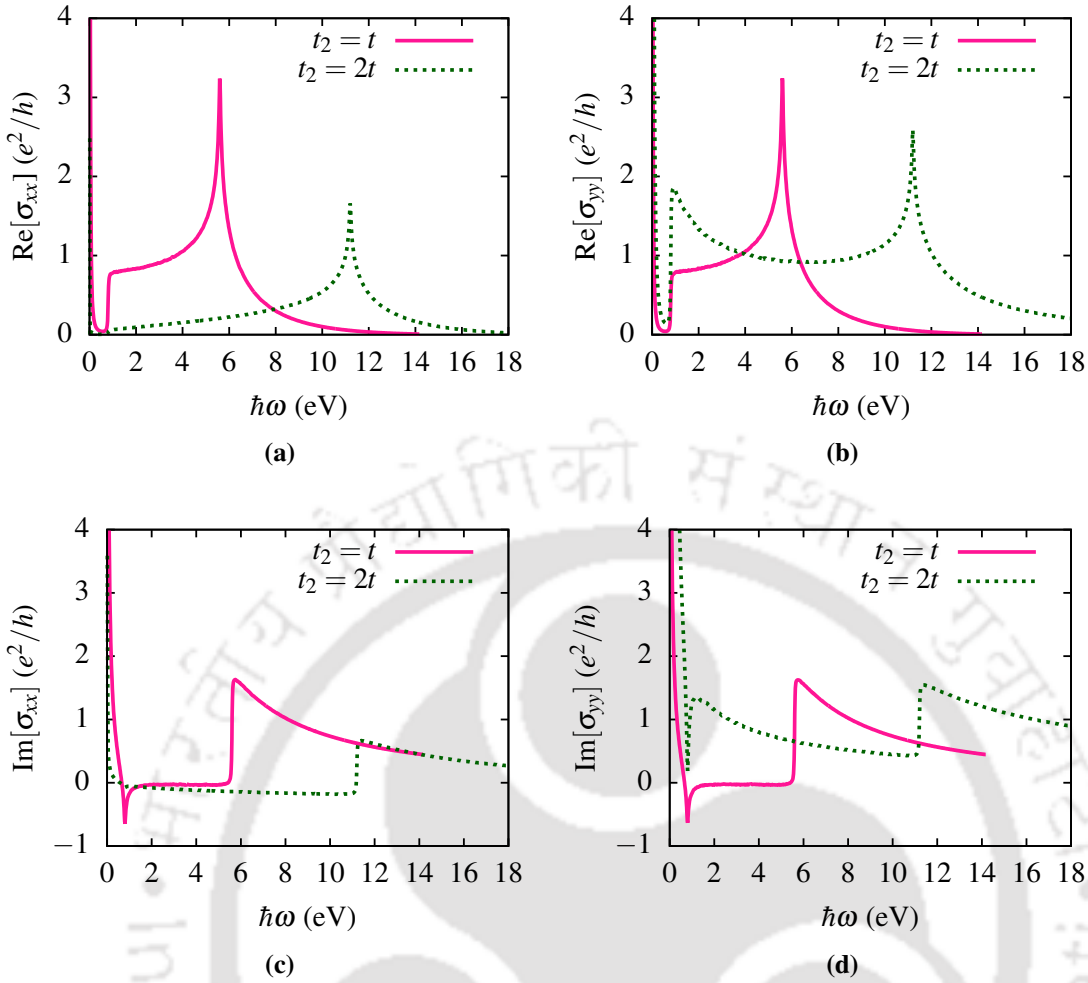


Figure 6.2. (Color online) The real and imaginary part of the optical conductivity (in units of e^2/h) as a function of photon energy $\hbar\omega$ (in units of eV) is shown for Dirac ($t_2 = t$) and semi-Dirac ($t_2 = 2t$) systems. The dark-pink (solid curve) corresponds to Dirac system whereas green one (dotted curve) corresponds to semi-Dirac. μ is set to be 0.4 eV.

spectrum yield different results for xx and yy . The real and the imaginary parts of σ_{yy} both show extra peaks near zero-frequency (along with the Drude peak) as seen from fig. (6.2b) and (6.2d). These peaks are associated with the splitting of the van Hove singularities in the density of states. These splits van Hove singularities move apart from each other as the hopping anisotropy becomes larger [229].

Since the chemical potential is tunable in experiments by application of a gate voltage [75, 238], we have shown the real part of optical conductivity for three different values of the chemical potential for these cases, namely, $t_2 = 2t$ and $t_2 = t$. Fig. (6.3a) and (6.3b) show that peaks near the low frequency region for the real part of σ_{xx} shifts towards the high frequency region with the increasing chemical potential for the Dirac ($t_2 = t$) and the semi-Dirac ($t_2 = 2t$) systems. The inset in the right frame is zoomed in, close to zero frequency,

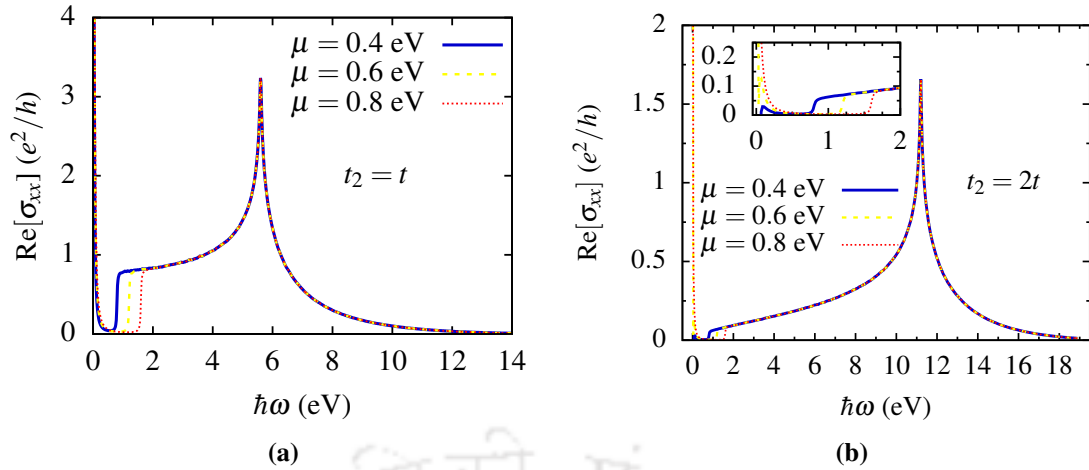


Figure 6.3. (Color online) The real part of the optical conductivity, σ_{xx} (in units of e^2/h) as a function of photon energy, $\hbar\omega$ (in units of eV) is shown with the variation of the chemical potential μ namely, $\mu = 0.4, 0.6, 0.8$ eV for (a) Dirac ($t_2 = t$) and (b) semi-Dirac ($t_2 = 2t$) systems. (b) The inset in the right frame is zoomed in, close to zero frequency.

which clearly depicts the frequency region where the changes in the chemical potential are important for the semi-Dirac case.

6.2.2 Magneto-transport

To study the optical transport properties in the presence of a perpendicular magnetic field, we consider a semi-Dirac nanoribbon that consists of approximately 10^6 number of atoms. In presence of a magnetic field, the off-diagonal terms in the xy and yx directions (σ_{xy} and σ_{yx}) and the diagonal terms in xx and yy directions (σ_{xx} and σ_{yy}) both contribute to the optical transport as seen from Eq. (6.1.13).

In the following, we wish to discuss the effect of a magnetic field on a semi-Dirac nanoribbon. Results for a Dirac ribbon are included for comparison all the while. In Figs. (6.4a) and (6.4b) we have shown the LLs, E_n (both above and below the zero energy) for different LL indices, n ($n = 0, 1, 2, 3, 4 \dots$) as a function of the magnetic field, B (in Tesla) for $t_2 = 2t$ (semi-Dirac) and $t_2 = t$ (Dirac) cases. It is known that the LLs for a semi-Dirac system [43] depend on the index, n and the magnetic field, B via $((|n + \frac{1}{2}|)B)^{2/3}$, while the corresponding dependence for a Dirac system [181] are more well-known, namely, $(|n|B)^{1/2}$. Thus these analytic forms can be used to compare with the numerical values obtained by us. In the upper panel of Fig. (6.4), we show these analytic forms via solid lines, while the numerical results are demonstrated via dotted lines. It is seen that the agreement is fairly good in both cases, which essentially becomes perfect for large values of n for the

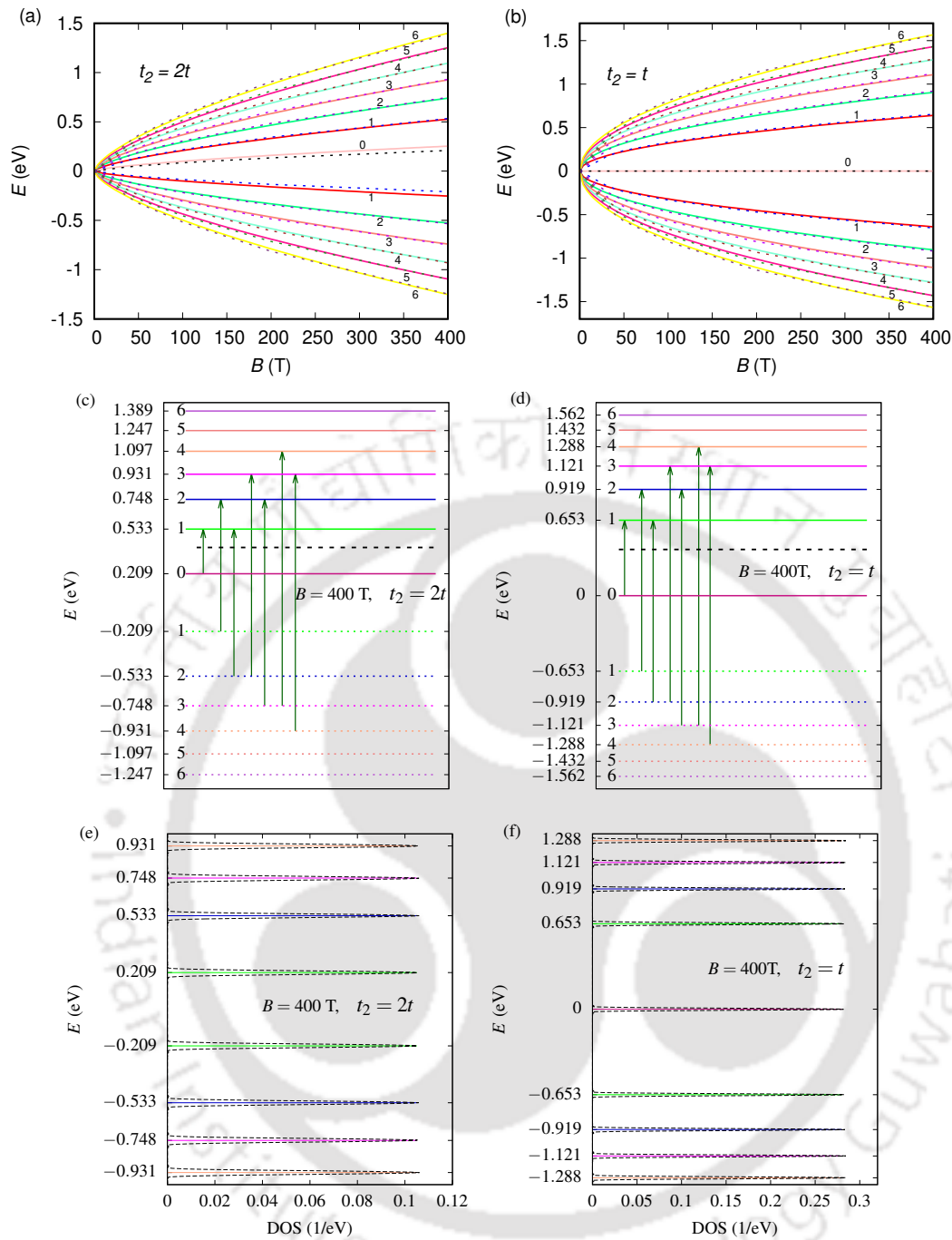


Figure 6.4. (Color online) The two upper panels give the Landau level energies, E (in units of eV) as a function of the magnetic field, B (in units of Tesla) for various values of Landau level indices n (labelled as 0, 1, 2, 3, 4, ...) for (a) $t_2 = 2t$ (semi-Dirac) and (b) $t_2 = t$ (Dirac). The solid and the dotted lines are obtained from theoretical scaling (E goes as $B^{2/3}$ for semi-Dirac case and \sqrt{B} for Dirac case) and simulation respectively. In the two middle panels ((c) and (d)), a few allowed optical transitions are indicated by the vertical (dark-green) arrows and the chemical potential ($\mu = 0.4$ eV) is shown by the horizontal black dashed line. The left and right panels correspond to $t_2 = 2t$ and $t_2 = t$ at $B = 400$ T respectively. In the two lower panels energy levels, E (in units of eV) versus density of states (DOS) (in units of 1/eV) are shown for (e) $t_2 = 2t$ (semi-Dirac) and (f) $t_2 = t$ (Dirac) at $B = 400$ T.

semi-Dirac case (for the Dirac case, we have a fairly good agreement for all values of n).

Let us look at the plots more closely. For the semi-Dirac case, the solid pink curve and the dashed black curve that correspond to the lowest LL ($n = 0$) are slightly shifted from $E = 0$ for all values of the magnetic field as seen from Fig. (6.4a). This is in contrast to the Dirac case, where the energy scales as \sqrt{B} and the solid lines coincide with the dotted ones for positive as well as negative energy levels, with the $n = 0$ LL occurring exactly at zero energy as shown in Fig. (6.4b). A particle-hole symmetry with respect to $E = 0$ is preserved for both the Dirac ($t_2 = t$) and the semi-Dirac cases ($t_2 = 2t$). In the middle panel of Fig. (6.4) (Fig. (6.4c) and Fig. (6.4d)), we show possible optical transitions at a particular value of the magnetic field, namely, $B = 400\text{T}$ for two different systems at a fixed value of the chemical potential, $\mu = 0.4\text{ eV}$. The solid lines denote the positive branches, whereas the negative branches are denoted by dotted lines. Apart from that, the arrows in the middle panel depict the transition from the occupied to the unoccupied levels through the absorption of a photon. The value of the chemical potential used in our computations is shown by a horizontal black dashed line, which falls between the two consecutive LLs. The effects of varying the chemical potential will be discussed later.

In Fig. (6.5) we have shown the real parts of the longitudinal MO conductivities, $\text{Re}(\sigma_{xx})$ and $\text{Re}(\sigma_{yy})$ as well as the MO Hall conductivity, $\text{Re}(\sigma_{xy})$ as a function of photon energy ($\hbar\omega$) for the semi-Dirac ($t_2 = 2t$) and the Dirac ($t_2 = t$) systems corresponding to a fixed chemical potential $\mu = 0.4\text{ eV}$ at $B = 400\text{T}$ (shown by the red curve) in the main frame. Plots with a more moderate value of the magnetic field (say, 100T) are shown in the inset of Fig. (6.5) (shown by the blue curve). The real parts are related to the optical absorption of the nanoribbon and hence characterize the MO properties.

The non-equidistant Landau levels in the semi-Dirac case mentioned above has a consequence on the transport properties presented below. Particularly, the peaks for the real as well as the imaginary parts of the MO conductivity are modified compared to the Dirac case. This is depicted in Fig. (6.5) and Fig. (6.6). For the real parts of σ_{xx} and σ_{yy} , a series of asymmetric absorption resonance peaks are observed for both the semi-Dirac ($t_2 = 2t$) and the Dirac ($t_2 = t$) cases, which result from the optical transitions between different LLs. Since in optical transitions, the selection rules allow the value of n to change only by 1, the transition from $n = 0$ to $n = 1$, indicated by the shortest green arrow in Figs. (6.4c) and (6.4d) gives the first peak (denoted by dark-violet arrow) in $\text{Re}(\sigma_{xx})$ for both $t_2 = 2t$ and $t_2 = t$ as shown in the top panels of Fig. (6.5) (Figs. (6.5a) and (6.5b)). The only difference that can be seen is that the peak has shifted slightly to lower energy with reduced intensity for the

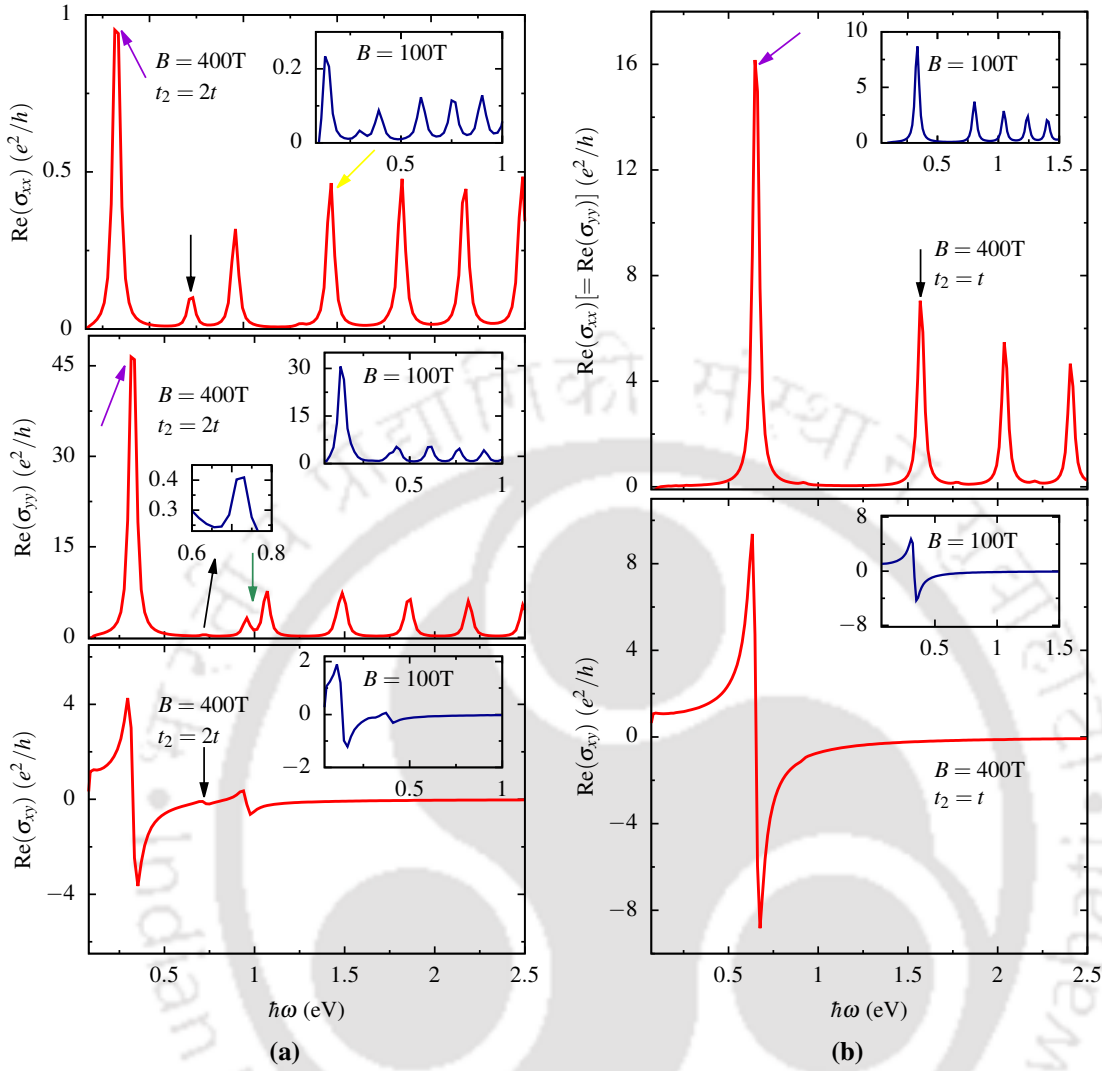


Figure 6.5. (Color online) The real parts of the longitudinal MO conductivities, σ_{xx} and σ_{yy} and the MO Hall conductivity, σ_{xy} (in units of e^2/h) are shown as a function of photon energy, $\hbar\omega$ (in units of eV) for (a) $t_2 = 2t$ (semi-Dirac) and (b) $t_2 = t$ (Dirac) at $B = 400\text{T}$ in the main frame (denoted by red curve). The inset plots show the same for more moderate values of magnetic field, say 100T (denoted by blue curve) for $t_2 = 2t$ and $t_2 = t$. μ is set to be 0.4 eV .

semi-Dirac case ($t_2 = 2t$).

Next, we observe that the two arrows, that is, from $n = 1$ (negative energy) to $n = 2$ (positive energy) and from $n = 2$ (negative energy) to $n = 1$ (positive energy) contribute to the formation of the second peak (denoted by a black arrow). For the Dirac case ($t_2 = t$), these two arrows have exactly the same length, and consequently, there is only one peak in the conductivity spectrum. In contrast to the Dirac case, these two arrows have slightly different lengths for the semi-Dirac case ($t_2 = 2t$) since the symmetry between the positive and the negative spectra ceases to exist. Still we have observed a single peak (denoted by black

arrow) in $\text{Re}(\sigma_{xx})$ because the energy difference between a transition from $n = 1$ (negative energy) to $n = 2$ (positive energy) and that from $n = 2$ (negative energy) to $n = 1$ (positive energy) is small, and hence not resolved in our studies. The rest of the peaks (third, fourth, and so on) are similar to the second peak; they come from a pair of transitions from $-n$ to $n + 1$ and $-(n + 1)$ to n as shown in Fig. (6.4). For example, the fourth peak (denoted by yellow arrow) observed in upper panel of Fig. (6.5a) is due to the combined transitions from $n = 4$ (negative) to $n = 3$ (positive) and $n = 3$ (negative) to $n = 4$ (positive). For the Dirac case ($t_2 = t$), the real part of σ_{yy} gives the same result as that of σ_{xx} due to the isotropic nature of the system. Nevertheless, we show that both σ_{xx} and σ_{yy} in the same plot (as shown in the upper panel of Fig. (6.5b)). Whereas for the semi-Dirac case ($t_2 = 2t$), we have $\sigma_{xx} \neq \sigma_{yy}$ owing to the anisotropic band dispersion along the k_x and the k_y directions (see the middle panel of Fig. (6.5a). In this case, the intensity of the absorption peak for $\text{Re}(\sigma_{yy})$ is much larger (roughly one order of magnitude) than those of $\text{Re}(\sigma_{xx})$. Also, the height of the second peak (indicated by black arrow) in the $\text{Re}(\sigma_{yy})$ is too small compared to other peaks as shown in the inset plot, whereas the third one (denoted by green arrow) splits due to the energy difference as mentioned earlier. The peak positions and the intensities of the transport phenomena are functions of both the velocities of the electrons in the LLs and electron filling. For a given LL, the carriers in the semi-Dirac case have lesser velocity. This causes a lower peak height than the Dirac case. As mentioned earlier, the electron density plays a role as well in shaping the peaks observed in the real parts of σ_{xx} and σ_{yy} for both the semi-Dirac and Dirac cases. This can be seen via the density of states (DOS) plotted in the lowest panels of Fig. (6.4), namely Figs. (6.4e) and (6.4f). The magnitude of the DOS plotted along the x -axis corresponding to the semi-Dirac case is at least small by a factor of two than those for the Dirac case.

So far, we have discussed the MO conductivity considering the diagonal term, namely σ_{xx} and σ_{yy} . It is also of interest to see the effects of the off-diagonal component, namely σ_{xy} , which we shall discuss here. In the bottom panel of Fig. (6.5), we have plotted the real part of the MO Hall conductivity, $\text{Re}(\sigma_{xy})$ as a function of the photon energy for both the semi-Dirac ($t_2 = 2t$) and the Dirac ($t_2 = t$) cases at $B = 400\text{T}$ (shown by the red curve) as shown in the main frame. The main features of the real part of the Hall response are its antisymmetric behavior about its zero value and the presence of a single peak on either side of zero intensity. The peak in the spectrum results from a single transition (that is, $n = 0$ to $n = 1$) that contributes to the MO Hall conductivity σ_{xy} . In the lower panel of Fig. (6.5a) for the semi-Dirac case ($t_2 = 2t$), the first peak (in the positive direction) with maximum

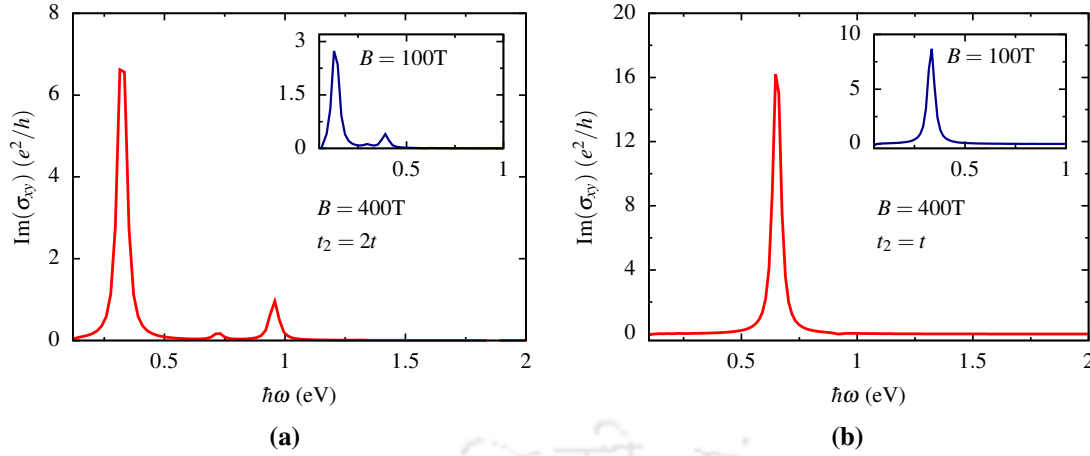


Figure 6.6. (Color online) The imaginary parts of the MO Hall conductivity, σ_{xy} (in units of e^2/h) are shown as a function of photon energy, $\hbar\omega$ (in units of eV) for (a) $t_2 = 2t$ (semi-Dirac) and (b) $t_2 = t$ (Dirac) at $B = 400\text{T}$ in the main frame (shown by the red curve). The inset plots show the same for moderate values of magnetic field, (for example, $B = 100\text{T}$) for $t_2 = 2t$ and $t_2 = t$. μ is set to be 0.4 eV.

intensity occurs at 0.29 eV, and the first peak (in the negative direction) with a minimum intensity occurs at 0.35 eV, both of which are shifted to lower energies as compared to the Dirac case. Also, two pairs of positive and negative peaks are observed in the vicinity of 0.72 eV (denoted by black arrow) and 0.95 eV for the semi-Dirac case, respectively. For the Dirac case ($t_2 = t$), $\text{Re}(\sigma_{xy})$ first shows a positive peak with maximum intensity occurring at 0.63 eV and hence a negative peak with minimum intensity occurring at 0.67 eV as shown in the lower panel of Fig. (6.5b). The similarity that exists between the semi-Dirac and the Dirac cases is that the MO Hall conductivity remains flat for low energies and tends to vanish for higher energies in both cases.

Next, we have shown the imaginary part of the MO Hall conductivity, namely $\text{Im}(\sigma_{xy})$ as a function of the photon energy, $\hbar\omega$ in Fig. (6.6). For the semi-Dirac case ($t_2 = 2t$), the imaginary part of σ_{xy} only shows positive peaks (see Fig. (6.6a)) exactly where the real part of the MO Hall conductivity, that is, $\text{Re}(\sigma_{xy})$ shows the absorption peaks as seen from lower panel of Fig. (6.5a). In the case of the Dirac system ($t_2 = t$), $\text{Im}(\sigma_{xy})$ shows a sharp single positive peak at the same energy that corresponds to the peak of the $\text{Re}(\sigma_{xy})$ as shown in Fig. (6.5b). The peak positions for the real and the imaginary parts of the MO Hall conductivity, σ_{xy} have a correspondence with the absorption peaks of the longitudinal MO conductivities for both the semi-Dirac and the Dirac cases as shown in Figs. (6.5) and (6.6). For example, the second peak of the real and imaginary part of the MO Hall conductivity, $\text{Re}(\sigma_{xy})$ and $\text{Im}(\sigma_{xy})$ occurs at energy very close to 0.72 eV that corresponds to the second peak (denoted by black

arrow) for the $\text{Re}(\sigma_{xx})$ for the semi-Dirac case as shown in Fig. (6.5a). This is expected as the absorption, and the transmission both correspond to the transition of the carriers from one LL to another.

In the following, we observe the effects of a few key quantities that characterize the MO phenomena and also aid in distinguishing the semi-Dirac and the Dirac cases. Specifically, we explore the effects of the electron filling via tuning the chemical potential, μ , and the polarization of the incident light. Further, we study another quantity that characterizes the MO property, namely the Faraday rotation angle.

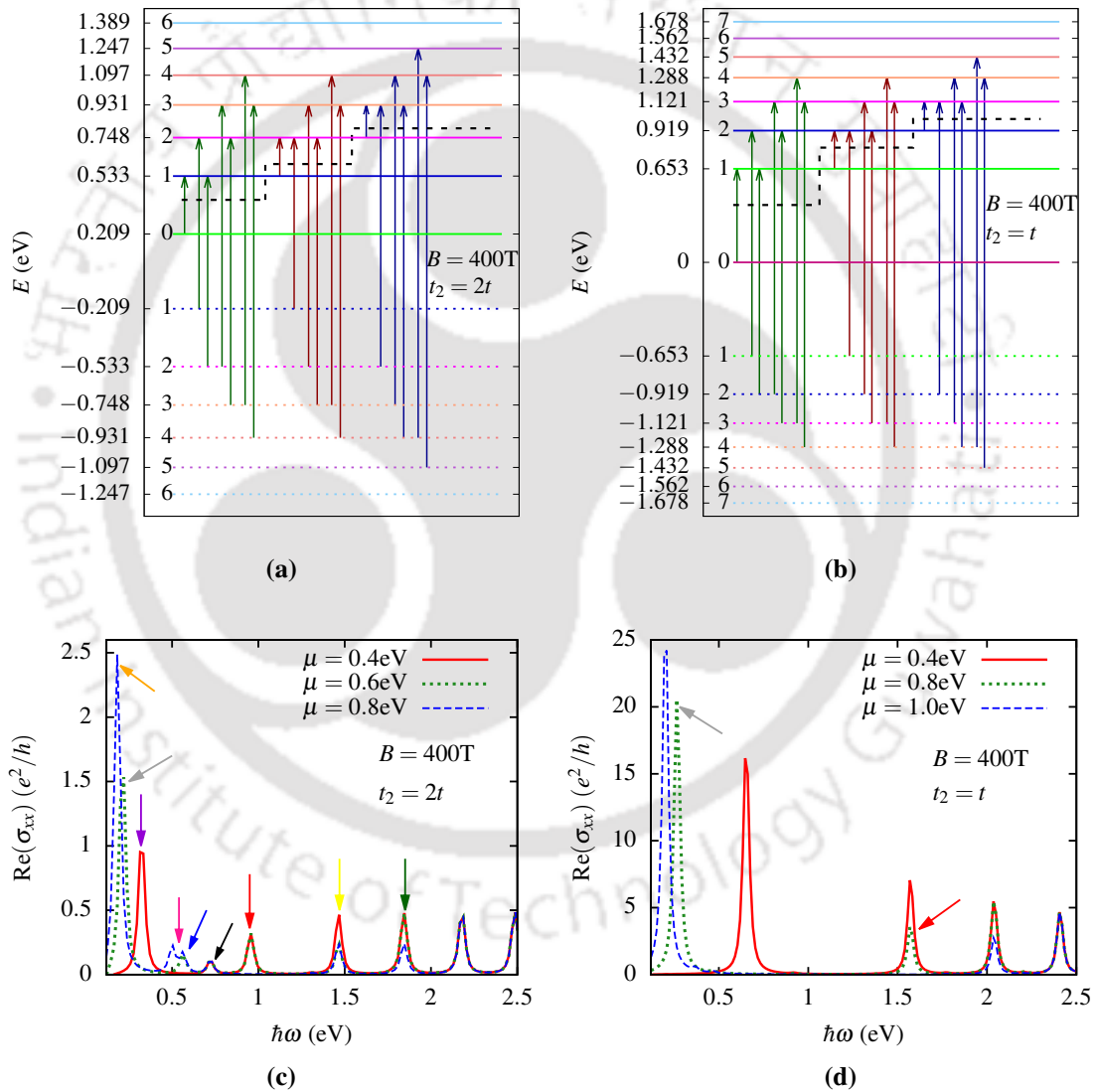


Figure 6.7. (Color online) In the upper two panels, a few allowed optical transitions are shown indicated by arrows for various values of the chemical potential for (a) $t_2 = 2t$ (semi-Dirac) and (b) $t_2 = t$ (Dirac) at $B = 400\text{T}$. Those μ values are marked with the horizontal black dashed lines. In the lower two panels, the real parts of the longitudinal MO conductivity, σ_{xx} in units of e^2/h are shown as a function of photon energy, $\hbar\omega$ in units of eV for various values of chemical potential μ for (c) $t_2 = 2t$ (semi-Dirac) and (d) $t_2 = t$ (Dirac) at $B = 400\text{T}$.

6.2.3 Electron filling

In this section, we shall see how the electron concentration affects the MO conductivities. The electron densities can be controlled by varying the chemical potential, μ , which can further be tuned using external means, for example, a gate voltage. The values of μ considered here are different for the Dirac and the semi-Dirac cases. However, care is taken so that the corresponding values lie between the same pairs of the LL in both cases. As μ is varied, it moves through the successive LLs. In Figs. (6.7a) and (6.7b), we have shown the allowed transitions for different values of the chemical potentials by arrows of different colors at $B = 400\text{T}$ for the semi-Dirac ($t_2 = 2t$) and the Dirac ($t_2 = t$) cases respectively. According to the transition rules, when μ falls between the n^{th} and $(n+1)^{\text{th}}$ LLs, the transitions from values lower n are blocked. So only the transitions passing through the μ value are allowed. For example, when μ lies between the LLs $n = 1$ and $n = 2$, the transition is shown by the shortest dark-red arrow in Fig. (6.7b) is allowed, whereas the transitions originating from LLs lower than $n = 1$ is blocked. For example, transition from $n = 0$ to $n = 1$ is forbidden. These values of the chemical potential are demonstrated in the upper panel of Fig. (6.7) via black dashed lines. In our case, we have chosen three different values of $\mu = 0.4\text{ eV}$, 0.6 eV , and 0.8 eV , which fall between the zeroth and the first (where the transitions are shown by dark-green arrow), the first and the second (where the transitions are shown by dark-red arrow), and the second and the third (where the transitions are shown by dark-blue arrow) LLs respectively. For example, in Fig. (6.7c), we have shown the $\text{Re}(\sigma_{xx})$ for the three different values of $\mu = 0.4\text{ eV}$ (falls between the zeroth and the first LL), 0.6 eV (falls between the first and the second LL) and 0.8 eV (falls between the second and the third LL) for the semi-Dirac case ($t_2 = 2t$). When $\mu = 0.4\text{ eV}$, the transition from $n = 0$ to $n = 1$ (shortest dark-green arrow in Fig. (6.7a)) yields the first peak (denoted by dark-violet arrow) at lower energies. As we increase μ to 0.6 eV (shown by the green dotted curve), only the first (denoted by grey arrow) and the second (denoted by the blue arrow) peaks shift to lower energies, which occur at 0.22 eV and 0.56 eV . Whereas the third (denoted by black arrow) and the fourth (denoted by red arrow) peaks coincide with the second and the third peaks that correspond to those for $\mu = 0.4\text{ eV}$ (solid red curve). When μ is increased further, that is, to 0.8 eV , though the first peak (dashed blue curve denoted by the orange arrow) shifts to lower frequencies, the second peak (denoted by the pink arrow) splits, in addition to getting shifted towards lower frequencies. Further, the third peak at an energy value of 0.72 eV remains intact, whereas the fourth one (at an energy value of 0.96 eV) vanishes.

It is worth mentioning that some of the transitions are strong, whereas some of them are weak. The relative strengths are determined by the height of the absorption peaks (see Fig. 6.7c). The transition probabilities are proportional to the height of the absorption peaks. The larger the transition probability, the absorption peaks are larger.

To compare with the Dirac case [220] ($t_2 = t$), we show that $\text{Re}(\sigma_{xx})$ as a function of the photon energy, $\hbar\omega$ for increasing values of the chemical potential $\mu = 0.4$ eV (falls between the zeroth and the first LL), 0.8 eV (falls between the first and the second LL) and 1 eV (falls between the second and the third LL) in Fig. (6.7d). Here, the effects of μ shown by the solid red curve for $\mu = 0.4$ eV (which falls between the zeroth and the first LL) and the corresponding results are already discussed in the previous section. If we increase μ from 0.4 eV to 0.8 eV, the first peak (dotted green curve denoted by grey arrow) that results from transition between the $n = 1$ to $n = 2$ levels (shown by the shortest dark-red arrow in Fig. (6.7a)) shifts to lower frequencies. Compared to the first peak, the second one (denoted by red arrow) does not shift, however, the intensity becomes half for the peak at an energy of 1.57 eV. The reason is obvious since the transition from $n = 1$ (negative energy) to $n = 2$ (positive energy) is allowed, whereas $n = 2$ (negative energy) to $n = 1$ (positive energy) ($n = 1$ level falls below the LL) is Pauli blocked. When μ is further increased to 1 eV (which falls between the second and the third LLs), the peak disappears since both the transitions ($n = 1$ (negative energy) to $n = 2$ (positive energy) and $n = 2$ (negative energy) to $n = 1$ (positive energy)) are forbidden. Further, there is a reduction in the height of the peak at about 1.57 eV.

6.2.4 Circular polarization

Here, we probe the effects of changing the polarization of the incident light as usually done in experiments. Instead of a linearly polarized light, we can take a circularly polarized one, whose effects can be simply incorporated by superposing the quantities obtained in our MO transport studies. For example, we can define $\sigma_{\pm} = \sigma_{xx} \pm i\sigma_{xy}$, where σ_{+} denotes light with right-handed polarization and σ_{-} denotes that with left-handed polarization. The real (absorptive) part of σ_{\pm} can be written as,

$$\text{Re}(\sigma_{\pm}(\omega)) = \text{Re}(\sigma_{xx}(\omega)) \mp \text{Im}(\sigma_{xy}(\omega)), \quad (6.2.1)$$

where the upper(lower) sign corresponds to MO conductivities with the right(left) circular polarization. In Fig. (6.8), we show the $\text{Re}(\sigma)$ as a function of the photon energy, $\hbar\omega$ for

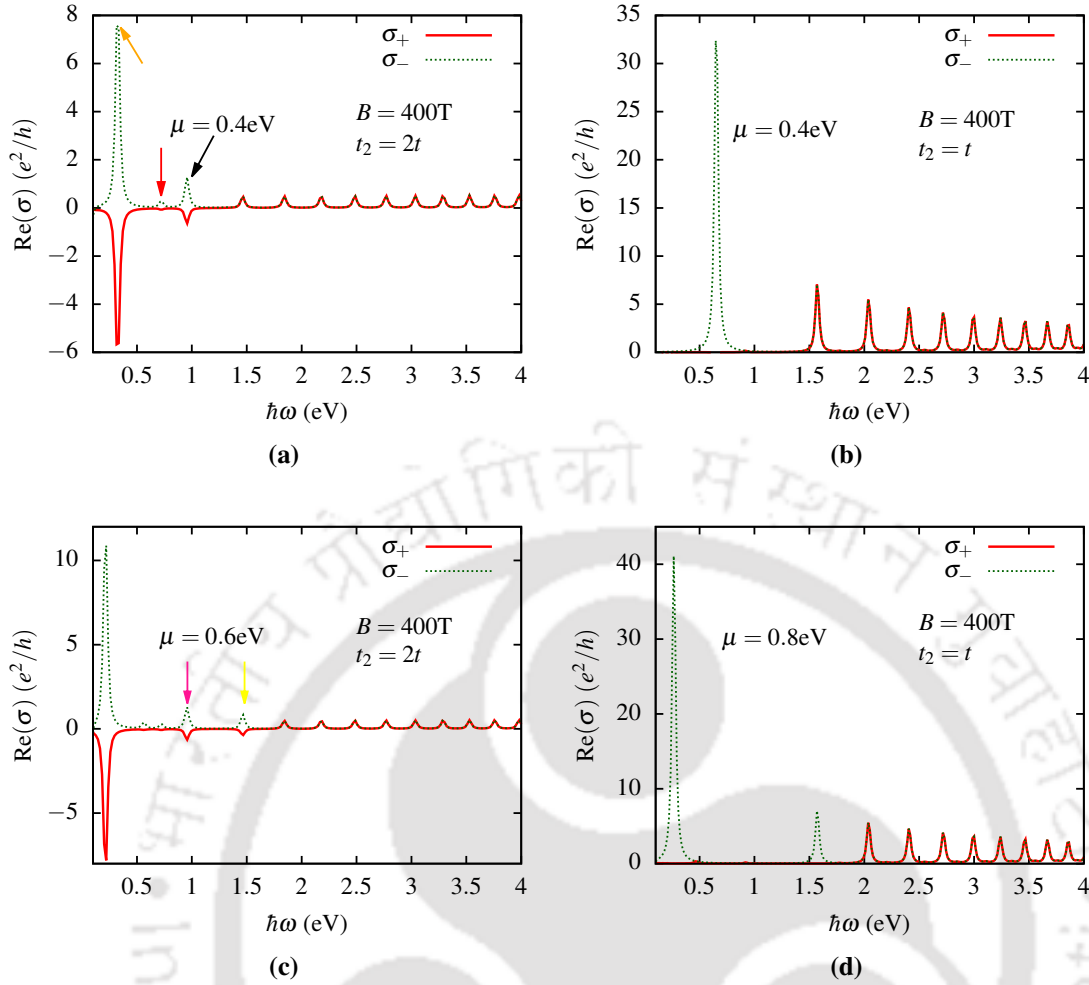


Figure 6.8. (Color online) In the upper two panels, the real parts of the right-handed polarized MO conductivity σ_+ and that of the left-handed polarized one σ_- (in units of e^2/h) are shown as a function of photon energy, $\hbar\omega$ (in units of eV) for a fixed value of chemical potential $\mu = 0.4\text{eV}$ for (a) $t_2 = 2t$ (semi-Dirac) and (b) $t_2 = t$ (Dirac) at $B = 400\text{T}$. The lower two panels ((c) and (d)) depict the same scenario by varying the chemical potential which falls between the $n = 1$ and $n = 2$ Landau levels.

$t_2 = 2t$ and $t_2 = t$ at $B = 400\text{T}$. The dotted green curve is for σ_- , and the solid red curve is for σ_+ . In the upper panels, μ is taken to be 0.4 eV which lies between the zeroth and the first LLs. For the semi-Dirac case ($t_2 = 2t$), the lowest frequency peaks in $\text{Re}(\sigma_-)$ differ significantly than in $\text{Re}(\sigma_+)$. It can be noted from Fig. (6.8a) that only the peaks with the first (denoted by the orange arrow), second (denoted by red arrow), and third (denoted by black arrow) lowest frequencies become positive for σ_- , whereas they are negative for σ_+ . Moreover, the magnitude of those three peaks is lesser for σ_+ than those for σ_- . The rest of the peaks have almost the same magnitude. However, when $t_2 = t$, $\text{Re}(\sigma_-)$ has only one peak at a low frequency which is absent in $\text{Re}(\sigma_+)$ due to the cancellation between the longitudinal MO and the MO Hall conductivities with each other [224, 226, 239]. For the

semi-Dirac case ($t_2 = 2t$), the anisotropy of the Dirac cone in the band structure leads to non-cancellation between the longitudinal MO and the MO Hall conductivities. This low-frequency peak in $\text{Re}(\sigma_-)$ is followed by a series of interband peaks that are identical to those in $\text{Re}(\sigma_+)$ as shown in Fig. (6.8b). When the chemical potential is increased such that it lies between the first and the second LLs, the fourth (denoted by the pink arrow) and fifth (denoted by yellow arrow) peak for σ_+ becomes negative with increased intensity for $t_2 = 2t$ as shown in Fig. (6.8c). For the Dirac case ($t_2 = t$), the first peak at an energy value 1.57 eV in σ_+ vanishes as seen from Fig. (6.8d). Thus our studies imply that the polarization of the incident light brings in significant changes to the MO transport that can be easily probed in experiments. Other polarizations, such as elliptical polarization, etc., may have similar observable changes.

6.2.5 Faraday rotation

Finally, we shall discuss Faraday rotation in a semi-Dirac system and compare it to the Dirac case. It is interesting to mention that the real part of transverse MO conductivity (that is, σ_{xy}) calculated here can be directly used in Faraday rotation experiments [210]. The Faraday-rotation angle θ_F , which is proportional to σ_{xy} can be written as,

$$\theta_F = \frac{2\pi}{c} \text{Re}(\sigma_{xy}(\omega)), \quad (6.2.2)$$

where c is the velocity of light in vacuum and $\text{Re}(\sigma_{xy})$ is the real part of MO Hall conductivity. Figs. (6.9a) and (6.9b) show the Faraday angle, θ_F as a function of the photon energy, $\hbar\omega$ in the UV-VIS range for different values of the magnetic field at a particular value of the chemical potential which falls between the zeroth and the first LL for the semi-Dirac ($t_2 = 2t$) and the Dirac ($t_2 = t$) cases respectively. The corresponding values of μ at given values of B are quoted in the plots. The spectra show an edge-like structure with a positive rotation at low energies and a negative rotation at higher energies for both the semi-Dirac and the Dirac cases. For the semi-Dirac case, the maximum peak of the Faraday rotation shifts towards lower energies, and the value of the maximum Faraday rotation is 1.8° (≈ 0.03 rad) at $B = 400\text{T}$ which is small compared to the Dirac case as shown in Fig. (6.9a). It is to be noted that a discernible Faraday rotation is also observed at 0.93 eV with a maximum value of 0.17° (≈ 0.003 rad) at $B = 400\text{T}$ which is absent for the Dirac case. For smaller values of magnetic field (say, for 200T and 100T), the plot shows qualitatively similar behavior. For the Dirac case, the maximum Faraday rotation is 3.9° (≈ 0.06 rad) at $B = 400\text{T}$, which is

larger than the other two magnetic fields, namely, $B = 200\text{T}$ (shown by green dotted curve) and 100T (shown by red dashed curve) as shown in Fig. (6.9b). For both cases, the spectra depend on the value of the magnetic field used. To further endorse the correspondence, we plot the maximum Faraday angle as a function of B for both the semi-Dirac and Dirac cases as shown in the inset of Fig. (6.9). There is a steady growth of θ^{max} (corresponding to the peak value of $\text{Re}(\sigma_{xy})$) and a decline in θ^{min} (corresponding to the peak in the negative direction) for both the cases. The behavior observed for the Faraday rotation angle and its dependence on the value of the magnetic field for the maximum and the minimum rotation angles in graphene [210], namely, θ^{max} and θ^{min} match well with the Dirac case presented here.

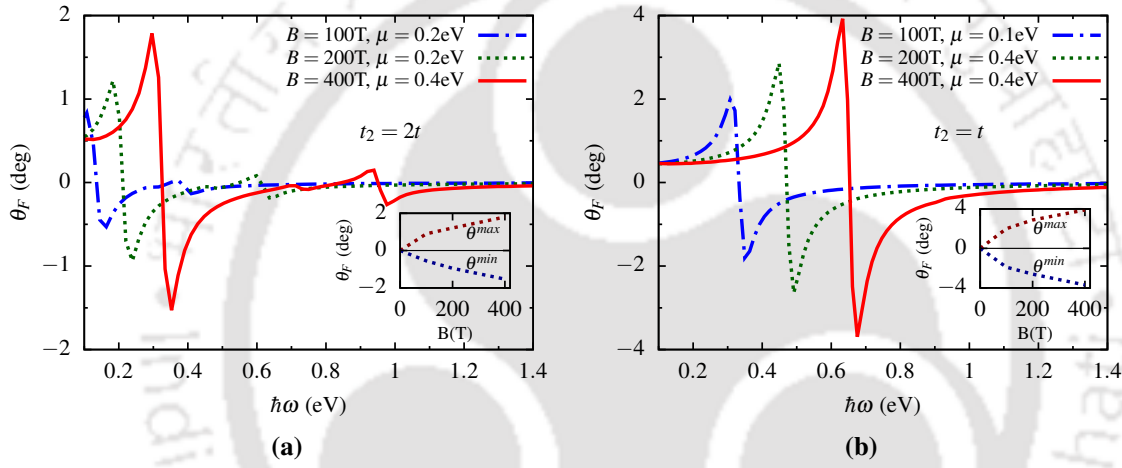


Figure 6.9. (Color online) The Faraday rotation angle, θ_F (in units of deg) is plotted as a function of photon energy, $\hbar\omega$ (in units of eV) for different values of magnetic field and chemical potential for (a) $t_2 = 2t$ (semi-Dirac) and (b) $t_2 = t$ (Dirac). The insets show the maximum (θ^{max}) and the minimum (θ^{min}) Faraday angle, θ_F (in units of deg) versus magnetic field, B (in units of Tesla).

6.3 Summary

We have investigated MO transport properties of a semi-Dirac system subjected to an external magnetic field and compared them to those for the Dirac systems. Owing to the different properties of the LLs, the MO conductivities show several distinct features for the semi-Dirac case as compared to the Dirac one. The real parts of the longitudinal MO conductivities ($\text{Re}(\sigma_{xx})$ and $\text{Re}(\sigma_{yy})$) in either of the cases acquire a series of absorption peaks owing to the transition between the LLs with the semi-Dirac case having additional features owing to an asymmetric distribution of the LLs and their densities of states. Also, the peak intensity

for $\text{Re}(\sigma_{yy})$ is one order of magnitude larger than that of $\text{Re}(\sigma_{xx})$ as the semi-Dirac case has relativistic dispersion in the y -direction (non-relativistic in the x -direction) and hence entails a larger velocity than that in the x -direction. Further, in the case of MO Hall conductivity, the semi-Dirac case shows extra absorption peaks for the real, as well as the imaginary parts, owing to the optical transitions. Moreover, we have studied the effect of electron filling on the absorption spectra by tuning chemical potential between the consecutive LLs. Also, to explore the interplay of the polarization of the incident radiation with MO transport, we consider the light of different polarization, namely, a circularly polarized light. Particularly, the right circularly polarized beam yields distinct features for the semi-Dirac case compared to the Dirac one. Finally, to ascertain the MO activity of the semi-Dirac systems, we study Faraday rotation, where we obtained two discernible Faraday rotation angles for the semi-Dirac case. It should be possible that this feature may be realized in the experiments.





7 Conclusions and outlooks

7.1 Summary of the work done

In this chapter, we conclude with the main outcome of this thesis and give a brief idea that could be the possible extension of the work done by us. In our thesis, we have largely explored the transport properties of 2D semi-Dirac materials within the framework of a tight-binding model on a honeycomb lattice in the presence of spin-orbit couplings and magnetic fields. The results are compared and contrasted with those for the Dirac systems. Magnetic field plays a significant role in studying the quantum Hall effect, whereas the spin-orbit coupling, which does not violate the time-reversal symmetry, helps us to understand the spin transport and hence should be applicable to spintronic systems. Also, the topological phases of matter of these systems open up new directions for better understanding and reveal many possible applications. We found several exotic quantum phenomena shown by the 2D semi-Dirac systems due to their anisotropic behavior as compared to the Dirac ones.

As a starting point, we have presented the band structure of a 2D Dirac and a semi-Dirac system using the tight-binding Hamiltonian. The anisotropic behavior of the band structure reveals that 2D semi-Dirac system is Dirac-like in one direction, whereas in the other direction it is like that of normal metals. We have shown the evolution of the edge states as we tune the band structure from being Dirac to semi-Dirac systems. To study the edge state properties, we derive the eigenvalue equations for the zero-energy edge modes of Dirac and semi-Dirac systems using nanoribbons. For the Dirac case (such as graphene), we see that the amplitude of the wave functions decays exponentially indicating the edge states are highly localized at the edges of the ribbon and there is an exponential decay as one moves into the bulk. We compute the band structure where the flat bands exist within a certain finite momentum range that corresponds to the two edge modes. We observe a quantized plateau at $2e^2/h$ around zero of the Fermi energy in the conductance spectra due to the presence of the edge modes. In the case of bilayer nanoribbon, the behavior of the edge states of a bilayer

graphene is different than that of a monolayer graphene as seen from the probability density plot. We calculated the band structure and found that there are four flat bands corresponding to four edge states. This implies that there exist two edge modes per edge. Instead of a $2e^2/h$ plateau, we observe a plateau at $4e^2/h$ for bilayer graphene near the zero of the Fermi energy as compared to a single layer. For the semi-Dirac nanoribbon, the edge states are more localized at both the edges of the ribbon and decay faster inside the ribbon than its Dirac counterpart. The band dispersion shows that the edge modes are completely separated from the bulk one. Also, the flat bands exist and are much more extended in the case of semi-Dirac ribbons. The conductance plateaus are quantized with the same value, namely $2e^2/h$, as observed for the Dirac case. However, the width of the plateau diminishes as compared to the Dirac case. The LDOS results provide robust support for our results on the edge states derived analytically for all these cases.

In the *third chapter*, we have computed analytical expressions for the zero-energy edge modes for a Dirac and a semi-Dirac nanoribbon in presence of the intrinsic and the Rashba SOC within the framework of the Kane-Mele model. We have calculated the band structure and the conductance for graphene with intrinsic SOC, graphene with Rashba SOC, and graphene with both SOC. We re-establish the existence of topologically protected edge states owing to the presence of parity and time-reversal symmetry of the Hamiltonian. The system acquires edge states in presence of spin-orbit couplings as observed from band structure and both analytic and numeric calculation of electron probability densities. The conductance spectra further show a plateau at a non-zero value ($= 2e^2/h$) near the zero of the Fermi energy. In addition, we derive analytical expressions for the edge modes for a bilayer Kane-Mele model in presence of both SOC. An asymmetry in the finite-size ribbon is observed in presence of intrinsic SOC, which otherwise is absent for a tight-binding model in the band structure. Moreover, the band structure plots show that the QSH phase can be destroyed with the inclusion of interlayer RSOC. Further, we observe a plateau at $= 4e^2/h$ for pristine bilayer graphene near the zero of the Fermi energy in the charge conductance spectra, while it decreases in presence of both intrinsic and Rashba SOC. Studies on spin transport reveal that bilayer graphene should be an appropriate material for spintronic applications. To make a connection with experiments, we have computed the effective mass and have shown that it can be tuned by the inclusion of Rashba SOC. Next, we have explored the similar characteristics for a semi-Dirac nanoribbon as described earlier. We have shown the analytic expressions for the zero-energy edge modes for a semi-Dirac nanoribbon in presence of both the SOC. With the inclusion of intrinsic SOC (Rashba SOC is turned off), we find that the

edge modes are completely separated from the bulk modes, similar to the tight-binding case. The charge conductance shows the same feature as observed from the band structure. When we turn on the Rashba SOC, the $2e^2/h$ plateau vanishes at some critical value when both the parameter values become equal, and the charge conductance becomes zero eventually, which is also true for higher values of Rashba SOC.

In the *fourth chapter*, we include a magnetic field and study the different physical properties of a semi-Dirac nanoribbon within the framework of a tight-binding model of a honeycomb lattice. We also present our results for the Dirac cases. We consider a semi-infinite semi-Dirac nanoribbon and study the Hofstadter butterfly and the properties of the Landau level spectra. We observe two identical gapped spectra in the Hofstadter butterfly spectrum for the semi-Dirac case, which is absent for the Dirac case. A zero-energy mode is seen in the spectrum in contrast to a Dirac system. The Landau levels become fully dispersive in bulk for moderate values of the magnetic flux, which is not true for the Dirac case.

In the *fifth chapter*, we have explored the quantum Hall properties of a semi-Dirac nanoribbon in presence of an external magnetic field using a tight-binding model on a honeycomb lattice and compared it with the Dirac case. We numerically explore the magneto-transport properties using the Kubo formula based on Kernel Polynomial Method (KPM) via calculating the longitudinal and Hall conductivities. We observe that the transverse or Hall conductivity shows standard quantization similar to that of a conventional semiconductor two-dimensional electron gas. This is sharply in contrast with respect to a Dirac system. The density of states shows the absence of a zero Landau level peak in the case of a semi-Dirac system. Owing to the anisotropic dispersion, the longitudinal conductivities in the xx and yy directions, that is, σ_{xx} and σ_{yy} show distinct behavior.

In the *sixth chapter*, we have explored the magneto-optical transport properties of a semi-Dirac system in presence of an external magnetic field using Keldysh formalism. For comparisons, we present the results for the Dirac systems. The MO conductivities show various distinct features for the semi-Dirac case as compared to the Dirac one. The real parts of the longitudinal conductivities show a series of absorption peaks owing to the transition between the Landau levels with the semi-Dirac case having additional features owing to an asymmetric distribution of the Landau levels and their densities of states. Further, the MO Hall conductivity shows a pair of extra absorption peaks for the real, as well as the imaginary parts, owing to the additional optical transitions for the semi-Dirac case. The effect of electron filling on the absorption spectra has been studied by tuning the chemical potential between the consecutive Landau levels. The polarization effect of the incident

radiation with MO transport has been explored. Finally, we have studied Faraday rotation which should be possible to be realized in the experiments.

7.2 Future prospects

The thermoelectric effect can be studied in many 2D Dirac materials which usually hold the key to exotic properties. This will help to find the thermoelectric responses with relevant quantities such as thermopower, Nernst coefficient, etc. Additionally, the thermoelectric Hall effect (transverse response) in presence of a magnetic field could be an interesting phenomenon. The implication of such a method could be a potential pathway for achieving efficient platforms for waste heat recovery in thermoelectric devices.

Interaction effects such as long-range interaction, short-range interaction can be studied by introducing an on-site Hubbard interaction term in a Kane-Mele model. The electron co-relation effects may play an most important role in the topological phase transitions.

Moreover, the behavior of the surface modes, band deformation, effects of spin-orbit coupling and magnetic field can be explored in the 3D TIs.



Appendices



A Chebyshev expansion

The first kind Chebyshev polynomials can be defined as, $T_n(x) = \cos(n \cos^{-1}(x))$ in the range $[-1, 1]$. The recursion relations, $T_0(x) = 1$, $T_1(x) = x$ and $T_{n+1}(x) = 2xT_n(x) - T_{n-1}(x)$ and the orthogonality relation,

$$\int_{-1}^1 T_n(x)T_m(x) \frac{dx}{\sqrt{1-x^2}} = \delta_{nm} \frac{1+\delta_{n0}}{2} \quad (\text{A.0.1})$$

are satisfied by these polynomials. The expansion of the Dirac delta in terms of Chebyshev polynomials, can be written as,

$$\delta(\epsilon - H_0) = \sum_{n=0}^{\infty} \Delta_n(\epsilon) \frac{T_n(H_0)}{1+\delta_{n0}}, \quad (\text{A.0.2})$$

where

$$\Delta_n(\epsilon) = \frac{2T_n(\epsilon)}{\pi \sqrt{1-\epsilon^2}}. \quad (\text{A.0.3})$$

Also the Green's function can be expressed in terms of the $T_n(x)$ as,

$$g^{\sigma,\lambda}(\epsilon, H_0) = \hbar \sum_{n=0}^{\infty} g_n^{\sigma,\lambda}(\epsilon) \frac{T_n(H_0)}{1+\delta_{n0}}, \quad (\text{A.0.4})$$

where

$$g_n^{\sigma,\lambda}(\epsilon) = -2\sigma i \frac{e^{-ni\sigma \cos^{-1}(\epsilon+i\sigma\lambda)}}{\sqrt{1-(\epsilon+i\sigma\lambda)^2}}. \quad (\text{A.0.5})$$

The function $g^{\sigma,\lambda}$ represents both the retarded and the advanced Green's function in the limit $\lambda \rightarrow 0^+$, where λ is the finite broadening parameter. $g^{+,0^+}$ and $g^{-,0^+}$ are the retarded and the advanced Green's function respectively. Hence, the Dirac deltas and Green's function are combinations of a polynomial of H_0 (the unperturbed Hamiltonian) and a coefficient which are functions of the frequency and the energy parameters. The trace in the conductivity can

be written as a trace over a product of polynomials and \hat{h} operators. The Γ matrix needed in the expression of conductivity is written as,

$$\Gamma_{n_1 \dots n_m}^{\alpha_1, \dots, \alpha_m} = \frac{\text{Tr}}{N} \left[\tilde{h}^{\alpha_1} \frac{T_{n_1}(H_0)}{1 + \delta_{n_1,0}} \dots \tilde{h}^{\alpha_m} \frac{T_{n_m}(H_0)}{1 + \delta_{n_m,0}} \right], \quad (\text{A.0.6})$$

where N is the number of unit cells. The upper indices can be used for any number of indices: $\alpha_1 = \alpha_1^1 \alpha_1^2 \dots \alpha_1^{N_1}$ and $\tilde{h}^{\alpha_1} = (i\hbar)^{N_1} \hat{h}^{\alpha_1}$. Here the coefficients of the Chebyshev expansion can be written similarly in a matrix form as,

$$\Lambda_n = \int_{-\infty}^{\infty} d\epsilon f(\epsilon) \Delta_n(\epsilon) \quad (\text{A.0.7})$$

and

$$\Lambda_{nm}(\omega) = \hbar \int_{-\infty}^{\infty} d\epsilon f(\epsilon) [g_n^R(\epsilon/\hbar + \omega) \Delta_m(\epsilon) + \Delta_n(\epsilon) g_m^A(\epsilon/\hbar - \omega)], \quad (\text{A.0.8})$$

where $f(\epsilon) = (1 + e^{\beta(\epsilon - \mu)})^{-1}$ is the Fermi-Dirac distribution function, where β is the inverse temperature and μ is the chemical potential. Hence the first-order conductivity becomes,

$$\sigma^{\alpha\beta}(\omega) = \frac{-ie^2}{\Omega_c \hbar^2 \omega} \left[\sum_n \Gamma_n^{\alpha\beta} \Lambda_n + \sum_{nm} \Lambda_{nm}(\omega) \Gamma_{nm}^{\alpha,\beta} \right] \quad (\text{A.0.9})$$

where Ω_c is the volume of the unit cell.

Also, the density of states can be found in terms of Chebyshev polynomials using Eq. (A.0.2)

as,

$$\rho(\epsilon) = \frac{1}{N} \text{Tr} \delta(\epsilon - H_0) = \frac{1}{\pi \sqrt{1 - \epsilon^2}} \sum_0^{\infty} \mu_n T_n(\epsilon), \quad (\text{A.0.10})$$

where $N = \dim \hat{H}_0$ is the Hilbert space dimension, μ_n denotes the Chebyshev moments. The Chebyshev moments μ_n is,

$$\mu_n = \frac{1}{N} \frac{1 + \delta_{n,0}}{2} \text{Tr} T_n(H_0). \quad (\text{A.0.11})$$

Bibliography

- [1] N. K. P. R. Mello, *Quantum Transport in Mesoscopic Systems: Complexity and Statistical Fluctuations*. Oxford University Press, 2004.
- [2] S. Datta, *Electronic Transport in Mesoscopic Systems*. Cambridge Studies in Semiconductor Physics and Microelectronic Engineering. Cambridge University Press, 1995.
- [3] R. Landauer, *Spatial variation of currents and fields due to localized scatterers in metallic conduction*, *IBM Journal of Research and Development* **1** no. 3, (1957) 223–231.
- [4] E. H. Hall, *On a new action of the magnet on electric currents*, *American Journal of Mathematics* **2** no. 3, (1879) 287–292. <http://www.jstor.org/stable/2369245>.
- [5] K. v. Klitzing, G. Dorda, and M. Pepper, *New method for high-accuracy determination of the fine-structure constant based on quantized hall resistance*, *Phys. Rev. Lett.* **45** (Aug, 1980) 494–497. <https://link.aps.org/doi/10.1103/PhysRevLett.45.494>.
- [6] D. C. Tsui, H. L. Stormer, and A. C. Gossard, *Two-dimensional magnetotransport in the extreme quantum limit*, *Phys. Rev. Lett.* **48** (May, 1982) 1559–1562. <https://link.aps.org/doi/10.1103/PhysRevLett.48.1559>.
- [7] D. J. Thouless, M. Kohmoto, M. P. Nightingale, and M. den Nijs, *Quantized hall conductance in a two-dimensional periodic potential*, *Phys. Rev. Lett.* **49** (Aug, 1982) 405–408. <https://link.aps.org/doi/10.1103/PhysRevLett.49.405>.
- [8] M. I. Dyakonov and V. Perel, *Current-induced spin orientation of electrons in semiconductors*, *Physics Letters A* **35** no. 6, (1971) 459–460.

- [9] M. N. Baibich, J. M. Broto, A. Fert, F. N. Van Dau, F. Petroff, P. Etienne, G. Creuzet, A. Friederich, and J. Chazelas, *Giant magnetoresistance of (001)fe/(001)cr magnetic superlattices*, *Phys. Rev. Lett.* **61** (Nov, 1988) 2472–2475.
<https://link.aps.org/doi/10.1103/PhysRevLett.61.2472>.
- [10] V. Cros, A. Fert, P. S  n  or, and F. Petroff, *The 2007 nobel prize in physics: Albert fert and peter gr  nberg*, in *The spin*, pp. 147–157, Springer. 2009.
- [11] S. Datta and B. Das, *Electronic analog of the electro-optic modulator*, *Applied Physics Letters* **56** no. 7, (1990) 665–667.
- [12] M. Wu, J. Jiang, and M. Weng, *Spin dynamics in semiconductors*, *Physics Reports* **493** no. 2-4, (Aug, 2010) 61–236.
<http://dx.doi.org/10.1016/j.physrep.2010.04.002>.
- [13] Y. A. Bychkov and E. I. Rashba, *Oscillatory effects and the magnetic susceptibility of carriers in inversion layers*, *Journal of Physics C: Solid State Physics* **17** no. 33, (Nov, 1984) 6039–6045. <https://doi.org/10.1088/0022-3719/17/33/015>.
- [14] J. B. Miller, D. M. Zumb  hl, C. M. Marcus, Y. B. Lyanda-Geller, D. Goldhaber-Gordon, K. Campman, and A. C. Gossard, *Gate-controlled spin-orbit quantum interference effects in lateral transport*, *Phys. Rev. Lett.* **90** (Feb, 2003) 076807. <https://link.aps.org/doi/10.1103/PhysRevLett.90.076807>.
- [15] C. L. Kane and E. J. Mele, *Quantum spin hall effect in graphene*, *Phys. Rev. Lett.* **95** (Nov, 2005) 226801.
<https://link.aps.org/doi/10.1103/PhysRevLett.95.226801>.
- [16] J. Klinovaja and D. Loss, *Giant spin-orbit interaction due to rotating magnetic fields in graphene nanoribbons*, *Phys. Rev. X* **3** (Jan, 2013) 011008.
<https://link.aps.org/doi/10.1103/PhysRevX.3.011008>.
- [17] A. Stern and N. H. Lindner, *Topological quantum computation—from basic concepts to first experiments*, *Science* **339** no. 6124, (2013) 1179–1184.
- [18] B. A. Bernevig and S.-C. Zhang, *Quantum spin hall effect*, *Phys. Rev. Lett.* **96** (Mar, 2006) 106802.
<https://link.aps.org/doi/10.1103/PhysRevLett.96.106802>.

- [19] B. A. Bernevig, T. L. Hughes, and S.-C. Zhang, *Quantum spin hall effect and topological phase transition in hgte quantum wells*, *Science* **314** no. 5806, (Dec, 2006) 1757–1761. <http://dx.doi.org/10.1126/science.1133734>.
- [20] M. Konig, S. Wiedmann, C. Brune, A. Roth, H. Buhmann, L. W. Molenkamp, X.-L. Qi, and S.-C. Zhang, *Quantum spin hall insulator state in hgte quantum wells*, *Science* **318** no. 5851, (Nov, 2007) 766–770. <http://dx.doi.org/10.1126/science.1148047>.
- [21] L. Fu and C. L. Kane, *Topological insulators with inversion symmetry*, *Phys. Rev. B* **76** (Jul, 2007) 045302. <https://link.aps.org/doi/10.1103/PhysRevB.76.045302>.
- [22] M. Z. Hasan and C. L. Kane, *Colloquium: Topological insulators*, *Rev. Mod. Phys.* **82** (Nov, 2010) 3045–3067. <https://link.aps.org/doi/10.1103/RevModPhys.82.3045>.
- [23] X.-L. Qi and S.-C. Zhang, *Topological insulators and superconductors*, *Rev. Mod. Phys.* **83** (Oct, 2011) 1057–1110. <https://link.aps.org/doi/10.1103/RevModPhys.83.1057>.
- [24] D. R. Cooper, B. D’Anjou, N. Ghattamaneni, B. Harack, M. Hilke, A. Horth, N. Majlis, M. Massicotte, L. Vandsburger, E. Whiteway, and V. Yu, *Experimental review of graphene*, *ISRN Condensed Matter Physics* **2012** (Apr, 2012) 501686. <https://doi.org/10.5402/2012/501686>.
- [25] M. O. Goerbig, *Electronic properties of graphene in a strong magnetic field*, *Rev. Mod. Phys.* **83** (Nov, 2011) 1193–1243. <https://link.aps.org/doi/10.1103/RevModPhys.83.1193>.
- [26] Y. Barlas, K. Yang, and A. H. MacDonald, *Quantum hall effects in graphene-based two-dimensional electron systems*, *Nanotechnology* **23** no. 5, (Jan, 2012) 052001. <http://dx.doi.org/10.1088/0957-4484/23/5/052001>.
- [27] D. Miller, K. D. Kubista, G. M. Rutter, M. Ruan, W. D. de Heer, P. First, and J. Stroscio, *Observing the quantization of zero mass carriers in graphene*, *Science* **324** (2009) 924 – 927.

- [28] X.-L. Qi and S.-C. Zhang, *The quantum spin hall effect and topological insulators*, *Physics Today* **63** (2010) 1–33.
- [29] C. L. Kane and E. J. Mele, *Z_2 topological order and the quantum spin hall effect*, *Phys. Rev. Lett.* **95** (Sep, 2005) 146802.
<https://link.aps.org/doi/10.1103/PhysRevLett.95.146802>.
- [30] J. Balakrishnan, G. K. W. Koon, M. Jaiswal, A. C. Neto, and B. Özyilmaz, *Colossal enhancement of spin–orbit coupling in weakly hydrogenated graphene*, *Nature Physics* **9** no. 5, (2013) 284–287.
- [31] X. Hong, S.-H. Cheng, C. Herding, and J. Zhu, *Colossal negative magnetoresistance in dilute fluorinated graphene*, *Physical Review B* **83** no. 8, (2011) 085410.
- [32] B. Yang, M. Lohmann, D. Barroso, I. Liao, Z. Lin, Y. Liu, L. Bartels, K. Watanabe, T. Taniguchi, and J. Shi, *Strong electron-hole symmetric rashba spin-orbit coupling in graphene/monolayer transition metal dichalcogenide heterostructures*, *Physical Review B* **96** no. 4, (2017) 041409.
- [33] A. H. Castro Neto, F. Guinea, N. M. R. Peres, K. S. Novoselov, and A. K. Geim, *The electronic properties of graphene*, *Rev. Mod. Phys.* **81** (Jan, 2009) 109–162.
<https://link.aps.org/doi/10.1103/RevModPhys.81.109>.
- [34] P. R. Wallace, *The band theory of graphite*, *Phys. Rev.* **71** (May, 1947) 622–634.
<https://link.aps.org/doi/10.1103/PhysRev.71.622>.
- [35] T. Zhang, S. Wu, R. Yang, and G. Zhang, *Graphene: Nanostructure engineering and applications*, *Frontiers of Physics* **12** no. 1, (Jan, 2017) 127206.
<https://doi.org/10.1007/s11467-017-0648-z>.
- [36] B. Song, G. F. Schneider, Q. Xu, G. Pandraud, C. Dekker, and H. Zandbergen, *Atomic-scale electron-beam sculpting of near-defect-free graphene nanostructures*, *Nano Letters* **11** no. 6, (Jun, 2011) 2247–2250.
<https://doi.org/10.1021/nl200369r>.
- [37] T. Kato and R. Hatakeyama, *Site- and alignment-controlled growth of graphene nanoribbons from nickel nanobars*, *Nature Nanotechnology* **7** no. 10, (Oct, 2012) 651–656. <https://doi.org/10.1038/nnano.2012.145>.

- [38] K. Nakada, M. Fujita, G. Dresselhaus, and M. S. Dresselhaus, *Edge state in graphene ribbons: Nanometer size effect and edge shape dependence*, *Phys. Rev. B* **54** (Dec, 1996) 17954–17961.
<https://link.aps.org/doi/10.1103/PhysRevB.54.17954>.
- [39] K. Wakabayashi, M. Fujita, H. Ajiki, and M. Sigrist, *Electronic and magnetic properties of nanographite ribbons*, *Phys. Rev. B* **59** (Mar, 1999) 8271–8282.
<https://link.aps.org/doi/10.1103/PhysRevB.59.8271>.
- [40] V. Pardo and W. E. Pickett, *Half-metallic semi-dirac-point generated by quantum confinement in TiO_2/VO_2 nanostructures*, *Phys. Rev. Lett.* **102** (Apr, 2009) 166803.
<https://link.aps.org/doi/10.1103/PhysRevLett.102.166803>.
- [41] V. Pardo and W. E. Pickett, *Metal-insulator transition through a semi-dirac point in oxide nanostructures: VO_2 (001) layers confined within TiO_2* , *Phys. Rev. B* **81** (Jan, 2010) 035111. <https://link.aps.org/doi/10.1103/PhysRevB.81.035111>.
- [42] P. Dietl, F. Piéchon, and G. Montambaux, *New magnetic field dependence of Landau levels in a graphenelike structure*, *Phys. Rev. Lett.* **100** (Jun, 2008) 236405.
<https://link.aps.org/doi/10.1103/PhysRevLett.100.236405>.
- [43] S. Banerjee, R. R. P. Singh, V. Pardo, and W. E. Pickett, *Tight-binding modeling and low-energy behavior of the semi-dirac point*, *Phys. Rev. Lett.* **103** (Jul, 2009) 016402.
<https://link.aps.org/doi/10.1103/PhysRevLett.103.016402>.
- [44] G. E. Volovik, *Reentrant violation of special relativity in the low-energy corner*, *Journal of Experimental and Theoretical Physics Letters* **73** no. 4, (Feb, 2001) 162–165. <http://dx.doi.org/10.1134/1.1368706>.
- [45] G. Montambaux, F. Piéchon, J.-N. Fuchs, and M. O. Goerbig, *Merging of Dirac points in a two-dimensional crystal*, *Phys. Rev. B* **80** (Oct, 2009) 153412.
<https://link.aps.org/doi/10.1103/PhysRevB.80.153412>.
- [46] K. Esaki, M. Sato, M. Kohmoto, and B. I. Halperin, *Zero modes, energy gap, and edge states of anisotropic honeycomb lattice in a magnetic field*, *Physical Review B* **80** no. 12, (2009) 125405.

- [47] V. M. Pereira, A. H. Castro Neto, and N. M. R. Peres, *Tight-binding approach to uniaxial strain in graphene*, *Phys. Rev. B* **80** (Jul, 2009) 045401.
<https://link.aps.org/doi/10.1103/PhysRevB.80.045401>.
- [48] E. Zhao and A. Paramekanti, *Bcs-bec crossover on the two-dimensional honeycomb lattice*, *Phys. Rev. Lett.* **97** (Dec, 2006) 230404.
<https://link.aps.org/doi/10.1103/PhysRevLett.97.230404>.
- [49] S.-L. Zhu, B. Wang, and L.-M. Duan, *Simulation and detection of dirac fermions with cold atoms in an optical lattice*, *Phys. Rev. Lett.* **98** (Jun, 2007) 260402.
<https://link.aps.org/doi/10.1103/PhysRevLett.98.260402>.
- [50] J.-M. Hou, W.-X. Yang, and X.-J. Liu, *Massless dirac fermions in a square optical lattice*, *Physical Review A* **79** no. 4, (2009) 043621.
- [51] L. Tarruell, D. Greif, T. Uehlinger, G. Jotzu, and T. Esslinger, *Creating, moving and merging dirac points with a fermi gas in a tunable honeycomb lattice*, *Nature* **483** no. 7389, (Mar, 2012) 302–305. <http://dx.doi.org/10.1038/nature10871>.
- [52] S. Katayama, A. Kobayashi, and Y. Suzumura, *Pressure-induced zero-gap semiconducting state in organic conductor α -(bedt-tf) $2i3$ salt*, *Journal of the Physical Society of Japan* **75** no. 5, (2006) 054705.
- [53] A. Kobayashi, S. Katayama, Y. Suzumura, and H. Fukuyama, *Massless fermions in organic conductor*, *Journal of the Physical Society of Japan* **76** no. 3, (2007) 034711.
- [54] K. L. Lee, B. Gremaud, R. Han, B.-G. Englert, C. Miniatura, *et al.*, *Ultracold fermions in a graphene-type optical lattice*, *Physical Review A* **80** no. 4, (2009) 043411.
- [55] N. W. Ashcroft and N. D. Mermin, *Solid state physics*, cornell university, 1976.
- [56] J. M. Ziman, *Principles of the Theory of Solids*. Cambridge university press, 1972.
- [57] S. Ganguly, *Quantum conductance in spin-orbit coupled devices: A focus on transport in Graphene*. PhD thesis, 2017.
- [58] C. Caroli, R. Combescot, P. Nozieres, and D. Saint-James, *Direct calculation of the tunneling current*, *Journal of Physics C: Solid State Physics* **4** no. 8, (Jun, 1971) 916–929. <https://doi.org/10.1088/0022-3719/4/8/018>.

- [59] D. S. Fisher and P. A. Lee, *Relation between conductivity and transmission matrix*, *Phys. Rev. B* **23** (Jun, 1981) 6851–6854.
<https://link.aps.org/doi/10.1103/PhysRevB.23.6851>.
- [60] R. Landauer, *Conductance determined by transmission: probes and quantised constriction resistance*, . <https://doi.org/10.1088/0953-8984/1/43/011>.
- [61] G. Thorgilsson, G. Viktorsson, and S. Erlingsson, *Recursive green's function method for multi-terminal nanostructures*, *Journal of Computational Physics* **261** (Mar, 2014) 256–266. <http://dx.doi.org/10.1016/j.jcp.2013.12.054>.
- [62] M. L. Sancho, J. L. Sancho, J. L. Sancho, and J. Rubio, *Highly convergent schemes for the calculation of bulk and surface green functions*, *Journal of Physics F: Metal Physics* **15** no. 4, (1985) 851.
- [63] C. W. Groth, M. Wimmer, A. R. Akhmerov, and X. Waintal, *Kwant: a software package for quantum transport*, *New Journal of Physics* **16** no. 6, (Jun, 2014) 063065. <http://dx.doi.org/10.1088/1367-2630/16/6/063065>.
- [64] A. Weiße, G. Wellein, A. Alvermann, and H. Fehske, *The kernel polynomial method*, *Rev. Mod. Phys.* **78** (Mar, 2006) 275–306.
<https://link.aps.org/doi/10.1103/RevModPhys.78.275>.
- [65] J. H. García, B. Uchoa, L. Covaci, and T. G. Rappoport, *Adatoms and anderson localization in graphene*, *Physical Review B* **90** no. 8, (Aug, 2014) .
<http://dx.doi.org/10.1103/PhysRevB.90.085425>.
- [66] J. H. García, L. Covaci, and T. G. Rappoport, *Real-space calculation of the conductivity tensor for disordered topological matter*, *Phys. Rev. Lett.* **114** (Mar, 2015) 116602.
<https://link.aps.org/doi/10.1103/PhysRevLett.114.116602>.
- [67] P. L. Chebyshev, *Théorie des mécanismes connus sous le nom de parallélogrammes*. Imprimerie de l'Académie impériale des sciences, 1853.
- [68] S. Butenko and P. M. Pardalos, *Numerical methods and optimization: An introduction*. CRC Press, 2014.
- [69] J. Plemelj, *Problems in the Sense of Riemann and Klein*. 1964.

- [70] R. Kubo, *Statistical-mechanical theory of irreversible processes. i. general theory and simple applications to magnetic and conduction problems*, *Journal of the Physical Society of Japan* **12** no. 6, (1957) 570–586,
<https://doi.org/10.1143/JPSJ.12.570>.
<https://doi.org/10.1143/JPSJ.12.570>.
- [71] H. Aoki and T. Ando, *Effect of localization on the hall conductivity in the two-dimensional system in strong magnetic fields*, *Solid State Communications* **38** no. 11, (1981) 1079–1082. <https://www.sciencedirect.com/science/article/pii/0038109881900211>.
- [72] G. D. Mahan, *Many Particle Physics, Third Edition*. Plenum, New York, 2000.
- [73] R. Landauer, *Electrical resistance of disordered one-dimensional lattices*, *The Philosophical Magazine: A Journal of Theoretical Experimental and Applied Physics* **21** no. 172, (1970) 863–867, <https://doi.org/10.1080/14786437008238472>.
<https://doi.org/10.1080/14786437008238472>.
- [74] S. M. João, M. Anđelković, L. Covaci, T. G. Rappoport, J. M. V. P. Lopes, and A. Ferreira, *Kite: high-performance accurate modelling of electronic structure and response functions of large molecules, disordered crystals and heterostructures*, *Royal Society Open Science* **7** no. 2, (Feb, 2020) 191809.
<http://dx.doi.org/10.1098/rsos.191809>.
- [75] K. S. Novoselov, *Electric field effect in atomically thin carbon films*, *Science* **306** no. 5696, (Oct, 2004) 666–669.
<http://dx.doi.org/10.1126/science.1102896>.
- [76] Y. Zhang, Y.-W. Tan, H. L. Stormer, and P. Kim, *Experimental observation of the quantum hall effect and berry's phase in graphene*, *Nature* **438** no. 7065, (Nov, 2005) 201–204. <http://dx.doi.org/10.1038/nature04235>.
- [77] V. P. Gusynin and S. G. Sharapov, *Unconventional integer quantum hall effect in graphene*, *Phys. Rev. Lett.* **95** (Sep, 2005) 146801.
<https://link.aps.org/doi/10.1103/PhysRevLett.146801>.
- [78] E.-J. Kan, Z. Li, J. Yang, and J. G. Hou, *Will zigzag graphene nanoribbon turn to half metal under electric field?*, *Applied Physics Letters* **91** no. 24, (Dec, 2007) 243116. <http://dx.doi.org/10.1063/1.2821112>.

- [79] X. Lin and J. Ni, *Half-metallicity in graphene nanoribbons with topological line defects*, *Phys. Rev. B* **84** (Aug, 2011) 075461.
<https://link.aps.org/doi/10.1103/PhysRevB.84.075461>.
- [80] M. I. Katsnelson, K. S. Novoselov, and A. K. Geim, *Chiral tunnelling and the klein paradox in graphene*, *Nature Physics* **2** no. 9, (Aug, 2006) 620–625.
<http://dx.doi.org/10.1038/nphys384>.
- [81] X. Du, I. Skachko, A. Barker, and E. Y. Andrei, *Approaching ballistic transport in suspended graphene*, *Nature Nanotechnology* **3** no. 8, (Jul, 2008) 491–495.
<http://dx.doi.org/10.1038/nnano.2008.199>.
- [82] K. I. Bolotin, K. J. Sikes, J. Hone, H. L. Stormer, and P. Kim, *Temperature-dependent transport in suspended graphene*, *Phys. Rev. Lett.* **101** (Aug, 2008) 096802.
<https://link.aps.org/doi/10.1103/PhysRevLett.101.096802>.
- [83] S. Das Sarma, S. Adam, E. H. Hwang, and E. Rossi, *Electronic transport in two-dimensional graphene*, *Rev. Mod. Phys.* **83** (May, 2011) 407–470.
<https://link.aps.org/doi/10.1103/RevModPhys.83.407>.
- [84] K. S. Novoselov, E. McCann, S. V. Morozov, V. I. Fal'ko, M. I. Katsnelson, U. Zeitler, D. Jiang, F. Schedin, and A. K. Geim, *Unconventional quantum hall effect and berry's phase of 2π in bilayer graphene*, *Nature Physics* **2** no. 3, (Feb, 2006) 177–180. <http://dx.doi.org/10.1038/nphys245>.
- [85] S. Ghosh, W. Bao, D. L. Nika, S. Subrina, E. P. Pokatilov, C. N. Lau, and A. A. Balandin, *Dimensional crossover of thermal transport in few-layer graphene*, *Nature Materials* **9** no. 7, (May, 2010) 555–558.
<http://dx.doi.org/10.1038/nmat2753>.
- [86] A. A. Balandin, *Thermal properties of graphene and nanostructured carbon materials*, *Nature Materials* **10** no. 8, (Aug, 2011) 569–581.
<https://doi.org/10.1038/nmat3064>.
- [87] C. R. Dean, A. F. Young, I. Meric, C. Lee, L. Wang, S. Sorgenfrei, K. Watanabe, T. Taniguchi, P. Kim, K. L. Shepard, and et al., *Boron nitride substrates for high-quality graphene electronics*, *Nature Nanotechnology* **5** no. 10, (Aug, 2010) 722–726. <http://dx.doi.org/10.1038/nnano.2010.172>.

- [88] M. Neek-Amal and F. M. Peeters, *Nanoindentation of a circular sheet of bilayer graphene*, *Phys. Rev. B* **81** (Jun, 2010) 235421.
<https://link.aps.org/doi/10.1103/PhysRevB.81.235421>.
- [89] Y. Zhang, C. Wang, Y. Cheng, and Y. Xiang, *Mechanical properties of bilayer graphene sheets coupled by sp^3 bonding*, *Carbon* **49** no. 13, (2011) 4511–4517.
<https://www.sciencedirect.com/science/article/pii/S0008622311004945>.
- [90] E. McCann and V. I. Fal'ko, *Landau-level degeneracy and quantum hall effect in a graphite bilayer*, *Phys. Rev. Lett.* **96** (Mar, 2006) 086805.
<https://link.aps.org/doi/10.1103/PhysRevLett.96.086805>.
- [91] E. V. Castro, K. S. Novoselov, S. V. Morozov, N. M. R. Peres, J. M. B. L. dos Santos, J. Nilsson, F. Guinea, A. K. Geim, and A. H. C. Neto, *Biased bilayer graphene: Semiconductor with a gap tunable by the electric field effect*, *Phys. Rev. Lett.* **99** (Nov, 2007) 216802.
<https://link.aps.org/doi/10.1103/PhysRevLett.99.216802>.
- [92] A. S. Rodin, A. Carvalho, and A. H. Castro Neto, *Strain-induced gap modification in black phosphorus*, *Phys. Rev. Lett.* **112** (May, 2014) 176801.
<https://link.aps.org/doi/10.1103/PhysRevLett.112.176801>.
- [93] J. Guan, Z. Zhu, and D. Tománek, *Phase coexistence and metal-insulator transition in few-layer phosphorene: A computational study*, *Phys. Rev. Lett.* **113** (Jul, 2014) 046804. <https://link.aps.org/doi/10.1103/PhysRevLett.113.046804>.
- [94] A. N. Rudenko, S. Yuan, and M. I. Katsnelson, *Toward a realistic description of multilayer black phosphorus: From gw approximation to large-scale tight-binding simulations*, *Phys. Rev. B* **92** (Aug, 2015) 085419.
<https://link.aps.org/doi/10.1103/PhysRevB.92.085419>.
- [95] C. Dutreix, E. A. Stepanov, and M. I. Katsnelson, *Laser-induced topological transitions in phosphorene with inversion symmetry*, *Phys. Rev. B* **93** (Jun, 2016) 241404. <https://link.aps.org/doi/10.1103/PhysRevB.93.241404>.
- [96] Y. Hasegawa, R. Konno, H. Nakano, and M. Kohmoto, *Zero modes of tight-binding electrons on the honeycomb lattice*, *Phys. Rev. B* **74** (Jul, 2006) 033413.
<https://link.aps.org/doi/10.1103/PhysRevB.74.033413>.

- [97] Y. Suzumura, T. Morinari, and F. Piéchon, *Mechanism of dirac point in α type organic conductor under pressure*, *Journal of the Physical Society of Japan* **82** no. 2, (2013) 023708, <https://doi.org/10.7566/JPSJ.82.023708>.
<https://doi.org/10.7566/JPSJ.82.023708>.
- [98] B. I. Halperin, *Quantized hall conductance, current-carrying edge states, and the existence of extended states in a two-dimensional disordered potential*, *Phys. Rev. B* **25** (Feb, 1982) 2185–2190.
<https://link.aps.org/doi/10.1103/PhysRevB.25.2185>.
- [99] R. B. Laughlin, *Quantized hall conductivity in two dimensions*, *Phys. Rev. B* **23** (May, 1981) 5632–5633. <https://link.aps.org/doi/10.1103/PhysRevB.23.5632>.
- [100] C. Wu, B. A. Bernevig, and S.-C. Zhang, *Helical liquid and the edge of quantum spin hall systems*, *Phys. Rev. Lett.* **96** (Mar, 2006) 106401.
<https://link.aps.org/doi/10.1103/PhysRevLett.96.106401>.
- [101] M. Onoda and N. Nagaosa, *Spin current and accumulation generated by the spin hall insulator*, *Phys. Rev. Lett.* **95** (Sep, 2005) 106601.
<https://link.aps.org/doi/10.1103/PhysRevLett.95.106601>.
- [102] O. V. Yazyev and M. I. Katsnelson, *Magnetic correlations at graphene edges: Basis for novel spintronics devices*, *Phys. Rev. Lett.* **100** (Jan, 2008) 047209.
<https://link.aps.org/doi/10.1103/PhysRevLett.100.047209>.
- [103] K.-i. Sasaki, J. Jiang, R. Saito, S. Onari, and Y. Tanaka, *Theory of superconductivity of carbon nanotubes and graphene*, *Journal of the Physical Society of Japan* **76** no. 3, (Mar, 2007) 033702. <http://dx.doi.org/10.1143/JPSJ.76.033702>.
- [104] D. Kang, B. Wang, C. Xia, and H. Li, *Perfect spin filter in a tailored zigzag graphene nanoribbon*, *Nanoscale Research Letters* **12** no. 1, (May, 2017) 357.
<https://doi.org/10.1186/s11671-017-2132-7>.
- [105] G. Zhang, X. Li, G. Wu, J. Wang, D. Culcer, E. Kaxiras, and Z. Zhang, *Quantum phase transitions and topological proximity effects in graphene nanoribbon heterostructures*, *Nanoscale* **6** (2014) 3259–3267.
<http://dx.doi.org/10.1039/C3NR05284B>.

- [106] Y.-W. Son, M. L. Cohen, and S. G. Louie, *Erratum: Half-metallic graphene nanoribbons*, *Nature* **446** no. 7133, (Mar, 2007) 342–342.
<https://doi.org/10.1038/nature05686>.
- [107] Y.-W. Son, M. L. Cohen, and S. G. Louie, *Energy gaps in graphene nanoribbons*, *Phys. Rev. Lett.* **97** (Nov, 2006) 216803.
<https://link.aps.org/doi/10.1103/PhysRevLett.97.216803>.
- [108] K. Wakabayashi, M. Sigrist, and M. Fujita, *Spin wave mode of edge-localized magnetic states in nanographite zigzag ribbons*, *Journal of the Physical Society of Japan* **67** no. 6, (1998) 2089–2093, <https://doi.org/10.1143/JPSJ.67.2089>.
<https://doi.org/10.1143/JPSJ.67.2089>.
- [109] E. V. Castro, N. M. R. Peres, J. M. B. Lopes dos Santos, A. H. C. Neto, and F. Guinea, *Localized states at zigzag edges of bilayer graphene*, *Phys. Rev. Lett.* **100** (Jan, 2008) 026802.
<https://link.aps.org/doi/10.1103/PhysRevLett.100.026802>.
- [110] B. K. Nikolić, *Statistical properties of eigenstates in three-dimensional mesoscopic systems with off-diagonal or diagonal disorder*, *Phys. Rev. B* **64** (Jun, 2001) 014203.
<https://link.aps.org/doi/10.1103/PhysRevB.64.014203>.
- [111] K. Saha, *Photoinduced chern insulating states in semi-dirac materials*, *Phys. Rev. B* **94** (Aug, 2016) 081103.
<https://link.aps.org/doi/10.1103/PhysRevB.94.081103>.
- [112] Q. Chen, L. Du, and G. A. Fiete, *Floquet band structure of a semi-dirac system*, *Phys. Rev. B* **97** (Jan, 2018) 035422.
<https://link.aps.org/doi/10.1103/PhysRevB.97.035422>.
- [113] S. F. Islam and A. Saha, *Driven conductance of an irradiated semi-dirac material*, *Phys. Rev. B* **98** (Dec, 2018) 235424.
<https://link.aps.org/doi/10.1103/PhysRevB.98.235424>.
- [114] J. Lado, N. García-Martínez, and J. Fernández-Rossier, *Edge states in graphene-like systems*, *Synthetic Metals* **210** (2015) 56–67. <https://www.sciencedirect.com/science/article/pii/S0379677915300072>.
- Reviews of Current Advances in Graphene Science and Technology.

- [115] R. Seshadri, K. Sengupta, and D. Sen, *Edge states, spin transport, and impurity-induced local density of states in spin-orbit coupled graphene*, *Phys. Rev. B* **93** (Jan, 2016) 035431.
<https://link.aps.org/doi/10.1103/PhysRevB.93.035431>.
- [116] S. Ganguly and S. Basu, *Adatoms in graphene nanoribbons: spintronic properties and the quantum spin hall phase*, *Materials Research Express* **4** no. 11, (Nov, 2017) 115004. <https://doi.org/10.1088/2053-1591/aa9508>.
- [117] H. Xu, T. Heinzl, and I. V. Zozoulenko, *Edge disorder and localization regimes in bilayer graphene nanoribbons*, *Phys. Rev. B* **80** (Jul, 2009) 045308.
<https://link.aps.org/doi/10.1103/PhysRevB.80.045308>.
- [118] E. Hill, A. Geim, K. Novoselov, F. Schedin, and P. Blake, *Graphene spin valve devices*, *IEEE Transactions on Magnetics* **42** no. 10, (Oct, 2006) 2694–2696.
<http://dx.doi.org/10.1109/TMAG.2006.878852>.
- [119] M. Nishioka and A. Goldman, *Spin transport through multilayer graphene*, *Applied Physics Letters* **90** no. 25, (2007) . Funding Information: The authors were grateful to Daniel C. Frisbie for useful advice. This work was supported by the National Science Foundation through the University of Minnesota Materials Research Science and Engineering Center under Grant No. NSF/DMR-0212032.
- [120] N. Tombros, C. Jozsa, M. Popinciuc, H. T. Jonkman, and B. J. van Wees, *Electronic spin transport and spin precession in single graphene layers at room temperature*, *Nature* **448** no. 7153, (Jul, 2007) 571–574.
<http://dx.doi.org/10.1038/nature06037>.
- [121] J. E. Moore, *The birth of topological insulators*, *Nature* **464** no. 7286, (Mar, 2010) 194–198. <https://doi.org/10.1038/nature08916>.
- [122] H. Min, J. E. Hill, N. A. Sinitsyn, B. R. Sahu, L. Kleinman, and A. H. MacDonald, *Intrinsic and rashba spin-orbit interactions in graphene sheets*, *Phys. Rev. B* **74** (Oct, 2006) 165310. <https://link.aps.org/doi/10.1103/PhysRevB.74.165310>.
- [123] Y. Yao, F. Ye, X.-L. Qi, S.-C. Zhang, and Z. Fang, *Spin-orbit gap of graphene: First-principles calculations*, *Phys. Rev. B* **75** (Jan, 2007) 041401.
<https://link.aps.org/doi/10.1103/PhysRevB.75.041401>.

- [124] C. Weeks, J. Hu, J. Alicea, M. Franz, and R. Wu, *Engineering a robust quantum spin hall state in graphene via adatom deposition*, *Phys. Rev. X* **1** (Oct, 2011) 021001.
<https://link.aps.org/doi/10.1103/PhysRevX.1.021001>.
- [125] L. Kou, B. Yan, F. Hu, S.-C. Wu, T. O. Wehling, C. Felser, C. Chen, and T. Frauenheim, *Graphene-based topological insulator with an intrinsic bulk band gap above room temperature*, *Nano Letters* **13** no. 12, (Dec, 2013) 6251–6255.
<https://doi.org/10.1021/nl4037214>.
- [126] J. Zhang, C. Triola, and E. Rossi, *Proximity effect in graphene–topological-insulator heterostructures*, *Phys. Rev. Lett.* **112** (Mar, 2014) 096802.
<https://link.aps.org/doi/10.1103/PhysRevLett.112.096802>.
- [127] K. Zollner, T. Frank, S. Irmer, M. Gmitra, D. Kochan, and J. Fabian, *Spin-orbit coupling in methyl functionalized graphene*, *Phys. Rev. B* **93** (Jan, 2016) 045423.
<https://link.aps.org/doi/10.1103/PhysRevB.93.045423>.
- [128] B. Lalmi, H. Oughaddou, H. Enriquez, A. Kara, S. Vizzini, B. Ealet, and B. Aufray, *Epitaxial growth of a silicene sheet*, *Applied Physics Letters* **97** no. 22, (Nov, 2010) 223109. <http://dx.doi.org/10.1063/1.3524215>.
- [129] P. Vogt, P. De Padova, C. Quaresima, J. Avila, E. Frantzeskakis, M. C. Asensio, A. Resta, B. Ealet, and G. Le Lay, *Silicene: Compelling experimental evidence for graphenelike two-dimensional silicon*, *Phys. Rev. Lett.* **108** (Apr, 2012) 155501.
<https://link.aps.org/doi/10.1103/PhysRevLett.108.155501>.
- [130] L. Chen, C.-C. Liu, B. Feng, X. He, P. Cheng, Z. Ding, S. Meng, Y. Yao, and K. Wu, *Evidence for dirac fermions in a honeycomb lattice based on silicon*, *Phys. Rev. Lett.* **109** (Aug, 2012) 056804.
<https://link.aps.org/doi/10.1103/PhysRevLett.109.056804>.
- [131] W.-F. Tsai, C.-Y. Huang, T.-R. Chang, H. Lin, H.-T. Jeng, and A. Bansil, *Gated silicene as a tunable source of nearly 100%* *Nature Communications* **4** no. 1, (Feb, 2013). <http://dx.doi.org/10.1038/ncomms2525>.
- [132] X. Wang, P. Wang, G. Bian, and T.-C. Chiang, *Topological phase transitions in stanene and stanene-like systems by scaling the spin-orbit coupling*, *Europhysics Letters* **115** no. 3, (Aug 2016) 5.

http://inis.iaea.org/search/search.aspx?orig_q=RN:51026457.

NANOSCIENCE AND NANOTECHNOLOGY.

- [133] J. Ding, Z. Qiao, W. Feng, Y. Yao, and Q. Niu, *Engineering quantum anomalous/valley hall states in graphene via metal-atom adsorption: An ab-initio study*, *Phys. Rev. B* **84** (Nov, 2011) 195444.
<https://link.aps.org/doi/10.1103/PhysRevB.84.195444>.
- [134] H. Zhang, C. Lazo, S. Blügel, S. Heinze, and Y. Mokrousov, *Electrically tunable quantum anomalous hall effect in graphene decorated by 5d transition-metal adatoms*, *Phys. Rev. Lett.* **108** (Feb, 2012) 056802.
<https://link.aps.org/doi/10.1103/PhysRevLett.108.056802>.
- [135] D. Marchenko, A. Varykhalov, M. Scholz, G. Bihlmayer, E. Rashba, A. Rybkin, A. Shikin, and O. Rader, *Giant rashba splitting in graphene due to hybridization with gold*, *Nature communications* **3** (2012) 1232.
<https://doi.org/10.1038/ncomms2227>.
- [136] Y. S. Dedkov, M. Fonin, U. Rüdiger, and C. Laubschat, *Rashba effect in the graphene/n(111) system*, *Phys. Rev. Lett.* **100** (Mar, 2008) 107602.
<https://link.aps.org/doi/10.1103/PhysRevLett.100.107602>.
- [137] F. Calleja, H. Ochoa, M. Garnica, S. Barja, J. J. Navarro, A. Black, M. M. Otrokov, E. V. Chulkov, A. Arnau, A. L. Vázquez de Parga, F. Guinea, and R. Miranda, *Spatial variation of a giant spin-orbit effect induces electron confinement in graphene on Pb islands*, *Nature Physics* **11** no. 1, (Jan., 2015) 43–47.
- [138] F. Guinea, *Spin-orbit coupling in a graphene bilayer and in graphite*, *New Journal of Physics* **12** no. 8, (Aug, 2010) 083063.
<http://dx.doi.org/10.1088/1367-2630/12/8/083063>.
- [139] W. Yao, S. A. Yang, and Q. Niu, *Edge states in graphene: From gapped flat-band to gapless chiral modes*, *Phys. Rev. Lett.* **102** (Mar, 2009) 096801.
<https://link.aps.org/doi/10.1103/PhysRevLett.102.096801>.
- [140] Z. Qiao, H. Jiang, X. Li, Y. Yao, and Q. Niu, *Microscopic theory of quantum anomalous hall effect in graphene*, *Phys. Rev. B* **85** (Mar, 2012) 115439.
<https://link.aps.org/doi/10.1103/PhysRevB.85.115439>.

- [141] W. Li and R. Tao, *Edge states of monolayer and bilayer graphene nanoribbons*, *Journal of the Physical Society of Japan* **81** no. 2, (2012) 024704, <https://doi.org/10.1143/JPSJ.81.024704>.
<https://doi.org/10.1143/JPSJ.81.024704>.
- [142] Z. Qiao, X. Li, W.-K. Tse, H. Jiang, Y. Yao, and Q. Niu, *Topological phases in gated bilayer graphene: Effects of rashba spin-orbit coupling and exchange field*, *Phys. Rev. B* **87** (Mar, 2013) 125405. <https://link.aps.org/doi/10.1103/PhysRevB.87.125405>.
- [143] H. Pan, X. Li, Z. Qiao, C.-C. Liu, Y. Yao, and S. A. Yang, *Topological metallic phases in spin-orbit coupled bilayer systems*, *New Journal of Physics* **16** no. 12, (Dec, 2014) 123015. <https://doi.org/10.1088/1367-2630/16/12/123015>.
- [144] Z. Qiao, W.-K. Tse, H. Jiang, Y. Yao, and Q. Niu, *Two-dimensional topological insulator state and topological phase transition in bilayer graphene*, *Phys. Rev. Lett.* **107** (Dec, 2011) 256801. <https://link.aps.org/doi/10.1103/PhysRevLett.107.256801>.
- [145] R. van Gelderen and C. M. Smith, *Rashba and intrinsic spin-orbit interactions in biased bilayer graphene*, *Phys. Rev. B* **81** (Mar, 2010) 125435. <https://link.aps.org/doi/10.1103/PhysRevB.81.125435>.
- [146] S. Das Sarma, E. H. Hwang, and E. Rossi, *Theory of carrier transport in bilayer graphene*, *Phys. Rev. B* **81** (Apr, 2010) 161407. <https://link.aps.org/doi/10.1103/PhysRevB.81.161407>.
- [147] M. Laubach, J. Reuther, R. Thomale, and S. Rachel, *Rashba spin-orbit coupling in the kane-mele-hubbard model*, *Phys. Rev. B* **90** (Oct, 2014) 165136. <https://link.aps.org/doi/10.1103/PhysRevB.90.165136>.
- [148] D. Huertas-Hernando, F. Guinea, and A. Brataas, *Spin-orbit coupling in curved graphene, fullerenes, nanotubes, and nanotube caps*, *Phys. Rev. B* **74** (Oct, 2006) 155426. <https://link.aps.org/doi/10.1103/PhysRevB.74.155426>.
- [149] P. Sinha, S. Ganguly, and S. Basu, *Analytic and numeric computation of edge states and conductivity of a kane-mele nanoribbon*, *Physica E-low-dimensional Systems & Nanostructures* **103** (2018) 314–322.

- [150] R. Seshadri and D. Sen, *Electron dynamics in graphene with spin–orbit couplings and periodic potentials*, *Journal of Physics: Condensed Matter* **29** no. 15, (Mar, 2017) 155303. <https://doi.org/10.1088/1361-648x/aa605b>.
- [151] Z.-F. Liu, Q.-P. Wu, A.-X. Chen, X.-B. Xiao, N.-H. Liu, and G.-X. Miao, *Helical edge states and edge-state transport in strained armchair graphene nanoribbons*, *Scientific reports* **7** no. 1, (August, 2017) 8854. <https://europepmc.org/articles/PMC5562773>.
- [152] M. Zarea and N. Sandler, *Rashba spin-orbit interaction in graphene and zigzag nanoribbons*, *Phys. Rev. B* **79** (Apr, 2009) 165442. <https://link.aps.org/doi/10.1103/PhysRevB.79.165442>.
- [153] S. Murakami, N. Nagaosa, and S.-C. Zhang, *Spin-hall insulator*, *Phys. Rev. Lett.* **93** (Oct, 2004) 156804. <https://link.aps.org/doi/10.1103/PhysRevLett.93.156804>.
- [154] P. Sinha and S. Basu, *Study of edge states and conductivity in spin-orbit coupled bilayer graphene*, *The European Physical Journal B* **92** no. 9, (Sep, 2019). <http://dx.doi.org/10.1140/epjb/e2019-100287-6>.
- [155] F. J. d. Santos, D. A. Bahamon, R. B. Muniz, K. McKenna, E. V. Castro, J. Lischner, and A. Ferreira, *Impact of complex adatom-induced interactions on quantum spin hall phases*, *Phys. Rev. B* **98** (Aug, 2018) 081407. <https://link.aps.org/doi/10.1103/PhysRevB.98.081407>.
- [156] Y. Li, E. Zhang, B. Gong, and S. Zhang, *Intrinsic spin-orbit coupling in zigzag and armchair graphene nanoribbons*, *Journal of Nanomaterials* **2011** (Apr, 2011) 364897. <https://doi.org/10.1155/2011/364897>.
- [157] P.-H. Chang, F. Mahfouzi, N. Nagaosa, and B. K. Nikolić, *Spin-seebeck effect on the surface of a topological insulator due to nonequilibrium spin-polarization parallel to the direction of thermally driven electronic transport*, *Phys. Rev. B* **89** (May, 2014) 195418. <https://link.aps.org/doi/10.1103/PhysRevB.89.195418>.
- [158] Q. Zhang, K. S. Chan, and J. Li, *Spin-polarized transport in graphene nanoribbons with rashba spin–orbit interaction: the effects of spatial symmetry*, *Phys. Chem. Chem. Phys.* **19** (2017) 6871–6877. <http://dx.doi.org/10.1039/C6CP06972J>.

- [159] Q. Zhang, Z. Lin, and K. S. Chan, Spin polarization switching in monolayer graphene through a Rashba multi-barrier structure, *Applied Physics Letters* **102** no. 14, (Apr., 2013) 142407.
- [160] K. Zou, X. Hong, and J. Zhu, Effective mass of electrons and holes in bilayer graphene: Electron-hole asymmetry and electron-electron interaction, *Phys. Rev. B* **84** (Aug, 2011) 085408.
<https://link.aps.org/doi/10.1103/PhysRevB.84.085408>.
- [161] A. AlZahrani and G. Srivastava, Graphene to graphite: electronic changes within dft calculations, *Brazilian Journal of Physics* **39** no. 4, (2009) 694–698.
- [162] J. Zhao, H. Liu, Z. Yu, R. Quhe, S. Zhou, Y. Wang, C. C. Liu, H. Zhong, N. Han, J. Lu, Y. Yao, and K. Wu, Rise of silicene: A competitive 2d material, *Progress in Materials Science* **83** (2016) 24–151. <https://www.sciencedirect.com/science/article/pii/S0079642516300068>.
- [163] D. R. Hofstadter, Energy levels and wave functions of bloch electrons in rational and irrational magnetic fields, *Phys. Rev. B* **14** (Sep, 1976) 2239–2249.
<https://link.aps.org/doi/10.1103/PhysRevB.14.2239>.
- [164] P. Streda, Quantised hall effect in a two-dimensional periodic potential, .
<https://doi.org/10.1088/0022-3719/15/36/006>.
- [165] P. G. Harper, Single Band Motion of Conduction Electrons in a Uniform Magnetic Field, *Proceedings of the Physical Society A* **68** no. 10, (Oct., 1955) 874–878.
- [166] T. Schlösser, K. Ensslin, J. P. Kotthaus, and M. Holland, Landau subbands generated by a lateral electrostatic superlattice-chasing the hofstadter butterfly, *Semiconductor Science and Technology* **11** no. 11S, (1996) 1582.
- [167] C. R. Dean, L. Wang, P. Maher, C. Forsythe, F. Ghahari, Y. Gao, J. Katoch, M. Ishigami, P. Moon, M. Koshino, T. Taniguchi, K. Watanabe, K. L. Shepard, J. Hone, and P. Kim, Hofstadter's butterfly and the fractal quantum hall effect in moiré superlattices, *Nature* **497** no. 7451, (May, 2013) 598–602.
<https://doi.org/10.1038/nature12186>.

- [168] L. Ponomarenko, R. Gorbachev, G. Yu, D. Elias, R. Jalil, A. Patel, A. Mishchenko, A. Mayorov, C. Woods, J. Wallbank, et al., *Cloning of dirac fermions in graphene superlattices*, *Nature* **497** no. 7451, (2013) 594–597.
- [169] M. Aidelsburger, M. Atala, M. Lohse, J. T. Barreiro, B. Paredes, and I. Bloch, *Realization of the hofstadter hamiltonian with ultracold atoms in optical lattices*, *Physical Review Letters* **111** no. 18, (Oct, 2013) .
<http://dx.doi.org/10.1103/PhysRevLett.111.185301>.
- [170] H. Miyake, G. A. Siviloglou, C. J. Kennedy, W. C. Burton, and W. Ketterle, *Realizing the harper hamiltonian with laser-assisted tunneling in optical lattices*, *Physical Review Letters* **111** no. 18, (Oct, 2013) .
<http://dx.doi.org/10.1103/PhysRevLett.111.185302>.
- [171] D. Greif, T. Uehlinger, G. Jotzu, L. Tarruell, and T. Esslinger, *Short-range quantum magnetism of ultracold fermions in an optical lattice*, *Science* **340** no. 6138, (Jun, 2013) 1307–1310. <http://dx.doi.org/10.1126/science.1236362>.
- [172] T. Uehlinger, G. Jotzu, M. Messer, D. Greif, W. Hofstetter, U. Bissbort, and T. Esslinger, *Artificial graphene with tunable interactions*, *Phys. Rev. Lett.* **111** (Oct, 2013) 185307.
<https://link.aps.org/doi/10.1103/PhysRevLett.111.185307>.
- [173] R. S. Deacon, K.-C. Chuang, R. J. Nicholas, K. S. Novoselov, and A. K. Geim, *Cyclotron resonance study of the electron and hole velocity in graphene monolayers*, *Phys. Rev. B* **76** (Aug, 2007) 081406.
<https://link.aps.org/doi/10.1103/PhysRevB.76.081406>.
- [174] G. Li and E. Y. Andrei, *Observation of landau levels of dirac fermions in graphite*, *Nature physics* **3** no. 9, (2007) 623–627.
- [175] R. Rammal, *Landau level spectrum of bloch electrons in a honeycomb lattice*, *Journal de Physique* **46** no. 8, (1985) 1345–1354.
<https://doi.org/10.1051/jphys:019850046080134500>.
- [176] N. M. R. Peres, F. Guinea, and A. H. Castro Neto, *Electronic properties of disordered two-dimensional carbon*, *Phys. Rev. B* **73** (Mar, 2006) 125411.
<https://link.aps.org/doi/10.1103/PhysRevB.73.125411>.

- [177] Y. Zheng and T. Ando, *Hall conductivity of a two-dimensional graphite system*, *Phys. Rev. B* **65** (Jun, 2002) 245420.
<https://link.aps.org/doi/10.1103/PhysRevB.65.245420>.
- [178] K. S. Novoselov, Z. Jiang, Y. Zhang, S. V. Morozov, H. L. Stormer, U. Zeitler, J. C. Maan, G. S. Boebinger, P. Kim, and A. K. Geim, *Room-temperature quantum hall effect in graphene*, *Science* **315** no. 5817, (Mar, 2007) 1379–1379.
<http://dx.doi.org/10.1126/science.1137201>.
- [179] K. S. Novoselov, A. K. Geim, S. V. Morozov, D. Jiang, M. I. Katsnelson, I. V. Grigorieva, S. V. Dubonos, and A. A. Firsov, *Two-dimensional gas of massless dirac fermions in graphene*, *Nature* **438** no. 7065, (Nov, 2005) 197–200.
<http://dx.doi.org/10.1038/nature04233>.
- [180] P. Plochocka, C. Faugeras, M. Orlita, M. L. Sadowski, G. Martinez, M. Potemski, M. O. Goerbig, J.-N. Fuchs, C. Berger, and W. A. de Heer, *High-energy limit of massless dirac fermions in multilayer graphene using magneto-optical transmission spectroscopy*, *Phys. Rev. Lett.* **100** (Feb, 2008) 087401.
<https://link.aps.org/doi/10.1103/PhysRevLett.100.087401>.
- [181] M. L. Sadowski, G. Martinez, M. Potemski, C. Berger, and W. A. de Heer, *Landau level spectroscopy of ultrathin graphite layers*, *Phys. Rev. Lett.* **97** (Dec, 2006) 266405. <https://link.aps.org/doi/10.1103/PhysRevLett.97.266405>.
- [182] J. Kim, S. Baik, S. Ryu, Y. Sohn, S. Park, B. Park, J. Denlinger, Y. Yi, H. Choi, and K. Kim, *Observation of tunable band gap and anisotropic dirac semimetal state in black phosphorus*, *Science* **349** no. 6249, (Aug., 2015) 723–726. Publisher Copyright: © 2015, American Association for the Advancement of Science. All rights reserved.
- [183] X. Y. Zhou, R. Zhang, J. P. Sun, Y. L. Zou, D. Zhang, W. K. Lou, F. Cheng, G. H. Zhou, F. Zhai, and K. Chang, *Landau levels and magneto-transport property of monolayer phosphorene*, *Scientific Reports* **5** no. 1, (Jul, 2015).
<http://dx.doi.org/10.1038/srep12295>.
- [184] S. Yuan, E. van Veen, M. I. Katsnelson, and R. Roldán, *Quantum hall effect and semiconductor-to-semimetal transition in biased black phosphorus*, *Phys. Rev. B* **93**

- (Jun, 2016) 245433.
<https://link.aps.org/doi/10.1103/PhysRevB.93.245433>.
- [185] S. Yuan, H. De Raedt, and M. I. Katsnelson, *Modeling electronic structure and transport properties of graphene with resonant scattering centers*, *Phys. Rev. B* **82** (Sep, 2010) 115448.
<https://link.aps.org/doi/10.1103/PhysRevB.82.115448>.
- [186] S. Yuan, T. O. Wehling, A. I. Lichtenstein, and M. I. Katsnelson, *Enhanced screening in chemically functionalized graphene*, *Phys. Rev. Lett.* **109** (Oct, 2012) 156601.
<https://link.aps.org/doi/10.1103/PhysRevLett.109.156601>.
- [187] R. Kubo, M. Yokota, and S. Nakajima, *Statistical-mechanical theory of irreversible processes. ii. response to thermal disturbance*, *Journal of the Physical Society of Japan* **12** no. 11, (1957) 1203–1211, <https://doi.org/10.1143/JPSJ.12.1203>.
<https://doi.org/10.1143/JPSJ.12.1203>.
- [188] A. Bastin, C. Lewiner, O. Betbeder-matibet, and P. Nozieres, *Quantum oscillations of the hall effect of a fermion gas with random impurity scattering*, *Journal of Physics and Chemistry of Solids* **32** no. 8, (1971) 1811–1824. <https://www.sciencedirect.com/science/article/pii/S0022369771801476>.
- [189] F. Ortmann, N. Leconte, and S. Roche, *Efficient linear scaling approach for computing the kubo hall conductivity*, *Phys. Rev. B* **91** (Apr, 2015) 165117.
<https://link.aps.org/doi/10.1103/PhysRevB.91.165117>.
- [190] A. F. Young, C. R. Dean, L. Wang, H. Ren, P. Cadden-Zimansky, K. Watanabe, T. Taniguchi, J. Hone, K. L. Shepard, and P. Kim, *Spin and valley quantum hall ferromagnetism in graphene*, *Nature Physics* **8** no. 7, (May, 2012) 550–556.
<http://dx.doi.org/10.1038/nphys2307>.
- [191] B. Hunt, J. D. Sanchez-Yamagishi, A. F. Young, M. Yankowitz, B. J. LeRoy, K. Watanabe, T. Taniguchi, P. Moon, M. Koshino, P. Jarillo-Herrero, and et al., *Massive dirac fermions and hofstadter butterfly in a van der waals heterostructure*, *Science* **340** no. 6139, (May, 2013) 1427–1430.
<http://dx.doi.org/10.1126/science.1237240>.

- [192] M. Novak, S. Sasaki, K. Segawa, and Y. Ando, *Large linear magnetoresistance in the dirac semimetal tlbisse*, *Phys. Rev. B* **91** (Jan, 2015) 041203.
<https://link.aps.org/doi/10.1103/PhysRevB.91.041203>.
- [193] A. K. Geim and K. Novoselov, *The rise of graphene.*, *Nature materials* **6** (2007) 183–91.
- [194] G. G. Guzmán-Verri and L. C. Lew Yan Voon, *Electronic structure of silicon-based nanostructures*, *Phys. Rev. B* **76** (Aug, 2007) 075131.
<https://link.aps.org/doi/10.1103/PhysRevB.76.075131>.
- [195] J. Qiao, X. Kong, Z.-X. Hu, F. Yang, and W. Ji, *High-mobility transport anisotropy and linear dichroism in few-layer black phosphorus*, *Nature Communications* **5** no. 1, (Jul, 2014) 4475. <https://doi.org/10.1038/ncomms5475>.
- [196] S. Lebègue and O. Eriksson, *Electronic structure of two-dimensional crystals from ab initio theory*, *Phys. Rev. B* **79** (Mar, 2009) 115409.
<https://link.aps.org/doi/10.1103/PhysRevB.79.115409>.
- [197] K. F. Mak, K. He, J. Shan, and T. F. Heinz, *Control of valley polarization in monolayer mos₂ by optical helicity*, *Nature Nanotechnology* **7** no. 8, (Jun, 2012) 494–498. <http://dx.doi.org/10.1038/nnano.2012.96>.
- [198] P. M. Krstajić, P. Vasilopoulos, and M. Tahir, *Spin- and valley-polarized transport in a monolayer of mos₂*, *Phys. Rev. B* **94** (Aug, 2016) 085413.
<https://link.aps.org/doi/10.1103/PhysRevB.94.085413>.
- [199] A. D. Zabolotskiy and Y. E. Lozovik, *Strain-induced pseudomagnetic field in the dirac semimetal borophene*, *Phys. Rev. B* **94** (Oct, 2016) 165403.
<https://link.aps.org/doi/10.1103/PhysRevB.94.165403>.
- [200] M. N. Ali, Q. D. Gibson, T. Klimczuk, and R. J. Cava, *Noncentrosymmetric superconductor with a bulk three-dimensional dirac cone gapped by strong spin-orbit coupling*, *Phys. Rev. B* **89** (Jan, 2014) 020505.
<https://link.aps.org/doi/10.1103/PhysRevB.89.020505>.
- [201] P. E. Allain and J. N. Fuchs, *Klein tunneling in graphene: optics with massless electrons*, *The European Physical Journal B* **83** no. 3, (Oct, 2011) 301–317.
<http://dx.doi.org/10.1140/epjb/e2011-20351-3>.

- [202] S. Banerjee and W. E. Pickett, *Phenomenology of a semi-dirac semi-weyl semimetal*, *Physical Review B* **86** no. 7, (Aug, 2012) .
<http://dx.doi.org/10.1103/PhysRevB.86.075124>.
- [203] H. Huang, Z. Liu, H. Zhang, W. Duan, and D. Vanderbilt, *Emergence of a chern-insulating state from a semi-dirac dispersion*, *Phys. Rev. B* **92** (Oct, 2015) 161115. <https://link.aps.org/doi/10.1103/PhysRevB.92.161115>.
- [204] P. V. Sriluckshmy, K. Saha, and R. Moessner, *Interplay between topology and disorder in a two-dimensional semi-dirac material*, *Phys. Rev. B* **97** (Jan, 2018) 024204. <https://link.aps.org/doi/10.1103/PhysRevB.97.024204>.
- [205] P. Delplace, A. Gómez-León, and G. Platero, *Merging of dirac points and floquet topological transitions in ac-driven graphene*, *Phys. Rev. B* **88** (Dec, 2013) 245422. <https://link.aps.org/doi/10.1103/PhysRevB.88.245422>.
- [206] F. Piéchon, J.-N. Fuchs, A. Raoux, and G. Montambaux, *Tunable orbital susceptibility in $\alpha - t_3$ tight-binding models*, *Journal of Physics: Conference Series* **603** (Apr, 2015) 012001.
<http://dx.doi.org/10.1088/1742-6596/603/1/012001>.
- [207] P. Sinha, S. Murakami, and S. Basu, *Quantum hall studies of a semi-dirac nanoribbon*, *Phys. Rev. B* **102** (Aug, 2020) 085416.
<https://link.aps.org/doi/10.1103/PhysRevB.102.085416>.
- [208] P. U. Jepsen, D. G. Cooke, and M. Koch, *Terahertz spectroscopy and imaging – Modern techniques and applications*, vol. 5. 2011.
<https://doi.org/10.1002/lpor.201000011>.
- [209] S. Koenig, D. Lopez-Diaz, J. Antes, F. Boes, R. Henneberger, A. Leuther, A. and Tessmann, R. Schmogrow, D. Hillerkuss, R. Palmer, T. Zwick, C. Koos, W. Freude, O. Ambacher, J. Leuthold, and I. Kallfass, *Wireless sub-thz communication system with high data rate*, *Nature Photonics* **7** no. 12, (Dec, 2013) 977–981. <https://doi.org/10.1038/nphoton.2013.275>.
- [210] I. Crassee, J. Levallois, A. L. Walter, M. Ostler, A. Bostwick, E. Rotenberg, T. Seyller, D. van der Marel, and A. B. Kuzmenko, *Giant faraday rotation in single- and multilayer graphene*, *Nature Physics* **7** no. 1, (Jan, 2011) 48–51.
<https://doi.org/10.1038/nphys1816>.

- [211] H. Yan, Z. Li, X. Li, W. Zhu, P. Avouris, and F. Xia *Nano Letters* **12** no. 7, (July, 2012) 3766–3771.
- [212] M. Glazov and S. Ganichev, *High frequency electric field induced nonlinear effects in graphene*, *Physics Reports* **535** no. 3, (Feb, 2014) 101–138.
<http://dx.doi.org/10.1016/j.physrep.2013.10.003>.
- [213] L. Ju, B. Geng, J. Horng, C. Girit, M. Martin, Z. Hao, H. A. Bechtel, X. Liang, A. Zettl, Y. R. Shen, and F. Wang, *Graphene plasmonics for tunable terahertz metamaterials*, *Nature nanotechnology* **6** no. 10, (September, 2011) 630–634.
<https://doi.org/10.1038/nnano.2011.146>.
- [214] P. Alonso-González, A. Y. Nikitin, Y. Gao, A. Woessner, M. B. Lundberg, A. Principi, N. Forcellini, W. Yan, S. Vélez, A. J. Huber, K. Watanabe, T. Taniguchi, F. Casanova, L. E. Hueso, M. Polini, J. Hone, F. H. L. Koppens, and R. Hillenbrand, *Acoustic terahertz graphene plasmons revealed by photocurrent nanoscopy*, *Nature Nanotechnology* **12** no. 1, (Jan, 2017) 31–35.
<https://doi.org/10.1038/nnano.2016.185>.
- [215] A. N. Grigorenko, M. Polini, and K. Novoselov, *Graphene plasmonics*, *Nature photonics* **6** no. 11, (2012) 749–758.
- [216] M. B. Lundberg, Y. Gao, R. Asgari, C. Tan, B. Van Duppen, M. Autore, P. Alonso-González, A. Woessner, K. Watanabe, T. Taniguchi, and et al., *Tuning quantum nonlocal effects in graphene plasmonics*, *Science* **357** no. 6347, (Jun, 2017) 187–191. <http://dx.doi.org/10.1126/science.aan2735>.
- [217] V. P. Gusynin, S. G. Sharapov, and J. P. Carbotte, *Magneto-optical conductivity in graphene*, *Journal of Physics: Condensed Matter* **19** no. 2, (Dec, 2006) 026222.
<http://dx.doi.org/10.1088/0953-8984/19/2/026222>.
- [218] Z. Jiang, E. A. Henriksen, L. C. Tung, Y.-J. Wang, M. E. Schwartz, M. Y. Han, P. Kim, and H. L. Stormer, *Infrared spectroscopy of landau levels of graphene*, *Phys. Rev. Lett.* **98** (May, 2007) 197403.
<https://link.aps.org/doi/10.1103/PhysRevLett.98.197403>.
- [219] A. A. Schafgans, K. W. Post, A. A. Taskin, Y. Ando, X.-L. Qi, B. C. Chapler, and D. N. Basov, *Landau level spectroscopy of surface states in the topological insulator*

- bi_{0,91}sb_{0,09} via magneto-optics*, *Phys. Rev. B* **85** (May, 2012) 195440.
<https://link.aps.org/doi/10.1103/PhysRevB.85.195440>.
- [220] V. P. Gusynin, S. G. Sharapov, and J. P. Carbotte, *Anomalous absorption line in the magneto-optical response of graphene*, *Phys. Rev. Lett.* **98** (Apr, 2007) 157402.
<https://link.aps.org/doi/10.1103/PhysRevLett.98.157402>.
- [221] Z. Li, E. A. Henriksen, Z. Jiang, Z. Hao, M. C. Martin, P. Kim, H. L. Stormer, and D. N. Basov, *Dirac charge dynamics in graphene by infrared spectroscopy*, *Nature physics* **4** no. 7, (2008) 532–535.
- [222] W.-K. Tse and A. H. MacDonald, *Magneto-optical faraday and kerr effects in topological insulator films and in other layered quantized hall systems*, *Phys. Rev. B* **84** (Nov, 2011) 205327.
<https://link.aps.org/doi/10.1103/PhysRevB.84.205327>.
- [223] R.-L. Chu, X. Li, S. Wu, Q. Niu, W. Yao, X. Xu, and C. Zhang, *Valley-splitting and valley-dependent inter-landau-level optical transitions in monolayer mos₂ quantum hall systems*, *Phys. Rev. B* **90** (Jul, 2014) 045427.
<https://link.aps.org/doi/10.1103/PhysRevB.90.045427>.
- [224] J. P. Carbotte, J. P. F. LeBlanc, and E. J. Nicol, *Emergence of plasmaronic structure in the near-field optical response of graphene*, *Phys. Rev. B* **85** (May, 2012) 201411.
<https://link.aps.org/doi/10.1103/PhysRevB.85.201411>.
- [225] M. Tahir, P. Vasilopoulos, and F. M. Peeters, *Magneto-optical transport properties of monolayer phosphorene*, *Phys. Rev. B* **92** (Jul, 2015) 045420.
<https://link.aps.org/doi/10.1103/PhysRevB.92.045420>.
- [226] P. E. C. Ashby and J. P. Carbotte, *Magneto-optical conductivity of weyl semimetals*, *Phys. Rev. B* **87** (Jun, 2013) 245131.
<https://link.aps.org/doi/10.1103/PhysRevB.87.245131>.
- [227] J. Shao and G. Yang, *Magneto-optical conductivity of weyl semimetals with quadratic term in momentum*, *AIP Advances* **6** no. 2, (2016) 025312.
- [228] M. Stålhammar, J. Larana-Aragon, J. Knolle, and E. J. Bergholtz, *Magneto-optical conductivity in generic weyl semimetals*, *Physical Review B* **102** no. 23, (2020) 235134.

- [229] K. Ziegler and A. Sinner, *Lattice symmetries, spectral topology and opto-electronic properties of graphene-like materials*, *EPL (Europhysics Letters)* **119** no. 2, (2017) 27001.
- [230] J. P. Carbotte, K. R. Bryenton, and E. J. Nicol, *Optical properties of a semi-dirac material*, *Phys. Rev. B* **99** (Mar, 2019) 115406.
<https://link.aps.org/doi/10.1103/PhysRevB.99.115406>.
- [231] A. Mawrie and B. Muralidharan, *Direction-dependent giant optical conductivity in two-dimensional semi-dirac materials*, *Phys. Rev. B* **99** (Feb, 2019) 075415.
<https://link.aps.org/doi/10.1103/PhysRevB.99.075415>.
- [232] X. Zhou, W. Chen, and X. Zhu, *Anisotropic magneto-optical absorption and linear dichroism in two-dimensional semi-dirac electron systems*, *Phys. Rev. B* **104** (Dec, 2021) 235403. <https://link.aps.org/doi/10.1103/PhysRevB.104.235403>.
- [233] P. Sinha, S. Murakami, and S. Basu, *Magneto-optical properties of a semi-dirac nanoribbon in the terahertz frequency regime*, 2021.
- [234] A. Ferreira, J. Viana-Gomes, Y. V. Bludov, V. Pereira, N. M. R. Peres, and A. H. Castro Neto, *Faraday effect in graphene enclosed in an optical cavity and the equation of motion method for the study of magneto-optical transport in solids*, *Phys. Rev. B* **84** (Dec, 2011) 235410.
<https://link.aps.org/doi/10.1103/PhysRevB.84.235410>.
- [235] R. Shimano, G. Yumoto, J. Yoo, R. Matsunaga, S. Tanabe, H. Hibino, T. Morimoto, and H. Aoki, *Quantum faraday and kerr rotations in graphene*, *Nature communications* **4** no. 1, (2013) 1–6.
- [236] L. V. Keldysh et al., *Diagram technique for nonequilibrium processes*, *Sov. Phys. JETP* **20** no. 4, (1965) 1018–1026. <http://www-thphys.physics.ox.ac.uk/talks/CMTjournalclub/sources/Keldysh.pdf>.
- [237] S. João and J. V. P. Lopes, *Basis-independent spectral methods for non-linear optical response in arbitrary tight-binding models*, *Journal of Physics: Condensed Matter* **32** no. 12, (2019) 125901.
- [238] Y. Zhang, Z. Jiang, J. P. Small, M. S. Purewal, Y.-W. Tan, M. Fazlollahi, J. D. Chudow, J. A. Jaszczak, H. L. Stormer, and P. Kim, *Landau-level splitting in*

graphene in high magnetic fields, Phys. Rev. Lett. **96** (Apr, 2006) 136806.

<https://link.aps.org/doi/10.1103/PhysRevLett.96.136806>.

- [239] J. Li, Y. Sun, M. Wu, and H. Pan, *Novel electric field effects on magneto-optical conductivity in eight-pmmn borophene*, Journal of Physics: Condensed Matter **33** no. 18, (2021) 185501.





Curriculum Vitae

Priyanka Sinha was born on 28th February, 1992 in Raghunathganj, India. She completed her B.Sc. with Physics Honours in 2012 from Maharajadhiraj Uday Chand Women's College, under University of Burdwan and M.Sc. in physics from Vidyasagar University in 2014. She had enrolled into the Ph.D. programme at Indian Institute of Technology Guwahati in 2016. She had qualified Graduate Aptitude Test in Engineering (GATE) in 2016. She has earned the Senior Research Fellowship in 2018 by Indian Institute of Technology Guwahati.